Helicity Methods in
LO and NLO QCD Calculations

Daniel Götz
geboren in Kirchheimbolanden

Mainz, 2014

JG|U

JOHANNES GUTENBERG
UNIVERSITÄT MAINZ

Abstract

The goal of this thesis is the acceleration of numerical calculations of QCD observables, both at leading order and next–to–leading order in the coupling constant. In particular, the optimization of helicity and spin summation in the context of *VEGAS* Monte Carlo algorithms is investigated. In the literature, two such methods are mentioned but without detailed analyses. Only one of these methods can be used at next–to–leading order.

This work presents a total of five different methods that replace the helicity sums with a Monte Carlo integration. This integration can be combined with the existing phase space integral, in the hope that this causes less overhead than the complete summation. For three of these methods, an extension to existing subtraction terms is developed which is required to enable next–to–leading order calculations. All methods are analyzed with respect to efficiency, accuracy, and ease of implementation before they are compared with each other. In this process, one method shows clear advantages in relation to all others.

Zusammenfassung

Ziel dieser Arbeit ist es, die numerische Berechnung von QCD Observablen sowohl auf führender Ordnung als auch auf nächst-führender Ordnung in der Kopplungskonstante zu beschleunigen. Konkret wird eine solche Optimierung im Gebiet der Helizitäts- und Spinsummen im Zusammenhang mit dem *VEGAS*-Monte-Carlo-Algorithmus untersucht. In der Literatur werden zwei solcher Methoden erwähnt, jedoch ohne detaillierte Analysen. Nur eine dieser Methoden ist auf die nächst-führende Ordnung anwendbar.

Diese Arbeit stellt insgesamt fünf verschiedene Methoden vor, welche die Helizitätssummen durch eine Monte-Carlo-Integration ersetzen. Diese kann mit dem existierenden Phasenraumintegral kombiniert werden, in der Hoffnung dass dies einen geringeren Mehraufwand als die vollständige Summation bietet. Für drei der Methoden wird eine Erweiterung von existierenden Subtraktionstermen entwickelt, die auf nächst-führender Ordnung benötigt wird. Alle Methoden werden analysiert im Bezug auf Effizienz, Genauigkeit und Implementierbarkeit, und anschließend verglichen. Dabei zeigt eine Methode klare Vorteile vor allen anderen.

Contents

Introduction

1

Since the discovery of the Higgs boson announced on July 4th, 2012 and its subsequent honor in terms of 2013's Nobel prize, there is no doubt that the LHC has fulfilled what the general public perceives as the purpose it was built for. Of course, discovering the last remaining building block of the Standard Model of particle physics is only one of main goals physicists had when designing the 27 km radius machine. First of all, merely discovering the Higgs boson does not answer all questions about its properties and its production and decay channels—this is ongoing research. Apart from the Higgs boson, it is also clear that the Standard Model is not the final answer to all open questions in particle physics. High energy physicists all over the world are waiting to find signs of so-called "physics beyond the standard model".

One might think that with the huge amount of data that the LHC collects during every minute of its runtime one should have discovered many new phenomena by now. However, reality is much more complicated than just the amount of data that is gathered per time. Due to the hadronic nature of LHC particle collisions in combination with the unprecedented high energies it is running at[1], the final states are populated by a large amount of QCD radiation that can easily obfuscate signals of new particles or phenomena that one wants to discover. An example which is taken from [1] is shown in figure 1.1. It is indispensable to have a very good knowledge of so-called *background processes* in order to be able to filter them out and reveal possible so-called *signals*.

The problem with knowing the background well is that QCD calculations quickly become very involved as one requires more precision. In the Standard Model which QCD is a part of, one performs calculations for high energy observables (high energy meaning with scales much larger than $\Lambda_{\mathrm{QCD}} \approx 1\,\mathrm{GeV}$, which is certainly the case at colliders such as the LHC) by means of *perturbation theory* which is essentially a series expansion of the full expression in the coupling constant of the theory. Leading order QCD calculations of this expansion are considered a solved problem since the end of the 20th century at least; there exist many automated numerical programs that can compute in principle any process that

---

[1] 8 TeV in 2012; an upgrade to 13 TeV is currently worked on and expected to be finished in early 2015, with its final center-of-mass energy of 14 TeV to be reached some time later.
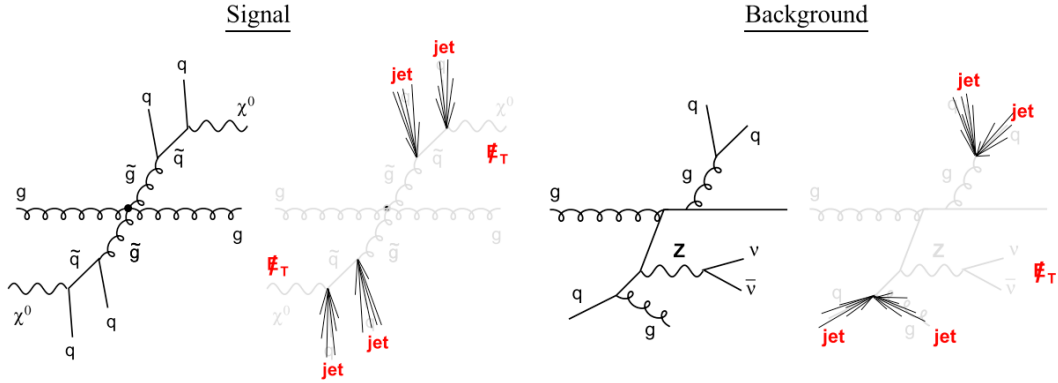
Figure 1.1: The left diagram shows a so-called *signal* process for gluino production with subsequent decay into quarks and neutralinos, which is the process one wants to investigate. In an experiment, shown in the second graph, the quarks are detected as QCD jets while the neutralinos cannot be detected directly and only appear in terms of missing energy, $\not{E}_T$. The two right hand diagrams show a corresponding *background* process, which is a Standard Model QCD process with the production of a Z boson; it decays into neutrinos. The QCD partons again appear as jets in the detector while we have missing energy from the neutrinos. Thus, the two are virtually indistinguishable. Picture taken from [1].

one desires. At the LHC's energies, however, leading order calculations are not enough to describe the processes accurately enough. During the last decade, many physicists have worked at devising methods to bring numerical QCD calculations to next–to–leading order, which is a big step up from leading order calculations as we will illustrate in this thesis. Part of the problem has been solved in the late 1990's by Catani and Seymour with their so-called *dipole formalism* that is almost ubiquitously used nowadays to cancel *infrared divergences*. This method is based on a more fundamental idea, the so-called *subtraction method* which we will detail in the thesis.

The remaining half of the problem, diagrams with loops that give rise to the *virtual contributions* are not so easily dealt with. By now, several groups have established different methods to perform such computations and it is sometimes even said that next–to–leading order QCD is on the verge of becoming a solved problem. Probably the most well-known of these groups is the *BlackHat* collaboration (see for example [2–6]) that uses *unitarity methods*, which in a very basic sense means decomposing amplitudes into known master integrals so that they only have to compute the coefficients to these integrals. Other groups that use (slightly) different methods are e.g. *OpenLoops* ([7], a more traditional approach related to Feynman diagrams combined with tensor reduction), *GoSam* ([8, 9], also Feynman diagrams and reduction methods), and *NJet* ([10, 11], similar to *BlackHat*).

In the last few years, another contender was born in the same group where this work was performed. It avoids the use of precomputed master integrals and extends the so-called *subtraction method* that forms the basis of the dipole formalism to the ultraviolet divergences of the virtual contributions; an introduction can be found in this thesis.

A problem that all of these methods share is the complexity of the calculations. Some

groups such as *BlackHat* do not worry much about the necessary time it takes to produce proper data by generating a large amount of very general samples once and then distributing them to interested experimenters; this has the disadvantage that the files they have to transfer are huge, $\mathcal{O}$ (TB) per process, which approaches the limit of modern hard disks. The method developed in the group of S. Weinzierl, on the other hand, aims at performing these calculations on demand. Experimenters download the (small) source code, install the program and run it with their choice of experimental parameters. Here, complexity and computation time are major concerns, but if tackled properly the user can obtain precise results tailored to his needs in short time.

This is where this work comes into play. A full next–to–leading order calculation consists of many building blocks, each providing room for optimization and acceleration of the calculation. In this thesis we investigate the treatment of helicities[2] as a possible place for optimization. The classical way of dealing with helicities of particles is to sum over all final state helicities and average the initial ones, since usually colliders cannot distinguish different helicities, neither in the beam nor in the detectors. Given that every QCD particle has two helicity settings, this amounts to a sum of 2^n terms where n is the total number of particles in the process. In numerical calculations, for reasons that will be detailed in this thesis, this amounts to the computation of 2^n squared amplitudes, which are by far the most involved quantities in these calculations. The goal is to reduce this growth as much as possible and thus decrease computation time, especially for high multiplicity observables which are increasingly important at high energies.

In this thesis, we illustrate three methods to reduce the number of helicity amplitudes down to one. Two of them can be implemented in two different ways, which in turn can have a large effect on their respective efficiency, as will become clear. All of these methods are simple to use for leading order calculations, while the subtraction method requires special attention at next–to–leading order. For half of the methods we present, the necessary so-called *subtraction terms* already exist and we will introduce the reader to these methods. For the other half, we develop new subtraction terms that enable the usage of the helicity methods also at next–to–leading order.

All but one of the helicity methods have been mentioned in the literature, but apart from definitions and short descriptions, there is not much information available. This thesis aims at providing a detailed description and analysis of these methods, which is completed by a comparison of their performance.

The thesis is structured as follows:

- First, we delve a bit deeper into the Standard Model, perturbation theory and the theoretical basics of QCD calculations to give the reader the necessary theoretical understanding.

- Then in chapter 3, we detail the realization of these calculations in terms of numerical

---

[2]Note that for massive particles, one usually uses the word spins instead of helicities. However, we will use *helicities* to avoid unnecessary distinction; a more detailed explanation and clarification on this follows in chapter 4.

algorithms that can be implemented in a computer program, such as color decomposition, recursive methods, spinor helicity methods, Monte Carlo integration, etc. Techniques presented there will be the backbone for all methods that are explained in the subsequent chapters.

- Chapter 4 presents the "classical" method of computing the helicity sum in numerical programs. We highlight the disadvantages of the method and present the subtraction terms of Catani and Seymour's *dipole formalism* that enables next–to–leading order computations.

- In chapters 5 to 7, we present different helicity methods that avoid the helicity sum. While subtraction terms exist for the first method, those presented in chapters 6 and 7 require new subtraction terms. The next–to–leading order method of chapter 6 has largely been developed in collaboration with C. Schwan and S. Weinzierl, whereas the adaptation of the method in chapter 7 is the work of the author of this thesis. For each method, we present all necessary terms to perform both leading order and next–to–leading order computations. Each method is analyzed with respect to the Monte Carlo integration algorithm.

- Chapter 8 compares the different methods and attempts to recommend a helicity method that yields the best results.

- Finally, we conclude all our findings in chapter 9 and give an outlook on what can be researched further in the area of helicity methods and numerical algorithms.

Principles of QCD and Collider Physics

2

Before we go into the details of the techniques employed in this thesis, we introduce the basics of particle physics and detail the fundamental building blocks this work is built upon. We start with the QCD Lagrangian and touch on all theoretical concepts that go into the calculation of observables. Since our code operates at the level of hard scattering, we focus on partonic cross sections. Note that most of this chapter is based on the introductory texts [1, 12].

2.1   The QCD Lagrangian and Feynman Rules

At the heart of the strong interactions lies the QCD Lagrangian

$$\mathcal{L}_{\text{QCD}} = \overline{q}_f \left(i \slashed{D} - m_f \right) q_f - \frac{1}{4} \mathcal{G}^a_{\mu\nu} \mathcal{G}^{\mu\nu}_a . \tag{2.1}$$

Therein, we find quark and antiquark fields with an explicit flavor index f which represents either an up-type flavor (up, charm, top) or a down-type flavor (down, strange, bottom) where each flavor has its own mass m_f. Also, we find the covariant derivative

$$D^\mu = \partial^\mu + i g_{\text{s}} T^a A^\mu_a \tag{2.2}$$

which couples quarks to gluons given by the field A_μ with the coupling strength g_{s}. The second term contains the kinetic term for the gluon fields where

$$\mathcal{G}^{\mu\nu}_a = \partial^\mu A^\nu_a - \partial^\nu A^\mu_a - g_{\text{s}} f^{abc} A^\mu_b A^\nu_c \tag{2.3}$$

and A^μ_a are the eight gluon fields ($a = 1, \dots, 8$; adjoint representation of $SU(3)$). Note that we omitted color information for the (anti-)quarks: they carry one of three (anti-)colors usually denoted by the letters i and j (fundamental representation of $SU(3)$). T^a as it occurs in the definition of the covariant derivative is one of eight color matrices which are usually given by the well-known Gell-Mann matrices divided by two, $T^a = {}^{\lambda^a}/_2$. Pictorially

speaking, these matrices only allow for certain color combinations of quarks and gluons to be coupled to one another. The same is true for the third term in the gluon field strength tensor, equation (2.3), where f^{abc} is the $SU(3)$ structure constant that determines what happens when gluons with different colors a, b and c interact. This is the term that differentiates QCD from Quantum Electrodynamics (QED) the most. It is only there due to the non-abelian nature of $SU(3)$ and causes gauge boson self-interactions in terms of three-gluon and four-gluon vertices which are not present in QED.

The fact that QCD is a $SU(3)$ gauge theory becomes apparent when we look at the associated transformations of the quark and gluon fields:

$$q_f \to \exp\left(\mathrm{i} \sum_{a=1}^{8} \theta_a(x) T^a \right) q_f \equiv U q_f \tag{2.4a}$$

$$A^\mu \equiv A_a^\mu T^a \to U A^\mu U^\dagger - \frac{\mathrm{i}}{g_\mathrm{s}} \partial^\mu U U^\dagger. \tag{2.4b}$$

Therein, $\theta_a(x)$ are eight functions of the space-time coordinate x which parameterize the $SU(3)$ transformation. The QCD Lagrangian is invariant under these transformations.

From QCD's Lagrangian, one can derive the corresponding Feynman rules which are then used to compute amplitudes for QCD processes. The first term of equation (2.1) where we only consider the partial derivative of the covariant derivative yields the quark propagator:

$$\underset{i}{\overset{f}{\longrightarrow}} \underset{j}{\overset{f'}{}} \quad = \quad \frac{\mathrm{i}\delta^{ij}\delta^{f'f}}{\not{p} - m_f + \mathrm{i}0} \tag{2.5}$$

Herein, we explicitly gave the quark and antiquark different flavor and color indices; note that this rule tells us that a free propagating quark can neither change its color nor its flavor. The symbol p denotes the momentum of the (anti-)quark.

Similarly, from the kinetic term for the gluon fields without the f^{abc} term (see equation (2.3)) we obtain the gluon propagator

$$\underset{\mu}{\overset{a}{}} \overset{k}{\underset{}{\text{〜〜〜〜〜}}} \underset{\nu}{\overset{b}{}} \quad = \quad \frac{-\mathrm{i}\delta^{ab}}{k^2 + \mathrm{i}0} \left(g^{\mu\nu} + (\xi - 1) \frac{k^\mu k^\nu}{k^2 + \mathrm{i}0} \right). \tag{2.6}$$

Here, k is the momentum of the gluon. ξ is an (arbitrary) gauge parameter; a frequent choice is the 't Hooft-Feynman gauge $\xi = 1$.

In diagrams with loops, we also need so-called *ghost* loops where an unphysical particle propagates to cancel superfluous degrees of freedom. These particles have the propagator

$$\underset{}{\overset{a}{}} \cdots\blacktriangleright\cdots \overset{b}{} \quad = \quad \frac{\mathrm{i}\delta^{ab}}{k^2 + \mathrm{i}0}. \tag{2.7}$$

The more interesting part of the Feynman rules are the interactions. From the quark

term together with the second part of the covariant derivative, we obtain the interaction vertex of two quarks and a gluon:

$$= -ig_s \delta^{f'f} (T^a)^{ij} \gamma^\mu. \tag{2.8}$$

Analogously, if we now consider all terms of the gluon piece that contain the f^{abc} term, we obtain gluon self-interactions, as discussed above:

$$= g_s f^{abc} \left[g^{\mu\nu}(k_1 - k_2)^\rho + g^{\nu\rho}(k_2 - k_3)^\mu + g^{\rho\mu}(k_3 - k_1)^\nu \right], \tag{2.9a}$$

$$= -ig_s^2 \left[\begin{array}{c} f^{abe} f^{cde} (g^{\mu\rho} g^{\nu\sigma} - g^{\mu\sigma} g^{\nu\rho}) \\ + f^{ace} f^{bde} (g^{\mu\nu} g^{\rho\sigma} - g^{\mu\sigma} g^{\nu\rho}) \\ + f^{ade} f^{bce} (g^{\mu\nu} g^{\rho\sigma} - g^{\mu\rho} g^{\nu\sigma}) \end{array} \right]. \tag{2.9b}$$

All rules that we discussed so far concern the internal structure of an amplitude; for example, propagators describe internal particle lines whose momenta are in general off shell momenta. External particles, on the other hand, are on shell ($p^2 = m^2$) and are described by polarization vectors and spinors:

$$\mu \;\;\;\;\; \overset{k}{\sim\!\sim\!\sim\!\sim}\;\bullet \;\; = \epsilon_\mu^{\lambda *}(k), \qquad \overset{\rightarrow\; p}{\longrightarrow}\;\bullet \;\; = u^\lambda(p), \qquad \overset{\rightarrow\; p}{\longleftarrow}\;\bullet \;\; = \bar{v}^\lambda(p), \tag{2.10a}$$

$$\bullet\;\overset{k}{\sim\!\sim\!\sim\!\sim}\; \mu \;\; = \epsilon_\mu^\lambda(k), \qquad \bullet\;\overset{\rightarrow\; p}{\longrightarrow}\;\; = \bar{u}^\lambda(p), \qquad \bullet\;\overset{\rightarrow\; p}{\longleftarrow}\;\; = v^\lambda(p). \tag{2.10b}$$

The upper row shows the case of ingoing particles while the lower row shows outgoing rules. Note that these rules apply generally to bosons (hence the wiggly line) and to fermions. Each external leg depends on the spin or helicity λ of the particle which we have indicated by a superscript. This is the information that this thesis is focused on. Note, however, that we will start discussing spins and helicities only from chapter 4 on; we first present all other fundamental aspects in order to simplify the discussion later on.

These rules are the necessary tools to build diagrams which are a pictorial representation of QCD amplitudes. It is clear that using the above set of rules, one can draw an infinite set of diagrams for any given number of external particles (i.e. lines where only one end

of the leg is connected to a vertex while the other one points outwards). To solve QCD one would indeed have to calculate exactly this infinite amount of diagrams, which is impossible in practice. This is where perturbation theory comes into play. Perturbation theory is based on an expansion of an observable into a series in the coupling constant $g = \sqrt{4\pi\alpha}$. As an example, one could write the full hadronic cross section σ_{tot} as follows:

$$\sigma_{\text{tot}} = \sigma_0 \alpha_s^0 + \sigma_1 \alpha_s^1 + \sigma_2 \alpha_s^2 + \sigma_3 \alpha_s^3 + \sigma_4 \alpha_s^4 + \ldots, \tag{2.11}$$

where the coefficients depend on the specific process considered.[1] Provided that the QCD coupling is a small constant, $\alpha_s \ll 1$, it is safe to approximate the full cross section by the first one or two terms in the above series and ignore the remaining terms since they should be much smaller.

2.2 The Strong Coupling Constant α_s

In fact, neither of the coupling constants of the Standard Model or any quantum field theory are really constant, as is well-known (see for example [1, 12, 13] and many others). Depending on the energy scale μ of the problem at hand, the value of the coupling constant changes, i.e. we will write $\alpha = \alpha(\mu^2)$. This change is governed by the so-called beta function via the renormalization equation

$$\mu^2 \frac{\mathrm{d}\alpha(\mu^2)}{\mathrm{d}\mu^2} = \frac{\mathrm{d}\alpha(\mu^2)}{\mathrm{d}\ln\mu^2} = \beta\big(\alpha(\mu^2)\big), \qquad \beta(\alpha) = \alpha(b_0 + b_1\alpha + b_2\alpha^2 + \ldots) \tag{2.12}$$

which is given here for a general coupling (for example, this could be the QED or the QCD coupling; however, each coupling has it's own beta function coefficients b_i). While QED exhibits a positive beta function meaning that the coupling increases with growing scale μ, QCD has the peculiar feature that the overall beta function is negative which becomes obvious when we look at the first two coefficients:

$$\begin{aligned} b_0 &= -\frac{11C_A - 4T_R N_f}{12\pi} = -\left(\frac{11}{4\pi} - \frac{N_f}{6\pi}\right), \\ b_1 &= -\frac{17C_A - 10T_R C_A N_f - 6T_R C_F N_f}{24\pi^2} = -\frac{153 - 19N_f}{24\pi^2}. \end{aligned} \tag{2.13}$$

The above formulas require some explanation concerning the different symbols that appear within. C_A, C_F and T_R are the usual Casimir operators of the group $SU(N)$. In QCD, $N = N_c = 3$ (N_c represents the *Number of Colors*) and we find

$$C_A = N_c = 3, \quad C_F = \frac{N_c^2 - 1}{2N_c} = \frac{4}{3}, \quad T_R = \frac{1}{2}. \tag{2.14}$$

---

[1]Hadronic cross sections start at α_s^2 while electron–positron annihilation processes also have non-zero σ_0 and σ_1 coefficients.
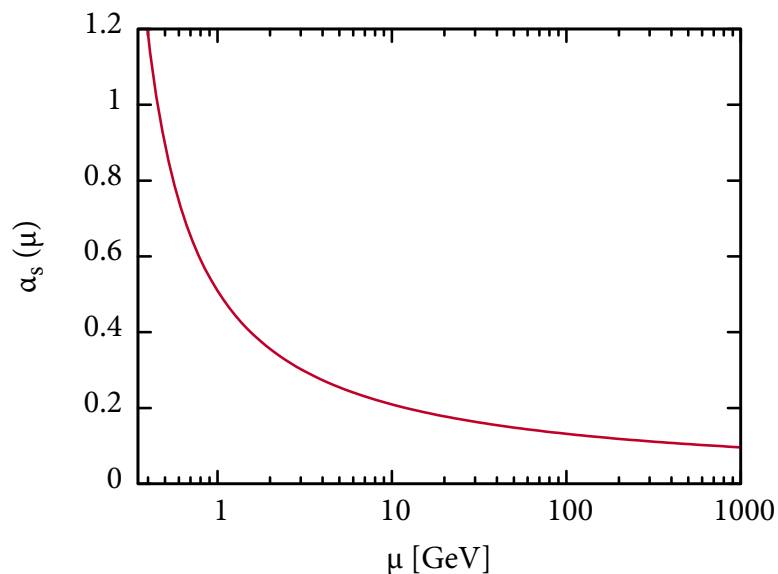
Figure 2.1: The running of α_s as given by equation (2.16).

N_f stands for the number of quark flavors whose mass is below the scale μ. Inserting these values, one can read off of the leading coefficient b_0 that the beta function has a positive sign if N_f is at least 17 (while the Standard Model contains only six quark flavors in total). Thus, it is clear that the QCD beta function has a negative sign.

This means that the coupling *decreases* as the energy scale increases while for small energies the coupling becomes large. Theories with this feature are called *asymptotically free* since the coupling approaches zero with high energies and quarks and gluons become increasingly "free". Assuming that we know the value of α_s at one scale μ_0, we can obtain the value at another scale μ by solving equation (2.12):

$$\alpha_s(\mu^2) = \frac{\alpha_s(\mu_0^2)}{1 + b_0 \alpha_s(\mu_0^2) \ln \frac{\mu^2}{\mu_0^2} + \mathcal{O}\left(\alpha_s^2\right)}. \tag{2.15}$$

Experimentally, it is well-known that the coupling becomes non-perturbative at scales below $\Lambda_{\mathrm{QCD}} \approx 200\,\mathrm{MeV}$ which determines the scale at which the coupling diverges. Setting $\mu_0 = \Lambda_{\mathrm{QCD}}$, we can re-write the above equation into

$$\alpha_s(\mu^2) \approx \frac{1}{b_0 \ln \frac{\mu^2}{\Lambda_{\mathrm{QCD}}^2}} \tag{2.16}$$

which gives us the behavior shown in figure 2.1. Note that this plot only gives a qualitative result since it is based on a perturbative calculation which should not be trusted in low-energy regions where the coupling becomes non-perturbative.

Now let us apply these observations to what happens at a collider, let us specifically consider the LHC where protons collide at some large center-of-mass energy of the order $Q \approx 1\,\mathrm{TeV}$. According to our previous observations Q is well within the perturbative

region. However, protons are no elementary particles but bounded QCD states that are essentially made up of three so-called valence quarks, two up quarks and one down quark. While these three constituents predict the total charge of the proton, i.e. $2 \times Q_u + 1 \times Q_d = 2 \times (2/3\,e) + 1 \times (-1/3\,e) = 1\,e$, they cannot predict the mass of the proton. In fact, the constituents' masses only make up about 1 % of the proton's total mass $m_p \approx 938\,\text{MeV}$ [14]. Note that this mass is of the same order as the scale Λ_{QCD} we defined earlier. This makes the proton a strongly bound non-perturbative object. At this energy, the valence quarks interact with one another via gluon exchange and vacuum fluctuations that contain quark-antiquark pairs (so-called sea quarks) which in total forms a highly complicated dynamical system. It is this phenomenon that accounts for most of the mass of the proton.

2.3   Factorization

What happens when two protons collide? A feature called *factorization* allows us to separate the calculation of observables into two parts: the non-perturbative hadronic part and a short distance part that describes the interactions of the constituents of the hadrons.

Due to their high energies, the particles taking part in the scattering are the so-called *partons*, i.e. quarks and gluons that make up the proton.[2] This interaction, the so-called *hard scattering* happens at some fraction of the total collision energy.

Let us denote the partons in the first proton by an index a and those from the second proton by an index b. For the above example of the center-of-mass energy $Q = 1\,\text{TeV}$ the protons each carry momenta p_a and p_b corresponding to the energies $E_a = E_b = 500\,\text{GeV}$. The interacting partons of these protons then each only carry a fraction of these total momenta which we parameterize by the parameters x_a and x_b as follows:

$$p'_a = x_a p_a, \quad p'_b = x_b p_b, \quad x \in [0,1]. \tag{2.17}$$

Having introduced this notation, we can write the total hadronic cross section as

$$\sigma = \sum_{a,b} \int_0^1 \mathrm{d}x_a\, f_a(x_a, \mu_{\text{F}}) \int_0^1 \mathrm{d}x_b\, f_b(x_b, \mu_{\text{F}})\, \hat{\sigma}_{ab}(x_a p_a, x_b p_b; \mu_{\text{F}}). \tag{2.18}$$

In order to take all possible interactions into account we have to sum over all possible partons inside the protons, a and b. Based on the same argument, we also have to integrate over all possible momentum fractions x_a and x_b of the two partons. The cross section $\hat{\sigma}_{ab}$ is the so-called *partonic cross section* which describes the hard scattering part of the two partons a and b. Of course, we cannot entirely rid ourselves of the fact that protons

---

[2]A more thorough explanation for this phenomenon is given in [15] where the authors use the example of deep inelastic scattering (i.e. $e^- + p \rightarrow X$) to explain that the proton underlies both Lorentz contraction and time dilation in the center-of-mass frame so that the lifetime of a proton state is much longer than the time it takes the electron to travel through the proton. Hence, the proton appears to be some fixed state of partons for the electron which means that the electron only interacts with a parton which it passes at a close distance of $\mathcal{O}\left(1/Q^2\right)$ due to the uncertainty principle.

are non-perturbative objects. All remaining information on the protons is encoded in the so-called *parton distribution functions* (PDFs) $f_i(x, \mu_F)$. These distributions give the probability of finding a parton of type i with the momentum fraction x inside a hadron. Note that each hadron has its own set of parton distribution functions which can be indicated by an additional index identifying the hadron type; since we only refer to protons in the following, we we leave this information out. PDFs are measured quantities that are usually extracted from deep inelastic scattering, the details of which are not relevant for this thesis.[3] However, note that in our notation above we introduced one further argument to the PDFs, the so-called *factorization scale* μ_F. It is the scale that determines the point of separation of the hadronic part from the partonic cross section. It is an unphysical, and essentially arbitrary scale which the final result of any computation should not depend on. In practice, this is not the case and one varies this scale (typically between $^{1}/_{2}\mu_F$ and $2\mu_F$) to estimate theoretical errors of a calculation. The dependence of the parton distributions on the factorization scale have to be understood as follows: the PDFs contain all kinds of QCD bremsstrahlung of partons that occurs at scales up to μ_F (to be specific, they contain a resummation of all bremsstrahlung contributions). Everything above that scale has to be taken care of by the partonic cross section. In conclusion, even though the factorization scale is in principle arbitrary, it still affects the calculation and the results. In fact, there are publications that are only concerned with choosing a proper value for the scale, one example is given by [17]; however, in the scope of this thesis we do not concern ourselves with the choice of this scale.

2.4 Perturbation Theory and Hard Scattering

Let us talk about some problems in the practical realizations of such computations of cross sections and similar observables. The perturbative partonic cross section $\hat{\sigma}_{ab}$ can be written as follows:

$$\hat{\sigma}_{ab} = \frac{1}{2s \, n_a^c n_b^c} \int d\Phi(p_a, p_b; p_1, \dots p_n) \, |\mathcal{A}(p_a, p_b; p_1, \dots, p_n)|^2 \qquad (2.19)$$

In this formula, we find several constant factors. $2s$ is the (inverse) flux factor where $s = Q^2$ is the squared (partonic) center-of-mass energy, $n_{a/b}^c$ is a color averaging factor for the initial state parton a or b; since there is no way to measure color, we have to take all possible colors into account which we do by averaging over them.[4] The important quantity in equation (2.19) is the so-called *(squared) matrix element* or *(squared) amplitude* $|\mathcal{A}(p_1, \dots, p_n)|^2$ which depends on all final state momenta $p_1, \dots p_n$, as well as the initial state momenta p_a and p_b. For the *total* cross section, we have to integrate over all of final

---

[3]The interested reader can find many detailed and thorough discourses on PDFs in the literature. For example, basic introductions can be found in [1,12,13] and other summary publications or textbooks. Readers desiring a more comprehensive treatment might want to take a look at the exhaustive report on an updated PDF set from the MSTW group [16].

[4]A similar factor exists for spin averaging. However, we postpone any discussion of spins and helicities until chapter 4.
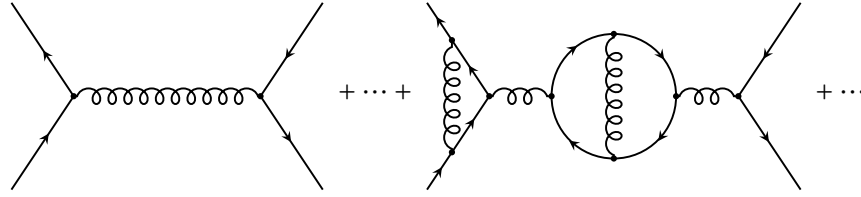
Figure 2.2: Example for two contributions to the total matrix element for the process $q\bar{q} \to q'\bar{q}'$; the left hand example is the lowest order possible, $\mathcal{O}\left(g_s^2\right)$ since it contains two vertices. The right hand example, on the other hand, is very complicated and of order $\mathcal{O}\left(g_s^8\right)$.

state phase space which is denoted by the integral over Φ. This integration depends on the momenta p_a and p_b of the initial-state partons due to momentum conservation, i.e. $p_a + p_b \stackrel{!}{=} p_1 + p_2 + \cdots + p_n$. Let us return to the squared amplitude, or to be more specific to the amplitude itself which is a complex-valued quantity: an amplitude has a definite amount of external particles, i.e. both initial and final state particles which is $n + 2$ in this case. In principle, an amplitude is given by all the diagrams that one can construct with the previously given Feynman rules (equations (2.5) – (2.9)) where there are (in our case) $n + 2$ external particles.

How many diagrams are there for a given number of external particles? The answer is: infinitely many. By introducing loops into the internals of diagrams they can become arbitrarily complicated, see for example the process $q\bar{q} \to q'\bar{q}'$ (where the prime denotes that the quarks in the final state have a different flavor than those in the initial state) in figure 2.2. This is the place where perturbation theory kicks in: decomposing an amplitude into separate diagrams exposes the perturbative expansion directly. From the Feynman rules it becomes obvious that all vertices are proportional to some power of the strong coupling constant g_s. All three-particle vertices have g_s while the four-gluon vertex has g_s^2. This makes it very simple to count the power of the coupling in each diagram and assign them to the proper order of the expansion. We already argued that the scale of the hard process is such that we are in the perturbative region of QCD, so it is justified to only calculate the lowest orders in g_s. This means that we can avoid the calculation of the complicated right hand diagram in figure 2.2. Another way to increase the power of the coupling is to add more external particles, we will consider an example below. In any *squared* amplitude $|\mathcal{A}|^2 = \mathcal{A}^*\mathcal{A}$ we will of course have squared diagrams as well as interference terms where different diagrams are multiplied. We can count the powers of the respective squared amplitudes by simply adding the powers of the two underlying diagrams.

If we gather all the information on perturbation theory that we have encountered so far, we can put it into a graphical form as shown in figure 2.3. Therein, we have written the
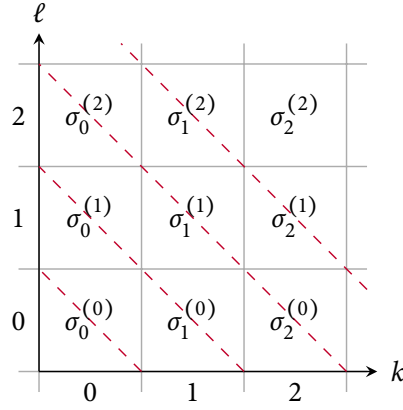
Figure 2.3: Diagram that shows the perturbative expansion in terms of loops ℓ and extra legs k. The contribution $\sigma_0^{(0)}$ marks the most basic process which is a $2 \to 2$ process. The red dashed lines indicate those contributions which are of the same order in the coupling constant. At next–to–lowest order, for example, we find two contributions, one with an extra leg, one with a loop.

expansion as follows:[5]

$$\hat{\sigma}_{ab} = \sigma_0^{(0)} + \sigma_1^{(0)} + \ldots + \sigma_0^{(1)} + \sigma_1^{(1)} + \ldots = \sum_k \sum_\ell \sigma_k^{(\ell)} \tag{2.20}$$

The expansion starts from the simplest of all processes which is a $2 \to 2 + k$ process. This means that k is the number of additional external particles. The number of loops within the squared amplitude is given by ℓ. Let us stress that this means that for example $\sigma_0^{(1)}$ is made up of the amplitudes

$$\mathcal{A}_0^{(0)^*} \mathcal{A}_0^{(1)} + \mathcal{A}_0^{(1)^*} \mathcal{A}_0^{(0)} = 2\Re\left\{\mathcal{A}_0^{(0)^*} \mathcal{A}_0^{(1)}\right\}, \tag{2.21}$$

i.e. there is only one loop amplitude instead of both amplitudes containing a loop. As will become clear below, this also means that $\sigma_0^{(1)}$ and $\sigma_1^{(0)}$ are of the same power in α_s. Generally, if $\sigma_0^{(0)}$ is of order $\mathcal{O}\left(\alpha_s^\rho\right)$, $\sigma_k^{(\ell)}$ will be of order $\mathcal{O}\left(\alpha_s^{\rho+k+l}\right)$ such that all contributions to the same power τ lie on a straight line from $(k = 0, \ell = \tau)$ to $(k = \tau, \ell = 0)$ in figure 2.3.

Let us examine this a little further by looking at electron–positron collisions into hadrons.[6] Usually, electron–positron collisions are investigated at the energies that the LEP collider operated at, i.e. typically one chooses $Q = m_Z \approx 91\,\text{GeV}$ [14]. There are five quark flavors with masses below this scale; these masses are so small compared to Q that one typically neglects them and treats all partons as massless. The top quark cannot be produced at these energies, which is why we can ignore it here and in any further analysis performed in this thesis.

---

[5]Note that the quantities $\sigma_k^{(\ell)}$ in this expansion are not the same that appear in equation (2.11). However, their relation will become clear on the following pages.

[6]This paragraph closely follows Salam's "Elements of QCD for hadron colliders" [1].
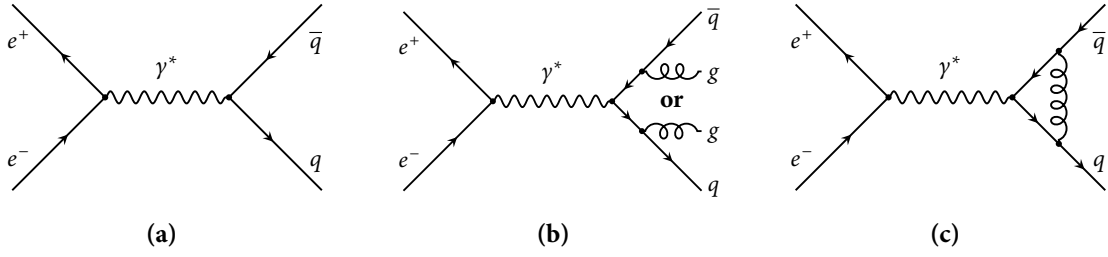
Figure 2.4: Leading and next–to–leading order diagrams for the process $e^-e^+ \rightarrow q\bar{q}$; we ignore electroweak coupling through a Z boson and only consider the coupling through a photon for simplicity. Note that diagram (b) represents two diagrams where either the upper or the lower gluon is present.

We start with the lowest order contribution which is shown in figure 2.4(a). This diagram makes up the contribution $\sigma_0^{(0)}$ since there are obviously no loops in the diagram and it contains the minimum number of external legs possible (total momentum conservation prohibits less than four particles). We are not interested in the exact expression of the amplitude at this point; let us simply denote the squared matrix element by $|\mathcal{A}_{q\bar{q}}|^2$. To compute the full cross section $\sigma_0^{(0)}$, we have to integrate the matrix element over final state phase space, which we shall denote by $\mathrm{d}\Phi_{q\bar{q}}$ so that

$$\mathrm{d}\sigma_0^{(0)} \equiv \mathrm{d}\sigma_{q\bar{q}} \approx |\mathcal{A}_{q\bar{q}}|^2 \mathrm{d}\Phi_{q\bar{q}}. \tag{2.22}$$

(Note that we omitted constant factors for simplicity.) We can integrate this contribution without any troubles; due to momentum conservation, both the quark and the antiquark momentum will be back to back and of the same size which is given by the center-of-mass energy Q.

What happens if we go one order higher in perturbation theory? One way to increase the power of α_s is to add an external particle after which we end up the contribution $\sigma_1^{(0)}$. Figure 2.4(b) shows us the two diagrams that contribute: a gluon is emitted either from the quark or from the antiquark line. Let us not take into account the full expression in the following but use an approximation instead: we are going to assume that the momentum k of the gluon is soft, i.e. $k \ll p_q, p_{\bar{q}}$ where p_q and $p_{\bar{q}}$ are the quark and antiquark momenta. We then obtain the following expression for the squared matrix element:

$$|\mathcal{A}_{q\bar{q}g}|^2 = |\mathcal{A}_{q\bar{q}}|^2 \times 4\pi\alpha_s C_F \frac{2p_q p_{\bar{q}}}{(p_q k)(p_{\bar{q}} k)}. \tag{2.23}$$

It turns out that in the soft limit the contribution from the additional gluon factorizes. For the cross section $\sigma_1^{(0)}$ we again have to add the integral over phase space. We can make use of the fact that phase space factorizes, i.e. we can add a soft gluon by simply multiplying a

one-particle Lorentz invariant phase space measure:

$$d\Phi_{q\bar{q}g} \approx d\Phi_{q\bar{q}} \frac{d^3 k}{(2\pi^3)2E_k}. \tag{2.24}$$

The cross section then reads

$$d\sigma_1^{(0)} \equiv d\sigma_{q\bar{q}g} \approx |\mathcal{A}_{q\bar{q}g}|^2 d\Phi_{q\bar{q}g} \approx |\mathcal{A}_{q\bar{q}}|^2 d\Phi_{q\bar{q}}dS = d\sigma_0^{(0)}dS, \tag{2.25}$$

where we have again neglected constant factors. The soft gluon element dS can be written as

$$dS = \frac{d^3 k}{(2\pi^3)2E_k} 4\pi\alpha_s C_F \frac{2p_q p_{\bar{q}}}{(p_q k)(p_{\bar{q}} k)} = \frac{2\alpha_s C_F}{\pi} \frac{dE}{E} \frac{d\theta}{\sin\theta} \frac{d\phi}{2\pi} \tag{2.26}$$

where we re-expressed the phase space measure in terms of spherical coordinates. Note that upon integration this formula exhibits two different divergences:

$$E \to 0 \qquad\qquad \text{soft divergence} \tag{2.27a}$$

$$\theta \to 0, \pi \qquad\qquad \text{collinear divergence.} \tag{2.27b}$$

Even though we originally restricted the calculation to electron positron collisions this observation is valid for QCD in general.

Note that this can be generalized to momentum invariants $s_{ij} = (p_i + p_j)^2 = 2p_i p_j$, where the last expression is only valid for massless particles, i.e. $p_i^2 = 0$, $p_j^2 = 0$. Within tree-level squared amplitudes, we usually find terms that are of the form [18]

$$\frac{1}{s_{12}s_{23}\cdots s_{(n-1)n}} \tag{2.28}$$

plus similar terms for permutations of the particles. This yields singularities for collinear partons,

$$s_{ij} \xrightarrow{p_i \parallel p_j} 0, \tag{2.29}$$

and for soft partons,

$$s_{ij}s_{jk} \xrightarrow{p_j \to 0} 0. \tag{2.30}$$

We will look at these cases in more detail later on.

The previous observation raises a new question: if the three-particle phase space integral is divergent, it seems like the cross section is not well-defined. However, note that we have not taken into account all contributions to $\mathcal{O}(\alpha_s)$. We still lack the contribution $\sigma_0^{(1)}$ which is the above discussed interference term, more specifically the product of diagrams 2.4(a) and 2.4(c) as specified in equation (2.21). Without writing down explicit expressions, let us discuss a few important details about this contribution. The detail that sets this contribution apart from the previous ones is that momentum conservation is *not* sufficient to fix all momenta in the one-loop diagram 2.4(c). One of the propagators taking part in the loop will have an undefined momentum ℓ which we have to integrate over. When

performing this integration, one finds that the integral diverges for $\ell \to \infty$, we encounter so called *ultraviolet singularities*. It turns out that one can avoid these singularities by generalizing the loop integral from four to $D = 4 - 2\epsilon$ dimensions, a procedure which is called dimensional regularization [19, 20]. Subsequent *renormalization* then renders the integral finite also in four dimensions.[7] More important for the purpose of our discussion is the fact that the loop also exhibits singular behavior when the gluon propagator becomes soft, i.e. when the loop momentum goes to zero, or when two loop propagators are collinear. It is the remarkable discovery of Kinoshita [21], Lee and Nauenberg [22] that all infrared (meaning soft and collinear) singularities cancel order by order in perturbation theory. Therefore, both $\sigma_1^{(0)}$ and $\sigma_0^{(1)}$ are divergent in the soft and collinear limits, however, their sum will lead to a cancellation of all divergent pieces so that the total cross section will be finite.

Our above discussion contained hints to a very important problem that we still face: as we increase the order in the strong coupling, not only does the complexity of the diagrams increase, but also their number. At lowest order, we found only one diagram while at next–to–leading order we had to face three diagrams already. One can easily imagine that with growing number of k and/or ℓ the combinatorial possibilities of adding another particle or of placing the loops inside the diagram increase strongly. In fact, if one considers the number of external particles for gluon-only processes at tree-level (no loops), i.e. $\sigma_k^{(0)}$ the growth in the number of diagrams is worse than $\mathcal{O}(k!)$ [23]. This clearly limits the number of contributions we can compute. In fact, the current state of the art is the calculation of a one-loop function with eight particles and even this calculation includes some approximations which we will detail later.[8]

2.5 Exclusive Cross Sections and Infrared Safety

So far, we have considered the total cross section which is an *inclusive* quantity, i.e. in the above calculation we considered both the contributions of two and three final state particles. Another class of observables that we will mainly deal with in this thesis is the class of *exclusive* cross sections, i.e. cross sections with a fixed number of final states. Let us once again consider the example of electron–positron collisions, more specifically the exclusive cross section with three particles in the final state. Obviously, our lowest order or *Born* contribution, $\sigma_1^{(0)}$ is then given by the two diagrams 2.4(b) which were formerly part of the next–to–leading order contribution. In the case of the inclusive cross section the soft and collinear divergences cancel against the one-loop contribution $\sigma_0^{(1)}$. However, this contribution does no longer fit our definition of the exclusive cross section since it

---

[7]Note that this is closely connected to the running of the coupling constant we discussed earlier. We will not go into further details because the procedure of ultraviolet renormalization does not play a crucial role for this thesis.

[8]This was first accomplished for electron–positron collisions by the group of Stefan Weinzierl in [24] with some algorithms detailed in this thesis. In 2013, the *BlackHat* collaboration presented a computation of $pp \to W + 5$ jets [6] which is also a one-loop function with eight external particles. The approximation mentioned above is the so-called *leading color* approximation which will be explained in section 3.1.4.

only has two final state particles. Can we obtain a finite result at all?

The answer is that the way we regarded our exclusive cross section is not sufficient to make it an observable. The real class of observables that we are looking for are *infrared safe* which means they should be insensitive to the emission of soft or collinear partons or, as defined in [25], they

"… *must be invariant to the branching*

$$\vec{p}_i \to \vec{p}_j + \vec{p}_k$$

whenever $\vec{p}_j$ and $\vec{p}_k$ are parallel [collinear] or one of them is small [infrared]."

To avoid any confusion, note that the quote uses the word *infrared* for soft emissions only; nowadays, it is common to refer to *both* soft and collinear emissions with the term infrared, which is what we do in this thesis.

Throughout this work, we will use the symbol $J_n(p_1, \ldots p_n)$ to denote a so-called *jet observable* that fulfills the requirements of infrared safety [26]. The index n indicates the number of external particles that it acts on. If we compute an n-jet observable, then J_m has the following two properties for all $m \geq n$:

$$J_{m+1}(p_1, \ldots, p_j = \lambda q, \ldots p_{m+1}) \to J_m(p_1, \ldots, \not{p}_j, \ldots, p_{m+1}) \tag{2.31a}$$

if p_j is soft, i.e. $\lambda \to 0$, and

$$J_{m+1}(p_1, \ldots, p_i, \ldots, p_j, \ldots, p_{m+1}) \to J_m(p_1, \ldots, \cancel{(p_i, p_j)} \to p, \ldots, p_{m+1}) \tag{2.31b}$$

if p_i and p_j are collinear, i.e. $p_i \to zp$ and $p_j \to (1 - z)p$. Furthermore, we require

$$J_n(p_1, \ldots, p_n) \to 0 \tag{2.31c}$$

if any particle invariant goes to zero, $p_i \cdot p_j \to 0$. This last property ensures that $\sigma_1^{(0)}$ in our above discussion yields a finite and well-defined result if we make use of our jet observable:

$$(\mathrm{d}\sigma_1^{(0)})_{\mathrm{excl}} \approx |\mathcal{A}_{q\bar{q}g}|^2 J_3(p_q, p_{\bar{q}}, p_g) \, \mathrm{d}\Phi_{q\bar{q}g} \tag{2.32}$$

where we neglected constant factors once again.

Let us try to make some more sense of the term *jet* that we introduced earlier by looking at an actual event detected by the ATLAS experiment at the LHC, figure 2.5. Obviously, we find many detected particles in the detector. However, the energy deposition in the calorimeters (red and green) is concentrated around two sharp peaks which are diametrically opposed. Each of these structures is called a *jet*—a cone-like structure inside which partons radiate other partons that are preferably soft and collinear to the original parton. The large amount of radiated partons then hadronizes into colorless particles which are detected by the detector. It turns out that if we describe a jet as the energy flow
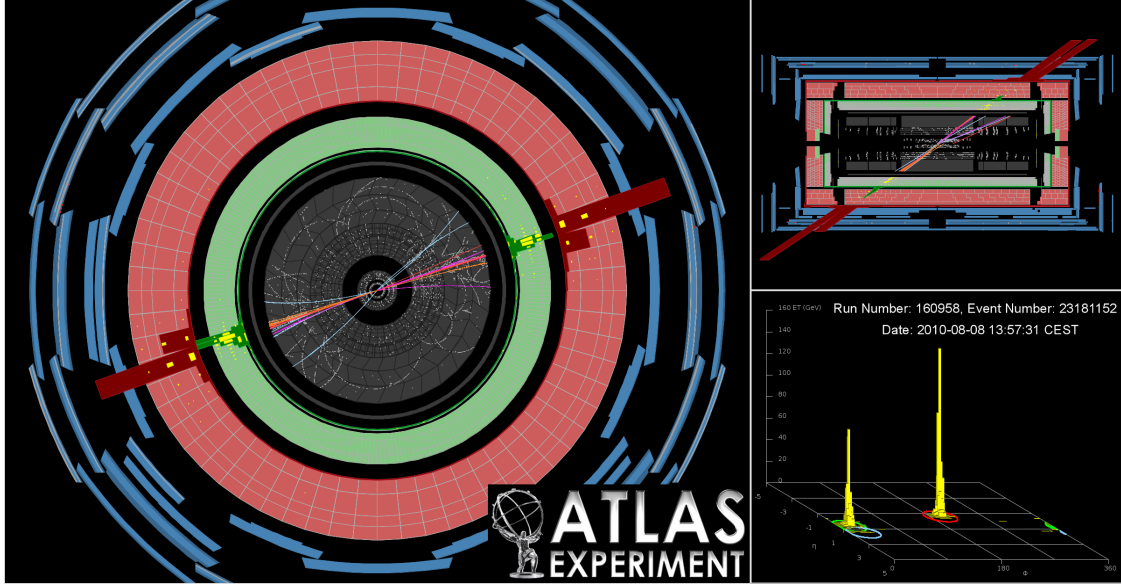
Figure 2.5: Event display of a dijet event detected by the ATLAS experiment at the LHC in August of 2010. The colored lines in the central gray areas show reconstructed particle traces while the dark green and dark red bands around them show the deposited energy. In the left hand plot the beam axis is perpendicular to the image while in the upper right image the beam axis is horizontal. Especially from the lower right plot it is obvious that there are two distinct particle jets that are made up of many individual particles each. Source: `http://atlas.ch/photos/events-collision-proton.html`.

into a cone, we end up with an infrared safe observable since neither collinear emissions nor soft emissions change the overall direction of and energy flow into the cone.

So far, our definition of a jet is still rather abstract. What we need is a prescription, a so-called *jet algorithm*, for turning final state particles into well-defined jets. There are many ways to realize such an algorithm, however, each depends on at least one free parameter, the jet resolution parameter y_{cut} which describes the "size" of a jet. In the following, we restrict ourselves to exclusive jet algorithms where each final state parton belongs to exactly one jet.[9] More specifically, we consider *sequential recombination* algorithms which consist of three simple steps. First, one defines the size y_{cut} of the jet. Then one computes the *resolution variable* y_{ij} for each pair of final state momenta (p_i, p_j). Finally one picks the two particles i and j that yielded the smallest $y_{ij} < y_{cut}$ and combines them into one jet using a algorithm-specific *recombination prescription*. This procedure is repeated until no more momentum pair has a resolution below y_{cut}. At this point all remaining final state momenta describe a single jet each.

We have not yet detailed the resolution variable and the recombination prescription. A comprehensive description of available jet algorithms is given in [27]. We will only make

---

[9]There are also inclusive jet algorithms where each final state parton belongs to either exactly one jet, or to not jet at all. These algorithms are not considered in this thesis.
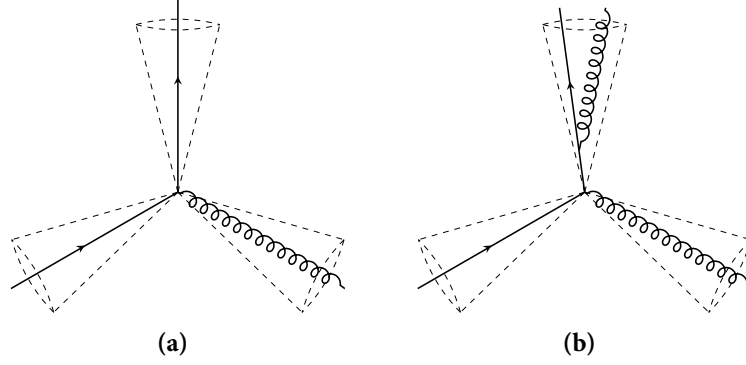
Figure 2.6: Examples for jets. The left hand diagram shows a three-jet final state where each particle corresponds to one jet (indicated by dashed cones). The right hand side illustrates a real emission event, i.e. a three-jet final state with four particles in the hard scattering where two are soft or collinear with respect to the jet definition.

use of the *Durham* algorithm [27–29] which is given by the resolution variable

$$y_{ij} = \frac{2\min(E_i^2, E_j^2)(1 - \cos\theta_{ij})}{Q^2} \tag{2.33}$$

where $E_{i/j}$ is the energy of the parton i/j and θ_{ij} is the angle between the momenta $\vec{p}_i$ and $\vec{p}_j$. The related recombination prescription is the so-called *E-Scheme* which conserves both energy and momentum, but does not yield massless recombined momenta even if the original final states were massless:[10]

$$p_{ij}^\mu = p_i^\mu + p_j^\mu. \tag{2.34}$$

Note that the Durham algorithm is specifically suited for electron–positron annihilation which we will consider in this thesis.

We can conclude from the above discussion that at leading order in perturbation theory, each such jet is described by exactly one parton. Returning to our example of the exclusive jet rate $(\sigma_1^{(0)})_{\text{excl}}$ from above, this means that we integrate over all of phase space but those regions where any of the three partons is "too close" to another parton, governed by the jet algorithm and the resolution y_{cut}—all of which is encompassed in our jet observable J_3. This is shown in figure 2.6(a). In practice, the jet algorithm acts as a cut-off for soft and collinear partons in the leading order contribution to the exclusive three jet cross section and equation (2.32) gives a finite result.

What happens if we want to compute the next–to–leading order correction to this exclusive cross section? Again, we find two contributions: the one-loop interference term with three final states, $\sigma_1^{(1)}$, and the contribution with one more particle, $\sigma_2^{(0)}$. Both fit the order in α_s, but the second contribution has to be considered a bit more carefully: $\sigma_2^{(0)}$ has four final state particles now. Since we want to obtain the three jet cross section, we

---

[10]It is possible to make the recombined momentum massless, however this comes at the cost of either violating energy conservation (P-scheme) or momentum conservation (E0-scheme).
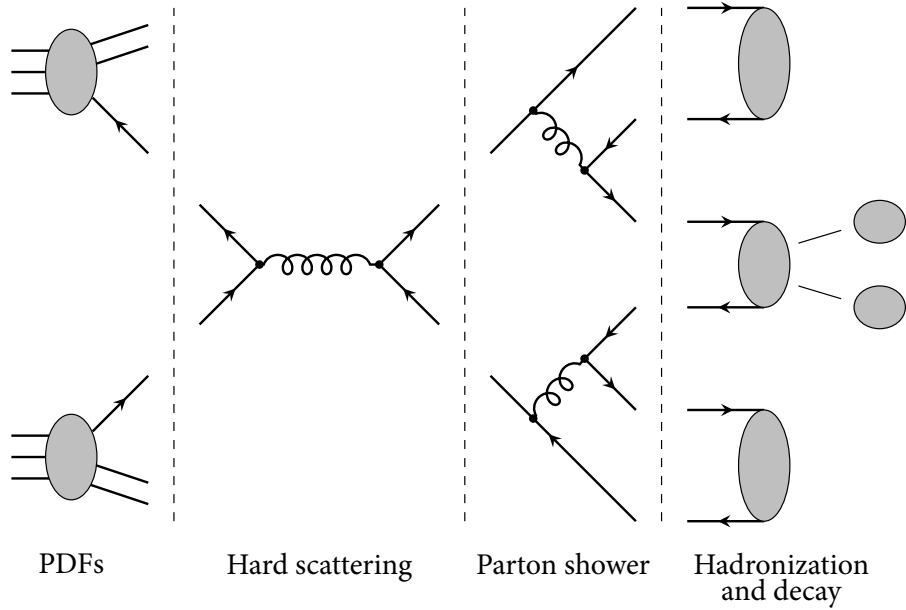
Figure 2.7: Rough pictorial representation of the four steps involved in a full computation of a hadron–hadron cross section.

have to pay special attention to the jet function J_4. This is where equations (2.31b) and (2.31c) enter. We can only allow final states where the momenta are such that the resulting number of jets is again three. This means that the additional fourth particle has to be a soft or collinear particle in such a way that the jet algorithm assigns the particle to the same jet as one of the other particles, see figure 2.6(b).

If we go to higher orders in α_s in the above example, we obviously still have to describe three jets, meaning that all additional partons have to combine with others into jets such that we find exactly three jets.

A generalization to other jet numbers is straight forward.

2.6   Parton Showers and Hadronization

We now know how to compute exclusive observables, but the full description of a particle collision process is still far from done. Say we only compute the leading order contribution where each jet is described by one parton. One parton is hardly sufficient to describe the abundance of final states we saw in figure 2.5. Indeed, the whole process necessary to describe such a process in its entirety is pictured in figure 2.7. So far, we discussed PDFs and the hard scattering performed in terms of perturbation theory. There are two more steps which we only mentioned shortly since they are not dealt with in this thesis.

The first is the so-called *parton shower* which makes sure that we are actually able to describe jets more accurately. In principle, it describes a cascade of soft and collinear emissions of the partons inside the jets. Without going into details, it is possible to derive a formula for the probability that no gluon is emitted above a certain momentum scale. From this, one can then use numerical methods to randomly generate branchings of the

partons inside the jets, thereby adding more final states to the hard scattering. Note that this process is still perturbative: it starts roughly at the scale Q (i.e. the scale of the final state partons after the hard scattering). From there the cascade starts, reducing the scale with every splitting until the non-perturbative scale Λ_{QCD} is reached.

This is where the last piece, *hadronization* enters. Hadronization is strongly non-perturbative and cannot be computed from first principles. Instead, one uses models, some of which take into account that the partons emerging from the parton shower are colored objects while hadrons are color neutral. The model then gathers partons in some way that creates clusters of partons that can then form colorless hadrons.

Basic reviews of parton showers and hadronization can be found in the already mentioned introductory texts [1, 12]. A more detailed introduction to parton showers for next–to–leading order calculations is given in [30].

Numerical Techniques

<div style="text-align:right">3</div>

To analyze the data they gather at colliders, experimentalists need to have reliable predictions tailored to the specific problem they are looking at (certain sets of phase space cuts, jet definitions, etc.). These predictions are usually obtained from numerical computer programs, so-called *event generators*. A full-fledged event generator is a tool that performs the computation of all four steps described in figure 2.7 automatically.[1] Examples for complete generators are for example *SHERPA* [31], *PYTHIA* [32,33] and *HERWIG++* [34].

Since parton showers are perfectly suited for automated calculations, event generators originally were mostly focused on them instead of the hard matrix element. In fact, the manual of the current *PYTHIA* version[2] states that *PYTHIA* includes a "reasonably complete setup of all $2 \to 1$ and $2 \to 2$ processes within the Standard Model, plus some examples of processes beyond that, again for low multiplicities". All higher multiplicities are generated using the parton shower instead of the hard matrix element. While this is possible, the parton shower is an approximation for soft and collinear emissions and thus increasingly unreliable for harder emissions.

This approach works reasonably well for some observables, but the jet multiplicity in the days of $\mathcal{O}\,(\text{TeV})$ colliders is much higher than at previous colliders requiring more precise calculations. Furthermore, leading order QCD calculations are very sensitive to scale variations. The usual test to determine the uncertainty of a theoretical prediction by varying the factorization scale μ_F shows that going to next–to–leading order reduces this dependence greatly. An example for this is given in figure 3.1. Additionally, next–to–leading order phase space is different from the leading order phase space which leads to different normalizations of cross sections. Results of leading order generators thus have to be fitted to data from which one extracts a so-called *K-factor*, a factor that is multiplied to the cross section to make the leading order result at all usable.

Thus, there are plenty of reasons why next–to–leading order calculations with high

---

[1]In fact, current event generators include even more effects that we have not even mentioned before, such as the interaction of two or more partons within the same proton (*multiple interactions*) or of partons within two or more proton–proton pairs (*pile-up*).

[2]See `http://home.thep.lu.se/~torbjorn/pythia81html/Welcome.html`, "Process Selection" subpage (last visited on 05/04/14).
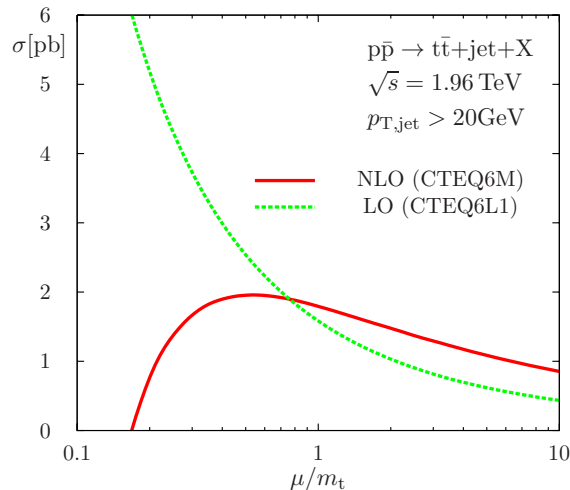
Figure 3.1: Example of scale dependence for top pair plus one jet production. Both the factorization and the renormalization scale are chosen to be equal to μ. While both the leading and next–to–leading order results show a dependence on the scale μ, the next–to–leading order result clearly shows a less pronounced dependence. Plot taken from [35].

particle multiplicities are a *necessity* and not just a desirable upgrade.

In this thesis, we will discuss the hard scattering part of such an event generator. This chapter presents the underlying concepts and methods that enable numerical calculations and the implementation in terms of computer programs. Note that the contents of section 3.1 have already been discussed in an earlier thesis by the author [36] and corresponding code has been implemented and extensively tested. Section 3.2 serves as an introduction to the subtraction method needed at next–to–leading order and provides a basis for developing methods for different helicity methods. All remaining sections are concerned with technical details concerning phase space integration and approximations that are used to speed up the computations.

3.1 Numerical Tree-Level Diagram Techniques

This section resembles many parts of chapter 2 of [36]. Its purpose is to recall and summarize the basics of the numerical techniques that underly the computation of amplitudes. For more information, we refer the interested reader to [36], references therein, and some references we give in the text. Also note that a very good review of many of the techniques we use and similar ones can be found in [37].

When thinking about implementing the calculation of a typical QCD amplitude in terms of numerical code, one is faced with three orthogonal mathematical structures given by Minkowski space (Lorentz indices), Dirac space (given by the four components of spinors and the 4×4 gamma matrices), and color space given by the $SU(3)$ generators $\mathbf{T}_i$ and the structure constants f^{abc}. In the following, we present techniques that allow a simple treatment of this apparently complicated situation.

3.1.1 Color Decomposition

The first method is called *color decomposition* [38]. It decomposes an amplitude $\mathcal{A}$ into a sum over color factors times kinematical quantities A called *partial amplitudes* or *color ordered amplitudes*. One frequently cited version of color decomposition is given by [39]:

$$\mathcal{A}(g_1, g_2, \ldots, g_n) = \sum_{S_{n-1}} \mathrm{Tr} \left\{ \mathbf{T}^{a_1} \mathbf{T}^{a_2} \cdots \mathbf{T}^{a_n} \right\} A(g_1, g_2, \ldots, g_n). \tag{3.1}$$

Note that this decomposition is only valid for gluon amplitudes; including quarks, leptons, and photons is possible and is discussed extensively in [36] and references therein. We restrict ourselves to gluon amplitudes here for readability, and because they cover all relevant aspects. The sum in equation (3.1) runs over all non-cyclic permutations of all gluons, i.e. the ordering of particle indices on the right hand side matters and is different for every term in the sum. The trace contains all color factors while the partial amplitude A contains all kinematical information of the corresponding Feynman diagrams. Our code uses a different version of color decomposition, the so-called *color-flow decomposition* [40] which makes use of the Fierz identity

$$\mathbf{T}^a_{ij} \mathbf{T}^a_{k\ell} = \frac{1}{2} \left(\delta_{i\ell} \delta_{jk} - \frac{1}{N_\mathrm{c}} \delta_{ij} \delta_{k\ell} \right) \tag{3.2}$$

to re-write equation (3.1) into

$$\mathcal{A}(g_1, g_2, \ldots, g_n) = \sum_{S_{n-1}} \delta_{i_1 j_2} \, \delta_{i_2 j_3} \cdots \delta_{i_n j_1} \, A(g_1, g_2, \ldots, g_n). \tag{3.3}$$

Since there is no more color information in the partial amplitudes, they have to be formulated using so-called *color stripped* or *color ordered* Feynman rules. These rules can be found in [40]; a derivation of these rules is given in [36], where they are also presented using the Weyl–van der Waerden formalism which we use for our implementation (see the section on spinor helicities below). It is important to note that the partial amplitudes are gauge invariant quantities, just like the full amplitudes, and thus replacing the polarization vector of any gluon with its corresponding four-momentum yields zero.

Obviously, the quantities we are interested in are squared amplitudes. To investigate this, let us write the color delta string in terms of a color index c_m where m is the permutation given by the sum. We can then write equation (3.3) as

$$\mathcal{A} = \sum_m c_m A_m, \tag{3.4}$$

from which follows:

$$|\mathcal{A}|^2 = \sum_{m,n} A^\dagger_m c^\dagger_m \otimes c_n A_n = \sum_{m,n} A^\dagger_m c^\dagger_m \, P \, c_n A_n = \sum_{m,n} A^\dagger_m \mathbf{C}_{mn} A_n = \vec{A}^\dagger \mathbf{C} \vec{A} \tag{3.5}$$

The actual implementation in our code is given by the vector–matrix–vector multiplication
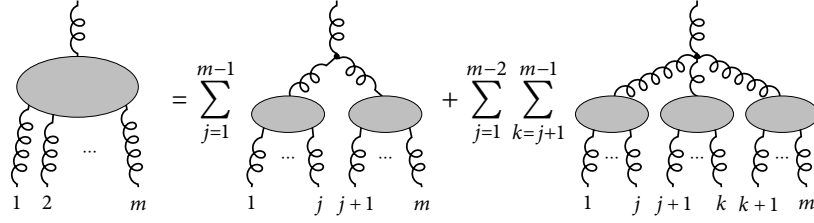
Figure 3.2: Visual representation of the Berends–Giele recursion for gluon amplitudes.

on the right hand side. The object **C** is the *color matrix* which is given by the product of the color strings $c_m^\dagger$ and c_n. This contraction is performed using *color projection* operators which implicitly realize the summation over color. For each parton, we have one of the following projection operators:

$$P_g = \delta_{\bar{i}i}\,\delta_{\bar{j}j} - \frac{1}{N_c}\delta_{ij}\,\delta_{\bar{i}\bar{j}}, \quad P_q = \delta_{\bar{i}i}, \quad P_{\bar{q}} = \delta_{\bar{j}j} \tag{3.6}$$

where the indices with bars are those from the color factor $c_m^\dagger$ while those without bars are those from c_n. The color factors $c_m^\dagger$ and c_n together with the projectors P give rise to traces over the color deltas δ_{ij} which obey $\delta_{ii} = N_c$, hence the color matrix acts as a color-weighting function for interferences between different partial amplitudes. This color matrix is process-specific, but entirely independent of phase space and kinematics. Thus, it can be computed once at the initialization phase of the program and never has to be evaluated again, which saves a lot of computation time.

Note that we will later deal with *color correlated* amplitudes, for example $\mathcal{A}^*\mathbf{T}_x\mathbf{T}_y\mathcal{A}$ instead of $|\mathcal{A}|^2$. These correlations can be computed by replacing the normal projectors for partons x and y with a corresponding correlation operator that depends on the type of the partons. Let us give one example for the case where x and y are both quarks. The usual projector has to be replaced as follows:

$$\delta_{\bar{i}_x i_x}\,\delta_{\bar{i}_y i_y} \quad \longrightarrow \quad \frac{1}{2}\left(\delta_{\bar{i}_x i_y}\,\delta_{\bar{i}_y i_x} - \frac{1}{N_c}\delta_{\bar{i}_x i_x}\,\delta_{\bar{i}_y i_y}\right) \tag{3.7}$$

Note that we will not require these correlation operators explicitly, which is why we refer the reader to [41] where a full list of all color correlations has been derived.

3.1.2 Berends–Giele Recursion

Having dealt with color information, we now turn to the computation of the partial amplitudes A. An efficient way is to use recursive relations that have originally been developed by Berends and Giele [42] which are best explained in terms of diagrams, as shown in figure 3.2. The diagram on the left is a so-called *off shell current*. Its upper particle an *off shell leg* which corresponds to an internal, virtual particle in the desired amplitude.

All lower particles are external on shell particles described by polarization vectors. The gray blobs denote unknown parts of the amplitude which are recursively determined by the following procedure. Starting from the off shell leg, one inserts a color ordered Feynman rule which splits the off shell leg into two or more particles. The resulting particles again go into gray blobs with less external particles each. We call these *sub-currents*. Note that we have to sum over all possible distributions of external particles among the sub-currents; for a partial amplitude, the particle order is fixed, thus it is sufficient to sum over all possible splitting positions given by j (and k in the case of the four gluon vertex). Each sub-current can be evaluated with the same recursive formula. Doing so reduces the amount of external legs with each recursion. The recursion ends once we find a sub-current with only one outgoing particle; this is the recursion start which is given by the corresponding particle's polarization vector (or spinor in the case of quarks).

A full amplitude has no external off shell legs, thus we have to ask question of how we can use this formalism to compute amplitudes. If we compute the current where the external particles $1, \ldots, m$ are given by all particles of the desired amplitude but one (let us call it n), momentum conservation will ensure that the off shell leg is in fact described by the on shell momentum of particle n. We can thus obtain the full amplitude from this expression by leaving out the propagator and replacing it with the polarization vector (or spinor) of particle n.

We already hinted at the fact that these relations can be extended to include quarks, photons, and leptons. The thesis [36] was devoted to this and contains extensive information as well as tests that verify the resulting algorithms.

Note that during the computation of partial amplitudes, many sub-currents will appear more than once; especially those with few external legs. If we approach the recursion naively, we will compute all sub-currents when they are needed and neglect any information on them afterwards. It is much more sensible to store the results of all sub-currents in memory and only compute them if they have not been computed before. We will not go into the details here, but refer once again to [36] where an efficient method for gluonic amplitudes has been discussed.

3.1.3 Spinor Helicity Formalism

The starting point for the Berends–Giele recursion is given by the polarization vectors for the external partons. This poses the question of how we can parameterize them numerically. It turns out that we can write them in terms of spinors [43–46]:

$$\epsilon_\mu^+(p, q) = \frac{\langle q-| \gamma_\mu |p-\rangle}{\sqrt{2} \langle q-|p+\rangle}, \qquad \epsilon_\mu^-(p, q) = \frac{\langle q+| \gamma_\mu |p+\rangle}{\sqrt{2} \langle p+|q-\rangle} = \epsilon_\mu^{+\,*}(p, q). \tag{3.8}$$

Therein, $|p\pm\rangle$ are Weyl spinors given by

$$|p\pm\rangle = P_\pm u(p) = \frac{1}{2} \left(\mathbb{1} \pm \gamma_5 \right) u(p) \tag{3.9}$$

where $P_\pm$ are the chirality projectors. Note that the polarization vectors depend on two momenta: p is the four-momentum of the particle; q is an auxiliary or *reference momentum* which is an arbitrary light-like four-momentum with the restriction that it may not be parallel to p since this would make the denominator vanish. One can show that changing the reference momentum amounts to a gauge transformation and we find the following useful relations:

$$p^\mu \epsilon_\mu^\pm(p, q) = 0, \qquad q^\mu \epsilon_\mu^\pm(p, q) = 0. \tag{3.10}$$

Furthermore, one can show that the polarization sum results in the expression

$$\sum_{\lambda = \pm} \epsilon_\mu^{\lambda *} \epsilon_\nu^\lambda = -g_{\mu\nu} + \frac{p_\mu q_\nu + q_\mu p_\nu}{pq} \tag{3.11}$$

which corresponds to an *axial gauge*. Note that when choosing the reference momenta for the particles, we are free to select one fixed reference momentum for all particles or to choose each one differently. While there are many choices that are convenient in different situations, we choose the reference momentum such that the spatial component is opposite to the four-momentum of the particle [23]

$$q = \left(\text{sign}(p_0) \sqrt{|\vec{p}|^2}, -\vec{p} \right). \tag{3.12}$$

For massless momenta the time-component is equal to p_0. We need the sign of the original momentum's energy component since we calculate all processes internally by moving all initial state particles into the final state by virtue of crossing symmetry. In the process of crossing momenta, they acquire an overall minus sign such that initial state particles have negative energies. Note that this choice of reference momenta has the advantage that the denominator of the polarization vector only vanishes if the momentum p becomes soft. Since the numerator vanishes with the same power, one would expect this not to pose a problem. Contrary to this expectation, the soft limit will actually pose some problems in chapter 6.

Let us now discuss the way we parameterize the spinors. We choose light-cone coordinates where

$$p_\pm = p_0 \pm p_3, \qquad p_\perp = p_1 + \mathrm{i} p_2. \tag{3.13}$$

The Weyl spinors are then given by [47]

$$|p+\rangle = \frac{e^{\mathrm{i}\frac{\theta}{2}}}{\sqrt{|p_+|}} \begin{pmatrix} -p_\perp^* \\ p_+ \end{pmatrix}, \qquad \langle p-| = \frac{e^{\mathrm{i}\frac{\theta}{2}}}{\sqrt{|p_+|}} \begin{pmatrix} p_+ \\ p_\perp \end{pmatrix},$$
$$\langle p+| = \frac{e^{\mathrm{i}\frac{\theta}{2}}}{\sqrt{|p_+|}} \left(-p_\perp, p_+ \right), \qquad |p-\rangle = \frac{e^{\mathrm{i}\frac{\theta}{2}}}{\sqrt{|p_+|}} \left(p_+, p_\perp^* \right). \tag{3.14}$$

Note that we can also define massive spinors with the help of a reference momentum. We use the reference momentum q to promote a massive four-momentum p to a light-like

four-momentum $p^\flat$:

$$p^\flat_\mu = p_\mu - \frac{p^2}{2pq} q_\mu \tag{3.15}$$

where $p^2 = m^2$ and $p^{\flat 2} = 0$. The reference momentum has to be light-like, too, which is the reason why we did not simply define the energy component in equation (3.12) as p_0; the above version will also work properly for massive spinors. We can then define massive spinors by

$$
\begin{aligned}
u^\pm(p,q) &= \frac{\not p + m}{\langle p^\flat \pm | q \mp \rangle} | q \mp \rangle\,, & \bar u^\pm(p,q) &= \langle q \mp | \frac{\not p + m}{\langle q \mp | p^\flat \pm \rangle}\,, \\
v^\mp(p,q) &= \frac{\not p - m}{\langle p^\flat \pm | q \mp \rangle} | q \mp \rangle\,, & \bar v^\mp(p,q) &= \langle q \mp | \frac{\not p - m}{\langle q \mp | p^\flat \pm \rangle}\,.
\end{aligned}
\tag{3.16}
$$

All spinors defined above obey the Dirac equation, the orthogonality relations

$$\bar u^\lambda u^{\lambda'} = 2m\delta_{\lambda\lambda'}\,, \qquad \bar v^\lambda v^{\lambda'} = -2m\delta_{\lambda\lambda'}\,, \tag{3.17}$$

and the completeness relations

$$\sum_{\lambda=\pm} u^\lambda \bar u^\lambda = \not p + m\,, \qquad \sum_{\lambda=\pm} v^\lambda \bar v^\lambda = \not p - m\,. \tag{3.18}$$

On a technical side, note that we implemented all spinors as four-component objects even though one can implement Weyl spinors only as two component spinors which might prove a bit faster. However, most of the helicity methods we are going to present in this thesis are based on linear combinations of helicity eigenstates so that we need all four components anyway. The advantage of such an implementation is that we can treat all spinors on the same footing. In addition, we also use the Weyl–van der Waerden formalism (see [48–50], the specific details on our implementation can be found in [36]) to turn the polarization vectors into 2×2 matrices, i.e. a total of four components. In summary, we can describe both polarization vectors and fermion spinors by four-component objects. We exploit this to define a single spinor class in our code that contains four complex components plus an information on the spinor type it describes. By defining a spinor multiplication function that is sensitive to the spinor types, we can code many operations very generally without having to distinguish between particle types: the spinor class will make sure that the spinors are multiplied in the correct way. This avoids duplicate code in many places and makes it easy to maintain an error-free code base.

3.1.4 The Leading Color Approximation

The color-flow decomposition exhibits a simple structure for the color factors in terms of Kronecker deltas which, as we saw, comes at the cost of a more complicated color projection operator

$$P_g = \delta_{\bar i i}\, \delta_{\bar j j} - \frac{1}{N_\mathrm{c}} \delta_{i j}\, \delta_{\bar i \bar j} \tag{3.19}$$

which has to be applied to each external gluon in the process. This gives rise to additional terms in the amplitude that are of order $\mathcal{O}\left(\frac{1}{N_c}\right)$, hence the amplitude can be written as

$$\mathcal{A} = \mathcal{A}^{\text{lc}} + \mathcal{A}^{\text{slc}} \tag{3.20}$$

where $\mathcal{A}^{\text{slc}}$ is the so-called *sub-leading color* contribution that encompasses all terms that are of order $\mathcal{O}\left(\frac{1}{N_c}\right)$ with respect to the *leading color* amplitude $\mathcal{A}^{\text{lc}}$. Empirically, it has been verified time and time again for different processes that the sub-leading color contributions amount to only a few percent of the total amplitude (i.e. up to approximately $1/N_c^2 \approx 10\,\%$).

Within the context of color decomposition it is especially simple to extract the leading color contribution: if one looks at the full expression for the squared amplitude,

$$|\mathcal{A}|^2 = \sum_{m,n} A_m^\dagger \mathbf{C}_{mn} A_n, \tag{3.21}$$

one can see that the leading color factors which are encoded in the color matrix $\mathbf{C}_{mn}$ are just the diagonal elements $\mathbf{C}_{mm}$, i.e. the leading color squared amplitude is given by

$$|\mathcal{A}^{\text{lc}}|^2 = \sum_m A_m^\dagger \mathbf{C}_{mm} A_m. \tag{3.22}$$

The color matrix can be written such that $\mathbf{C}_{mm}$ is a constant for all m such that it can be dragged out of the sum and we are left with

$$|\mathcal{A}^{\text{lc}}|^2 = \mathbf{C}_{00} \sum_m |A_m|^2. \tag{3.23}$$

In the special case of electron–positron annihilation where the initial states are given by colorless non-QCD particles, we can simplify this even further. Upon integration over phase space, we note that if all particles are massless, the ordering of particles is not important since we integrate each particle over the same phase space volume. Taking this into account, we can simply replace the sum over m by a factor that is equal to the number of terms in the sum to obtain the integrated version of any leading order matrix element.

Let us stress that this is a remarkable simplification of the original full color decomposition: instead of computing $\mathcal{O}(n!)$ (where n is the number of external particles) partial amplitudes, we only have to compute one to obtain a physically reasonable result.

In addition, there is another benefit that enters through the leading color approximation which has to do with the processes that contribute to the desired observable. The tests and analyses we will perform in this thesis are done for exclusive cross sections for electron–positron annihilation into n QCD jets. If we consider the example of four jets, there are two basic processes that contribute to the full observable at Born level:

$$e^- e^+ \rightarrow \begin{cases} q\bar{q}gg \\ q\bar{q}q'\bar{q}'. \end{cases} \tag{3.24}$$

Those quarks with a prime represent quarks that can have the same or a different flavor with respect to the first quark pair. In the leading color approximation, we can drop the latter processes (i.e. all contributions with more than one quark pair) since they are sub-leading with respect to the color information of the first process. Independent of the number of jets, the leading color process for electron–positron annihilation is always given by

$$e^- e^+ \to q\bar{q} + (n-2)g. \tag{3.25}$$

An indication for the reason can be found in the color structure of gluons versus quarks, see for example the color projectors in equation (3.6). Quarks have one color line, indicated by a single color delta (or basically, one index i or j, while gluons come with two color lines (or two indices i *and* j; the reason being that they transform according to the adjoint representation). Looking at the leading color contribution for a given process, we find eventually that each color line gives rise to a factor of $\sqrt{N_c}$.[3] Thus, each gluon contributes N_c to the overall color factor, while each quark only contributes $\sqrt{N_c}$ (or, equivalently, each quark pair contributes N_c). This makes it easy to see that the leading color contribution of the process with only two quarks is of a higher color order than the leading color contribution for any process with multiple quark pairs.

Note that with the above information, it is also easy to derive the color factor $\mathbf{C}_{00}$ for electron–positron annihilation at leading color:

$$\mathbf{C}_{00} = N_c^{\frac{n_q}{2}+n_g} = N_c^{1+n_g}, \tag{3.26}$$

where $n_q = 2$ is the number of quarks and antiquarks (thus $n_q/2 = 1$ is the number of quark pairs) and n_g is the number of gluons in the process. The electron–positron pair obviously does not contribute to the color information.

The code used for this thesis is especially optimized for leading color electron–positron annihilation. The plot in fig. 3.3 shows that the program used for the present work performs optimally: shown is the computation time for one phase space point of the Born process $e^+ e^- \to n$ jets, i.e. $e^+ e^- \to \bar{q}q + (n-2)g$. As derived in [23], the naive recursive approach should give a 4^n scaling behavior, while the current memory that we discussed earlier reduces the scaling down to n^4 which is due to the four–gluon vertex. The plot shows that our implementation provides the desired scaling. In fact, it is even a little better since the four–gluon vertex only comes into play if there are at least three gluons in the process which is true for five jets and above. Below that the scaling is dominated by the three–gluon vertex giving a n^3 behavior, which is reflected in the fit value.

---

[3]Let us stress that this is only valid for leading color contributions. The calculations to see this are not difficult, but they require some more information than we have given here; hence, we do not perform them here. To that end, we refer the reader to [36, 40, 41] where color calculations in the color-flow decomposition are described in great detail.
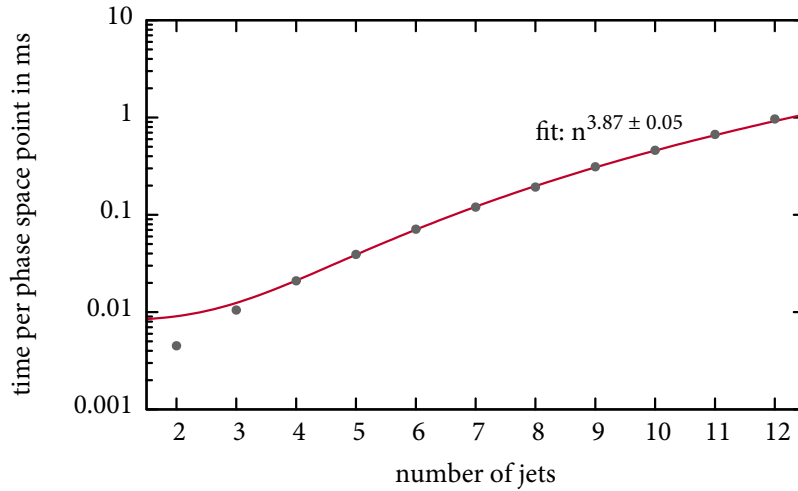
Figure 3.3: Scaling behavior of leading color Born amplitudes for $e^-e^+ \rightarrow q\bar{q} + (n-2)g$. The red line and corresponding dark gray dots show the data points and fit taken for the time it takes to evaluate an integrand at one phase space point. Note that the expected $\mathcal{O}(n^4)$ behavior is due to the four-gluon vertex which can appear only for five jets or more. The fit was done for all values starting with four jets; this explains why the fit result is slightly better than n^4.

3.2 Next–To–Leading Order: Coping with Infinities

So far, we have discussed methods to compute tree-level amplitude such as they appear in the Born contribution and for the real emission matrix element. As we already saw in the previous chapter, next–to–leading order calculations pose a wholly different problem of infrared and ultraviolet divergences. As we will see, the numerical treatment of divergences is very different from analytical methods and requires special attention. While we briefly discuss a method to tackle the ultraviolet divergences numerically, we first put special emphasis on removing infrared poles from our calculations.

3.2.1 The Subtraction Method

Let us begin by formalizing some things we have established about next–to–leading order calculations in chapter 2. To this end, we will first restrict ourselves to observables with non-hadronic initial states (e.g. electron–positron collisions) and we only consider massless partons, i.e. quark masses are set to zero. We will relax both restrictions later on.

First, let us introduce a new notation for cross sections that will simplify the discussion. We will write any leading–order or Born cross section as

$$\sigma^{\text{LO}} = \int_n d\sigma^{\text{B}} \qquad (3.27)$$

where n now indicates the number of final state particles, as opposed to the total number of particles. The integrand, the phase space measure, and the jet function are contained in

$\mathrm{d}\sigma^{\mathrm{B}}$:

$$\mathrm{d}\sigma^{\mathrm{B}} \propto \mathrm{d}\Phi_n \, |\mathcal{A}_n^{(0)}|^2 \, J_n \qquad (3.28)$$

(we left out averaging factors and constants as usual).

At next–to–leading order, we find the following contributions:

$$\sigma^{\mathrm{NLO}} = \int_{n+1} \mathrm{d}\sigma^{\mathrm{R}} + \int_n \mathrm{d}\sigma^{\mathrm{V}} \qquad (3.29)$$

where we denoted the real corrections by $\mathrm{d}\sigma^{\mathrm{R}}$ and the virtual corrections that contain an additional loop (whose integral we have hidden—that is, we assume that the virtual contributions are already regularized and renormalized) by $\mathrm{d}\sigma^{\mathrm{V}}$. These contributions are given by

$$\mathrm{d}\sigma^{\mathrm{R}} \propto \mathrm{d}\Phi_{n+1} \, |\mathcal{A}_{n+1}^{(0)}|^2 \, J_{n+1}, \qquad (3.30\mathrm{a})$$

$$\mathrm{d}\sigma^{\mathrm{V}} \propto \mathrm{d}\Phi_n \, 2\Re\left\{ \left(\mathcal{A}_n^{(0)}\right)^* \mathcal{A}_n^{(1)} \right\} J_n. \qquad (3.30\mathrm{b})$$

As we mentioned in chapter 2, both of these contributions are singular with respect to soft or collinear external partons in the case of the real correction and soft or collinear loop particles in the case of the virtual correction. As stated before, one performs an analytical continuation of the integral to $D = 4 - 2\epsilon$ dimensions in an analytical calculation where all singularities manifest themselves as poles at $D = 4 \Leftrightarrow \epsilon = 0$ in both the real and virtual corrections. Upon summation of the two contributions, one finds that these poles cancel exactly: both $\mathrm{d}\sigma^{\mathrm{R}}$ and $\mathrm{d}\sigma^{\mathrm{V}}$ have terms proportional to $1/\epsilon^2$ and $1/\epsilon$ that only differ by their relative sign. What remains after the summation are terms that are of order ϵ^0 or higher—setting $D = 4 \Leftrightarrow \epsilon = 0$ then yields a finite result.

Automated numerical calculations exhibit a problem at this point: obviously, it is impossible to perform a calculation in non-integer dimensions and thus to extract the pole behavior from a numerical value. If one naively integrates for example the real correction using Monte Carlo methods, the poles reveal themselves in terms of huge matrix elements when the phase space configuration is rather soft or collinear, compared to those of harder configurations. Of course, the Monte Carlo integration will not converge in such a case but approach (negative) infinity.

What can be done about this? Integrating both contributions "together" is not an alternative since their phase space elements do not match, which is already obvious from the fact that the real corrections have an additional external parton. What we have to achieve instead, is a *local* or *point-wise* (i.e. per phase space point) cancellation of divergences.

One ubiquitously used method to do this is called the *subtraction method* (first detailed

in [51]) and can be written as follows:

$$
\sigma^{\mathrm{NLO}} = \int\limits_{n+1} \left[\mathrm{d}\sigma^{\mathrm{R}} - \mathrm{d}\sigma^{\mathrm{A}} \right] + \int\limits_{n+1} \mathrm{d}\sigma^{\mathrm{A}} + \int\limits_{n} \mathrm{d}\sigma^{\mathrm{V}}
$$
$$
= \int\limits_{n+1} \left[\mathrm{d}\sigma^{\mathrm{R}} - \mathrm{d}\sigma^{\mathrm{A}} \right] + \int\limits_{n} \left[\mathrm{d}\sigma^{\mathrm{V}} + \int\limits_{1} \mathrm{d}\sigma^{\mathrm{A}} \right]
$$

(3.31)

In principle, this is the same equation as (3.29) with an added zero in the form of the new auxiliary contribution $\mathrm{d}\sigma^{\mathrm{A}}$. As the integral reveals, this new term is formulated for the $(n+1)$–particle phase space of the real emission contribution. In order to make the integration finite, it has to fulfill a couple of requirements:

- $\mathrm{d}\sigma^{\mathrm{A}}$ has to be formulated such that it matches all poles of $\mathrm{d}\sigma^{\mathrm{R}}$ locally for each phase space point. If this requirement is met, the left hand integral in equation (3.31) has no poles in ϵ and is integrable in four dimensions by construction.

- The two right hand integrals in the first line of equation (3.31) are still divergent. However, we know that $\mathrm{d}\sigma^{\mathrm{A}}$ contains the same poles as $\mathrm{d}\sigma^{\mathrm{R}}$ and thus, due to the KLN theorem, the same poles as $\mathrm{d}\sigma^{\mathrm{V}}$ with a negative sign. While this seems to be no better than the original problem, it is in fact possible to formulate the auxiliary term such that its $(n+1)$–particle phase space factorizes with respect to the additional parton. One can then perform the integration over the extra particle analytically (once and for all) and find that the resulting poles in ϵ cancel the infrared poles from the virtual contribution exactly—provided that $\mathrm{d}\sigma^{\mathrm{A}}$ has been constructed correctly. Then, one cancels the poles analytically and performs the Monte Carlo integration over the remaining finite terms in four dimensions, which is stated in the right hand integral of the second line of equation (3.31).

Having such a $\mathrm{d}\sigma^{\mathrm{A}}$ at hand will not help if the term is hopelessly complicated, which would make any implementation in a numerical program an arduous and error-prone task and which could also possibly lead to a very slow performance. In other words: we also require that the auxiliary term is "easily" implementable in a numerical program and suited for Monte Carlo algorithms. The above discussion suggests the natural requirement of making the auxiliary term as independent as possible; in fact, the term we will construct will be independent of the jet observable that we use. Furthermore, the term will be designed such that it can be implemented in an automated way such that it automatically works for any QCD process.

The question that remains is how to formulate this new auxiliary term. Note that we will have to construct different terms for different helicity methods, thus we present only those aspects that are common to all methods in this section. Our starting point for this discussion will be going back to the beginning and re-capitulating what it is exactly that we have to capture inside $\mathrm{d}\sigma^{\mathrm{A}}$. In the following let us discuss the computation of an exclusive $e^- e^+ \to n$ jet cross section where our leading–order result is given by a partonic event with n massless final state particles that all describe separate jets with respect to the jet
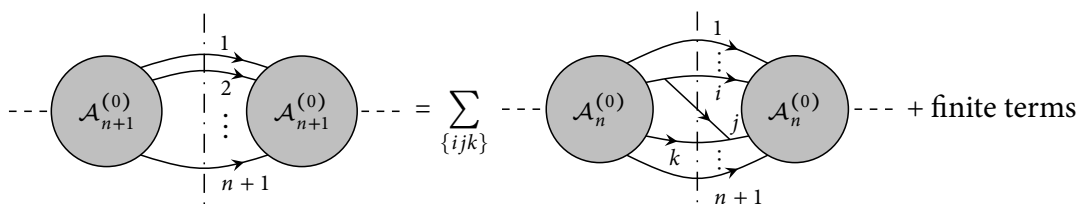
Figure 3.4: The external-leg insertion rule says that all soft and collinear poles of a (n + 1)–parton amplitude can be approximated by inserting leg j as a correlation over all possible pairs i and k. The graphs show the squared amplitudes graphically in terms of the amplitudes and their complex conjugates (the conjugation is not specially indicated). The dashed lines illustrate non-QCD particles (e.g. $e^- e^+$ in the initial state). The lines with arrows illustrate how external QCD lines are connected between the amplitudes. Original picture from [26, 52].

(a) $q \to qg$ **(b)** $\bar{q} \to g\bar{q}$ **(c)** $g \to gg$ **(d)** $g \to q\bar{q}$
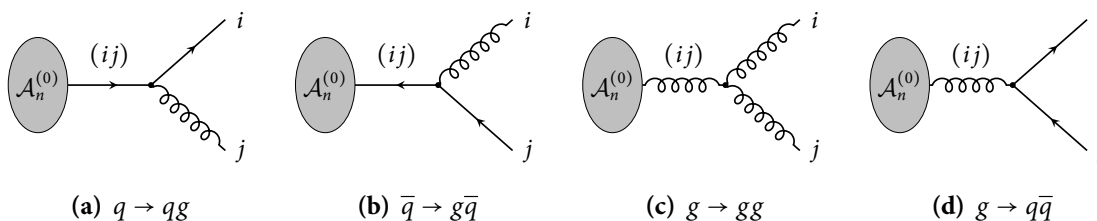
Figure 3.5: All possible splittings for the insertion of an extra soft or collinear parton. The gray blob denotes the remaining n-parton amplitude.

resolution y_{cut}. We will later review the whole procedure and generalize it to massive quarks and initial state partons, see chapter 4.

The real emission contribution $d\sigma^R$ captures the addition of a parton to the leading–order result in such a way that the number of jets that we produce is unchanged, i.e. we still describe n jets. By virtue of the jet algorithm, this means that the added parton will be part of the same jet as one of the other partons—we denote the pair by the indices (i, j)—and thus j will be soft or collinear to i. We have already discussed the soft and collinear singularities arising from the emission of an extra gluon in section 2.4. In fact, this behavior is *universal* in the sense that we do not need to consider the specific structure of the real emission amplitude $|\mathcal{A}_{n+1}^{(0)}|^2$ to describe its singular behavior. Instead, this universality can be expressed in terms of the external-leg insertion rule which tells us that we can extract all poles from $|\mathcal{A}_{n+1}^{(0)}|^2$ by looking at the corresponding tree-level amplitude $|\mathcal{A}_n^{(0)}|^2$ and inserting the additional leg j as shown in figure 3.4. On the level of a single amplitude (as opposed to the squared amplitude), we see that the new external leg j appears as a splitting of a three–particle vertex $(ij) \to i + j$, where we denoted the particle that splits—the *splitting particle*—by (ij). Depending on the types of the partons i and j, there are four possible splittings: $g \to gg$, $q \to qg$, $\bar{q} \to g\bar{q}$, and $g \to q\bar{q}$, see figure 3.5. We can easily see that it is in fact these splittings that cause soft and collinear poles. The

propagators for any of the four splittings are proportional to

$$\frac{1}{(p_i + p_j)^2} = \frac{1}{2p_i p_j} = \frac{1}{s_{ij}}. \tag{3.32}$$

The numerator vanishes both in the soft limit, $p_j \to 0$, and in the collinear limit, $(p_i + p_j)^2 \to p_{ij}^2 = 0$.

To determine an actual form of the auxiliary term $d\sigma^A$ we need to know the two limits better. Let us therefore analyze these in more detail.

3.2.2   The Soft Limit of an Amplitude

We start from a leading–order amplitude $\mathcal{A}_n$ to which we add a soft gluon j with momentum p_j. Note that we drop the superscript (0) from now on for all amplitudes to improve readability; unless an amplitude has an explicit superscript (1), we understand it to be a tree-level amplitude. We parameterize the momentum of the soft gluon as follows:

$$p_j^\mu = \lambda_{\text{soft}} k^\mu, \quad \lambda_{\text{soft}} \to 0. \tag{3.33}$$

It is well-known that this limit can be written as [26, 47, 52]

$$\lim_{\lambda_{\text{soft}} \to 0} \mathcal{A}_{n+1}(p_1, \ldots, p_{n+1}) = g_s \mu^\epsilon \, \epsilon_\mu(p_j) \, J^\mu(p_j) \, \mathcal{A}_n(p_1, \ldots, \not{p}_j, \ldots, p_{n+1}) \tag{3.34}$$

where the coupling is equipped with the usual scale factor μ^ϵ to keep it dimensionless in $D = 4 - 2\epsilon$ dimensions. We write the n–parton amplitude on the right in terms of the momenta of the $(n+1)$–parton amplitude and simply remove the soft parton j. Furthermore, we have the polarization vector $\epsilon(p_j)$ of the soft gluon and the *eikonal current* or *soft gluon emission current*

$$J^\mu \equiv J^\mu(p_j) = \sum_{\substack{i=1 \\ i \neq j}}^{n+1} \mathbf{T}_i \frac{p_i^\mu}{p_i p_j}, \qquad (p_j)_\mu J^\mu(p_j) = 0 \tag{3.35}$$

which describes the emission of the soft gluon p_j off all other final state partons and which is conserved with respect to the momentum of the soft parton.

Since subtraction works at the level of integrands, i.e. squared amplitudes, we have to square the above expression:

$$\lim_{\lambda_{\text{soft}} \to 0} \left| \mathcal{A}_{n+1} \right|^2 = 4\pi\alpha_s \mu^{2\epsilon} \mathcal{A}_n^* \, \epsilon_\mu^*(p_j) \epsilon_\nu(p_j) \, J^{\mu\dagger} J^\nu \, \mathcal{A}_n. \tag{3.36}$$

Using color algebra and some sum acrobatics we can re-formulate the product of the eikonal currents into

$$J^{\mu\dagger} J^\nu = \sum_{\substack{i,k=1 \\ i \neq k \neq j}}^{n+1} \mathbf{T}_i \mathbf{T}_k \left(-\frac{p_i^\mu p_i^\nu}{(p_i p_j)^2} + \frac{p_i^\mu p_k^\nu + p_k^\mu p_i^\nu}{(p_k p_j)(p_i p_j + p_k p_j)} \right) \tag{3.37}$$

which looks more complicated than the simple product but which will serve well as a common starting point for the discussion of different helicity methods.

Looking at equation (3.37), it is clear that the poles come from the numerators of the eikonal currents. Inserting equation (3.33), we find that both terms are of order $1/\lambda^2_{\text{soft}}$ which is exactly the pole we have to subtract.

Any further analysis depends on the parameterization of helicities that we use for $\epsilon(p_j)$; we continue the discussion when we detail the real subtraction for the respective helicity methods.

Before turning to the collinear limit, let us make one more remark concerning equation (3.36). In the literature, this formula is often called a *factorization* formula into the n–parton squared amplitude and soft eikonal factor. This is not strictly true and equations (3.36) and (3.37) expose the reason for this. We cannot write the two leading–order amplitudes as a squared amplitude since their color structure is altered: the eikonal currents introduce color correlations between the amplitudes through the color factors $\mathbf{T}_i\mathbf{T}_k$. These can be computed using the aforementioned method of replacing the appropriate color projectors.

3.2.3 The Collinear Limit of an Amplitude

Let us now turn to the collinear limit. Just like we did for the soft case, we try to find a simplified expression for the amplitude. To this end, we again re-parameterize our momenta. Since the two momenta p_i and p_j become collinear, we have to parameterize both of them with what is called the *Sudakov parameterization* [53–55]:

$$
\begin{aligned}
p_i^\mu &= x p_{\text{coll}}^\mu + k_\perp^\mu - \frac{k_\perp^2}{x} \frac{n^\mu}{2(n p_{\text{coll}})}, \\
p_j^\mu &= \overline{x} p_{\text{coll}}^\mu - k_\perp^\mu - \frac{k_\perp^2}{\overline{x}} \frac{n^\mu}{2(n p_{\text{coll}})}.
\end{aligned}
\tag{3.38}
$$

This parameterization introduces several new variables:

- p_{coll} is the unified collinear momentum of the two particles in the sense that the vector sum of the two momenta $p_i + p_j$ is equal to p_{coll} plus a remainder of order $\mathcal{O}\left(k_\perp^2\right)$:

$$
p_{ij}^\mu = p_i^\mu + p_j^\mu = p_{\text{coll}}^\mu - \frac{k_\perp^2}{x\overline{x}} \frac{n^\mu}{2(n p_{\text{coll}})} = p_{\text{coll}}^\mu + \mathcal{O}\left(k_\perp^2\right).
\tag{3.39}
$$

  p_{coll} is a light-like four-vector $p_{\text{coll}}^2 = 0$.

- x is a real value between zero and one that contains the energy fraction of particle i with respect to the collinear momentum p_{coll}. If particle i is soft x is very small, if particle j is soft x is close to one.

- $\overline{x} = 1 - x$ is the corresponding energy fraction for particle j. We use the "bar" notation frequently to indicate that the quantity below the bar has to be subtracted from one.
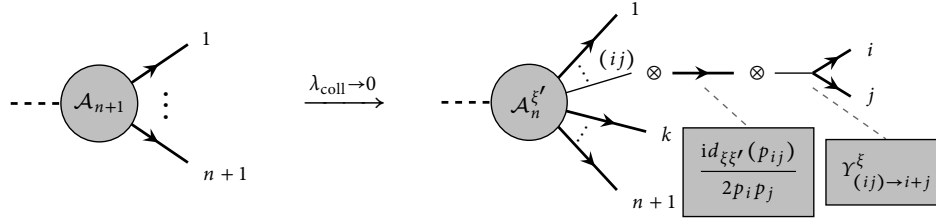
Figure 3.6: Pictorial representation of how one splits the $(n+1)$–parton amplitude into three separate parts that make up the decomposition in equation (3.41). Note that lines with arrows indicate partons in general (not just fermions, possibly also gluons) while thin lines without arrows only illustrate connections, not actual polarization vectors or spinors.

- $k_\perp$ is the important quantity that distinguishes the two momenta from the collinear direction. It is a space-like momentum, $k_\perp^2 < 0$ which is perpendicular to the collinear direction, $p_{\text{coll}} \cdot k_\perp = 0$ and, in the collinear limit, goes to zero. To analyze the collinear limit, we set

$$k_\perp^\mu = \lambda_{\text{coll}} \, k^\mu, \quad \lambda_{\text{coll}} \to 0. \tag{3.40}$$

- Finally, a third quantity n is introduced which is an arbitrary light-like four-vector $n^2 = 0$ which is perpendicular to $k_\perp$, $k_\perp \cdot n = 0$ and necessary to determine the final configuration uniquely.

In this limit, we can write the amplitude as

$$
\begin{aligned}
\lim_{\lambda_{\text{coll}} \to 0} & \mathcal{A}_{n+1}(p_1, \ldots, p_{n+1}) \\
&= g_s \mu^\epsilon \, \mathbf{T}_{(ij) \to i+j} \Upsilon^\xi_{(ij) \to i+j} \frac{\mathrm{i} d_{\xi \xi'}(p_{ij})}{2 p_i p_j} \mathcal{A}_n^{\xi'}(p_1, \ldots, (\not{p}_i, \not{p}_j) \to p_{ij}, \ldots, p_{n+1}).
\end{aligned}
\tag{3.41}
$$

This equation introduces quite a few new symbols and requires some explanation. The situation is sketched in figure 3.6. The amplitude on the right is again an n–parton amplitude where the collinear particles i and j have been replaced by the splitting parton (ij). However, the amplitude is not a scalar but it lacks the usual polarization vector or spinor for the splitting particle (ij) and therefore has an open index ξ'. This open index is a generalized index which can either be a Lorentz index or a Dirac index, depending on whether parton (ij) is a gluon or a quark. Henceforth, we will denote such an incomplete amplitude with the term *open amplitude*.

The fraction inside equation (3.41) is the propagator of the splitting particle. To make this more concrete, we have to distinguish between gluons and quarks:

Gluons: With our parameterization of polarization vectors (see equation (3.8)), we automatically work in axial gauge. In this gauge the polarization sum of a particle with

momentum p and helicities λ reads

$$d_{\mu\nu}(p) \equiv \sum_\lambda \epsilon_\mu^{\lambda\,*} \epsilon_\nu^\lambda = -g_{\mu\nu} + \frac{p_\mu n_\nu + n_\mu p_\nu}{pn} - \frac{p_\mu p_\nu}{(pn)^2} n^2 \qquad (3.42)$$

(where the last term vanishes with our choice that n is light-like). At the same time, the gluon propagator (without color information) in axial gauge reads

$$G_{\mu\nu}(p, n) = \frac{\mathrm{i}\left(-g_{\mu\nu} + \frac{p_\mu n_\nu + n_\mu p_\nu}{pn} - \frac{p_\mu p_\nu}{(pn)^2} n^2\right)}{p^2 + \mathrm{i}0} = \frac{\mathrm{i} d_{\mu\nu}(p)}{p^2 + \mathrm{i}0}, \qquad (3.43)$$

i.e. we can write the propagator in terms of the polarization sum.

Quarks: Even simpler, the fermionic spin sum is already of the form that we require to rewrite the propagator $F_{\alpha\beta}$:

$$d_{\alpha\beta}(p) \equiv \sum_\lambda u_\alpha^\lambda \overline{u}_\beta^\lambda = (\slashed{p} + m)_{\alpha\beta} \qquad (3.44)$$

$$F_{\alpha\beta}(p, m) = \frac{\mathrm{i}(\slashed{p} + m)_{\alpha\beta}}{p^2 - m^2 + \mathrm{i}0} = \frac{\mathrm{i} d_{\alpha\beta}(p)}{p^2 - m^2 + \mathrm{i}0}. \qquad (3.45)$$

Here, we neglected both color and flavor information. We indicated the Dirac structure explicitly with the Dirac indices α and β to be able to write it in the same form as the gluon propagator, which we will make use of below. Note that this formula is obviously also valid for $m = 0$.

Finally, we find the pieces that together make up the splitting of particle (ij) to i and j: $\Upsilon_{(ij)\to i+j}^\xi(p_i, p_j)$ which is essentially the kinematical part of the splitting vertex times its color factor $\mathbf{T}_{(ij)\to i+j}$ and the coupling.

Squaring the amplitude, we obtain the total expression

$$\lim_{\lambda_{\mathrm{coll}}\to 0} \mathcal{A}_{n+1}(p_1, \dots, p_{n+1}) = 4\pi\alpha_s \mu^{2\epsilon} \mathbf{T}_{(ij)\to i+j}^2 \mathcal{A}_n^{*\,\zeta'} \frac{d_{\xi'\xi}}{2p_i p_j} \Upsilon^{*\xi} \Upsilon^\zeta \frac{d_{\zeta\zeta'}}{2p_i p_j} \mathcal{A}_n^{\zeta'} \qquad (3.46)$$

where we omitted some indices and arguments for better readability. Again, we find no true factorization since the amplitude's open indices are connected with the splitting functions and thereby introduce *spin correlations*. In order to develop this formula further, we need to define these splittings $\Upsilon_{(ij)\to i+j}$ more closely. The exact definition will again vary depending on the splitting $(ij) \to i + j$ but also on the helicity method that we use.[4]

Before we start constructing the subtraction terms from the two limits we discussed so far, let us clarify a little further how these limits are connected with $\mathrm{d}\sigma^{\mathrm{A}}$. Both equations (3.36) and (3.46) are only valid in the respective strict limit. Consider the soft limit, which is only valid if parton j is truly soft, i.e. $\lambda_{\mathrm{soft}} = 0$. In any other case, momentum conservation

---

[4]We will rarely give an exact definition for $\Upsilon_{(ij)\to i+j}$. Instead, we will define other symbols that contain the splittings. The purpose of introducing the symbol $\Upsilon_{(ij)\to i+j}$ is to provide a means of comparing the definitions for different helicity methods.

will either be violated for the n–parton amplitude on the right side of equation (3.34), or the $(n+1)$–parton amplitude on the left side, depending on how the momenta are defined. The same applies to the collinear limit. For our numerical computation, however, we need to approach these limits smoothly, something which is not possible with the above formulas. Nevertheless, our subtraction term must match the soft and collinear limits so these serve both as a check and also as a means of constructing $d\sigma^A$ as we will see.

There are several methods on the market that realize proper subtraction terms. In principle, these methods only differ by some finite remainders that they contain. Since we effectively add zero when performing the subtraction, we can basically include as many finite terms as we want in $d\sigma^A$. In practice, the specific parameterization of these methods varies greatly. We restrict ourselves in this thesis to the *dipole formalism* by Catani and Seymour [26, 56] which is probably the most-used and best studied of all algorithms.[5]

3.2.4 Virtual Corrections

The subtraction we described previously takes care of the infrared singularities that occur both in the real emission and in the virtual contribution. However, it assumes that the ultraviolet divergences that occur for large loop momenta in the virtual corrections have already been regularized and renormalized. As a matter of fact, this regularization and renormalization is once again a highly non-trivial step.

The analytical method is comprised of going to D dimensions and extracting poles in terms of $\epsilon = {}^{4-D}\!/_2$. The reason for these poles is given by the fact that the coupling constants, masses, and the wave function normalizations that appear in the Lagrangian are not actually the quantities that are measured, but are *bare* quantities which neglect vacuum fluctuations in the form of loop corrections that screen the bare quantities in an actual measurement. The solution is to absorb these ultraviolet poles into a redefinition of the couplings, masses and wave function normalizations by virtue of a *renormalization scale μ_R*.

In practice, one uses *renormalized perturbation theory*, where for each order in the coupling one defines so-called *counter term* Feynman rules that have to be applied in addition to the normal Feynman rules. These counter term rules then render the virtual corrections ultraviolet finite. In terms of our symbolic notation, the ultraviolet finite virtual contribution can be written as follows:

$$\int_n d\sigma^V = \int_n \left(\int_\ell d\sigma^V_{\mathrm{bare}} + d\sigma^V_{\mathrm{CT}} \right). \tag{3.47}$$

Note that while being ultraviolet finite, this contribution is still infrared divergent, which is the reason why we have to add the integrated subtraction term in the subtraction method. The index "bare" represents the virtual contribution computed "naively" with the normal Feynman rules; we indicated the integration over the loop momentum ℓ explicitly. The

---

[5]Other methods are for example FKS subtraction [57, 58] or Nagy–Soper subtraction [59, 60].

right hand contribution is obtained from also using the counter term Feynman rules.

Once again, this cannot be easily computed numerically. The point is that, similar to the problem with infrared divergences, both the bare and the counter term are divergent on their own. The sum cannot be formed in a numerical program since the integration dimensions are once again different: the bare contribution has four additional dimensions for the loop momentum.

This is the place where the different methods that were mentioned earlier diverge strongly in the way they overcome this problem. One conventional method is to realize that all divergent diagrams can be reformulated in terms of a fixed set of so-called *master integrals* that are computed once analytically and whose results can be implemented in numerical programs. The numerical code is then left with evaluating coefficients to these integrals that are process dependent, but finite quantities.

The method we illustrate in the following is very different; it has been developed in the group of Stefan Weinzierl [24, 61–66], but was not directly worked on in the context of this thesis. Since it still forms a part of the framework that this thesis contributes to, we present an introduction to the basic ideas. It aims at performing the integral over the loop momentum numerically, using the same Monte Carlo integration that we perform the phase space integral with (this will be explained in detail in sections 3.3 and 3.4).

The basic idea is to introduce a new subtraction term $d\sigma^L$ which is formulated on the level of the loop integrand (i.e. it has to be integrated over the loop momentum). Similar to the infrared subtraction term $d\sigma^A$, it has to be analytically integrable over the loop momentum. This term subtracts *all* poles, both infrared and ultraviolet, from the bare one-loop contribution, rendering the loop contribution finite. As a consequence, we now have three contributions to the full next–to–leading order cross section which reads as follows:

$$\sigma^{\mathrm{NLO}} = \int_{n+1} \left[d\sigma^R - d\sigma^A \right] + \int_{n+\ell} \left[d\sigma_{\mathrm{bare}}^V - d\sigma^L \right] + \int_n \left[d\sigma_{\mathrm{CT}}^V + \int_\ell d\sigma^L + \int_1 d\sigma^A \right]. \quad (3.48)$$

The first integral is the known real emission contribution with the subtraction term. The second contribution is now only comprised of the bare one-loop integrand and the new subtraction term; we stated above that this yields a finite result by construction. The last integral gathers all "leftovers" and is called *insertion term*. We have the counter term $d\sigma_{\mathrm{CT}}^V$ which contains the global ultraviolet poles, the integrated loop subtraction term which is both ultraviolet and infrared divergent, and the integrated infrared subtraction term. Note that all poles in the insertion term are known analytically and can be canceled before performing a numerical integration. For this to work, the ultraviolet counter term and the integrated loop subtraction term have to use the same renormalization scheme, which influences the construction of $d\sigma^L$.

Let us comment shortly on the construction of the loop subtraction term $d\sigma^L$. The bare integrand is singular for soft and collinear configurations (i.e. when the loop momentum becomes soft or when two loop propagators become collinear) and for ultraviolet configu-

rations. In practice, each of these three cases is treated with a separate local subtraction term whose derivations are explicitly shown in [61]:

$$\int\limits_{n+\ell} \left[d\sigma_{\text{bare}}^{\text{V}} - d\sigma^{\text{L}} \right] \approx \int d\Phi_n \frac{d^4\ell}{(2\pi)^4} \, 2\Re\left[\mathcal{A}^{(0)\,*} \mathcal{G}_{\text{bare}}^{(1)} - \mathcal{A}^{(0)\,*} \left(\mathcal{G}_{\text{UV}}^{(1)} + \mathcal{G}_{\text{soft}}^{(1)} + \mathcal{G}_{\text{coll}}^{(1)} \right) \right] J_n, \quad (3.49)$$

where $\mathcal{G}^{(1)}$ denotes the integrand of the amplitude,

$$\mathcal{A}^{(1)} = \int \frac{d^4\ell}{(2\pi)^4} \mathcal{G}^{(1)}, \quad (3.50)$$

for the bare contribution and the ultraviolet (UV), soft, and collinear (coll) subtraction terms. It turns out that the soft and collinear poles can be written as an n–parton tree-level amplitude times some factors, where the external particles of the amplitude are the same as those of the original loop amplitude. The ultraviolet term is given through *local* counter term Feynman rules on the level of the loop momenta (this is not to be confused with those counter term Feynman rules from renormalized perturbation theory which are global, i.e. not depending on the loop momentum). These can be incorporated into a Berends–Giele like recursion formula. Note that again, the external particles are unaffected. Furthermore, the bare integrand is also computed using recursion relations that include rules for loops (see [61, 62]); its external particles are also unaffected by the loop since it is an internal structure of the diagram.

We stress the fact that the external particles are unaffected by the subtraction formalism since this will enable a straight forward use of the various helicity methods we present in this thesis.

The details on the construction of the subtraction terms are not important in the context of this thesis. Instead, let us take a short look at another feature of the method which is *contour deformation*. Even after rendering the integration finite with respect to ultraviolet and infrared divergences, the loop momentum can still become on shell (after all, the integration is over all possible configurations of the loop momentum, not only off shell momenta). In this case, we find a pole due to the fact that the corresponding loop propagator vanishes. This problem can be overcome by deforming the integration contour into the complex plane. A simple example is Wick rotation; generally, the integrands are much more complicated than those examples where one uses Wick rotation. What is done in practice, is a so-called *direct deformation* of the loop momentum [61, 62, 64, 65, 67]. After subtraction, the loop integrand in general has the following form:

$$\int \frac{d^4\ell}{(2\pi)^4} \frac{f(\ell)}{\prod_j (\ell_j^2 - m_j^2)} \quad (3.51)$$

where the product runs over all momenta ℓ_j of the loop propagator. In the case where any $\ell_j^2 = m_j^2$, we find a pole. The basic idea of the direct deformation is to re-parameterize the loop momentum by $\ell = \widetilde{\ell} + i\kappa(\widetilde{\ell})$, where κ is a function that has to be chosen appropriately.

This transforms the integrand into

$$\int \frac{\mathrm{d}^4\widetilde{\ell}}{(2\pi)^4} \left|\frac{\partial\ell^\mu}{\partial\widetilde{\ell}^\nu}\right| \frac{f\big(\ell(\widetilde{\ell})\big)}{\prod_j(\widetilde{\ell}_j^2 - m_j^2 - \kappa^2 + 2\mathrm{i}\widetilde{\ell}_k\cdot\kappa)}. \tag{3.52}$$

In order to match the sign of the usual i0 prescription (e.g. the gluon propagator in equation (2.6)) we choose κ small, such that $\kappa^2 = 0$, and then we find for the propagators:

$$\widetilde{\ell}_j \cdot \kappa \geq 0. \tag{3.53}$$

This restricts the choice of κ, which is vital for the performance of the integration. Proper choices are discussed in detail in the aforementioned publications.

Combining the contour deformation with the virtual subtraction terms yields a finite overall result. The method has been verified in [24] for electron–positron annihilation into QCD jets.

The biggest virtues of this method are that it is very general in the sense that once all necessary subtraction terms have been derived, it is independent of the observable. In the case of electron–positron annihilation to jets, changing the number of jets is just a matter of changing a single variable n in the numerical code. Furthermore, the method is very fast and scales in the same way as a computation of leading order contributions; in particular, the leading color contributions have been shown to scale as n^4, equal to the Born contribution [24].

3.3 Monte Carlo Integration and *VEGAS*

One of the most important building blocks in the numerical calculation of observables is the integration over final state phase space.

While there are several methods for numerical integration available[6], our method of choice is Monte Carlo integration along with an optimization called *VEGAS*. We will first discuss the basic idea of Monte Carlo and justify why Monte Carlo algorithms are generally best suited for high energy phase space integrals. Then, we will shed some light on the *VEGAS* optimization and its requirements regarding the integrand. Finally, we detail the specific phase space generator that is used for the analysis in the present thesis.

3.3.1 Basic Monte Carlo

Let us begin by specifying what we want to achieve: in general, we have a function $g(\vec{y}) \equiv g(y_1, y_2, \ldots, y_d)$ which we want to integrate over some set of limits $[a_i, b_i]$, $i = 1, \ldots, d$.

First of all, we can simplify this to a problem that is integrated over the d-dimensional

---

[6]Several examples are discussed in [18].

hypercube $[0, 1]^d$ by transforming the integrand. Setting $x_i = \frac{y_i - a_i}{b_i - a_i}$, we find

$$\int_{a_1}^{b_1} \cdots \int_{a_d}^{b_d} \mathrm{d}^d y \, g(\vec{y}) \to \int_0^1 \cdots \int_0^1 \mathrm{d}^d x \, \det\left[J(x_1, x_2, \ldots, x_d)\right] g(\vec{y}) \qquad (3.54)$$

where the inverse of the transformation, $y_i = a_i - (b_i - a_i)x_i$ (no sum convention!), has to be used for $\vec{y}$ in the function's argument for each component. The determinant of the Jacobian matrix, $\det\left[J(x_1, x_2, \ldots, x_d)\right]$, reads

$$\det\left[J(x_1, x_2, \ldots, x_d)\right] = \prod_{i=1}^d (b_i - a_i). \qquad (3.55)$$

With the above in mind, let us re-state the problem: our goal is the numerical computation of the integral

$$I = \int_{[0,1]^d} \mathrm{d}^d x \, f(\vec{x}). \qquad (3.56)$$

The basic idea of Monte Carlo integration is to approximate or *estimate* the value of I as the mean value of a sample of the integrand using random numbers. Let us therefore first define the term *random variable* [68]. A random variable X (possibly multi-dimensional, we drop the vector notation from now on) can generally take several values (either discrete or continuous) that are random in the sense that they cannot be predicted. Each such variable is distributed in some way which we describe by a *probability density function* $p(x)$ with the usual constraint that the total probability is unity:

$$\begin{aligned} \sum_{x \in \mathcal{X}} p(x) &= 1 \qquad \text{(discrete)} \\ \int_{x \in \mathcal{X}} \mathrm{d}x \, p(x) &= 1 \qquad \text{(continuous)}, \end{aligned} \qquad (3.57)$$

where $\mathcal{X}$ denotes the set of all values the random variable X can take. Then, we can express the *expectation value* of a function f with respect to the random variable X as [69]

$$E[f(X)] = \sum_{x \in \mathcal{X}} f(x) p(x) \qquad (3.58)$$

if the random variable is discrete, and as

$$E[f(X)] = \int_{x \in \mathcal{X}} \mathrm{d}x \, f(x) p(x) \qquad (3.59)$$

if it is continuous.

If we now consider a continuous random variable that takes values in the d-dimensional hypercube which are uniformly distributed, i.e. $p(x) = 1$, we see that the expectation value

is formally identical to the result of the integral I we defined above:

$$E[f(X)] = \int\limits_{x \in \mathcal{X}} \mathrm{d}x\, f(x) p(x) \equiv \int\limits_{[0,1]} \mathrm{d}x\, f(x) = I. \tag{3.60}$$

Let us now consider a discrete sample of the function $f(x)$ for N uniformly distributed and continuous random variables $(u_1, u_2, \dots, u_N) \in \mathcal{X}$ and compute the average:

$$e_N[f(X)] = \frac{1}{N} \sum_{i=1}^{N} f(u_i). \tag{3.61}$$

$e_N[f(X)]$ is the so-called *Monte Carlo estimate*. Using the (weak) law of large numbers we find

$$\lim_{N \to \infty} P(|e_N[f(X)] - E[f(X)]| \geq \epsilon) = 0 \tag{3.62}$$

where ϵ is arbitrarily small. This tells us that for large N the estimate $e_N[f(X)]$ approaches the expectation value $E[f(X)]$ so that we can write

$$\lim_{N \to \infty} e_N[f(X)] = \lim_{N \to \infty} \frac{1}{N} \sum_{n=1}^{N} f(u_n) = E[f(X)] = I, \tag{3.63}$$

where we used equation (3.60). We can conclude that the Monte Carlo estimate is indeed an estimate for the true value of the integral. Hence, a basic Monte Carlo algorithm does exactly what (3.61) requires: it samples a large amount of random numbers, calculates the integrand function for each of them and averages over their sum.

An estimate for an integral is no use without providing some information on its error. Let us therefore introduce the *variance S^2* of the function f:

$$S^2[f] = \int \mathrm{d}x \left(f(x) - I \right)^2. \tag{3.64}$$

We can use this to calculate the variance of our Monte Carlo estimate where we find

$$S^2[e_N] = \frac{S^2[f]}{N}. \tag{3.65}$$

Since the error of our integral behaves like the square root of the variance, $S[e_N]$, we see that for Monte Carlo integration it scales like $1/\sqrt{N}$ which is independent of the dimension d of the integral. This is what distinguishes Monte Carlo methods from other numerical integration methods, which all scale with the dimension (i.e. the higher the dimension of the integral, the worse the scaling). Since the integrals we will perform are high-dimensional (see section 3.4) this is a very important feature.

In practice, however, we cannot use the above definition of $S^2[e_N]$ to obtain an error for our Monte Carlo integration since we typically want to compute integrals whose result

I we do not know. Instead of I, we can always use the estimate that we have computed:

$$S^2[e_N] \equiv \frac{1}{N-1} \sum_{i=1}^{N} \left(f(u_i) - e_N[f] \right)^2 = \frac{1}{N} \sum_{i=1}^{N} \left(f(u_i) \right)^2 - \left(e_N[f] \right)^2. \qquad (3.66)$$

With this definition, the error that we obtain for our estimate is only a probabilistic error so that it will never indicate how far the result is actually off the "true" result I but it will only indicate how reliably the estimate was reached during the sampling of the N integrands.

Furthermore, note that the whole procedure of defining a variance and thus an error requires that the function is square integrable. If it is not, the estimate will still be reliable, however, the error might be completely unreliable which can manifest itself in a growing error with the number of integrand evaluations, for example.

3.3.2 The *VEGAS* Algorithm

While the basic Monte Carlo algorithm is sufficient for basic tasks, most integrands require more sophisticated methods. Consider, for example, an integrand function with some peak structures that exhibit differences in function values of the order of several magnitudes. Clearly, a uniformly distributed Monte Carlo algorithm will find a large variance and thus a large Monte Carlo error. In fact, our phase space integral over the squared amplitudes, equation (2.19), shows this behavior due to the soft and collinear enhancements.

What can we do to improve this situation? There exist several so-called *variance reduction* techniques that can be used, an overview is given in [18]. Let us focus on one technique here which is called *importance sampling*. The basic idea is to move away from uniformly distributed random numbers, but use a probability distribution that is suited for the integrand, instead. In essence, this corresponds to a change of variables:

$$\int \mathrm{d}x \, f(x) = \int \mathrm{d}x \, p(x) \frac{f(x)}{p(x)} = \int \mathrm{d}P(x) \frac{f(x)}{p(x)} \qquad (3.67)$$

where we defined $\mathrm{d}P(x) = p(x)\mathrm{d}x$. If $p(x)$ is not uniformly distributed, we have to change our definition of the Monte Carlo estimate and variance, as follows:

$$e_N[f(X)] = \frac{1}{N} \sum_{i=1}^{N} \frac{f(u_i)}{p(u_i)}, \qquad (3.68a)$$

$$S^2[e_N] = \frac{1}{N} \sum_{i=1}^{N} \left(\frac{f(u_i)}{p(u_i)} \right)^2 - \left(e_N[f] \right)^2. \qquad (3.68b)$$

The question that remains is: how do we choose $p(x)$? One can show that the optimal probability function is

$$p(x) = \frac{|f(x)|}{\int \mathrm{d}x \, |f(x)|} \qquad (3.69)$$

which yields a zero variance $S^2 = 0$, meaning that we would find the correct value of the integral I after only one sampled point. However, this also means that we need to know

the behavior of the function we integrate as well as possible. In practice, we integrate functions whose behavior do *not* know in advance, hence applying this method does not seem feasible.

In 1977, G. Peter Lepage came to the rescue by developing an *adaptive algorithm* that realizes importance sampling without requiring knowledge of the integrand beforehand [70, 71]. Basically, the algorithm superimposes a grid onto the integration axis that subdivides the integration range into B "bins". At the start of the integration, each of these bins have equal width $\Delta b_i = {}^1\!/_B$, $i = 1, \ldots, B$. The integration itself is then subdivided into separate *iterations* where each consists of a certain amount of integrand evaluations or *calls*. During each iteration, each bin receives the same amount of integrand evaluations. After each iteration, the data generated in each bin can be used to describe an approximate, discretized version of the integrand function $f(x)$. This is then used to resize and move the bins (the Δb_i) such that during the next iteration, most points are thrown into regions where the integrand is largest.[7] With each iteration, the grid adjusts more to the actual form of the integrand so that each successive iteration yields a smaller variance. An "optimal" grid that does not change much anymore is usually found after a few iterations—as we will see, our integrations generally require around five iterations.

Dividing the integration into iterations obviously requires us to obtain an estimate e_{N_j} and a variance S_j^2 for each iteration j. These are given by equations (3.68) where the sums run over all samples of the respective iteration. The final integration result is not obtained by using these formulas for all samples, but by combining the results of each iteration into a cumulative estimate:

$$e_{\mathrm{cum}}[f(X)] = \left(\sum_{j=1}^{m} \frac{N_j}{S_j^2} \right)^{-1} \sum_{j=1}^{m} \frac{N_j e_{N_j}}{S_j^2}, \tag{3.70}$$

where N_j is the number of calls in iteration j and m is the total number of iterations. Furthermore, *VEGAS* provides us with a check for the consistency of the integration which is given by the χ^2 value per degrees of freedom:

$$\frac{\chi^2}{n_{\mathrm{dof}}} = \frac{1}{m-1} \sum_{j=1}^{m} \frac{(e_{N_j} - e_{\mathrm{cum}})^2}{S_j^2} \tag{3.71}$$

For all our integrations, we verify that this value does not deviate too strongly from one, which indicates that the cumulative estimate can be trusted.

Let us discuss the *VEGAS* grid and its adaptation a little further. The probability distribution that *VEGAS* models is given by

$$p(x) = \frac{1}{B \, \Delta b_i} \tag{3.72}$$

---

[7]Let us remark that the technical realization of this algorithm is neither important at this point (since we use existing libraries [72–74] that provide working and tested *VEGAS* implementations) nor are the formulas illuminating. Hence, we refer the interested reader to the original publication [70].
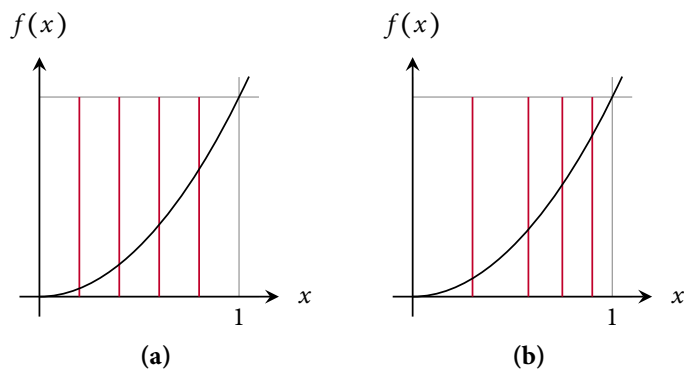
Figure 3.7: Example for a *VEGAS* grid with five bins in one dimension. The left hand diagram shows the grid before and during the first iteration—the bins are of equal size, thus the grid has no effect and mimics a plain Monte Carlo setting. The right hand diagram depicts the grid after adjustment. Since every bin receives the same amount of integrand evaluations on average, those regions where the bins are the most narrow receive more evaluations than those with wide bins. Thus, regions where the integrand is large are most thoroughly checked.

where i is the number of the bin that x corresponds to. This exposes the fact that the algorithm models a discretized probability distribution.

A pictorial representation of the grid and the adaptation is given in figure 3.7. Note that this example is given for a one-dimensional integral. The algorithm has specifically been developed for higher-dimensional integrals for which the above description still applies. However, note that each integral dimension has exactly one set of bins that has to be valid independently of all other dimensions. In other words, the *VEGAS* algorithm requires that the probability function factorizes with respect to the different dimensions:

$$p(x) = p(\vec{x}) = p_1(x_1)\, p_2(x_2)\cdots p_d(x_d). \tag{3.73}$$

Since the optimal probability density is strongly coupled to the integrand function $f(x)$ itself, see equation (3.69), a good grid adaptation can only happen if the integrand itself factorizes well enough. This is illustrated and explained further in figure 3.8.

3.4 Phase Space Generation

In this section, we discuss the generation of phase space in general and describe an algorithm that is suitable for the *VEGAS* algorithm as well as two algorithms that we need to test our subtraction terms later on. The discussion is mostly based on [18, 75, 76]. Unless otherwise noted, we restrict ourselves to massless particles.

In general, the phase space integral for one physical particle is simply given by the integral over all four components of the Minkowski momentum vector (four-momentum). Since we integrate over a *physical* particle, we have to impose the necessary constraints
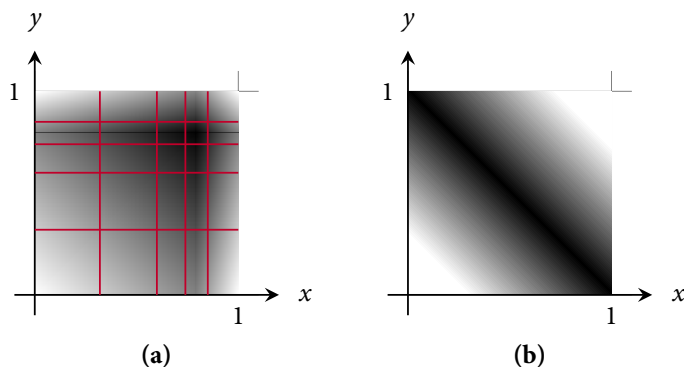
Figure 3.8: Example for a *VEGAS* grid with five bins in two dimensions. x and y are the two random numbers. The function value is sketched in terms of gray scale shading: white indicates a small function value (e.g. zero) while darker shades indicate larger function values. The left hand diagram shows a superposition of two Gauss-like functions, one on the x-plane, the other on the y-plane. This is a situation that is perfectly suited for *VEGAS*, as is indicated by the red superimposed grid. The right hand diagram again depicts a Gauss-like function which is, however, not aligned with either of the axes and thus does not factorize. *VEGAS* has no chance of adapting well to the function. As an example, consider fixing y to a low value, e.g. $y = 0$, for which the appropriate grid in x-direction would roughly match the one depicted in figure 3.7(b). If the integrand was suited for *VEGAS*, this grid would have to be valid for any y, however, if one chooses for example $y = 1$, the optimal x grid would be exactly the opposite as for $y = 0$.

that the particle is on the mass shell, i.e. $p^2 = m^2$, and that its energy is positive, $E = p_0 > 0$:

$$d\Phi_1 = \frac{d^4 p}{(2\pi)^4}(2\pi)\delta(p^2 - m^2)\theta(E) = \frac{d^3 p}{(2\pi)^3 2E} \tag{3.74}$$

Phase space for more than one particle can then be described as a product of one particle phase space elements. Note, however, that for any physical application such as collider physics, we always have conservation of total energy and momentum, which we have to include in the phase space measure. This total momentum conservation is governed by the center-of-mass energy of the reaction, namely by Q. We can write

$$d\Phi_n(Q, p_1, \ldots, p_n) = \prod_{i=1}^{n} \left[\frac{d^4 p_i}{(2\pi)^4}(2\pi)\delta(p_i^2 - m_i^2)\theta(E_i^0) \right] (2\pi)^4 \delta^4 \left(Q - \sum_{i=1}^{n} p_i \right)$$

$$= \prod_{i=1}^{n} \left[\frac{d^3 p_i}{(2\pi)^3 2E_i} \right] (2\pi)^4 \delta^4 \left(Q - \sum_{i=1}^{n} p_i \right). \tag{3.75}$$

Phase space has the general property of factorization which manifests itself in the relation

$$\mathrm{d}\Phi_n(Q, p_1, \ldots, p_n) = \frac{\mathrm{d}P^2}{2\pi} \, \mathrm{d}\Phi_i(P, p_1, \ldots, p_i) \, \mathrm{d}\Phi_{n-i+1}(Q, P, p_{i+1}, \ldots, p_n),$$

$$\text{where} \quad P = \sum_{j=1}^{i} p_j. \tag{3.76}$$

3.4.1 A Generator for QCD Antennas

The first algorithm we will consider generates QCD antennas and adapts especially well to the integrand in combination with the *VEGAS* algorithm. It is almost identical to the approach mentioned in [75, 76] which we will explain in detail while emphasizing the differences to our algorithm.

By using the phase space factorization relation (3.76) recursively, we can build the full phase space starting from just the center-of-mass energy of the process and sequentially adding or inserting more and more momenta until we have n final states. The first step in this process is to generate two opposite momenta which is the most basic final state one can construct due to the conservation of momentum.[8] One can show that the two-particle phase space is given by

$$\mathrm{d}\Phi_2(Q, p_1, p_2) = \frac{1}{(2\pi)^2} \frac{\sqrt{\lambda(Q^2, p_1^2, p_2^2)}}{8Q^2} \, \mathrm{d}\phi_2 \, \mathrm{d}\cos\theta_2 = \frac{1}{8(2\pi)^2} \, \mathrm{d}\phi_2 \, \mathrm{d}\cos\theta_2 \tag{3.77}$$

where the *Källén* function $\lambda(a, b, c) = a^2 + b^2 + c^2 - 2(ab + bc + ca)$ was calculated in the second step (due to the masslessness we find $\lambda(Q^2, p_1^2, p_2^2) = \lambda(Q^2, 0, 0) = Q^4$). Note that we only integrate over two angles instead of the naive count of eight for the four components of each of the two momenta. This is a result of the energy–momentum relation

$$E^2 = \vec{p}^2 + m^2 \xrightarrow{m \to 0} \vec{p}^2 \tag{3.78}$$

that reduces the degrees of freedom per momentum by one, leaving six variables. However, the total conservation of momentum fixes the momentum of one particle (above p_1) as the opposite of the other momentum (p_2), and it also determines the energy and thus also the spatial norm of p_2, leaving just two degrees of freedom. Hence, we can provide a very simple algorithm for the creation of these two momenta:

1. Choose two random numbers u_1 and u_2 and set

$$\phi_2 = 2\pi u_1, \qquad \cos\theta_2 = u_2 \quad \left(\sin\theta_2 = \sqrt{1 - \cos^2\theta_2}\right) \tag{3.79}$$

---

[8]The algorithm described in the following is based on the "sequential approach" from [18] with the additional restriction to only two (massless) particles.

2. Set the spatial norm of $\vec{p}_2$ to

$$|\vec{p}_2| = \frac{\lambda(Q^2, p_1^2, p_2^2)}{2Q} \xrightarrow{m \to 0} \frac{Q}{2}.$$ (3.80)

3. Set the momenta to

$$p_2 = \begin{pmatrix} \sqrt{|\vec{p}_2|^2 + m_2^2} \\ |\vec{p}_2| \sin\theta_2 \sin\phi_2 \\ |\vec{p}_2| \sin\theta_2 \cos\phi_2 \\ |\vec{p}_2| \cos\theta_2 \end{pmatrix}, \qquad p_1 = \begin{pmatrix} \sqrt{|\vec{p}_2|^2 + m_1^2} \\ -|\vec{p}_2| \sin\theta_2 \sin\phi_2 \\ -|\vec{p}_2| \sin\theta_2 \cos\phi_2 \\ -|\vec{p}_2| \cos\theta_2 \end{pmatrix}$$ (3.81)

4. Set the weight of the generated configuration to

$$w_2 = \frac{1}{(2\pi)^2} \frac{\sqrt{\lambda(Q^2, p_1^2, p_2^2)}}{8Q^2} \xrightarrow{m \to 0} \frac{1}{8(2\pi)^2}$$ (3.82)

which is identical to the factor we found in equation (3.77).

The above algorithm generates only the first two momenta. Let us now consider inserting the remaining four-momenta into this event, and let us do this in such a way that the algorithm is suited for *VEGAS*.

To this end, we have to think about where our integrand, i.e. the squared amplitude, exhibits large variations. We have already discussed the soft and collinear singular behavior of our squared matrix element. In terms of invariants $s_{ij} = (p_i + p_j)^2 \xrightarrow{m \to 0} 2p_i p_j$, we find the following general behavior of leading order and leading color amplitudes, as we saw before:[9]

$$|\mathcal{A}(p_1, p_2, \ldots, p_n)|^2 \propto \frac{f(p_1, p_2, \ldots, p_n)}{s_{12}s_{23}s_{34}\cdots s_{(n-1)n}}.$$ (3.83)

At leading order, we said that the singularities arising from these invariants are cut off through the jet algorithm. However, we still see that the integrand grows strongly with shrinking invariants and, depending on the cut parameter y_{cut} the amplitudes with small jet resolution parameters are still much larger than typical hard amplitudes with moderate or large resolution parameters. Furthermore, as we have briefly addressed before and will discuss in detail in the following chapters, the real corrections at next–to–leading order describe one jet by two particles so that again invariants become small and yield huge matrix elements. In summary, the structure of the squared amplitude as we saw above is very common and it is a good idea to construct the phase space generator based on invariants.

Starting from the two momenta we obtained using the algorithm above which we will denote by p_a and p_b, let us now consider the insertion of a third soft or collinear parton p_s between them while keeping the total momentum conserved. This will force a

---

[9] To support this statement, one can take a look at the specific example of Parke–Taylor formulas for maximally helicity violating amplitudes [42, 77].

modification of the two original hard momenta which we will denote by a prime. We now find the following invariants:

$$s_{as} = (p'_a + p_s)^2, \quad s_{sb} = (p_s + p'_b)^2, \quad s_{ab} = (p_a + p_b)^2 = (p'_a + p_s + p'_b)^2. \quad (3.84)$$

Note that from now on, we directly assume all momenta to be massless. In order to describe this situation we use the phase space factorization formula (3.76) as follows:

$$d\Phi_{n+1} = d\Phi_{n-1}(\ldots)\frac{dP^2}{2\pi} d\Phi_3(P, p'_a, p_s, p'_b) \quad (3.85)$$

This formula is already a generalization to n partons: it assumes that we start with n partons and then insert one more parton. For this to be evident, we re-express the three-particle phase space by

$$d\Phi_3(P, p'_a, p_s, p'_b) = \frac{ds_{as} ds_{sb} d\phi_s}{4(2\pi)^3 s_{ab}} d\Phi_2(P, p_a, p_b) \quad (3.86)$$

to obtain

$$d\Phi_{n+1} = d\Phi_n \frac{ds_{as} ds_{sb} d\phi_s}{4(2\pi)^3 s_{ab}}. \quad (3.87)$$

We now have to choose the invariants s_{ab} and s_{sb} such that their sum is not larger than s_{ab}

$$s_{as} + s_{sb} \leq s_{ab}. \quad (3.88)$$

Up to this point, the description correlates with section 5.3.3 in [18] and with [75, 76]. The algorithm described there relies on some technical cut off $s_{\min}$ that neither s_{as} nor s_{sb} falls below. Both invariants are parameterized by

$$s_{as} = s_{ab}\left(\frac{s_{\min}}{s_{ab}}\right)^{u_1}, \qquad s_{sb} = s_{ab}\left(\frac{s_{\min}}{s_{ab}}\right)^{u_2} \quad (3.89)$$

where u_1 and u_2 are random numbers with $u_1, u_2 \in [0, 1]$. It is clear that for example $u_1 = u_2 = 1$ yields $s_{as} + s_{sb} = 2s_{ab} > s_{ab}$ which violates equation (3.88). In this case, the event has to be rejected.

In this thesis, however, we want our phase space generator to always yield a valid configuration of momenta. Any technical cuts will be performed outside the generator, if necessary at all; this will be discussed again in section 4.3. Thus, we use a different—and also numerically faster since exponentiation is computationally expensive—parameterization for the invariants:

$$s_{sb} = s_{ab}u_2, \quad s_{as} = (s_{ab} - s_{sb})u_1 = s_{ab}(1 - u_2)u_1. \quad (3.90)$$

Note that the special definition of s_{as} which depends on both random numbers u_1 and u_2 ensures that equation (3.88) is always valid. Unlike during the generation of the first two opposite momenta where total momentum conservation fixed the energy of both momenta, the insertion of an additional momentum is not so restricted. Hence, we need a

third random number u_3 to fix an angle, as one can see in equation (3.87):

$$\phi_s = 2\pi u_3. \tag{3.91}$$

The creation of the soft insertion is very similar to the one presented in [18, 75, 76] and requires only minor modifications due to the changed parameterization of the invariants:

1. Starting from an n-particle configuration, choose two momenta p_a and p_b. Using three random numbers u_1, u_2 and u_3, set $s_{ab} = (p_a + p_b)^2$ and choose s_{as}, s_{sb} and ϕ_s as given in equations (3.90) and (3.91).

2. We assume that $s_{as} < s_{sb}$, otherwise exchange a and b in the following equations. Set

$$E_a = \frac{s_{ab} - s_{sb}}{2\sqrt{s_{ab}}}, \qquad E_s = \frac{s_{as} + s_{sb}}{2\sqrt{s_{ab}}}, \qquad E_b = \frac{s_{ab} - s_{as}}{2\sqrt{s_{ab}}} \tag{3.92}$$

$$\theta_{ab} = \arccos\left(1 - \frac{s_{ab} - s_{as} - s_{sb}}{2E_a E_b}\right), \qquad \theta_{sb} = \arccos\left(1 - \frac{s_{sb}}{2E_s E_b}\right) \tag{3.93}$$

In the center-of-mass frame of $p_a + p_b$ where we choose p_b' to be along the $+z$ axis, the above definitions can be used to easily set the momenta. We indicate quantities in this system by a tilde:

$$\begin{aligned}
\widetilde{p}_a' &= E_a\big(1, \sin\theta_{ab}\cos(\phi_s + \pi), \sin\theta_{ab}\sin(\phi_s + \pi), \cos\theta_{ab}\big), \\
\widetilde{p}_s &= E_s\big(1, \sin\theta_{sb}\cos(\phi_s), \sin\theta_{sb}\sin(\phi_s), \cos\theta_{sb}\big), \\
\widetilde{p}_b' &= E_a\big(1, \sin\theta_{ab}\cos(\phi_s + \pi), \sin\theta_{ab}\sin(\phi_s + \pi), \cos\theta_{ab}\big).
\end{aligned} \tag{3.94}$$

The relation between the momenta p and $\widetilde{p}$ is given by

$$p = \Lambda_{\text{boost}}\Lambda_{xy}(\phi)\Lambda_{xz}(\theta)\,\widetilde{p} \tag{3.95}$$

for all three momenta. The explicit expressions for the transformation can be found in appendix A.

3. Finally, using $\mathrm{d}s_{as} = (s_{ab} - s_{sb})\mathrm{d}u_1$, $\mathrm{d}s_{sb} = s_{ab}\mathrm{d}u_2$ and $\mathrm{d}\phi_s = 2\pi$, the total weight for the new configuration reads

$$w_{n+1} = w_n \frac{(s_{ab} - s_{sb})s_{ab}2\pi}{4(2\pi)^3 s_{ab}} = w_n \frac{s_{ab} - s_{sb}}{4(2\pi)^2} \tag{3.96}$$

where w_n is the weight obtained from the original n-particle configuration.

The parameterization in terms of invariants ensures that changing one random number in the integration acts as a direct scaling of the respective invariant. Furthermore, since we always scale invariants with respect to the new momentum p_s (as opposed to s_{ab}, for example which would directly modify one of the previously set momenta p_a and p_b) we ensure the highest degree of independence between the different random numbers possible. In conclusion, this generator is perfectly suited for the *VEGAS* integration procedure.

One last remark regarding the total integration dimension of our phase space integral is in order. We already explained that creating the first two momenta only requires two random numbers while each additional momentum requires three random numbers. If we denote the total number of final state particles by n, we find for the total dimension

$$n_{\text{PS}} = 3(n-2) + 2 = 3n - 4. \tag{3.97}$$

As an example, consider a six jet exclusive jet rate at leading order. In this calculation, we find $n = 6$ final state partons resulting in $n_{\text{PS}} = 14$ integral dimensions, which is certainly high-dimensional, as promised before.

3.4.2 Generating Soft Configurations

In the course of this thesis, we will introduce different subtraction terms for the real emission contribution, where each is suited for a specific helicity configuration. In order to test the subtraction terms, we need to be able to generate phase space configurations where one momentum is soft while having full control over the softness via a parameter λ_{soft}.

It turns out that we can use the algorithm presented above and tune it by choosing the random numbers in a specific way to obtain a soft configuration. Consider equation (3.92) together with equation (3.90) which gives us the following result for the energy E_s of the inserted momentum:

$$E_s = \frac{s_{as} + s_{sb}}{2\sqrt{s_{ab}}} = \frac{\sqrt{s_{ab}}}{2} \left(u_1 + u_2 - u_1 u_2 \right) \approx \frac{\sqrt{s_{ab}}}{2} \left(u_1 + u_2 \right), \tag{3.98}$$

where the last result is valid for small random numbers. By choosing for example $u_1 = u_2 = \lambda_{\text{soft}}$, we have control over the softness of the inserted parton. To make sure that this control is not spoiled by insertions of further momenta (consider equation (3.92) once more, where the energies of partons a and b are re-parameterized), we modify only the random numbers of the last inserted momentum.

Thus, to approach the soft region of a momentum configuration, we use the following algorithm:

1. Create a set of $(3n - 4)$ random variables, $(u_1, u_2, \ldots, u_{3n-4})$.

2. Change the two variables that govern the invariants of the last inserted parton as follows:

$$u_{3n-6} = \lambda_{\text{soft}}, \quad u_{3n-5} = \lambda_{\text{soft}} \tag{3.99}$$

   where $\lambda_{\text{soft}} \ll 1$ is the softness of the final inserted parton.

3. Let the QCD antenna generator from section 3.4.1 create a phase space configuration with the previously determined "random" numbers u_i.

By repeating step 2 for different values of λ_{soft} but for the same set of random numbers otherwise, we can probe how squared amplitudes behave in the soft limit.

Note that with this method, momentum conservation will always be fulfilled. Thus, changing the value of λ_{soft} will also affect the momenta of all other partons. However, since we choose λ_{soft} to be very small, the effect of this can be neglected.

3.4.3 Generating Collinear Configurations

In addition to the previous section, we also need to test the collinear region to ensure that our subtraction terms work. In order to have full control over the collinear limit, we need to be able to create phase space depending on the parameter λ_{coll} or, equivalently, the square of the transverse momentum $k_\perp^2$ (see section 3.2.3). The easiest way to do this is to control the virtuality of the propagator that splits into the collinear partons i and j which is given by

$$\frac{1}{p_i p_j} = -\frac{2x\overline{x}}{k_\perp^2} \propto \frac{1}{\lambda_{\text{coll}}^2} \tag{3.100}$$

where we inserted the Sudakov parameterization.

We can achieve this by again creating phase space sequentially, using the following algorithm:

1. Choose a phase space generator that can create massive momenta. We use the *RAMBO* generator [78] which creates uniformly distributed momenta with respect to the total phase space volume.

2. Choose a set of random numbers suited for the generator such that n momenta can be produced. In the case of *RAMBO*, we need four random numbers per momentum amounting to a total of $4n$ random values.

3. Have the phase space generator create a configuration of $(n-1)$ massless momenta and one momentum with the mass $m = \lambda_{\text{coll}}$. This momentum represents the parton that splits into the collinear parton pair (i, j). By setting its mass, we automatically set its virtuality to m provided that we treat the parton as massless in the following.

4. Finally, use the two particle decay algorithm described in equation (3.77) and the text following this formula. Setting $Q = m = \lambda_{\text{coll}}$ replaces the massive momentum by two massless collinear momenta (as guaranteed by momentum conservation). The mass of the mother particle gives us control over the collinearity.

Again, we can probe the collinear sector by repeating steps 3 and 4 with different values of λ_{coll}. Furthermore, momentum conservation once more results in a correction of all momenta when changing λ_{coll}. Just like in the soft limit, the collinear limit is probed by choosing small values $\lambda_{\text{coll}} \ll 1$ so that this effect can be neglected.

Helicity Summation

4

This chapter presents the "classical" method to perform the helicity summation in numerical calculations which is based on helicity amplitudes. Using this method, we detail the dipole formalism by Catani and Seymour [26] and we explain its massive generalization [79, 80]. Finally, we explain our implementation in terms of leading color electron–positron annihilation and we analyze some results; this will serve as a basis for the analyses of the forthcoming chapters.

4.1 Helicity Amplitudes

Measurements taken at colliders such as the LHC, or its predecessor LEP are normally insensitive to the spins and helicities of particles. This has to be reflected in any theoretical prediction used for data analysis. Naturally, each ingoing particle has a fixed spin while for the outgoing particles, each spin setting is possible. Thus in a computation one takes the average over the spins of the initial state particles and sums over the spins in the final state. The unpolarized squared matrix element then reads

$$\overline{|\mathcal{A}|^2}(p_i, p_f) = \frac{1}{n_s} \sum_{\{\lambda_i\}} \sum_{\{\lambda_f\}} |\mathcal{A}(\{p_i, \lambda_i\}, \{p_f, \lambda_f\})|^2, \tag{4.1}$$

where quantities with an index i denote initial state particles while those with index f denote final state particles. The second sum is the spin sum in the final state. The first sum including the factor $1/n_s$ originates from averaging in the initial state. n_s is a product of the discrete number of spin settings that each initial state particle has, i.e. one can write n_s as

$$n_s = \prod_{a=1}^{n_i} s_a \tag{4.2}$$

where the index a runs over all particles in the initial state ($n_i = 2$ at colliders) and s_a denotes the number of spin settings for the particle. For almost all Standard Model particles, $s_a = 2$ since all fermions have spin $1/2$ and thus two spin settings, and all massless vector

bosons (gluons and photons) also have two states. Note that massive spin one vector bosons such as the $W^\pm$ or the Z bosons have three spin settings, spin 1, 0 or −1, which means $s_a = 3$. Since we discuss QCD in this thesis, we restrict ourselves to cases with $s_a = 2$. Thus, the factor for all processes we examine in this thesis will be $n_s = 2 \cdot 2 = 4$.

These spin sums are performed using two identities we already came across in chapter 3:

$$d_{\alpha\beta}(p) = \sum_\lambda u^\lambda(p)\,\overline{u}^\lambda(p) = \not{p} + m \qquad \text{(fermions)} \qquad (4.3a)$$

$$d_{\mu\nu}(p) = \sum_\lambda \epsilon_\mu^{\lambda\,*}(p)\,\epsilon_\nu^\lambda(p) = -g_{\mu\nu} + \frac{p_\mu q_\nu + q_\mu p_\nu}{p \cdot q} \qquad \text{(bosons)}. \qquad (4.3b)$$

Let us stress again, that the fermion relation also applies for $m = 0$, and that q is the same reference momentum that is used in the spinor helicity formalism, i.e. for $\epsilon(p, q)$, see equation (3.12).

How do the above equations relate to equation (4.1)? Every physical amplitude contains one polarization vector $\epsilon^\lambda, \epsilon^{\lambda\,*}$ or spinor $u^\lambda, \overline{u}^\lambda, v^\lambda, \overline{v}^\lambda$ for each external particle according to the Feynman rules. The squared amplitude $|\mathcal{A}|^2 = \mathcal{A}^*\mathcal{A}$ is computed by multiplying the complex conjugate amplitude with the normal amplitude. Complex conjugation of the amplitude swaps the types $\epsilon^\lambda \leftrightarrow \epsilon^{\lambda\,*}$, $u^\lambda \leftrightarrow \overline{u}^\lambda$, and $v^\lambda \leftrightarrow \overline{v}^\lambda$, respectively.[1] Thus, we end up with spinor products and products of polarization vectors that have the same basic structure as equations (4.3). The right hand side of equation (4.1) is made up of many sums, one sum per particle to be specific. If we now match the spin or polarization products with the corresponding sum, we obtain one relation as in equation (4.3) per particle.

Example: Gluon Amplitudes

We can illustrate this by looking at a helicity summed gluon amplitude:

$$\sum_{\lambda_1,\dots,\lambda_n} |\mathcal{A}_{\lambda_1\dots\lambda_n}|^2 = \prod_{m=1}^n \left[\sum_{\lambda_m} \epsilon_{\mu_m}^{\lambda_m} \epsilon_{\nu_m}^{\lambda_m\,*} \right] \times \mathcal{M}^{\mu_1,\dots\mu_n,\nu_1,\dots,\nu_n}.$$

The product runs over all external gluons; each gluon thus contributes a polarization sum as in equation (4.3b) to the squared helicity summed amplitude. By $\mathcal{M}$ we denoted all internal parts of the diagram, i.e. vertices and propagators.

Distinguishing helicities/spins and polarizations/spinors only matters when one has to compute these quantities directly. For a general discussion, this distinction is cumbersome. We will henceforth only refer to particle *polarizations* and *helicities* with the understanding that this applies to both boson polarizations and helicities as well as fermion spinors and spins.

---

[1]Of course, spinors and conjugated spinors are *not* related via complex conjugation on their own. Only the conjugation of full fermion lines effectively leads to this, e.g.

$$\left(\overline{u}(p_1)\,\gamma^\mu\,v(p_2)\right)^* = \overline{v}(p_2)\,\gamma^\mu\,u(p_1).$$

In a numerical program we cannot deal with analytic expressions such as equation (4.3). All building blocks are given by numbers—although we arrange them in terms of vectors or matrices, the calculation still boils down to multiplications of numbers. How do we perform the helicity sums in this case? The "traditional" method is to use *helicity amplitudes*: instead of using analytic formulas to perform the sum, we simply calculate all squared amplitudes for the different helicity eigenstates of the external particles and sum them up afterwards. The unpolarized amplitude then reads

$$\overline{|\mathcal{A}|^2} = \frac{1}{n_s} \sum_{\lambda_1,\ldots,\lambda_n} |\mathcal{A}_{\lambda_1,\ldots,\lambda_n}|^2 = \frac{1}{n_s} \left(|\mathcal{A}_{++\ldots+}|^2 + |\mathcal{A}_{-+\ldots+}|^2 + |\mathcal{A}_{--\ldots+}|^2 + \ldots + |\mathcal{A}_{--\ldots-}|^2 \right). \quad (4.4)$$

Here, we modified our notation with respect to equation (4.1): for clarity, we dropped the momentum arguments and denoted helicities as subscripts of the amplitude, one helicity per particle. We also no longer distinguish between initial and final states.

In addition, let us make another remark on the terminology we use: throughout this thesis, we will frequently refer to *helicity configurations* by which we denote elements of the set $\mathfrak{H}_n$ of all helicities of the external particles, i.e.

$$\mathfrak{H}_n = \{ (\lambda_1, \ldots, \lambda_n) \mid \lambda_i \in \pm 1 \ \forall \ i \}. \quad (4.5)$$

Equation (4.4) can then also be seen as a sum over all helicity configurations. As an example, $\mathcal{A}_{++-+-}$ is a helicity amplitude with the helicity configuration $(+, +, -, +, -) \in \mathfrak{H}_5$.

Let us discuss the method of helicity summation a bit further in the context of a numerical algorithm. Formula (4.4) is very simple to implement, but it also has some serious drawbacks which we will elaborate on in the following. To this end, let us shed some light on the computational cost of this method. In the context of our color ordered recursive formalism (see section 3.1) it is reasonable to assume that each helicity amplitude takes the same CPU time to compute since the recursive tree required is exactly the same for each amplitude, only the numerical values of the building blocks change. Performing the helicity sum according to equation (4.4) requires the computation of 2^n helicity amplitudes where n is the number of external particles with two spin states.[2] Hence, the computation of the helicity summed amplitude takes 2^n times as long as a single squared amplitude. Consider the example of nine external particles (e.g. the leading order contribution to $e^+e^- \to 7$ jets process) which has $2^9 = 512$ helicity amplitudes. Since all helicity amplitudes have to be evaluated for each phase space point, this is a serious slow down factor in numerical computations.

Can we do anything to reduce this number? In fact, there are several possibilities.

1. If we only take parity conserving interactions into account such as they occur in QCD and QED, any helicity amplitude can be related to its counterpart with opposite

---

[2]Again, we assumed that all particles have two spin settings. In the general case, where massive vector bosons could be present in the final state, one has to distinguish between particles with two and three spin states. If we denote the number of particles with two and three spin states by n_2 and n_3, respectively, the total number of helicity amplitudes is $2^{n_2} \cdot 2^{n_3}$.

helicities by the relation [23]

$$\mathcal{A}_{\lambda_1,\cdots,\lambda_n} = -\mathcal{A}^*_{-\lambda_1,\cdots,-\lambda_n}. \tag{4.6}$$

Thus, we only need to evaluate half of the helicity amplitudes, 2^{n-1}, to get the full information. Let us stress, however, that once electroweak interactions enter the game, e.g. due to a Z boson as intermediary particle in the process $e^+e^- \to$ jets, this relation is lost.

2. It is well-known (analytically) that some helicity amplitudes vanish. Examples are the Parke–Taylor formulas or the fact that fermion–boson vertices vanish if the fermion helicities do not match. This can be included in the algorithm to avoid costly computations of zero. However, one should note that this is process-dependent in general and can thus harm the generality of the code.

3. The third method is directly related to the current memory discussed in chapter 3. If the current memory is made sensitive to the helicities of particles, one can remember currents across all helicity amplitudes per phase space point and re-use sub-currents with the same helicity configurations. As an example consider the helicity amplitudes $\mathcal{A}_{+-+++}$ and $\mathcal{A}_{+-++-}$ which only differ by the helicity of the last particle. All sub-currents containing only the first four particles will be identical in both helicity amplitudes and do not have to be recomputed.

In the program written for this thesis, we employ methods 1 and 3 where applicable.

But even with the use of the above methods, helicity summation still has an inherent $\mathcal{O}\left(2^n\right)$ growth which we aim to reduce to $\mathcal{O}\left(1\right)$ in this thesis.

Before we go on to describe the methods that enable us to reach this goal, let us first look at helicity summation at next–to–leading order. There is no conceptual difference in computing an n–parton amplitude for the Born contribution, an $(n+1)$–parton amplitude for the real corrections—which is simply a tree-level amplitude with one more external leg—or the interference of a n–parton Born amplitude and the one–loop matrix element with the method of helicity amplitudes. The only difficulty arises from the fact that the next–to–leading order contributions are infinite and that we have to cancel poles with the subtraction method. The subtraction terms have to match the pole structure of the helicity summed real and virtual contributions and have to be constructed to be suitable for helicity summation. This was done in the 1990's by Catani and Seymour in the form of the *dipole formalism*.

4.2   Real Emission and the Dipole Formalism

Having already discussed the basic ideas of the subtraction method in section 3.2.1, we now turn to the specific formulation of the dipole formalism. As stated before, the poles that the subtraction term has to match are those that the real emission amplitude exhibits

in the soft and the collinear limit. Before discussing the details of the dipole formalism itself, we will first continue the discussion of the soft and the collinear limits in the case where we sum over all external helicities.

Note that we restrict ourselves to massless partons and to final state radiation at the beginning which is applicable for electron–positron collisions at the LEP collider, for example. In sections 4.2.5 and 4.2.6 we will lift these restrictions.

4.2.1 The Soft Limit

In order to sum over all helicities, we change the soft limit from equation (3.36) to the following:

$$
\begin{aligned}
\lim_{\lambda_{\text{soft}} \to 0} \sum_{\{\lambda\}_{n+1}} \left|\mathcal{A}_{n+1}\right|^2 &= 4\pi\alpha_s\mu^{2\epsilon} \sum_{\{\lambda\}_n} \mathcal{A}_n^* \left(\boldsymbol{J}^\mu\right)^\dagger \left(\sum_{\lambda_j} \epsilon_\mu^{\lambda_j\,*}(p_j)\epsilon_\nu^{\lambda_j}(p_j)\right) \boldsymbol{J}^\nu \,\mathcal{A}_n \\
&= 4\pi\alpha_s\mu^{2\epsilon} \sum_{\{\lambda\}_n} \mathcal{A}_n^* \left(\boldsymbol{J}^\mu\right)^\dagger d_{\mu\nu}(p_j) \boldsymbol{J}^\nu \,\mathcal{A}_n.
\end{aligned}
\tag{4.7}
$$

Therein, we introduced a new notation for helicity sums. The sum over $\sum_{\{\lambda\}_{n+1}}$ denotes a summation over all helicities of the $(n+1)$–parton event, i.e. $(\lambda_a, \lambda_b, \lambda_1, \ldots, \lambda_{n+1})$ including the initial state helicities λ_a and λ_b. Equally, $\sum_{\{\lambda\}_n}$ sums over all helicities of the n–parton amplitude. Note that this does *not* include parton j whose sum we wrote separately. Using equation (3.42), we can perform the contraction of the eikonal currents with j's polarization sum. Due to the fact that the current is conserved with respect to particle j and since the gauge terms in $d_{\mu\nu}(p_j)$ are either proportional to $(p_j)_\mu$ or $(p_j)_\nu$, we immediately know that only the metric part of the polarization sum survives and we can write

$$
\left(\boldsymbol{J}^\mu\right)^\dagger d_{\mu\nu} \boldsymbol{J}^\nu = -\left(\boldsymbol{J}^\mu\right)^\dagger g_{\mu\nu} \boldsymbol{J}^\nu = -\left(\boldsymbol{J}^\mu\right)^\dagger \boldsymbol{J}_\mu.
\tag{4.8}
$$

This contraction can be easily obtained from equation (3.37):

$$
\left(\boldsymbol{J}^\mu\right)^\dagger \boldsymbol{J}_\mu = \sum_{\substack{i,k=1 \\ i\neq k\neq j}}^{n+1} \boldsymbol{T}_i \boldsymbol{T}_k \left(-\frac{p_i^2}{(p_i p_j)^2} + 2\frac{p_i p_k}{(p_i p_j)(p_i p_j + p_k p_j)}\right)
\tag{4.9}
$$

where the first term drops out, $p_i^2 = m_i^2 = 0$, since we are discussing massless partons at the moment. Altogether, we find the following expression in the (massless) soft limit:

$$
\lim_{\lambda_{\text{soft}} \to 0} \sum_{\{\lambda\}_{n+1}} \left|\mathcal{A}_{n+1}\right|^2 = -8\pi\alpha_s\mu^{2\epsilon} \sum_{\substack{i=1 \\ i\neq j}}^{n+1} \frac{1}{p_i p_j} \sum_{\substack{k=1 \\ k\neq i\neq j}}^{n+1} \frac{p_i p_k}{p_i p_j + p_k p_j} \sum_{\{\lambda\}_n} \mathcal{A}_n^* \,\boldsymbol{T}_i \boldsymbol{T}_k \,\mathcal{A}_n.
\tag{4.10}
$$

4.2.2 The Collinear Limit

The collinear limit with helicity summation can be written as follows:

$$\lim_{p_i \| p_j} \sum_{\{\lambda\}_{n+1}} |\mathcal{A}_{n+1}|^2 = \frac{4\pi\alpha_s \mu^{2\epsilon}}{p_i p_j} \sum_{\substack{\{\lambda\}_{n+1} \setminus \\ \{\lambda_i, \lambda_j\}}} \sum_{\eta, \eta'} \mathcal{A}_n^*(\eta) \, P_{(ij) \to i+j}^{\eta\eta'} \, \mathcal{A}_n(\eta'). \tag{4.11}$$

This formula looks very different from the general case in equation (3.46), however, we will show below that it is just a different formulation. The factor in front contains all constants, as well as one propagator denominator from equation (3.46). We have explicitly written down all helicity summations that occur. The first sum denotes the sum over all helicities of the $(n+1)$–parton amplitude except those of particles i and j: these are included in the definition of $P_{(ij) \to i+j}$, as we will see below. The second sum over η and η' contains both summations of the polarization sums $d_{\zeta\xi}(p_{ij})$ we found in equation (3.46); we renamed them to avoid any confusion with regard to the external particles of the process. Both the amplitudes and $P_{(ij) \to i+j}$ depend on these helicities. This is obtained from the general collinear limit by decomposing the propagators into their components

$$\frac{d_{\mu\nu}(p_{ij})}{2p_i p_j} = \frac{\sum_\eta \epsilon_\mu^{\eta*} \epsilon_\nu^\eta}{2p_i p_j} \quad \text{or} \quad \frac{d_{\alpha\beta}(p_{ij})}{2p_i p_j} = \frac{\sum_\eta u_\alpha^\eta \bar{u}_\beta^\eta}{2p_i p_j} \tag{4.12}$$

and then redistributing them as follows. The sum is pulled out as discussed above. One polarization or spinor is included in the corresponding amplitude—hence the dependence of the amplitude on the helicity—while the other one is included in $P_{(ij) \to i+j}$. As mentioned above, one propagator denominator is pulled to the front (without the factor 2) while the other is also included in $P_{(ij) \to i+j}$. Thus, we end up with the following definition:

$$P_{(ij) \to i+j}^{\eta\eta'} \equiv \frac{\mathbf{T}_{(ij) \to i+j}^2}{4 p_i p_j} \sum_{\lambda_i, \lambda_j} \begin{cases} \epsilon^\eta_{\ \mu} \, \Upsilon_{(ij) \to i+j}^{*\mu} \, \Upsilon_{(ij) \to i+j}^\nu \, \epsilon_\nu^{\eta'*} & \text{(gluons)} \\ \bar{u}_\alpha^\eta \left[\Upsilon_{(ij) \to i+j}^* \right]_\alpha \left[\Upsilon_{(ij) \to i+j} \right]_\beta u_\beta^{\eta'} & \text{(quarks)} \end{cases} \tag{4.13}$$

(and similar for antiquarks). Therein, the splittings $\Upsilon_{(ij) \to i+j}$ are given by the kinematical part of the respective Feynman rule (i.e. we strip the Feynman rule both of its color information and of the coupling constant, which instead resides in the factor $4\pi\alpha_s$).

Example: Splitting $\Upsilon_{q \to qg}$

An example for the splitting $q \to qg$ will clarify this:

$$[\Upsilon_{q \to qg}]_\beta = -i\bar{u}_\alpha^{\lambda_i}(p_i) \, \gamma_{\alpha\beta}^\mu \, \epsilon_\mu^{\lambda_j}(p_j). \tag{4.14}$$

The kinematical part of the vertex rule, see equation (2.8), is just $(-i\gamma^\mu)$ while the remaining parts are the spinors and polarizations for partons i and j.

The squared color factors again depend on the splitting and are given by

$$\mathbf{T}^2_{g \to gg} = C_A, \quad \mathbf{T}^2_{g \to q\bar{q}} = T_R, \quad \mathbf{T}^2_{q \to qg} = C_F = \mathbf{T}^2_{\bar{q} \to g\bar{q}}. \tag{4.15}$$

One piece of information is not indicated in equation (4.13): the dipole formalism as originally formulated by Catani and Seymour also requires the $\boldsymbol{P}_{(ij) \to i+j}$ to be evaluated in the limit $k_\perp \to 0$, i.e. we insert Sudakov's parameterization (3.38) and then drop all terms starting with $\mathcal{O}\left(k_\perp\right)$. If we do this, the final $\boldsymbol{P}_{(ij) \to i+j}$ are identical to the well-known *Altarelli–Parisi splitting kernels* [26, 81]:

$$\boldsymbol{P}^{\eta\eta'}_{g \to gg} = 2C_A \left[-g_{\mu\nu} \left(\frac{x}{\bar{x}} + \frac{\bar{x}}{x} \right) - 2(1-\epsilon)x\bar{x} \frac{(k_\perp)_\mu (k_\perp)_\nu}{k_\perp^2} \right] \epsilon^\mu_\eta \epsilon^{*\nu}_{\eta'}, \tag{4.16a}$$

$$\boldsymbol{P}^{\eta\eta'}_{g \to q\bar{q}} = T_R \left[-g^{\mu\nu} + 4x\bar{x} \frac{k_\perp^\mu k_\perp^\nu}{k_\perp^2} \right] \epsilon^\mu_\eta \epsilon^{*\nu}_{\eta'}, \tag{4.16b}$$

$$\boldsymbol{P}^{\eta\eta'}_{q \to qg} = C_F \left[\frac{1+x^2}{\bar{x}} - \epsilon\bar{x} \right] \delta_{\eta\eta'}, \tag{4.16c}$$

$$\boldsymbol{P}^{\eta\eta'}_{\bar{q} \to g\bar{q}} = C_F \left[\frac{1+\bar{x}^2}{x} - \epsilon x \right] \delta_{\eta\eta'}. \tag{4.16d}$$

They have a couple of features that are worth discussing:

- From the last two lines, we can directly read off that the $q \to qg$ and $\bar{q} \to g\bar{q}$ kernels are related by exchanging $x \leftrightarrow \bar{x}$. Hence, we will only talk about the $q \to qg$ splitting from now on.

- Equations (4.16a), (4.16c) and (4.16d) have poles in the limits $x \to 0$ and/or $\bar{x} \to 0$ which are the limits where either particle i or j becomes soft. Note that these singularities overlap with the soft divergences we discussed in the previous section 4.2.1. Obviously, this overlap is the case where we find a collinear parton pair where one is soft, in addition. When formulating $d\sigma^A$, we have to be careful to avoid double counting of any poles.

- In the previous item we omitted the kernel for the splitting $g \to q\bar{q}$, equation (4.16b), which has no such soft divergence. This is a general feature: soft quarks are not singular enough to produce a divergence. It is also the reason why we only treated the insertion of soft gluons when analyzing the soft limit.

- Lastly, note that neither of the splitting kernels has a pole in λ_{coll}. These poles reside solely in the denominator of the factor in equation (4.11) which becomes obvious after inserting the Sudakov parameterization:

$$\frac{1}{p_i p_j} = -\frac{2x\bar{x}}{k_\perp^2} = -\frac{1}{\lambda_{\text{coll}}^2} \frac{2x\bar{x}}{k^2}. \tag{4.17}$$

Note that equation (4.11) only describes the behavior of two specific partons i and j

becoming collinear. To obtain all collinear poles of the $(n+1)$–parton amplitude, we have to sum over all parton pairs (i, j) in the final state. In the soft case, this is implicit since the eikonal current J^μ already contains the sum over all possible partons. We will omit that sum in the collinear limit to avoid cluttered notation—as we will see, this is sufficient.

4.2.3   The Dipole Formalism

With the results from the previous two subsections, we can now go further and formulate the subtraction term.[3] In order to do so, we have to overcome two shortcomings of our preceding analysis of the soft and collinear limits:

1. both limits have to be approached smoothly, i.e. we require a parameterization that obeys momentum conservation everywhere;

2. we have to avoid double counting of poles in the soft *and* collinear limit.

The first item is achieved by treating the universality of the divergences as we did in the discussion of the collinear limit where we factorized the $(n+1)$–parton amplitude into a splitting $(ij) \rightarrow i + j$ times an n–parton amplitude. However, we parameterize the momenta in a different way. In order to keep momentum conservation implemented exactly at all points, i.e. also away from the collinear or soft limits, we define new momenta as follows:

$$\tilde{p}^\mu_{ij} = p^\mu_i + p^\mu_j - \frac{y}{\bar{y}}\, p^\mu_k,$$

$$\tilde{p}^\mu_k = \frac{1}{\bar{y}}\, p^\mu_k. \tag{4.18}$$

Therein, all momenta on the right hand side and without a tilde sign are those of the $(n+1)$–parton amplitude. The variable y is given by

$$y \equiv y_{ij,k} = \frac{p_i p_j}{p_i p_j + p_j p_k + p_k p_i}, \qquad \bar{y} \equiv 1 - y_{ij,k} = \frac{p_j p_k + p_k p_i}{p_i p_j + p_j p_k + p_k p_i}. \tag{4.19}$$

It tends to zero in the soft or collinear limit (while $\bar{y}$ obviously tends to one). The new tilde momenta on the left hand side will be denoted as *dipole momenta* and they belong to the following partons:

- Parton $\widetilde{ij}$, the so-called *emitter* parton, takes the role of the splitting parton (ij): it is the intermediary particle that splits into partons i and j. In terms of parton types and possible splittings, it is identical to the splittings we discussed before (see figure 3.5).

- Parton $\widetilde{k}$ is the so-called *spectator* parton which we require to implement momentum conservation; it takes up "recoil" momentum from the emitter. It has the same particle type, flavor and helicity as parton k of the $(n+1)$–parton amplitude.

---

[3]Note that the rest of this section is based on [26, 79].

One can easily verify that exact momentum conservation is guaranteed everywhere:

$$\tilde{p}_{ij}^{\mu} + \tilde{p}_{k}^{\mu} = p_i^{\mu} + p_j^{\mu} + p_k^{\mu}. \tag{4.20}$$

In particular, both $\tilde{p}_{ij}$ and $\tilde{p}_k$ are also (massless) on shell momenta: $\tilde{p}_{ij}^2 = 0$, $\tilde{p}_k^2 = 0$.

Item 2 from the list above is achieved by merging both the soft and collinear poles into one term. To see this, let us first discuss the final form of the subtraction term $d\sigma^A$. Afterwards, we will analyze this term in the soft and collinear limit which matches the expressions we developed in the former two subsections.

The dipole formalism approximates all poles of the real emission matrix element in terms of a sum over dipoles $\mathcal{D}_{ij,k}$,

$$|\mathcal{A}_{n+1}|^2 = \sum_{\substack{(i,j) \\ k \neq i,j}} \mathcal{D}_{ij,k}(p_1, \ldots p_{n+1}) + \text{finite terms}, \tag{4.21}$$

where each dipole is explicitly formulated for partons i and j (which also determines the emitter parton) and a parton k which is the spectator. The sum runs over all pairs (i, j) and all possible spectators, ensuring that all poles of the real emission amplitude are covered. The total subtraction term can be written as

$$d\sigma^A \propto d\Phi_{n+1} \sum_{\substack{(i,j) \\ k \neq i,j}} \mathcal{D}_{ij,k}(p_1, \ldots p_{n+1}) J_n(\tilde{p}_{ij}, \tilde{p}_k) \tag{4.22}$$

where we omitted the usual factors which are the same as for the real emission contribution $d\sigma^R$. Note that the jet definition acts on the underlying n–parton event: the n jets must be described by one hard parton each which are exactly those of the n–parton amplitude. In order to perform a proper subtraction of all poles, they have to be under total control meaning that they always have to appear inside the splitting $\widetilde{ij} \to i + j$. If the jet definition acted differently, dipoles would be computed where soft or collinear poles could possibly reside in the amplitude which would destroy the subtraction. Each dipole is given by

$$\mathcal{D}_{ij,k}(p_1, \ldots p_{n+1}) = -\frac{1}{2p_i p_j} \sum_{\substack{\{\lambda\}_{n+1} \backslash \\ \{\lambda_i, \lambda_j\}}} \sum_{\eta, \eta'} \mathcal{A}_n^*(\widetilde{ij}, \widetilde{k}) \left(\frac{\mathbf{T}_k \cdot \mathbf{T}_{ij}}{\mathbf{T}_{ij}^2} V_{ij,k}^{\eta\eta'} \right) \mathcal{A}_n(\widetilde{ij}, \widetilde{k}). \tag{4.23}$$

If we compare this definition to our final results for the soft and collinear limits, we find the familiar propagator factor $^1/_{p_i p_j}$ in front. In addition, we find two n–parton amplitudes with some correlation terms in between. The color matrices $\mathbf{T}_k \cdot \mathbf{T}_{ij}/\mathbf{T}_{ij}^2$ for the emitter and spectator partons realize the color correlations in the soft limit, while the spin–correlation matrix $V_{ij,k}$ captures all kinematic information that we found in the soft and collinear limits, as we will see below.

In order to construct the spin–correlation matrices for the different splittings, let us define some more variables:

$$z \equiv z_{ij,k} = \frac{p_i p_k}{p_i p_k + p_j p_k}, \qquad \overline{z} = 1 - z_{ij,k} = \frac{p_j p_k}{p_i p_k + p_j p_k}. \tag{4.24}$$

These have a special meaning in the soft limit of particle j where $z \to x$ and thus $\overline{z} \to \overline{x}$. In that sense, they provide a generalization of the Sudakov symbols $x, \overline{x}$. With this, the spin–correlation matrices are given by

$$V_{gg,k}^{\eta\eta'} = 4\pi\alpha_s\mu^{2\epsilon}(4C_A)\left[-g^{\mu\nu}\left(\frac{1}{1 - z\,\overline{y}} + \frac{1}{1 - \overline{z}y} - 2\right) + \frac{1 - \epsilon}{p_i p_j}K^\mu K^\nu\right]\epsilon_\mu^\eta\epsilon_\nu^{\eta'\,*}, \tag{4.25a}$$

$$V_{q\overline{q},k}^{\eta\eta'} = 4\pi\alpha_s\mu^{2\epsilon}(2T_R)\left[-g^{\mu\nu} - \frac{2}{p_i p_j}K^\mu K^\nu\right]\epsilon_\mu^\eta\epsilon_\nu^{\eta'\,*}, \tag{4.25b}$$

$$V_{qg,k}^{\eta\eta'} = 4\pi\alpha_s\mu^{2\epsilon}(2C_F)\left[\frac{2}{1 - z\overline{y}} - (1 + z) - \epsilon\overline{z}\right]\delta_{\eta\eta'} \tag{4.25c}$$

where

$$K^\mu = zp_i^\mu - \overline{z}p_j^\mu. \tag{4.26}$$

Note that the spin correlation is due to the terms $K^\mu K^\nu$ and is only present in the splittings (4.25a) and (4.25b) where the emitter is a gluon. The matrix for the splitting $\overline{q} \to g\overline{q}$ can be obtained from $V_{qg,k}$ by exchanging $z \leftrightarrow \overline{z}$.

Using equations (4.22), (4.23) and (4.25a) – (4.25c) (plus the definitions for the necessary variables within), we can construct the full subtraction term for electron–positron annihilation processes. To prove this, let us now consider the soft and collinear limits of the dipoles. A table in appendix B shows these limits for many variables and terms which can be used to re-write the dipole terms. As an example, we only consider the case of the splitting $g \to gg$.

The Soft Limit of the Dipoles

First, let us consider the spin–correlation matrix. Using the formulas in the aforementioned appendix (and dropping all non-leading terms as soon as they become obvious), we obtain

$$\lim_{p_j \to 0} V_{gg,k}^{\eta\eta'}$$

$$= 4\pi\alpha_s\mu^{2\epsilon}(4C_A)\left[-g^{\mu\nu}\left(\frac{p_i p_k}{p_i p_j + p_k p_j} + 1 - 2\right) + \frac{1 - \epsilon}{p_i p_j}z^2 p_i^\mu p_i^\nu\right]\epsilon_\mu^\eta(p_i)\epsilon_\nu^{\eta'\,*}(p_i). \tag{4.27}$$

Note especially that $\tilde{p}_{ij} \to p_i$ which affects the momentum arguments of the polarizations. The second term in the bracket vanishes since $p_\mu\epsilon^\mu(p) = 0$ and the terms $(+1 - 2)$ can be neglected since they are also sub-leading with respect to the first term in the round braces (which is of order $1/\lambda_{soft}$). We also know that $C_A = \mathbf{T}_g^2 = \mathbf{T}_{ij}^2 = \mathbf{T}_i^2$. And finally, the Minkowski product of the polarization vectors yields zero for unlike helicities and one for

$\eta = \eta'$, so we can rewrite this product into $-\delta_{\eta\eta'}$. We are then left with

$$\lim_{p_j \to 0} V^{\eta\eta'}_{gg,k} = 4\pi\alpha_s\mu^{2\epsilon}(4\mathbf{T}^2_{ij})\frac{p_i p_k}{p_i p_j + p_k p_j}\delta_{\eta\eta'}. \tag{4.28}$$

We find the same for the splitting (4.25c) while splitting (4.25b) vanishes entirely due to $p_\mu \epsilon^\mu(p) = 0$. The total dipole contribution then reads

$$\lim_{p_j \to 0} \sum_{\substack{(i,j)\\ k \neq i,j}} \mathcal{D}_{ij,k}$$
$$= -\sum_{\substack{(i,j)\\ k \neq i,j}} \frac{4\pi\alpha_s\mu^{2\epsilon}}{2p_i p_j} \sum_{\substack{\{\lambda\}_{n+1}\backslash\\ \{\lambda_i,\lambda_j\}}} \sum_{\eta,\eta'} \mathcal{A}^*_n(\widetilde{ij},k)\left(\frac{\mathbf{T}_k \cdot \mathbf{T}_{ij}}{\mathbf{T}^2_{ij}}\frac{4\mathbf{T}^2_{ij}\,p_i p_k}{p_i p_j + p_k p_j}\delta_{\eta\eta'}\right)\mathcal{A}_n(\widetilde{ij},k) \tag{4.29}$$

Note that also in the amplitudes $\tilde{p}_k \to p_k$ and $\tilde{p}_{ij} \to p_i$. We can do the same for the helicity sum over η and η': one of them can be performed along with the Kronecker delta, the other one can be renamed to λ_i so that we can write

$$\sum_{\substack{\{\lambda\}_n\backslash\\ \{\lambda_i,\lambda_j\}}} \sum_{\eta,\eta'} \delta_{\eta\eta'} \to \sum_{\{\lambda\}_n}. \tag{4.30}$$

We then end up with

$$\lim_{p_j \to 0} \sum_{\substack{(i,j)\\ k \neq i,j}} \mathcal{D}_{ij,k} = -8\pi\alpha_s\mu^{2\epsilon}\sum_{\substack{i=1\\ i \neq j}} \frac{1}{p_i p_j} \sum_{\substack{k=1\\ k \neq i \neq j}} \frac{p_i p_k}{p_i p_j + p_k p_j} \sum_{\{\lambda\}_n} \mathcal{A}^*_n(i,k)\,\mathbf{T}_k\mathbf{T}_i\,\mathcal{A}_n(i,k) \tag{4.31}$$

which is the same as equation (4.10)—hence the dipole subtraction term matches the soft singularities of the real emission amplitude.

The Collinear Limit of the Dipoles

Now we repeat the above steps for the collinear limit. With the help of the relations in the appendix, we find

$$\lim_{p_i \| p_j} V^{\eta\eta'}_{gg,k} = 4\pi\alpha_s\mu^{2\epsilon}(4C_A)\left[-g^{\mu\nu}\left(\frac{1}{\bar{x}} + \frac{1}{x} - 2\right) - \frac{1-\epsilon}{k^2_\perp}2x\bar{x}k^\mu_\perp k^\nu_\perp\right] \times$$
$$\times \epsilon^\eta_\mu(p_{\text{coll}})\,\epsilon^{\eta'\,*}_\nu(p_{\text{coll}}) \tag{4.32}$$

An explanation for the apparent replacement $K_\mu \to (k_\perp)_\mu$ in the second term is in order. Actually, we find

$$\lim_{p_i \| p_j} K^\mu = \lim_{p_i \| p_j}(zp^\mu_i - \bar{z}p^\mu_j) = (zx - \overline{zx})p^\mu_{\text{coll}} + k^\mu_\perp. \tag{4.33}$$

However, the first term proportional to p_{coll} gets contracted with its polarization vector and thus the contribution vanishes. Furthermore, we can re-write the term in round brackets,

$$\frac{1}{\bar{x}} + \frac{1}{x} - 2 = \frac{x}{\bar{x}} + \frac{\bar{x}}{x}, \tag{4.34}$$

so that we can re-write the result in terms of the corresponding Altarelli–Parisi splitting kernel:

$$\begin{aligned}
\lim_{p_i \| p_j} \mathbf{V}_{gg,k}^{\eta\eta'} \\
= 8\pi\alpha_s\mu^{2\epsilon}(2C_A)\left[-g^{\mu\nu}\left(\frac{x}{\bar{x}} + \frac{\bar{x}}{x}\right) - \frac{1-\epsilon}{k_\perp^2}2x\bar{x}k_\perp^\mu k_\perp^\nu\right]\epsilon_\mu^\eta(p_{\text{coll}})\,\epsilon_\nu^{\eta'\,*}(p_{\text{coll}}) \tag{4.35} \\
= 8\pi\alpha_s\mu^{2\epsilon}\,\mathbf{P}_{g\to gg}^{\eta\eta'}.
\end{aligned}$$

Similar relations can be found for all other splitting matrices. Let us now consider the full dipole (i.e. not the sum, but only one dipole):

$$\lim_{p_i \| p_j} \mathcal{D}_{gg,k} = -\frac{4\pi\alpha_s\mu^{2\epsilon}}{p_i p_j} \sum_{\substack{\{\lambda\}_{n+1}\backslash \\ \{\lambda_i,\lambda_j\}}} \sum_{\eta,\eta'} \mathcal{A}_n^*(ij,k)\left(\frac{\mathbf{T}_k\cdot\mathbf{T}_{ij}}{\mathbf{T}_{ij}^2}\mathbf{P}_{g\to gg}^{\eta\eta'}\right)\mathcal{A}_n(ij,k). \tag{4.36}$$

Again, we find similar results for all types of splittings, hence this formula can be generalized to all kinds of dipoles and we find for the full sum:

$$\lim_{p_i \| p_j} \sum_{\substack{(i,j) \\ k\neq i,j}} \mathcal{D}_{ij,k} = -\frac{4\pi\alpha_s\mu^{2\epsilon}}{p_i p_j} \sum_{\substack{\{\lambda\}_{n+1}\backslash \\ \{\lambda_i,\lambda_j\}}} \sum_{\eta,\eta'} \mathcal{A}_n^*(ij,k)\left(\frac{\mathbf{T}_k\cdot\mathbf{T}_{ij}}{\mathbf{T}_{ij}^2}\mathbf{P}_{(ij)\to i+j}^{\eta\eta'}\right)\mathcal{A}_n(ij,k). \tag{4.37}$$

When we examine this relation more closely, we find that the only quantity depending on the summation index k is the color matrix $\mathbf{T}_k$.[4] With respect to the n–parton amplitude, we can once again make use of color conservation and re-write the generator and the sum as follows:

$$\sum_{k\neq i\neq j} \mathbf{T}_k = -\mathbf{T}_{ij}. \tag{4.38}$$

Then, the total result

$$\lim_{p_i \| p_j} \sum_{\substack{(i,j) \\ k\neq i,j}} \mathcal{D}_{ij,k} = \frac{4\pi\alpha_s\mu^{2\epsilon}}{p_i p_j} \sum_{\substack{\{\lambda\}_{n+1}\backslash \\ \{\lambda_i,\lambda_j\}}} \sum_{\eta,\eta'} \mathcal{A}_n^*(ij,k)\,\mathbf{P}_{(ij)\to i+j}^{\eta\eta'}\,\mathcal{A}_n(ij,k) \tag{4.39}$$

is equal to the collinear limit of the real emission amplitude, equation (4.11), and thus the subtraction term also matches these poles exactly.

---

[4]Note that while the amplitude depends on particle k, it is not affected by the sum. The fact that the index appears in the amplitude is an artifact of our notation: we wrote it that way to indicate the dependence on the momenta and helicities; in this case we used it to distinguish between the dipole momentum $\tilde{p}_k$ and the unaltered momentum p_k.

In the previous discussion, we did not *construct* the dipole formulas—we merely gave their results and showed that they do what we want them to do. How can one construct or derive those terms? There is no simple scheme to follow which will guarantee proper dipoles at the end; in principle, one has to find terms that match the desired expressions in the two limits. To this end, the variable y plays a crucial role in connecting the soft and collinear limits: it behaves like λ_{coll}^2 in the collinear limit and λ_{soft} in the soft limit and thus helps combining both limits in a single spin–correlation matrix. The fact that deriving these terms is all but a straight forward exercise is one of the reasons why the derivation of subtraction terms for random polarizations, see chapter 6, looks very different from the derivation here.

4.2.4 The Integrated Subtraction Term

Using the formulas we derived so far, we can render the real emission contribution finite. However, we have not yet derived the integrated subtraction that will cancel the poles of the virtual contributions; recall the next–to–leading order contribution (second term in the right bracket):

$$\sigma^{\text{NLO}} = \int_{n+1} \left[\mathrm{d}\sigma^{\text{R}} - \mathrm{d}\sigma^{\text{A}} \right] + \int_n \left[\mathrm{d}\sigma^{\text{V}} + \int_1 \mathrm{d}\sigma^{\text{A}} \right]. \tag{4.40}$$

In the following, we will illustrate that the dipole formalism enables us to factorize phase space such that we can perform the integral over the one unresolved particle separately. Furthermore, we give the final integrated term and sketch its derivation. Note that for the purpose of this work, it is sufficient to know that the integrated term exists. Hence, we do not put too much emphasis on it but refer the interested reader to [26] where a more thorough derivation is presented.

First, let us re-write phase space so that we actually have a factorized one–particle integral. To this end, let us consider the three–parton contribution for particles i, j, and k of the total $(n+1)$–parton phase space which we directly perform in D dimensions:

$$
\begin{aligned}
&\mathrm{d}\Phi_3(Q, p_i, p_j, p_k) \\
&= \frac{\mathrm{d}^D p_i}{(2\pi)^{D-1}} \delta_+(p_i^2) \frac{\mathrm{d}^D p_j}{(2\pi)^{D-1}} \delta_+(p_j^2) \frac{\mathrm{d}^D p_k}{(2\pi)^{D-1}} \delta_+(p_k^2) (2\pi)^D \delta(Q - p_i - p_j - p_k).
\end{aligned} \tag{4.41}
$$

There, the δ_+–distribution also includes the positive energy restriction which we indicated by an additional function $\theta(p_0)$ earlier on. Our goal is to re-write this phase space element into the momenta $\tilde{p}_{ij}$, $\tilde{p}_k$, and p_i so that we can perform the integral over p_i once and for all. Using factorization, the phase space element reads

$$\mathrm{d}\Phi_3(Q, p_i, p_j, p_k) = \mathrm{d}\Phi_2(Q, \tilde{p}_{ij}, \tilde{p}_k) \, \mathrm{d}p_i(\tilde{p}_{ij}, \tilde{p}_k) \tag{4.42}$$

Therein, we can express the one–particle phase space element for p_i in terms of the new

dipole momenta and the corresponding Jacobian $\mathcal{J}(p_i, \tilde{p}_{ij}, \tilde{p}_k)$ as follows:

$$
\begin{aligned}
\mathrm{d}p_i(\tilde{p}_{ij}, \tilde{p}_k) &= \frac{\mathrm{d}^D p_i}{(2\pi)^{D-1}} \delta_+(p_i^2)\, \mathcal{J}(p_i, \tilde{p}_{ij}, \tilde{p}_k) \\
&= \frac{\mathrm{d}z\,\mathrm{d}y\,\mathrm{d}\Omega^{D-3}}{16\pi^2\,(2\pi)^{D-3}} \,(yz\bar{z})^{D/2-2}\, \bar{y}^{D-3}\, \Theta(z\bar{z})\, \Theta(y\bar{y})
\end{aligned}
\tag{4.43}
$$

This reveals the factorization: the two–particle phase space element $\mathrm{d}\Phi_2(Q, \tilde{p}_{ij}, \tilde{p}_k)$ depends on neither of the quantities z, y or Ω^{D-3} (which is the solid angle element for momentum p_i).

Using this relation, we can integrate the dipole subtraction term separately over $\mathrm{d}p_i$. The final result can be written as follows:

$$
\int\limits_{n+1} \mathrm{d}\sigma^{\mathrm{A}} = \int\limits_{n} \mathrm{d}\sigma^{\mathrm{B}} \otimes \boldsymbol{I}(\epsilon) \propto \int\limits_{n} \mathrm{d}\Phi_n \left(\mathcal{A}_n^* \, \boldsymbol{I}(\epsilon)\mathcal{A}_n\right) J_n
\tag{4.44}
$$

where the tensor product $\otimes$ denotes color correlations between the matrix elements. Let us stress that the basic amplitudes in that formula are *Born amplitudes* and thus easily computable with the methods from section 3.1. We introduced a new operator $\boldsymbol{I}(\epsilon)$, the so-called *insertion* operator which is formulated in $D = 4 - 2\epsilon$ dimensions and explicitly depends on the dimension parameter. It is given by

$$
\boldsymbol{I}(\epsilon) = -\frac{\alpha_{\mathrm{s}}}{2\pi\, \Gamma(1-\epsilon)} \sum_i \frac{1}{\boldsymbol{T}_i^2} \mathcal{V}_i(\epsilon) \sum_{k\neq i} \boldsymbol{T}_i \cdot \boldsymbol{T}_k \left(\frac{4\pi\mu^2}{2p_i p_k}\right)^\epsilon,
\tag{4.45}
$$

where

$$
\mathcal{V}_i(\epsilon) = \boldsymbol{T}_i^2 \left(\frac{1}{\epsilon^2} - \frac{\pi^2}{3}\right) + \frac{\gamma_i}{\epsilon} + \gamma_i + K_i + \mathcal{O}(\epsilon),
\tag{4.46}
$$

and

$$
\gamma_i = \begin{cases} \frac{3}{2} C_{\mathrm{F}} & i = q, \bar{q} \\ \frac{11}{6} C_{\mathrm{A}} - \frac{2}{3} T_{\mathrm{R}} N_f & i = g \end{cases},
\tag{4.47}
$$

$$
K_i = \begin{cases} \left(\frac{7}{2} - \frac{\pi^2}{6}\right) C_{\mathrm{F}} & i = q, \bar{q} \\ \left(\frac{67}{18} - \frac{\pi^2}{6}\right) C_{\mathrm{A}} - \frac{10}{9} T_{\mathrm{R}} N_f & i = g. \end{cases}
\tag{4.48}
$$

These formulas are sufficient to implement the integrated subtraction term. To understand where they come from, let us re-write $\mathcal{V}_i(\epsilon)$ into a different form which depends on yet another set of functions $\mathcal{V}_{ij}(\epsilon)$:

$$
\mathcal{V}_i(\epsilon) = \begin{cases} \mathcal{V}_{qg}(\epsilon) & i = q, \bar{q} \\ \frac{1}{2}\mathcal{V}_{gg}(\epsilon) + N_f \mathcal{V}_{q\bar{q}}(\epsilon) & i = g \end{cases}.
\tag{4.49}
$$

This is where the dependence on the different splittings becomes obvious. In fact, the $\mathcal{V}_{ij}(\epsilon)$ are directly related to the *spin averaged* spin correlations $\overline{V}_{ij,k}$:

$$\mathcal{V}_{ij}(\epsilon) = \int\limits_0^1 \frac{\mathrm{d}z}{(z\overline{z})^\epsilon} \int\limits_0^1 \mathrm{d}y \frac{\overline{y}^{1-2\epsilon}}{y^{1+\epsilon}} \overline{V}_{ij,k}. \tag{4.50}$$

Note that after spin averaging, they are no longer matrices and thus no longer mediate spin correlations. They are obtained from

$$\overline{V}_{ij,k} = \frac{1}{N} \sum_{\eta,\eta'} \boldsymbol{V}_{ij,k}^{\eta\eta'} \delta^{\eta\eta'}, \quad N = \begin{cases} 2 & \widetilde{ij} = q,\overline{q} \\ (D-2) & \widetilde{ij} = g. \end{cases} \tag{4.51}$$

Also note that the above definition of $\mathcal{V}_{ij}(\epsilon)$ includes parts of the phase space measure $\mathrm{d}p_i$ we discussed in equation (4.43). The reason for this is that if we integrate a single dipole over the unresolved phase space, we obtain

$$\int \mathrm{d}p_i(\tilde{p}_{ij}, \tilde{p}_k) \mathcal{D}_{ij,k}$$
$$= -\int \mathrm{d}p_i \frac{1}{2p_i p_j} \sum_{\substack{\{\lambda\}_n\backslash \\ \{\lambda_i,\lambda_j\}}} \sum_{\eta,\eta'} \mathcal{A}_n^*(\widetilde{ij}, \widetilde{k}) \left(\frac{\boldsymbol{T}_k \cdot \boldsymbol{T}_{ij}}{\boldsymbol{T}_{ij}^2} \boldsymbol{V}_{ij,k}^{\eta\eta'} \right) \mathcal{A}_n(\widetilde{ij}, \widetilde{k})$$
$$= -\frac{\alpha_s}{2\pi \, \Gamma(1-\epsilon)} \left(\frac{4\pi\mu^2}{2\tilde{p}_{ij}\tilde{p}_k} \right)^\epsilon \mathcal{V}_{ij}(\epsilon) \sum_{\substack{\{\lambda\}_n\backslash \\ \{\lambda_i,\lambda_j\}}} \sum_{\eta} \mathcal{A}_n^*(\widetilde{ij}, \widetilde{k}) \frac{\boldsymbol{T}_k \cdot \boldsymbol{T}_{ij}}{\boldsymbol{T}_{ij}^2} \mathcal{A}_n(\widetilde{ij}, \widetilde{k}). \tag{4.52}$$

To verify that the integral over *all* dipoles actually yields the insertion term requires some careful rearrangement of the sums which is presented in detail in [26] and which we do not repeat here.

We mentioned earlier that $\mathcal{V}_{ij}(\epsilon)$ only depends on the spin averaged correlation functions $\overline{V}_{ij,k}$. Let us illustrate why we do not have to integrate the full spin–correlation matrices. To this end, let us consider only those terms from the $\boldsymbol{V}_{ij,k}$ that actually contribute a spin correlation. These are given by

$$\frac{K_\mu K_\nu}{p_i p_j} = \frac{(zp_i^\mu - \overline{z}p_j^\mu)(zp_i^\nu - \overline{z}p_j^\nu)}{p_i p_j} \tag{4.53}$$

in equations (4.25a) and (4.25b). One can show that

$$\tilde{p}_{ij}^\mu K_\mu = z - \overline{z} - (z^2 - \overline{z}^2) = 0 \tag{4.54}$$

so that the spin–correlation terms are perpendicular to $\tilde{p}_{ij}^\mu$ and $\tilde{p}_{ij}^\nu$. Also, due to Lorentz invariance the integral of the subtraction term can only depend on the momenta $\tilde{p}_{ij}$ and $\tilde{p}_k$. Using these two arguments, we find that the result of the integration over $\mathrm{d}p_i$ will give

a term with the following Lorentz structure:

$$A\, g^{\mu\nu} + B\, \frac{\tilde{p}_{ij}^{\mu}\tilde{p}_{k}^{\nu} + \tilde{p}_{k}^{\mu}\tilde{p}_{ij}^{\nu}}{\tilde{p}_{ij}\tilde{p}_{k}} + C\tilde{p}_{ij}^{\mu}\tilde{p}_{ij}^{\nu}. \tag{4.55}$$

Since this will be contracted with polarization vectors of the emitter partons $\widetilde{ij}$ (again, see (4.25a) and (4.25b)) the terms with coefficients B and C vanish due to gauge invariance. The contraction of the polarizations with $g^{\mu\nu}$, however, is no spin correlation but simply leads to a spin summation. If we now average the spin–correlation matrices over their spins, we obtain exactly the term $A\, g^{\mu\nu}$. This is why we can restrict the problem to integrating the spin averaged correlation functions.

4.2.5 Extension to Massive Quarks

So far, we restricted our discussion to massless partons. The inclusion of massive partons has first been discussed and derived in [80] and formulated in a more general way in [79]. This section presents the general ideas and results from the latter publication.

In general, including massive partons merely complicates the involved kinematics since the square of parton momenta do not vanish any longer, for example

$$p_i^2 = m_i^2, \quad p_j^2 = m_j^2, \quad p_k^2 = m_k^2, \quad p_{ij}^2 = m_{ij}^2 \tag{4.56}$$

where the mass depends on the flavor of the respective parton. Since the mass serves the purpose of a regulator, there are in principle no new infrared divergences that we need to take care of. While not being divergent, the infrared contributions yield for example logarithmic contributions of the type

$$\int\limits_{n+1} d\sigma^{\mathrm{R}} \propto \ln\frac{Q^2}{m^2} + \text{ finite terms} \tag{4.57}$$

where Q is the hard process scale and m is the mass of a massive parton in the process. The above equation is valid in cases where the two scales vary greatly, i.e. $Q \gg m$, resulting in a large logarithm. This logarithm is again canceled by an equal contribution from the virtual corrections $d\sigma^{\mathrm{V}}$ with opposite sign. Thus, this poses no conceptual problem. In numerical calculations, however, these logarithms can create problems. $Q \gg m$ means that both the real emission contribution and the virtual corrections are large numerical values which, after summation, result in a much smaller total next–to–leading order cross section. If we do not subtract these logarithms separately for both contributions (i.e. as part of $d\sigma^{\mathrm{A}}$), the numerical program might experience numerical instabilities. Since computers can only store a limited number of decimal digits for any numerical value[5], the subtraction of two

---

[5]Normally, one uses double-precision floating-point variables that occupy 64 bits or 8 bytes in computer memory. Such variables are usually implemented according to the IEEE 754 floating-point standard [82] which yields roughly 16 significant decimal digits.

almost equal numbers (i.e. almost all leading digits are equal) will result in a much smaller number of significant decimal digits. This creates instabilities in the actual results and can seriously harm the convergence of the Monte Carlo algorithm.

Thus, to ensure that the Monte Carlo integral evaluates properly, we impose the following requirement:

$$\lim_{m \to 0} \int_{n+1} \left[d\sigma^{R}(m) - d\sigma^{A}(m) \right] = \int_{n+1} \left[d\sigma^{R}(m = 0) - d\sigma^{A}(m = 0) \right] \qquad (4.58)$$

where we denoted the mass dependence explicitly (and where m can refer to one or more massive partons). It enforces a smooth parameterization of the massless limit.

As a next step, let us consider the soft and collinear limits of an $(n+1)$–parton amplitude with massive partons. The above condition affects our parameterization of the collinear limit, as we will see.

The Soft Limit for Massive Amplitudes

Since only gluons yield contributions to the soft limit, the soft limit is almost identical to what we derived earlier in section 4.2.1. The only difference comes from the fact that in the contraction of the eikonal currents, equation (4.9) on page 61, the first term no longer vanishes since $p_i^2 = m_i^2$. We thus obtain

$$\lim_{\lambda_{\text{soft}} \to 0} \sum_{\{\lambda\}_{n+1}} \left| \mathcal{A}_{n+1} \right|^2$$
$$= -8\pi\alpha_s \mu^{2\epsilon} \sum_{\substack{i=1 \\ i \neq j}}^{n+1} \frac{1}{p_i p_j} \sum_{\substack{k=1 \\ k \neq i \neq j}}^{n+1} \left(-\frac{m_i^2}{2 p_i p_j} + \frac{p_i p_k}{p_i p_j + p_k p_j} \right) \sum_{\{\lambda\}_n} \mathcal{A}_n^* \, \mathbf{T}_i \mathbf{T}_k \, \mathcal{A}_n . \qquad (4.59)$$

The Quasi-Collinear Limit for Massive Amplitudes

To ensure that the smoothness condition (4.58) is fulfilled, we have to investigate the so-called *quasi-collinear* limit [83] which generalizes the collinear limit. Here, we not only let the transverse momentum approach zero, $k_\perp \to 0$, but also the parton mass $m \to 0$ in such a way that $|k_\perp|/m$ stays constant:

$$k_\perp = \lambda_{\text{coll}} k, \qquad m_x \to \lambda_{\text{coll}} m_x \quad \left(x = i, j, (ij) \right) \qquad (4.60)$$

In this way, the logarithmic contributions discussed before are treated as if they were divergent similar to the massless case, thus guaranteeing their subtraction later on in $d\sigma^A$.

The Sudakov parameterization for the emitter and spectator momenta, equation (3.38)

now becomes

$$
p_i^\mu = x p_{\mathrm{coll}}^\mu + k_\perp - \frac{k_\perp^2 + x^2 m_{ij}^2 - m_i^2}{x} \frac{n^\mu}{2(n p_{\mathrm{coll}})},
$$
$$
p_j^\mu = \overline{x} p_{\mathrm{coll}}^\mu - k_\perp - \frac{k_\perp^2 + \overline{x}^2 m_{ij}^2 - m_j^2}{\overline{x}} \frac{n^\mu}{2(n p_{\mathrm{coll}})}.
$$

$$(4.61)$$

Here, p_{coll} is not light-like but a massive four-momentum with $p_{\mathrm{coll}}^2 = m_{ij}^2$. The invariant that carries the singular behavior now reads

$$
(p_i + p_j)^2 = \lambda_{\mathrm{coll}}^2 \left(-\frac{k^2}{x\overline{x}} + \frac{m_i^2}{x} + \frac{m_j^2}{\overline{x}} \right).
$$

$$(4.62)$$

However, since the emitter parton is generally regularized by the parton's mass, the actual propagator is not divergent as the quasi-collinear limit of the amplitude shows:

$$
\lim_{\lambda_{\mathrm{coll}} \to 0} \sum_{\{\lambda\}_{n+1}} |\mathcal{A}_{n+1}|^2
$$
$$
= \frac{4\pi\alpha_s\mu^{2\epsilon}}{(p_i + p_j)^2 - m_{ij}^2} \sum_{\substack{\{\lambda\}_{n+1}\backslash \\ \{\lambda_i,\lambda_j\}}} \sum_{\eta,\eta'} \mathcal{A}_n^*(\eta)\, \boldsymbol{P}_{(ij)\to i+j}^{(m),\eta\eta'}\, \mathcal{A}_n(\eta').
$$

$$(4.63)$$

This expression contains re-derived Altarelli–Parisi splitting kernels that are obtained like in the collinear limit, but with the appropriate Feynman rules for massive particles (i.e. spinors):

$$
\boldsymbol{P}_{g\to q\overline{q}}^{(m),\eta\eta'} = T_{\mathrm{R}} \left[-g^{\mu\nu} + 4\frac{k_\perp^\mu k_\perp^\nu}{(p_i + p_j)^2} \right] \epsilon_\eta^\mu \epsilon_{\eta'}^{*\nu},
$$

$$(4.64a)$$

$$
\boldsymbol{P}_{q\to qg}^{(m),\eta\eta'} = C_{\mathrm{F}} \left[\frac{1 + x^2}{\overline{x}} - \epsilon\overline{x} - \frac{m_i^2}{p_i p_j} \right] \delta_{\eta\eta'}.
$$

$$(4.64b)$$

The kernel for the splitting $g \to gg$ is unaffected since all partons are gluons and thus always massless, it is given by equation (4.16a) on page 63.

Dipoles for Massive Partons

Let us now turn to the dipoles themselves. The definition of the dipole is almost identical to the previously given form, equation (4.23):

$$
\mathcal{D}_{ij,k}(p_1, \ldots p_{n+1})
$$
$$
= -\frac{1}{(p_i + p_j)^2 - m_{ij}^2} \sum_{\substack{\{\lambda\}_{n+1}\backslash \\ \{\lambda_i,\lambda_j\}}} \sum_{\eta,\eta'} \mathcal{A}_n^*(\widetilde{ij}, \widetilde{k}) \left(\frac{\mathbf{T}_k \cdot \mathbf{T}_{ij}}{\mathbf{T}_{ij}^2} \boldsymbol{V}_{ij,k}^{\eta\eta'} \right) \mathcal{A}_n(\widetilde{ij}, \widetilde{k}).
$$

$$(4.65)$$

However, the momentum parameterization obviously differs from what we had in the massless case and so do the spin–correlation matrices. The momenta now read

$$\tilde{p}_{ij}^{\mu} = P^{\mu} - \tilde{p}_{k}^{\mu}$$

$$\tilde{p}_{k}^{\mu} = \frac{\sqrt{\lambda(P^2, m_{ij}^2, m_k^2)}}{\sqrt{\lambda(P^2, (p_i + p_j)^2, m_k^2)}} \left(p_k^{\mu} - \frac{P p_k}{P^2} P^{\mu} \right) + \frac{P^2 + m_k^2 - m_{ij}^2}{2 P^2} P^{\mu} \qquad (4.66)$$

where P is the total momentum of the dipole momenta

$$P^{\mu} = p_i^{\mu} + p_j^{\mu} + p_k^{\mu} = \tilde{p}_{ij}^{\mu} + \tilde{p}_k^{\mu} \qquad (4.67)$$

and λ is the *Källén* function we saw before,

$$\lambda(x, y, z) = x^2 + y^2 + z^2 - 2(xy + yz + zx) \qquad (4.68)$$

which often occurs in phase space factorization formulas with massive partons. The momenta are chosen such that all momenta are (massive) on shell momenta obeying

$$p_i^2 = m_i^2, \quad p_j^2 = m_j^2, \quad p_k^2 = m_k^2, \quad \tilde{p}_{ij}^2 = m_{ij}^2, \quad \tilde{p}_k^2 = m_k^2. \qquad (4.69)$$

The spin–correlation matrices themselves are more complicated due to the complicated kinematics arising from the masses. Like in the massless case, they depend on the variables $z, \overline{z}, y,$ and $\overline{y}$ whose definition is unaltered. However, they also depend on several other variables that vanish in the massless limit. These are listed in table 4.1. Therein, we find a definition for normalized masses μ_x, some definitions for relative velocities $v_{x,y}$ between partons x and y that are equal to one for massless particles (the tilde version $\tilde{v}_{ij,k}$ refers to the dipole momenta $\tilde{p}_{ij}$ and $\tilde{p}_k$), and a massive variant of the variables z and $\overline{z}$ which carries an additional superscript (m). Lastly, the range of values that z and $\overline{z}$ can take is no longer given by the interval $[0,1]$ but by $[z_-, z_+]$ in the massive case which is important for the limits of the integral over the unresolved phase space, but also in the definition of the spin–correlation matrices. These matrices are finally given by

$$V_{gg,k}^{\eta\eta'} = 4\pi\alpha_s \mu^{2\epsilon} (4C_A) \left[-g^{\mu\nu} \left(\frac{1}{1 - z\,\overline{y}} + \frac{1}{1 - \overline{z}y} - \frac{2 - \kappa\, z_+ z_-}{v_{ij,k}} \right) \right.$$
$$\left. + \frac{1 - \epsilon}{p_i p_j\, v_{ij,k}} K^{(m)\mu} K^{(m)\nu} \right] \epsilon_{\mu}^{\eta} \epsilon_{\nu}^{\eta'\,*}, \qquad (4.70\text{a})$$

$$V_{q\overline{q},k}^{\eta\eta'} = 4\pi\alpha_s \mu^{2\epsilon} \frac{2 T_R}{v_{ij,k}} \left\{ -g^{\mu\nu} \left[1 - \frac{2\kappa}{1 - \epsilon} \left(z_+ z_- - \frac{m_i^2}{(p_i + p_j)^2} \right) \right] \right.$$
$$\left. - \frac{4}{(p_i + p_j)^2} K^{(m)\mu} K^{(m)\nu} \right\} \epsilon_{\mu}^{\eta} \epsilon_{\nu}^{\eta'\,*}, \qquad (4.70\text{b})$$

$$V_{qg,k}^{\eta\eta'} = 4\pi\alpha_s \mu^{2\epsilon} (2C_F) \left[\frac{2}{1 - z\overline{y}} - \frac{\tilde{v}_{ij,k}}{v_{ij,k}} \left((1 + z) + \frac{m_i^2}{p_i p_j} + \epsilon\overline{z} \right) \right] \delta_{\eta\eta'} \qquad (4.70\text{c})$$

$$\mu_x = \frac{m_x}{\sqrt{P^2}}, \qquad\qquad \xrightarrow{m\to 0} 0 \qquad \left(x = i, j, k, \widetilde{ij}\right)$$

$$v_{ij,k} = \frac{\sqrt{\left(2\mu_k^2 + (1 - \mu_i^2 - \mu_j^2 - \mu_k^2)\overline{y}\right)^2 - 4\mu_k^2}}{(1 - \mu_i^2 - \mu_j^2 - \mu_k^2)\overline{y}} \qquad \xrightarrow{m\to 0} 1$$

$$\overline{v}_{ij,k} = 1 - v_{ij,k} \qquad\qquad \xrightarrow{m\to 0} 0$$

$$\tilde{v}_{ij,k} = \frac{\sqrt{\lambda(1, \mu_{ij}^2, \mu_k^2)}}{1 - \mu_{ij}^2 - \mu_k^2} \qquad\qquad \xrightarrow{m\to 0} 1$$

$$v_{ij,i} = \frac{\sqrt{(1 - \mu_i^2 - \mu_j^2 - \mu_k^2)^2 y^2 - 4\mu_i^2\mu_j^2}}{(1 - \mu_i^2 - \mu_j^2 - \mu_k^2)y + 2\mu_i^2} \qquad \xrightarrow{m\to 0} 1$$

$$z^{(m)} = z - \frac{1}{2}\overline{v}_{ij,k} \qquad\qquad \xrightarrow{m\to 0} z$$

$$\tilde{z}^{(m)} = \overline{z} - \frac{1}{2}\overline{v}_{ij,k} \qquad\qquad \xrightarrow{m\to 0} \overline{z}$$

$$z_{\pm} = \frac{2\mu_i^2 + (1 - \mu_i^2 - \mu_j^2 - \mu_k^2)y}{2\left(\mu_i^2 + \mu_j^2 + (1 - \mu_i^2 - \mu_j^2 - \mu_k^2)y\right)}\left(1 \pm v_{ij,i}\, v_{ij,k}\right) \qquad \xrightarrow{m\to 0} \begin{cases} 1 & + \\ 0 & - \end{cases}$$

Table 4.1: New variables for massive final state dipoles along with their corresponding limits in the case where all masses go to zero.

with the spin correlation

$$K^{(m)\mu} = z^{(m)}p_i^\mu - \tilde{z}^{(m)}p_j^\mu \tag{4.71}$$

and an arbitrary parameter κ which controls the distribution of finite pieces among the terms. With the help of table 4.1 one can easily see that if all masses are zero, the spin–correlation matrices are equal to the ones we defined earlier, equations (4.25a) to (4.25c).

Of course, these new spin–correlation matrices yield a new integrated subtraction term. In order to derive it, one first has to factorize phase space such that the unresolved particle can be integrated over. Just like the formulas above, this is very technical and involved and copying the formulas here will not serve any purpose in the scope of this thesis. Hence, we refer the reader to the detailed explanations in [79].

4.2.6 Initial State Hadrons

So far, we have merely discussed the treatment of final state radiation which is sufficient if we compute observables for electron–positron collisions. If we look at LHC physics, however, we also have initial state partons in the partonic cross section that can either radiate further partons (i.e. it can be an emitter parton) or take part as a spectator parton.

(a) $\mathcal{D}_{ij,k}$ **(b)** $\mathcal{D}_{ij}^a$ **(c)** $\mathcal{D}_k^{aj}$ **(d)** $\mathcal{D}^{aj,b}$
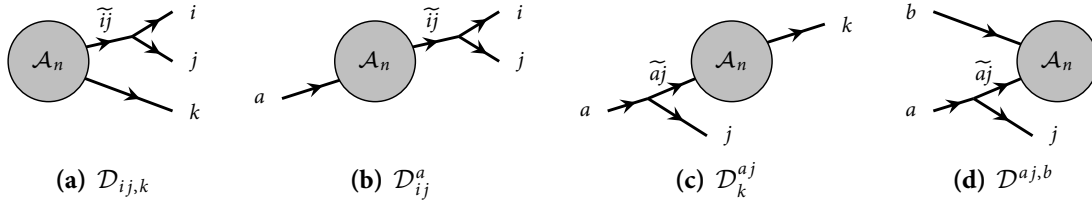
Figure 4.1: The different types of dipoles. Blobs denote n–parton amplitudes; external lines to the left of plots are initial state partons, lines to the right are final state partons. From left to right the following emitter–spectator cases are shown: final–final, final–initial, initial–final, initial–initial. Picture adapted from [26, 79].

In total, there are four types of dipoles that we have to deal with. They can be categorized by the channel (i.e. initial or final state) of the emitter and the spectator parton. Figure 4.1 shows the four contributions pictorially. Our naming convention follows [26] and is used in any publication that we will refer to in this thesis: initial state partons are labeled a and b while final state particles have indices i, j, and k. Depending on the channel of the emitter and the spectator, the indices are given as superscripts in the initial state and as subscripts in the final state (as in our previous discussion).

Our discussion so far was limited to non–hadronic initial states, hence we only discussed final–final dipoles. Deriving the other dipoles is very similar[6] although the treatment of an initial state emitter bears some new complications, not only in terms of its formulation but also conceptually. We discussed factorization shortly in chapter 2 and initial state radiation is where it practically enters our discussion. In order to obtain a finite cross section, we have to alter equation (3.29) such that it reads

$$\sigma^{\mathrm{NLO}} = \int\limits_{n+1} \mathrm{d}\sigma^{\mathrm{R}} + \int\limits_{n} \mathrm{d}\sigma^{\mathrm{V}} + \int\limits_{n} \mathrm{d}\sigma^{\mathrm{C}}(\mu_{\mathrm{F}}), \qquad (4.72)$$

where $\mathrm{d}\sigma^{\mathrm{C}}$ is the so-called *collinear counterterm*. The reason for its existence is that collinear divergences stemming from initial state partons are *not* canceled by equivalent poles from the virtual contributions, unlike those from final state partons. Instead, these collinear emissions have to be regarded as part of the parton distribution functions which they should be absorbed into—as we discussed before, this is the reason for the existence of (and for $\mathrm{d}\sigma^{\mathrm{C}}$'s dependence on) the factorization scale μ_{F}. In numerical calculations, this is done the other way around: instead of absorbing the collinear divergences into the PDFs, they are still contained in $\mathrm{d}\sigma^{\mathrm{R}}$ (otherwise, $\mathrm{d}\sigma^{\mathrm{R}}$ would depend on the factorization scale and they would have to be filtered out). The re-definition of the PDFs, on the other hand, is given explicitly in terms of the collinear counterterm $\mathrm{d}\sigma^{\mathrm{C}}$. It contains divergences which are exactly canceled by the initial state collinear divergences of $\mathrm{d}\sigma^{\mathrm{R}}$. $\mathrm{d}\sigma^{\mathrm{C}}$ can be written as a convolution of a process-independent factor $\Gamma(x, x', \mu_{\mathrm{F}})$ and a leading–order cross

---

[6]In principle, we have to analyze the soft and collinear limits once more for each case, derive new subtraction terms that match in those limits, obtain the integrated term, etc.

section:

$$\int_n d\sigma^{\mathrm{C}}(\mu_{\mathrm{F}}) = \int_0^1 dx \int_0^1 dx' \int_n d\sigma^{\mathrm{B}}(x p_a, x' p_b) \, \Gamma(x, x', \mu_{\mathrm{F}}). \qquad (4.73)$$

The process-independent $\Gamma(x, x', \mu_{\mathrm{F}})$ is proportional to the Altarelli–Parisi splitting functions (which is expected since the Altarelli–Parisi equations mediate parton evolution) plus a term that depends on the factorization scheme that is used (e.g. $\overline{\mathrm{MS}}$ scheme); we are not interested in the exact form here. The two integrals force the Born cross section to be integrated over the initial state momenta intervals $[0, p_{a/b}]$.

The next–to–leading order cross section now reads

$$\sigma^{\mathrm{NLO}} = \int_{n+1} \left[d\sigma^{\mathrm{R}} - d\sigma^{\mathrm{A}} \right] + \int_n \left[d\sigma^{\mathrm{V}} + d\sigma^{\mathrm{C}} + \int_1 d\sigma^{\mathrm{A}} \right] \qquad (4.74)$$

where both square brackets are integrable in four dimensions. In the right hand bracket, we find the following structure

$$d\sigma^{\mathrm{C}} + \int_1 d\sigma^{\mathrm{A}} = d\sigma^{\mathrm{B}} \otimes (\boldsymbol{I} + \boldsymbol{P} + \boldsymbol{K}) \qquad (4.75)$$

where $\boldsymbol{I}$ is the insertion operator that contains all poles which are canceled by the virtual corrections $d\sigma^{\mathrm{V}}$. The other two operators are finite remainders of the cancellation of the initial state collinear divergences: $\boldsymbol{P}$ corresponds to the piece proportional to the Altarelli–Parisi functions while $\boldsymbol{K}$ results from the term that depends on the factorization scheme, both of which were mentioned before in the context of $\Gamma(x, x', \mu_{\mathrm{F}})$. The tensor product again represents color correlations between the amplitudes in $d\sigma^{\mathrm{B}}$.

Let us now discuss the structure of the subtraction term $d\sigma^{\mathrm{A}}$. With two partons in the initial state, we have to add the remaining dipoles such that our new subtraction term takes the form

$$d\sigma^{\mathrm{A}}_{\mathrm{CS}} \propto d\Phi_{n+1} \Bigg(\sum_{\substack{(i,j) \\ k \neq i,j}} \mathcal{D}_{ij,k} \, J_n(\tilde{p}_{ij}, \tilde{p}_k) + \sum_{c \in \{a,b\}} \sum_{(i,j)} \mathcal{D}_{ij}^c \, J_n(\tilde{p}_{ij}; \tilde{p}_a)$$

$$+ \sum_{c \in \{a,b\}} \sum_{(j,k)} \mathcal{D}_k^{cj} \, J_n(\tilde{p}_k; \tilde{p}_{cj}) + \sum_{\substack{c,d \in \{a,b\} \\ c \neq d}} \sum_j \mathcal{D}^{cj,d} \, J_n(\widetilde{\Phi}_n; \tilde{p}_{cj}, p_d) \Bigg) \qquad (4.76)$$

as opposed to equation (4.22). Each new term contains a sum over both initial state partons which essentially means that each new dipole term has to be applied for each parton. The jet functions J_n obviously always act on all final state momenta. However, having initial state emitters and spectators means re-parameterized momenta and thus a different process scale. We indicate this by initial state momenta that follow a semicolon in the argument list of the jet function. The last dipole case even contains a re-parameterization (Lorentz transformation) of all final state momenta, indicated by $\widetilde{\Phi}_n$. Note that we indicated the

subtraction term with a subscript "CS" that stands for Catani–Seymour. The reason is that we will use this subtraction term in the following chapters where we will usually talk about the full massive term including initial state radiation.

In the following, we will discuss each of the remaining cases briefly where we focus on the differences to the already discussed final–final case. For more details, we refer the reader to [26] and [79] where all terms are carefully worked out. Since the formulas for massless dipoles can always be obtained by letting $m \to 0$ in the relations for massive dipoles, we directly present the massive versions.

With respect to parton masses, one more remark is in order. The factorization theorem only holds provided that any incoming partons are *massless*, or can be treated as such (i.e. their masses are small and can be neglected in a theoretical calculation). The cancellation of soft divergences is guaranteed by Bloch–Nordsieck procedure, originally formulated in 1937 when QCD was not yet known, which says that electrons are "unaffected by the interaction with radiation" [84]. The generalization is that in QCD, poles due to soft gluons cancel—a fact we have exploited many times in this thesis. However, this is no longer valid if incoming partons are massive which leads to divergent contributions proportional to the mass m of the ingoing parton, see for example [85–88]. Even though these violations only start appearing at two–loop order which is next–to–next–to–leading order, they prevent a general formulation of the factorization theorem for massive initial state partons. Thus, no formulation of the dipole formalism exists for this case.

In the following discussion, we give the subtraction terms, but not their integrated versions and the factorization of phase space into n–parton times unresolved contribution. Since these steps are performed in great detail in [26, 79], we refrain from copying the formulas which would exceed the scope of this thesis. Furthermore, the focus in this work lies on the subtraction terms and not on their integration, for reasons that will become obvious in chapters 5 to 7.

Final State Emitter and Initial State Spectator

First, we deal with the case where an initial state parton can take the role of the spectator parton which is depicted in figure 4.1(b). This case is analogous to the final–final case but depends on a different momentum parameterization and slight modifications. For the momenta, we use

$$\tilde{p}_{ij}^\mu = p_i^\mu + p_j^\mu - \overline{x}\, p_a^\mu, \qquad \tilde{p}_a^\mu = x\, p_a^\mu \tag{4.77}$$

where we defined the symbol

$$x \equiv x_{ij,a} = \frac{p_i p_a + p_j p_a - p_i p_j + \frac{1}{2}\left(m_{ij}^2 - m_i^2 - m_j^2\right)}{p_i p_a + p_j p_a}, \qquad \overline{x} \equiv 1 - x_{ij,a}, \tag{4.78}$$

which takes the role of y and $\overline{y}$ from the final–final dipoles. Note that this variable should not be confused with the energy fraction x we used for the Sudakov parameterization (see equations (3.38) and (4.61)); in the context of initial state dipoles, we will henceforth use x in the above sense.

The dipole definition is also slightly altered with respect to $\mathcal{D}_{ij,k}$:

$$\mathcal{D}_{ij}^a = -\frac{1}{(p_i + p_j)^2 - m_{ij}^2} \frac{1}{x} \sum_{\substack{\{\lambda\}_{n+1}\backslash \\ \{\lambda_i, \lambda_j\}}} \sum_{\eta, \eta'} \mathcal{A}_n^*(\widetilde{ij}; \widetilde{a}) \left(\frac{\mathbf{T}_a \cdot \mathbf{T}_{ij}}{\mathbf{T}_{ij}^2} (V_{ij}^a)^{\eta\eta'} \right) \mathcal{A}_n(\widetilde{ij}; \widetilde{a}). \qquad (4.79)$$

where the factor $1/x$ is due to the initial state spectator. The spin–correlation matrices are given by the following relations

$$V_{gg,k}^{\eta\eta'} = 4\pi\alpha_s\mu^{2\epsilon}(4C_A)\left[-g^{\mu\nu}\left(\frac{1}{1-z+\overline{x}} + \frac{1}{1-\overline{z}+\overline{x}} - 2\right) + \frac{1-\epsilon}{p_i p_j}K^\mu K^\nu\right]\epsilon_\mu^\eta\epsilon_\nu^{\eta'*}, \quad (4.80a)$$

$$V_{q\bar{q},k}^{\eta\eta'} = 4\pi\alpha_s\mu^{2\epsilon}(2T_R)\left[-g^{\mu\nu} - \frac{4}{(p_i+p_j)^2}K^\mu K^\nu\right]\epsilon_\mu^\eta\epsilon_\nu^{\eta'*}, \qquad (4.80b)$$

$$V_{qg,k}^{\eta\eta'} = 4\pi\alpha_s\mu^{2\epsilon}(2C_F)\left[\frac{2}{1-z+\overline{x}} - (1+z) - \epsilon\overline{z}\right]\delta_{\eta\eta'}. \qquad (4.80c)$$

Note that they are significantly shorter than the ones for the massive final–final case, equations (4.70a) to (4.70c), for two reasons. First, the free parameter κ has been set to zero and second, since the spectator is in the initial state and thus massless, the velocities $v_{ij,a}$ and $\tilde{v}_{ij,a}$ are equal to one (see table 4.1). Hence, z and $\overline{z}$ are defined as in the massless final–final case with the exchange $k \to a$ (i.e. $z = z_{ij,a}$, see equation (4.24)). Furthermore, the spin–correlation K^μ is exactly the same as in the massless final–final case, equation (4.26). Due to the change of the spectator parton into the initial state, we have the following replacement with respect to the final–final case:

$$\frac{1}{1-z\,\overline{y}} \to \frac{1}{1-z+\overline{x}}, \qquad \frac{1}{1-\overline{z}\,\overline{y}} \to \frac{1}{1-\overline{z}+\overline{x}}, \qquad (4.81)$$

(this affects only two of the three matrices). One can easily check that this new parametrization leads to the same collinear and to a similar soft limit (one has to include initial state partons in the definition of the eikonal currents) we derived earlier for the final–final case.

Initial State Emitter and Final State Spectator

In the case where an initial state parton becomes an emitter, the kinematical situation is different than before. Since the initial state emitter momentum $\tilde{p}_{aj}$ is the one that describes the "remnant" parton that goes into the hard scattering and parton j actually radiates off of p_a (compare figure 4.1(c)), the kinematic situation is as follows:

$$\tilde{p}_{aj}^\mu = xp_a^\mu, \qquad \tilde{p}_k^\mu = p_k^\mu + p_j^\mu - \overline{x}p_a^\mu \qquad (4.82)$$

where

$$x \equiv x_{jk,a} = \frac{p_j p_a + p_k p_a - p_j p_k}{p_j p_a + p_k p_a}, \qquad \overline{x} \equiv 1 - x_{jk,a} = \frac{p_j p_k}{p_j p_a + p_k p_a}. \qquad (4.83)$$

Here, only the spectator can be massive, $\tilde{p}_k^2 = m_k^2$, since initial state partons have to be massless as we discussed before.

The dipole then reads

$$
\mathcal{D}_k^{aj}(p_1, \ldots p_{n+1})
$$
$$
= -\frac{1}{2p_a p_j} \frac{1}{x} \sum_{\substack{\{\lambda\}_{n+1}\backslash \\ \{\lambda_a, \lambda_j\}}} \sum_{\eta, \eta'} \mathcal{A}_n^*(\widetilde{k}; \widetilde{aj}) \left(\frac{\mathbf{T}_k \cdot \mathbf{T}_{aj}}{\mathbf{T}_{aj}^2} (V_k^{aj})^{\eta\eta'} \right) \mathcal{A}_n(\widetilde{k}; \widetilde{aj}). \tag{4.84}
$$

Let us now discuss the spin–correlation matrices by clarifying the differences between final and initial state emitters, first. For final state emitters, the parton $\widetilde{ij}$ couples the two final state partons i and j to the matrix element. The fact that both i and j were external particles in the final state meant we did not have to distinguish between the splittings $q \to qg$ and $q \to gq$, for example. In the case where the emitter is in the initial state, however, we actually describe the splitting $a \to \widetilde{aj} + j$. The matrix character of the spin–correlation matrices is now due to the helicities of particle $\widetilde{aj}$ which, from the perspective of the splitting, is an outgoing parton as opposed to $\widetilde{ij}$ which is ingoing in terms of the splitting. If we compare the splittings $q \to qg$ and $q \to gq$ in the initial state, we find that we have to distinguish between the two since the splitting parton is a quark and a gluon, respectively. This affects the definition of the spin–correlation matrix and we end up with a total of four terms:

$$
(V_k^{gg})^{\eta\eta'} = 4\pi\alpha_s \mu^{2\epsilon}(4C_A) \left[-g^{\mu\nu} \left(\frac{1}{1-x+u} - 1 + x\overline{x} \right) + (1-\epsilon)\frac{\overline{x}}{x} \frac{u\overline{u}}{p_j p_k} L^\mu L^\nu \right] \times
$$
$$
\times \epsilon_\mu^\eta \epsilon_\nu^{\eta'\,*}, \tag{4.85a}
$$

$$
(V_k^{qq})^{\eta\eta'} = 4\pi\alpha_s \mu^{2\epsilon}(2C_F) \left[-g^{\mu\nu} x + \frac{\overline{x}}{x} \frac{2u\overline{u}}{p_i p_j} L^\mu L^\nu \right] \epsilon_\mu^\eta \epsilon_\nu^{\eta'\,*}, \tag{4.85b}
$$

$$
(V_k^{g\overline{q}})^{\eta\eta'} = 4\pi\alpha_s \mu^{2\epsilon}(2T_R) \left[1 - \epsilon - 2x\overline{x} \right] \delta_{\eta\eta'}, \tag{4.85c}
$$

$$
(V_k^{qg})^{\eta\eta'} = 4\pi\alpha_s \mu^{2\epsilon}(2C_F) \left[\frac{2}{1-x+u} - (1+x) - \epsilon\overline{x} \right] \delta_{\eta\eta'}, \tag{4.85d}
$$

where the spin–correlation is given by

$$
L^\mu = \frac{p_j^\mu}{u} - \frac{p_k^\mu}{\overline{u}} \tag{4.86}
$$

and

$$
u = \frac{p_j p_a}{p_j p_a + p_k p_a}, \qquad \overline{u} \equiv 1 - u = \frac{p_k p_a}{p_j p_a + p_k p_a} \tag{4.87}
$$

which takes the role of z.

In order to verify that the above dipoles yield the proper soft and collinear description of all poles, one has to re-calculate the Altarelli–Parisi splitting functions (see equations (4.16a) to (4.16d)) for the splitting $a \to (aj) + j$ of an initial state parton. This requires the

use of a slightly altered Sudakov parameterization. We do not present these terms and the momentum parameterization here, both can be found in section 4.3 of [26].

Initial State Emitter and Initial State Spectator

While the two previously discussed cases have to be applied to both deep inelastic scattering (one initial state hadron) and Tevatron/LHC physics (two initial state hadrons), the initial–initial case in figure 4.1(d) is only applicable when there are two hadrons in the initial state. Furthermore, this case will be treated for massless partons only due to the aforementioned fact that the factorization theorem no longer holds if there are two initial state massive partons.

We parameterize the emitter parton by

$$\tilde{p}_{aj}^{\mu} = x p_a^{\mu} \tag{4.88}$$

where we define

$$x \equiv x_{j,ab} = \frac{p_a p_b - p_j p_a - p_j p_b}{p_a p_b}, \qquad \overline{x} \equiv 1 - x_{j,ab} = \frac{p_j p_a + p_j p_b}{p_a p_b}. \tag{4.89}$$

In contrast to all other cases, we do not re-parameterize the spectator parton in this case, but we perform a Lorentz transformation on all final state momenta (which includes final state leptons, weak bosons, etc, not just partons) to compensate. The transformation is given by

$$\Lambda^{\mu}_{\ \nu} = g^{\mu}_{\ \nu} - 2\frac{(\kappa + \tilde{\kappa})^{\mu}(\kappa + \tilde{\kappa})_{\nu}}{(\kappa + \tilde{\kappa})^2} + 2\frac{\tilde{\kappa}^{\mu}\kappa_{\nu}}{\kappa^2} \tag{4.90}$$

where κ and $\tilde{\kappa}$ are the sums of the dipole momenta:

$$\kappa^{\mu} = p_a^{\mu} + p_b^{\mu} - p_j^{\mu}, \qquad \tilde{\kappa}^{\mu} = \tilde{p}_{aj}^{\mu} + p_b^{\mu}. \tag{4.91}$$

Once again, momentum conservation is fulfilled (albeit not as obviously as before; we do not verify this here).

The dipoles are given by

$$\mathcal{D}^{aj,b}(p_1, \dots p_{n+1})$$
$$= -\frac{1}{2p_a p_j}\frac{1}{x}\sum_{\substack{\{\lambda\}_{n+1}\backslash \\ \{\lambda_a, \lambda_j\}}}\sum_{\eta, \eta'}\mathcal{A}_n^*(\widetilde{\Phi}_n; \widetilde{aj}, p_b)\left(\frac{\mathbf{T}_b \cdot \mathbf{T}_{aj}}{\mathbf{T}_{aj}^2}(V^{aj,b})^{\eta\eta'}\right)\mathcal{A}_n(\widetilde{\Phi}_n; \widetilde{aj}, p_b). \tag{4.92}$$

Like in the initial–final case, we find four spin–correlation matrices which read

$$(V^{gg,b})^{\eta\eta'} = 4\pi\alpha_s\mu^{2\epsilon}(4C_A)\left[-g^{\mu\nu}\left(\frac{x}{\overline{x}} + x\overline{x}\right) + (1-\epsilon)\frac{\overline{x}}{x}u'M^{\mu}M^{\nu}\right]\epsilon_{\mu}^{\eta}\epsilon_{\nu}^{\eta'*}, \tag{4.93a}$$

$$(V^{qq,b})^{\eta\eta'} = 4\pi\alpha_s\mu^{2\epsilon}(2C_F)\left[-g^{\mu\nu}x + 2\frac{\overline{x}}{x}u'M^{\mu}M^{\nu}\right]\epsilon_{\mu}^{\eta}\epsilon_{\nu}^{\eta'*}, \tag{4.93b}$$

$$\left(V^{g\bar{q},b}\right)^{\eta\eta'} = 4\pi\alpha_s\mu^{2\epsilon}(2T_R)\left[1 - \epsilon - 2x\overline{x}\right]\delta_{\eta\eta'}, \tag{4.93c}$$

$$\left(V^{qg,b}\right)^{\eta\eta'} = 4\pi\alpha_s\mu^{2\epsilon}(2C_F)\left[\frac{2}{1-x} - (1+x) - \epsilon\overline{x}\right]\delta_{\eta\eta'}, \tag{4.93d}$$

where the spin–correlation is given by

$$M^\mu = p_i^\mu - \frac{p_i p_a}{p_b p_a}p_b^\mu \tag{4.94}$$

and

$$u' = \frac{p_a p_b}{(p_i p_a)(p_i p_b)}. \tag{4.95}$$

One can verify the correct description of the collinear limit by these dipoles using the Altarelli–Parisi kernels for the splitting $a \to (aj) + j$ mentioned above.

This concludes our discussion of the "classical" dipole formalism by which we mean its formulation for helicity summed matrix elements. There are some more features and publications that we have not discussed but which deserve to be mentioned briefly for the interested reader. Note that this work focuses on jet production in QCD which is the reason why we do not discuss the following items here.

The original publication by Catani and Seymour [26] also deals with *identified* partons which require parton–to–hadron fragmentation functions. These are treated separately from non-identified partons as they occur in jet production and thus require extra dipoles.

As we mentioned briefly, QED also experiences singular behavior due to photon radiation off of fermions which can also be treated within the dipole framework. Extensions of this kind have been proposed in [89, 90].

4.3 Implementation for Leading Color $e^-e^+ \to n$ Jets

The general implementation of the summation procedure using helicity amplitudes is straight forward. The numerical calculation of amplitudes is based on the parameterizations of the particle polarizations $\epsilon^+(p,q)$ and $\epsilon^-(p,q)$ and corresponding spinors we gave in chapter 3. Agreement between the long established program MadGraph (current version [91]) and our color ordered recursive approach has been extensively tested and confirmed in [36], both for massive and for massless amplitudes. Thus we can safely assume that the evaluation of Born amplitudes works properly and produces correct results. Instead, we will focus on the implementation of the dipole subtraction procedure for the real emission contribution which has not been discussed in [36].

We have implemented both the Born algorithm and the dipole formalism for $e^-e^+ \to n$ jet production in the leading color approximation and for five massless quark flavors (i.e. for massless up, down, strange, charm, and bottom quarks; as stated before we ignore the top quark). The only partial amplitude we have to evaluate is $A(q, g_1, g_2, \ldots, g_{n-1}, \overline{q}; e^-, e^+)$.
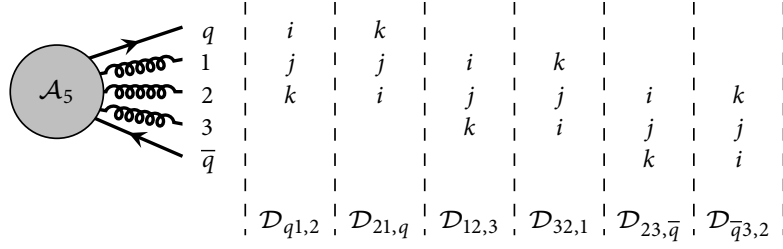
Figure 4.2: Example for the leading color dipoles for $e^-e^+ \to 4$ jets.

Since the ordering of particles is fixed, the only invariants that can yield soft or collinear poles are those of neighboring partons. This allows us to restrict the dipoles that we compute to those where all three indices i, j, and k are direct neighbors, reducing the total number of dipoles from $\mathcal{O}\left(n^3\right)$ to $(2n-2)$ dipoles for n jets:

$$\mathcal{D}_{q1,2}, \quad \mathcal{D}_{21,q}, \quad \mathcal{D}_{12,3}, \quad \mathcal{D}_{32,1}, \quad \ldots, \quad \mathcal{D}_{(n-2)(n-1),\bar{q}}, \quad \mathcal{D}_{\bar{q}(n-1),(n-2)}. \tag{4.96}$$

Note that the order of the emitter partons is not relevant. Furthermore, there is no dipole $\mathcal{D}_{q\bar{q},k}$ since the underlying Born amplitude would then be given by the process $e^-e^+ \to g_1g_2\cdots g_n$ which is not a physically possible process at tree-level. The apparently unintuitive backwards order of every second dipole (e.g. $\mathcal{D}_{21,q}$) is due to a very simple algorithm that can be used to generate the dipoles for an arbitrary number of jets. If we label the quark with the number 0 and the antiquark with n, i.e. the final state partons are labeled from 0 to n in the above order, we can use the following pseudo-code to generate the indices of all dipoles:

Algorithm: Generation of Leading Color Dipoles

```
for (unsigned a = 1; a < (n + 1); ++a) {
    unsigned i = a - 1;
    unsigned j = a;
    unsigned k = a + 1;
    // (ij, k) is the first dipole.
    // (kj, i) is the second dipole.
}
```

A pictorial example for this is given in figure 4.2.

Implementing the Kinematical Parts of the $V_{ij,k}$

When we calculate only those dipoles with neighboring partons, we also have to make sure that we adapt our spin–correlation matrices to this case. In order to get the soft limit right, we can only allow for parton j in the above dipoles to be treated as soft, otherwise we would obtain terms where non-neighboring partons are described by dipoles.[7] We can achieve

---

[7]Confer equation (4.27) on page 66 and the following description together with the external–leg insertion rule, figure 3.4 on page 35.

this by shifting terms that are singular in the soft limit of parton i (like $1/1 - \bar{z}\bar{y}$) between dipoles—thereby turning into parton j in the context of another dipole—so that all poles are accounted for by the soft singularity of parton j. The end result of this procedure is that we essentially "remove" all terms of the form $1/1 - \bar{z}\bar{y}$ from the dipoles and compensate for them by multiplying a factor two to the singular term $1/1 - z\bar{y}$ for parton j. Furthermore, due to the color flow decomposition, our definition of the coupling changes from $4\pi\alpha_s$ to $2\pi\alpha_s$. Taking everything together, the implemented spin–correlation matrices in four dimensions read

$$\boldsymbol{V}^{\eta\eta'}_{gg,k} = 2\pi\alpha_s(2C_A)\left[-g^{\mu\nu}\left(\frac{2}{1-z\,\bar{y}} - 2\right) + \frac{1}{p_i p_j}K^\mu K^\nu\right]\epsilon^\eta_\mu \epsilon^{\eta'}_\nu{}^*, \qquad (4.97a)$$

$$\boldsymbol{V}^{\eta\eta'}_{qg,k} = 2\pi\alpha_s(2C_F)\left[\frac{2}{1-z\bar{y}} - (1+z)\right]\delta_{\eta\eta'}. \qquad (4.97b)$$

Note that the $g \to q\bar{q}$ splitting leads to an underlying Born amplitude with two quark pairs which is sub-leading in terms of its color structure and which we thus drop. We now have to determine how to implement these formulas most efficiently. The basic kinematical structure of a dipole is in a symbolical notation given by

$$\begin{aligned}
\mathcal{D} &\propto \sum_{\eta,\eta'} \mathcal{A}^{\eta\,*}_n \boldsymbol{V}^{\eta\eta'} \mathcal{A}^{\eta'}_n \\
&= \mathcal{A}^{+\,*}_n \boldsymbol{V}^{++} \mathcal{A}^+_n + \mathcal{A}^{+\,*}_n \boldsymbol{V}^{+-} \mathcal{A}^-_n + \mathcal{A}^{-\,*}_n \boldsymbol{V}^{-+} \mathcal{A}^+_n + \mathcal{A}^{-\,*}_n \boldsymbol{V}^{--} \mathcal{A}^-_n
\end{aligned} \qquad (4.98)$$

where the amplitudes depend on the emitter helicities η and η' but are otherwise summed over all helicities. We realize this by first computing an open helicity summed amplitude $\mathcal{A}^\xi_n$ where the emitter polarization or spinor is missing. We then use this to obtain the amplitudes

$$\mathcal{A}^+_n = \mathcal{A}^\mu_n \epsilon^+_\mu(\tilde{p}_{ij}) \quad \text{and} \quad \mathcal{A}^-_n = \mathcal{A}^\mu_n \epsilon^-_\mu(\tilde{p}_{ij}) \qquad (4.99)$$

(for gluon emitters; analogously for fermion emitters) which are complex numbers that can be simply conjugated to obtain the corresponding $\mathcal{A}^*_n$. This means we only calculate *one* (open) amplitude instead of two. There are three cases to consider for the spin–correlation matrices which we now re-write into a form which makes use of the amplitudes in equation (4.99):[8]

- The splittings where the emitter parton is a quark are proportional to $\delta_{\eta\eta'}$. The above sum then trivially reduces to

$$\mathcal{D} \propto \sum_{\eta,\eta'} \mathcal{A}^{\eta\,*}_n \delta_{\eta\eta'} \mathcal{A}^{\eta'}_n = \mathcal{A}^{+\,*}_n \mathcal{A}^+_n + \mathcal{A}^{-\,*}_n \mathcal{A}^-_n. \qquad (4.100)$$

- In the case of gluon emitters we have one term proportional to $-g^{\mu\nu}\epsilon^\eta_\mu \epsilon^{\eta'}_\nu{}^*$. We find

---

[8]Note that these three cases have been presented before in a similar form in [41, 76].

for the full structure

$$\mathcal{D} \propto \sum_{\eta,\eta'} \mathcal{A}_n^{\rho\,*}\, \epsilon_\rho^{\eta\,*}(\tilde{p}_{ij}) \left(-g^{\mu\nu}\epsilon_\mu^\eta(\tilde{p}_{ij})\, \epsilon_\nu^{\eta'\,*}(\tilde{p}_{ij})\right) \epsilon_\sigma^{\eta'}(\tilde{p}_{ij})\, \mathcal{A}_n^\sigma, \qquad (4.101)$$

where we can replace the two left hand polarizations and the two right hand polarizations by the polarization sum, see equation (3.42). The gauge terms vanish when contracted with the amplitude and we are just left with the metric tensors:

$$\mathcal{D} \propto -\mathcal{A}_n^{\rho\,*}\, g_{\rho\mu}g^{\mu\nu}g_{\nu\sigma}\, \mathcal{A}_{n\cdot}^\sigma = -\mathcal{A}_n^{\rho\,*}\, g_{\rho\sigma}\, \mathcal{A}_n^\sigma. \qquad (4.102)$$

Using the polarization sum for $-g_{\rho\sigma}$ and gauge invariance once more, we can write

$$\mathcal{D} \propto \sum_\eta \mathcal{A}_n^{\rho\,*}\, \epsilon_\rho^{\eta\,*}(\tilde{p}_{ij})\, \epsilon_\sigma^{\eta'}(\tilde{p}_{ij})\, \mathcal{A}_n^\sigma = \mathcal{A}_n^{+\,*}\mathcal{A}_n^+ + \mathcal{A}_n^{-\,*}\mathcal{A}_n^-. \qquad (4.103)$$

- Finally, the gluon emitter has the spin correlation which is given by

$$
\begin{aligned}
\mathcal{D} &\propto \sum_{\eta,\eta'} \mathcal{A}_n^{\rho\,*}\, \epsilon_\rho^{\eta\,*}(\tilde{p}_{ij}) \left(\epsilon_\mu^\eta(\tilde{p}_{ij})\left(zp_i^\mu - \bar{z}p_j^\mu\right) \times \right.\\
&\qquad\qquad\qquad\qquad \left. \times \left(zp_i^\nu - \bar{z}p_j^\nu\right)\epsilon_\nu^{\eta'\,*}(\tilde{p}_{ij})\right) \epsilon_\sigma^{\eta'}(\tilde{p}_{ij})\, \mathcal{A}_n^\sigma \\
&= \sum_{\eta,\eta'} \mathcal{A}_n^{\eta\,*} E^\eta E^{\eta'\,*} \mathcal{A}_n^{\eta'} \\
&= \mathcal{A}_n^{+\,*} E^+ E^{+\,*} \mathcal{A}_n^+ + \mathcal{A}_n^{+\,*} E^+ E^{-\,*} \mathcal{A}_n^- + \mathcal{A}_n^{-\,*} E^- E^{+\,*} \mathcal{A}_n^+ + \mathcal{A}_n^{-\,*} E^- E^{-\,*} \mathcal{A}_n^- \\
&= \left| E^+ \mathcal{A}_n^+ + E^- \mathcal{A}_n^- \right|^2
\end{aligned}
\qquad (4.104)
$$

where we defined

$$E^+ = \epsilon_\mu^+(\tilde{p}_{ij})\left(zp_i^\mu - \bar{z}p_j^\mu\right), \qquad E^- = \epsilon_\mu^-(\tilde{p}_{ij})\left(zp_i^\mu - \bar{z}p_j^\mu\right) = E^{+\,*} \qquad (4.105)$$

which can be easily implemented in the spinor helicity formalism.

This enables us to implement the kinematical parts of the dipoles.

Implementing Color Correlations

We still have to take care of the color correlations. A general algorithm for computing the color correlations in the framework of color-flow decomposition has been detailed in [41]. However, as we already mentioned in section 3.1.4, we can avoid the computation of the color matrix in the case of leading color amplitudes and simply use the color factor $N_c^{n_g+n_q/2}$ for the corresponding squared amplitude where n_g is the number of gluons in the process and n_q is the number of quarks and antiquarks. For the real emission matrix element of electron–positron annihilation, this is given by

$$|\mathcal{A}_{n+1}|^2 \propto N_c^n \qquad (4.106)$$

where n equals the number of jets. In the case of the dipoles, we have a more complicated color structure:

$$\mathcal{D}_{ij,k} \sim \mathcal{A}_n^* \otimes \frac{\mathbf{T}_{ij} \cdot \mathbf{T}_k}{\mathbf{T}_{ij}^2} V_{ij,k} \otimes \mathcal{A}_n$$
$$\sim \mathcal{A}_n^* \otimes \mathbf{T}_{ij} \cdot \mathbf{T}_k \otimes \mathcal{A}_n, \tag{4.107}$$

where we used the fact that for leading color calculations, we only require the splittings $q \to qg, \bar{q} \to g\bar{q}$, and $g \to gg$ for which we can write $V_{ij,k} \propto \mathbf{T}_{ij}^2$ and thus this factor cancels the denominator in the above equation.[9] The color correlation can now be computed in several ways. One way is to use the color-flow basis together with the correlation operators given in [41] to determine the effects. After dropping all sub-leading color contributions, it becomes obvious that the color correlations for our electron–positron jet rates simplify to a multiplicative factor $-N_c/2$ with respect to the color factor of the uncorrelated Born amplitude, which reads symbolically:

$$\mathcal{D}_{ij,k} \sim \mathcal{A}_n^* \otimes \mathbf{T}_{ij} \cdot \mathbf{T}_k \otimes \mathcal{A}_n \sim -\frac{N_c}{2}|\mathcal{A}_n|^2 \sim -\frac{1}{2}N_c^n. \tag{4.108}$$

We do not show the computation here since it is a simple but tedious matter of reducing strings of Kronecker deltas.[10]

A Technical Cut-Off to Avoid Numerical Problems

There is one more ingredient of our implementation that has not been mentioned so far. To see its necessity, consider the strict soft limit where a parton momentum is truly zero, $p_j = 0$, or the strict collinear limit where two momenta point in the exact same direction, $p_i = \text{const} \cdot p_j$. In either of these cases any numerical calculation will come across a numerical problem because the associated propagator, i.e. the inverse invariant(s) connected to the soft or collinear poles, then gives a division by zero.

In the integration of the Born contribution, any invariants smaller than allowed by the jet definition do not appear by construction so this poses no problem.

When integration the real emission contribution, however, it is possible to come across one of these two cases. While being highly improbable since such a configuration requires very specific sets of random numbers for the phase space generator, it turns out that in longer integrations with many calls and iterations occasionally the program stops because of a division by zero. This error code can be traced back to the problem described above.

We can solve this problem by introducing a second cut off parameter $y_{\min} \ll y_{\text{cut}}$ that cuts off an event where the jet parameter of two momenta is smaller than $y_{\min}$, i.e. $y_{ij} \overset{!}{>} y_{\min} \,\forall\, (i, j)$. Note that this is an entirely unphysical procedure whose sole purpose is

---

[9]Note that the only splitting that violates the relation $V_{ij,k} \propto \mathbf{T}_{ij}^2$ is the $g \to q\bar{q}$ splitting; as mentioned before, this leads to a Born process which is sub-leading in terms of its color contribution and thus does not appear in leading color electron–positron computations.

[10]The interested reader can find all the necessary details to perform these calculations in [36, 41]. Note that a slightly different argumentation with the same outcome has been presented in [92].

to solve the numerical problem discussed above. Hence, we have to ensure that all physical results that we produce are *independent* of the parameter y_{min}. It turns out that the choice

$$y_{\text{min}} = 10^{-10} y_{\text{cut}} \qquad (4.109)$$

is small enough to not alter the numerical results and at the same time ensure that we circumvent the division by zero problem.

4.4 Checks and Analysis

Developing a complex numerical code such as the one we described in the previous chapters requires extensive testing and verification with known results in order to be able to provide reliable results. We will present checks and analyses at several points in this thesis. After describing each helicity method and the corresponding subtraction scheme, we verify that our subtraction terms work and we discuss some properties of the method with respect to the *VEGAS* integration. A comparison of the different helicity methods and related analyses are presented in chapter 8 where we also discuss actual numerical results of our integrations.

In this section, we present checks and results for helicity summation. We will verify that our implementation of the Catani–Seymour terms works as desired and we will analyze the performance of the phase space generator described in section 3.4.1 with respect to the *VEGAS* algorithm. Note that the basic algorithms for computing tree-level amplitudes have already been analyzed and optimized in detail in [36]. Since only minor modifications have been made to enable the calculation of electron–positron annihilation amplitudes which do not affect the general results, we do not repeat any analyses here.

Checks of the Subtraction Terms

There are two ways of checking the correctness of the subtraction terms and their implementation. The first one is to perform an actual phase space integration over the real emission contribution and observing whether it converges as expected. At this point, we only state that we have performed this check for up to six jets and we observe the desired behavior. We will return to this check in chapter 8 where we also compare the results obtained with different helicity methods.

However, one cannot rely on this check alone since non-converging integrations sometimes wrongly appear to give convergent results. Therefore, we implemented two further checks that concern themselves with the behavior of the matrix elements in the soft and collinear limits.

We saw before that the unsubtracted real emission amplitude scales like $1/\lambda^2_{\text{soft}}$ or $1/\lambda^2_{\text{coll}}$ in the respective limits which gives a divergent result. Applying the dipole subtraction, we reduce this to $1/\lambda_{\text{soft}}$ and $1/\lambda_{\text{coll}}$ which is integrable. This behavior can be investigated by using the soft and collinear phase space generators discussed in sections 3.4.2 and 3.4.3.

To this end, we chose the random numbers for both phase space generators such that they generate $(n + 1)$ momenta which describe n jets for all values in the ranges $[\lambda_{\text{soft}}^{\min}, \lambda_{\text{soft}}^{\max}]$ and $[\lambda_{\text{coll}}^{\min}, \lambda_{\text{coll}}^{\max}]$, given some fixed jet cut parameter y_{cut}. The parameters we used are

$$y_{\text{cut}} = 0.0006, \quad \lambda_{\text{soft}} \in [10^{-3}, 10^{-1}], \quad \lambda_{\text{coll}} \in [10^{-3}, 10^{0}]. \quad (4.110)$$

The results are shown in figure 4.3. For each limit, we show two plots. The upper plot shows the squared real emission amplitude; the gray data points show the behavior of the unsubtracted matrix element while the red data points show the fully subtracted integrand including the sum over all dipoles. Each of these data sets was fitted using the function

$$|\mathcal{A}_{n+1}|^2(\lambda) = a \cdot \lambda^x + b \quad (4.111)$$

where x is the slope whose fit result is given inside the plots. Note that these fits are only meant as a rough check of the slope. As one can see, the subtraction obviously works well in both limits. In the soft limit, we can even observe that the integrable remainder proportional to $1/\lambda_{\text{coll}}$ is very small so that the slope tends towards a constant.

As a further measure to verify the subtraction, we added the lower plots for each limit. They display the ratio of the subtraction term, i.e. the sum over all dipoles, and the unsubtracted real emission amplitude. As the plots show, this ratio tends to one when approaching the soft or collinear limit, meaning that the numerical values are identical up to a few digits. Note that this ratio can help identify wrong factors inside the dipole contribution. If one forgot a coupling constant in the implementation, for example, the ratio would approach this factor instead of one while the slopes for both data sets in the upper plots would be −2.

Judging from figure 4.3, we can say that the Catani–Seymour subtraction works and is correctly implemented.

Analysis of the Phase Space Integral

We have performed extensive phase space integrations to test both the Born contribution and the real emission contribution with respect to the *VEGAS* algorithm. We do not present any explicit results here, this will be done in chapter 8 where we compare the different helicity methods. Let us merely state that we have verified that the numerical results of the Born contribution agree with results published in [24]. Since we have not implemented code for virtual corrections, we cannot compare any full next–to–leading order cross sections or jet rates. Nevertheless, an independent implementation of the Catani–Seymour subtraction has been performed in parallel by C. Schwan [93] which confirms the numerical values of our next–to–leading order results.

Let us discuss the analyses we performed. One of the free parameters of the *VEGAS* algorithm is the number of bins that is used per integration variable to realize the adaptable grid. The obvious lower limit of one bin per dimension is the case of "classical" Monte Carlo integration, often called *plain* Monte Carlo, where no adaptation to the integrand takes
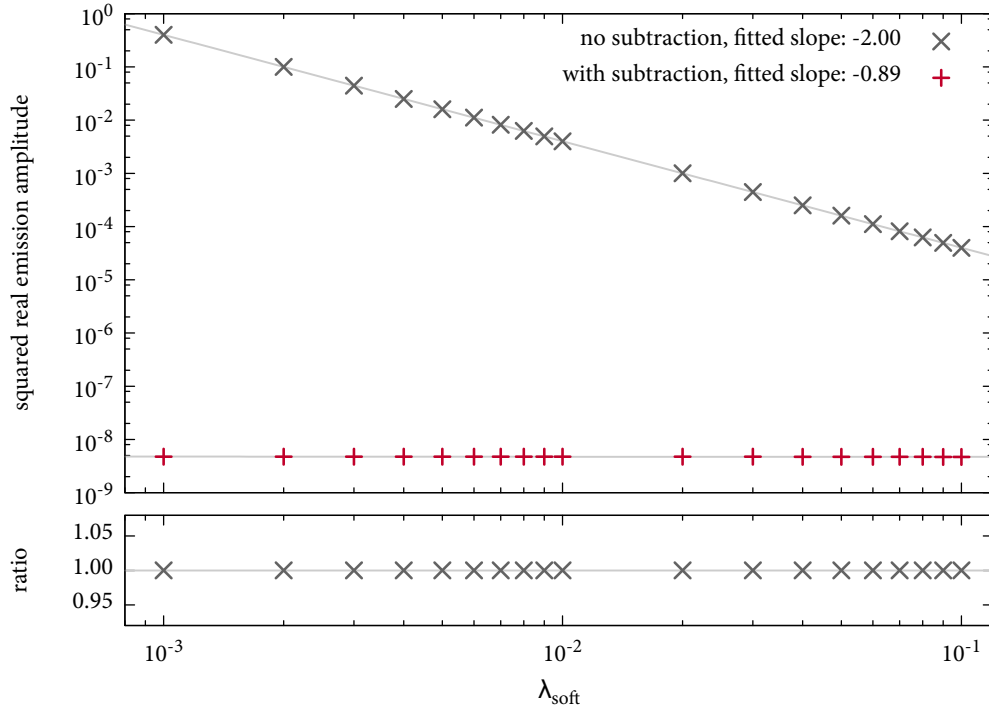
(a) Soft limit for $e^-e^+ \to qg_1g_2g_3g_4g_5g_6\overline{q}$; The unresolved soft gluon is g_1.
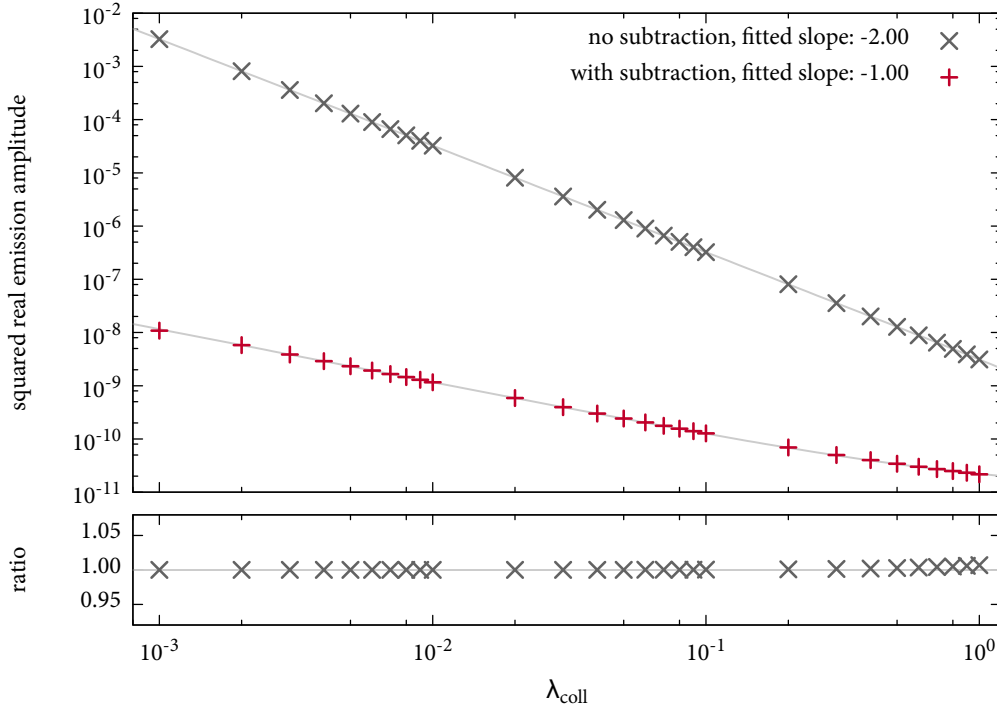
(b) Collinear limit for $e^-e^+ \to qg_1g_2g_3g_4g_5g_6\overline{q}$; The collinear pair is $(g_6, \overline{q})$.

Figure 4.3: Soft (a) and collinear (b) behavior of the unsubtracted and subtracted real emission amplitudes for helicity summation. The lower plots show the absolute ratio of the unsubtracted matrix element and the subtraction term; the expectation (gray line) is approximately 1.

place. There is no upper limit, on the other hand. The original *VEGAS* publication [70] gives a typical number of 50 to 100 bins which *"[...] is limited by the computer storage space available [...]"*. This limit is obviously an artifact of the time of publication, 1977, and is obsolete nowadays: we have performed integrations with up to 1024 bins where no excessive memory consumption could be noticed. In principle, the boundaries of each bin have to be stored as a floating point number. Assuming an integration with d dimensions, b bins per dimension, and the use of eight byte double-precision floating point variables results in a memory consumption of

$$VEGAS \text{ memory consumption} = b \cdot d \times 8 \text{ byte} = \frac{8bd}{1024} \text{ kB} = \frac{bd}{128} \text{ kB} \qquad (4.112)$$

purely for the storing the grid. Assuming $d = 30$ integration dimensions which acts as an upper limit for all integrations that we performed, we obtain a total memory consumption of 240 kB which is negligible on modern computers.

Thus, the question arises which choice for the number of bins should be made. hep-mc [74] allows for an arbitrary choice in terms of a parameter of the *VEGAS* call. All other codes that the author is aware of use fixed, hard-coded values; for example Cuba [72,73] uses 128 bins while the GSL implementation [94] uses only 50 bins.

We performed several integrations with different numbers of bins. The results for the Born integration are shown in figures 4.4 and 4.5, the results for the real emission contribution are shown in figures 4.6 and 4.7. We first discuss the Born results. Plot 4.4 shows an integration for $e^-e^+ \rightarrow 6$ jets where each sub-plot was created with the indicated number of bins. The plots show how the *VEGAS* estimate and its error progress in the course of a 10 hour long integration. All results are normalized to the weighted average result of all plots after 10 hours of integration. It is immediately obvious that the results with 32 and more bins agree well with the weighted average and are similar in their overall behavior, while the result with one bin underestimates the other results by more than 11 standard deviations. This immediately proves the necessity of the *VEGAS* adaptation. When analyzing the behavior for different numbers of jets (not shown here), a similar picture emerges where the one bin result typically shows the most fluctuations and by far the biggest error. The underestimation only becomes obvious starting from four jets, and increases with growing number of jets. This is due to the fact that the phase space volume grows and gets more complicated with increasing numbers of particles and thus increasing integration dimensions; *VEGAS* adapts well in the sense that it finds those regions which give the largest contributions to the integrand. Without *VEGAS* the algorithm pokes randomly into the pictorial haystack, while not even looking for the needle. Figure 4.4 does not make it easy to see whether any given number of bins is preferred by the program. Therefore, another plot is shown on the left hand side in figure 4.5 which is made up of the same data, but this time we look at the development of the relative Monte Carlo error for the different bin numbers. Obviously, the one bin result is far worse than all the others—as was obvious from the previous plot. Among the other results, 32 bins stand out as a winner while it 1024 bins seem to be least effective. We can explain this behavior by looking at the
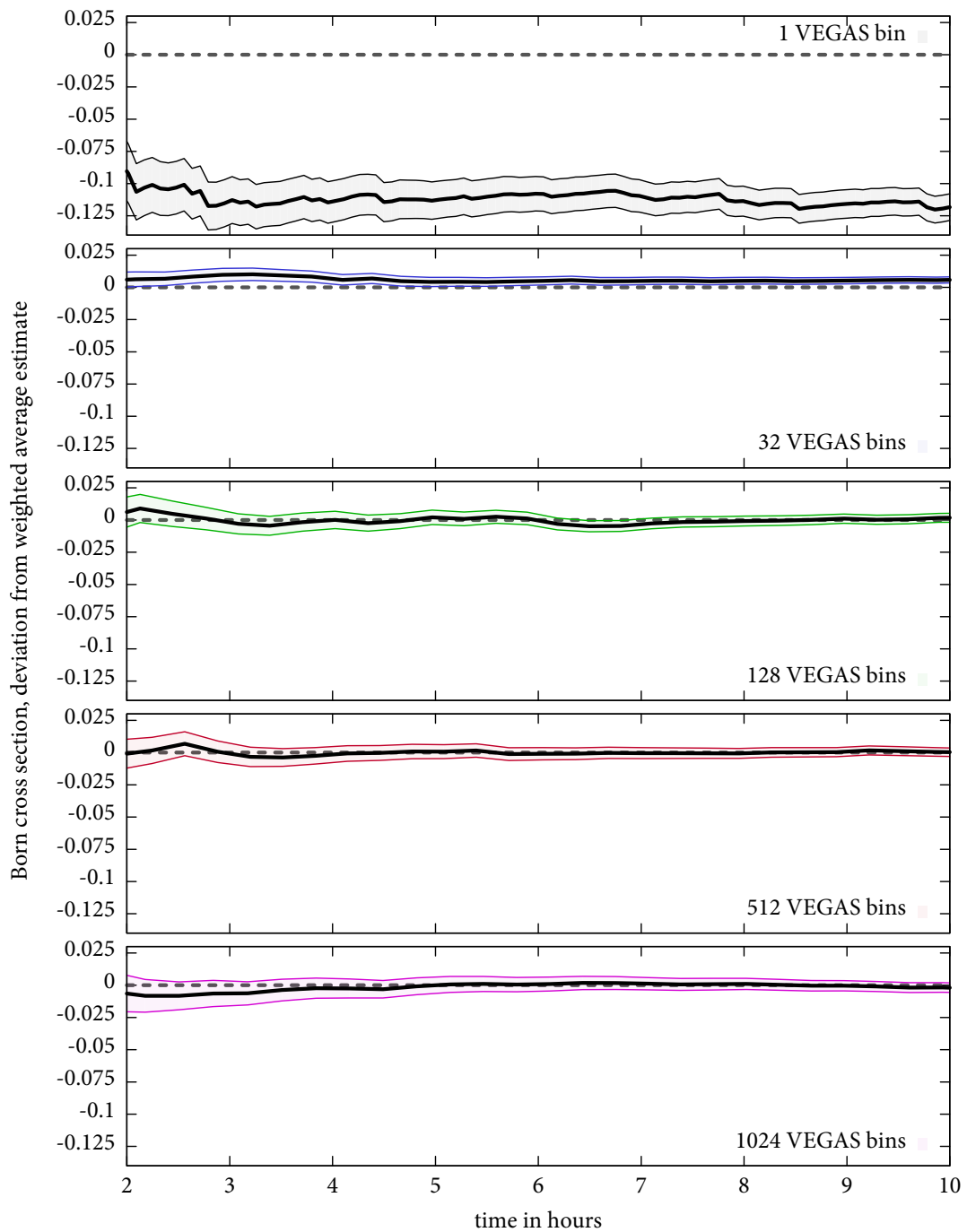
Figure 4.4: The graphs show the progress of an integration for the Born contribution to the process $e^- e^+ \rightarrow 6$ jets. Each plot shows the Monte Carlo estimate (thick black line) and a colored error band which displays the corresponding Monte Carlo error (i.e. one standard deviation) after the time given on the horizontal axis. The vertical axis is normalized to the weighted average of all bin numbers after 10 hours integration time (i.e. the average of all values at the right ends of the plots). The result with one *VEGAS* bin strongly underestimates all other integrations, making *VEGAS* a necessity. There is no visible difference between bin numbers starting from 32 bins.
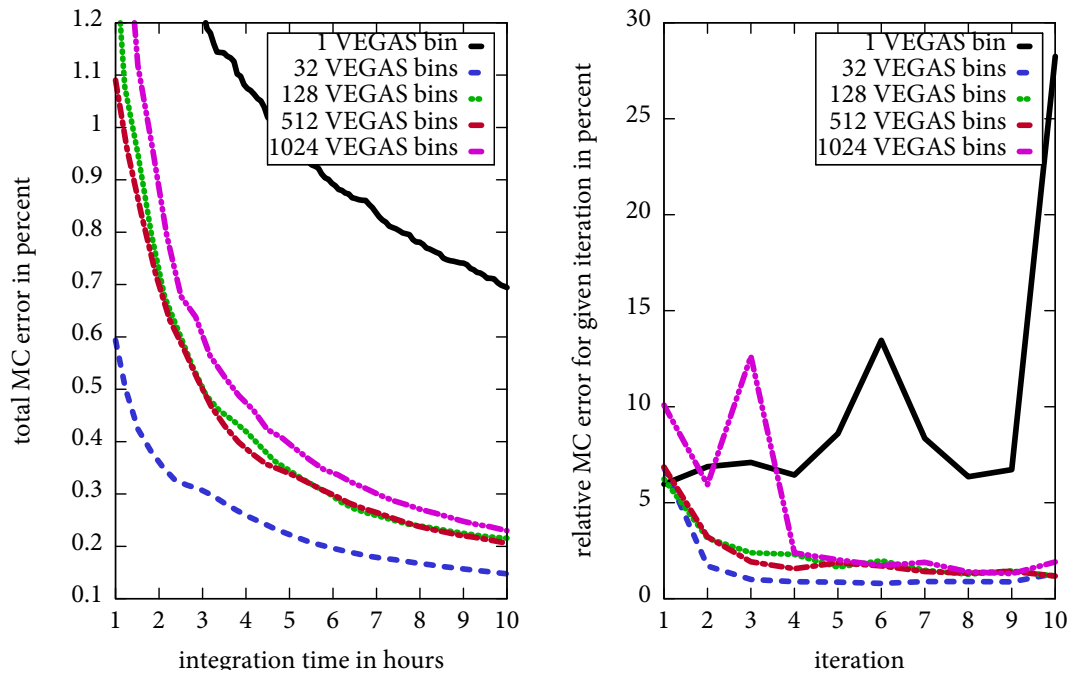
Figure 4.5: Both plots display the same data as figure 4.4, but here the errors are examined. The left hand plot shows the cumulative relative errors after the given integration time. The right hand plot shows the local errors for each iteration; all bin numbers starting from 32 bins show a good adaptation and thus a reduced error after only three to five iterations.

right hand side of the figure: it shows the relative Monte Carlo error again, but this time not the accumulated error after a given time, but the relative error for the given iteration. In the first iteration, where the grid has not yet adjusted and which basically acts as a plain Monte Carlo, the error should be large while one would expect the grid to adjust and thus the error to become smaller in the following iterations until it reaches a roughly asymptotic value. This is clearly the case in the right hand side of figure 4.5 where all data lines approach an asymptotic value after approximately four to five iterations. Note that the 32 bit result becomes especially small very quickly, while the 1024 bin result apparently hits a large integration region in the third iteration that was missed during the first two. This is the reason why the 1024 bin result has a slightly worse behavior than the others. The right hand plot also shows nicely that without any grid adaptation, the algorithm is subject to whatever phase space point it comes across, resulting in strongly varying errors per iteration that are in general much bigger than with adaptation.

For other numbers of jets, the results look similar, while most checks that we performed show even less distinguishable patterns for the different graphs of 32 to 1024 bins. Thus, we conclude that for helicity summation, the actual number of bins is not significant provided

that the grid adapts.[11]

Let us now turn to the real emission contribution. Figures 4.6 and 4.7 show plots for $e^-e^+ \rightarrow 4$ jets which corresponds to five QCD partons in the final state. Since we have established already that one bin or plain Monte Carlo yields inaccurate and slowly converging results, we do not show the results for one bin here, but for eight bins instead. In this way, we can investigate the effect of a sparsely populated grid on a complex integrand function. Other than the change from one to eight bins, the plots are identical. Figure 4.6 shows again that the results from 32 to 1024 bins agree well. The eight bin result, however, has a visibly larger error band than all other plots. The left hand side of figure 4.7 supports this statement. Judging from this picture, it is tempting to declare the higher numbers of bins, i.e. 512 and 1024, as winners. However, a look at the error per iteration on the right hand side shows that while we clearly see a good adaptation to the grid after four or five iterations once more, the fluctuations afterwards are much higher than in the Born case. This is caused by the much more complicated structure of the real emission phase space that we integrate over. A global look at other numbers of jets (again not shown here) reveals a similar picture.

To analyze the adaptation to the grid further, we also visualized the *VEGAS* grids in the two plots shown in figure 4.8. These show the grid configuration after six integration iterations. The Born graph 4.8(a) shows all eleven integration dimensions for $e^-e^+ \rightarrow 5$ jets while the real emission graph 4.8(b) shows all eleven integration dimensions for $e^-e^+ \rightarrow 4$ jets. Recall that the first two variables, indicated by p_1 and p_2 determine the solid angle of the initial back to back momentum configuration while the next three variables (p_3, p_4 and p_5, etc.) add another soft parton in between the previous ones. Of the three variables for the soft momenta, the first two determine the invariants between one existing momentum and the newly inserted soft parton. The third variable determines the angle.[12]

In the Born case, we can see that all angular variable are more or less unaffected, i.e. the grid only adapts a little. The variables determining the invariants, however, mostly show a strong trend towards the left hand side which indicates zero as the value of the random number. This is in agreement with our earlier statement that those regions closest to the soft and collinear limits exhibit the largest matrix elements, which is what *VEGAS* adapts to; small invariants indicate soft or collinear partons, in the end. Note that this also proves that the phase space generator we use is well suited for an integration with *VEGAS*.

The real emission grid shows a similar overall performance with the same variables p_i tending to zero and thus small invariants. Across all variables, however, one can also see apparently randomly distributed peaks where *VEGAS* bins are concentrated—this emphasizes the complexity of the real emission integration once more.

In the following chapters, we will encounter similar plots for other helicity methods; they all come with at least one additional integration dimension for the helicity. We can

---

[11]The detailed behavior of the integration also depends on the seed for the random number generator which was chosen to be a random number itself in the plots, thus mimicking the typical use of an event generator where the user does not necessarily want to deal with technical details such as seeds.

[12]This was discussed in detail in section 3.4.1.
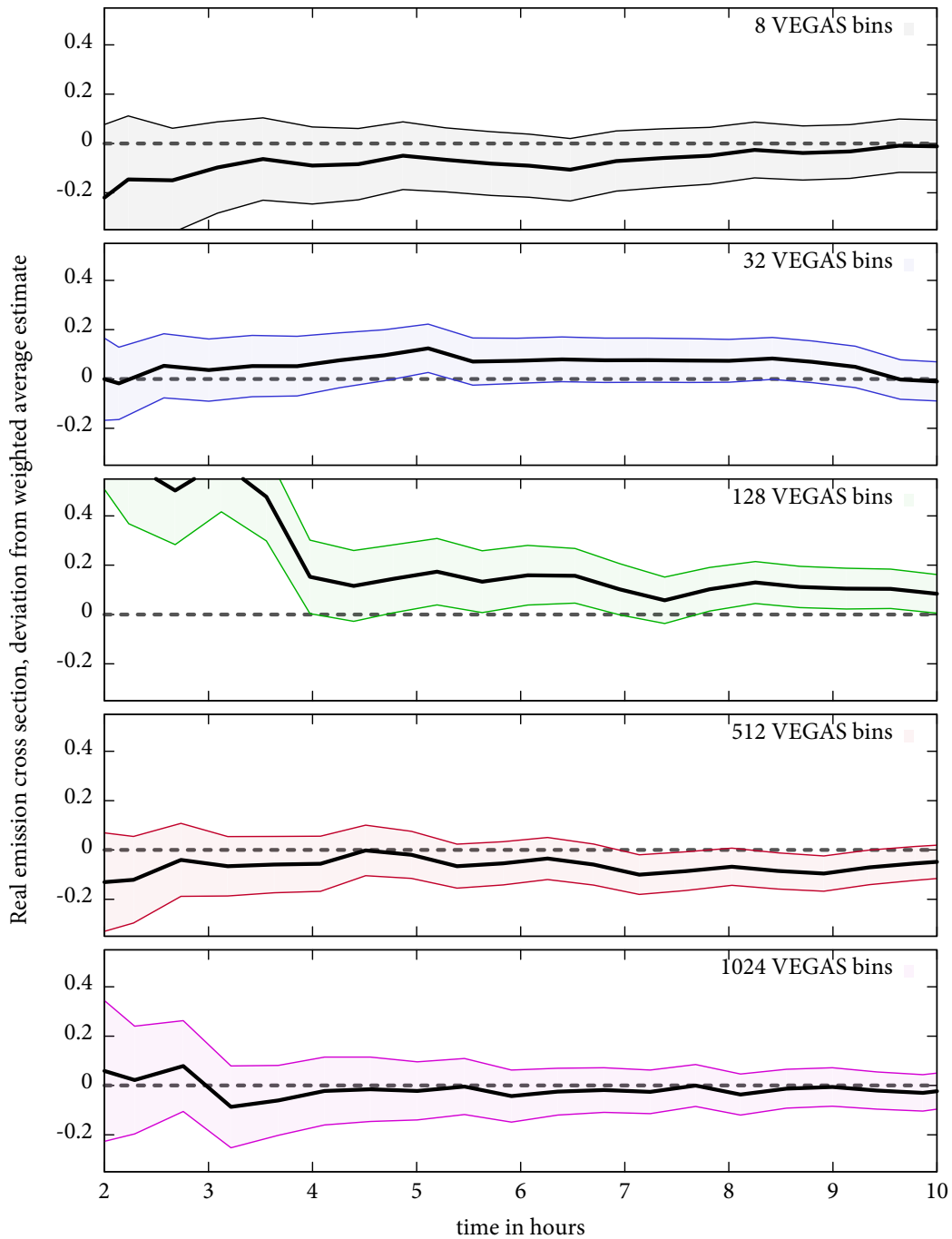
Figure 4.6: This plot presents results for electron–positron annihilation to four jets for the real emission contribution similarly to figure 4.4. All results agree well while the eight bin result has a visibly bigger error. The 128 bins result obviously faces some difficulties below four hours; note that this is not a generic problem, but an artifact of the specific run (seed for the random number generator).
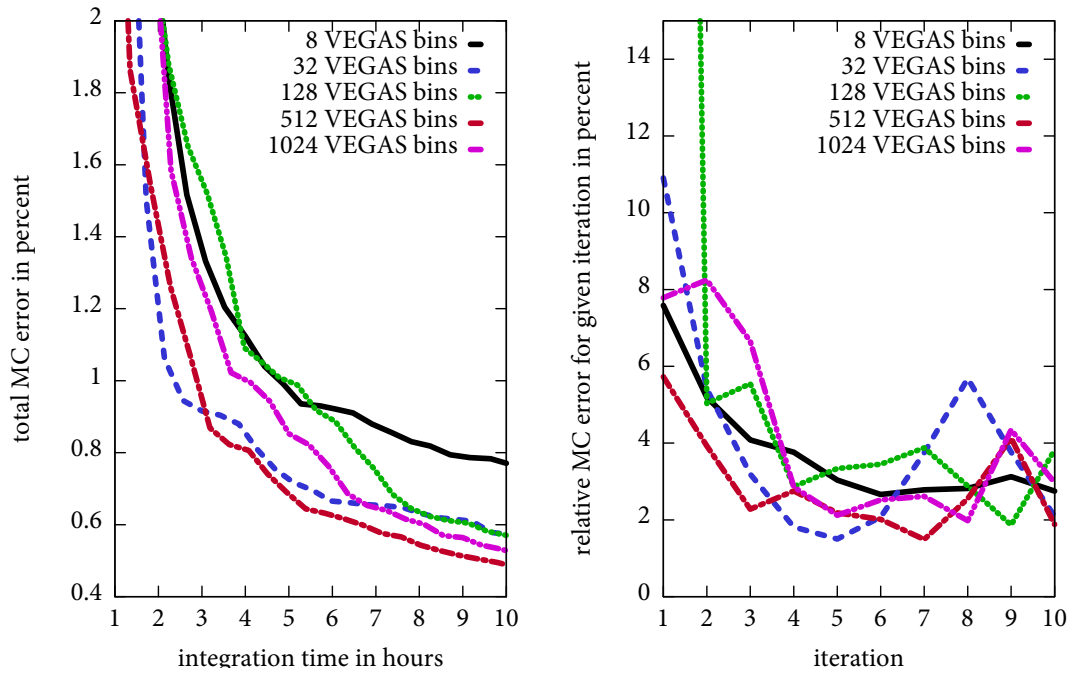
Figure 4.7: Similar to figure 4.5, these graphs present the errors to the real emission results from figure 4.6. The general picture is similar to the Born result, while there are more fluctuations, a result of the more complicated phase space structure.

use the results from this section for general comparison, but especially also to identify any changes in the phase space adaptation caused by the changes in helicities.
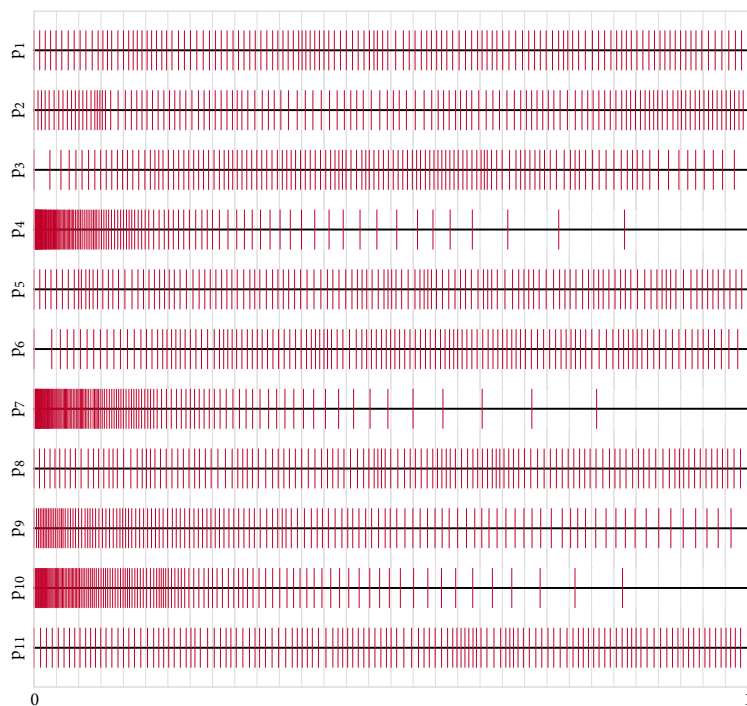
(a) Born 5 Jets
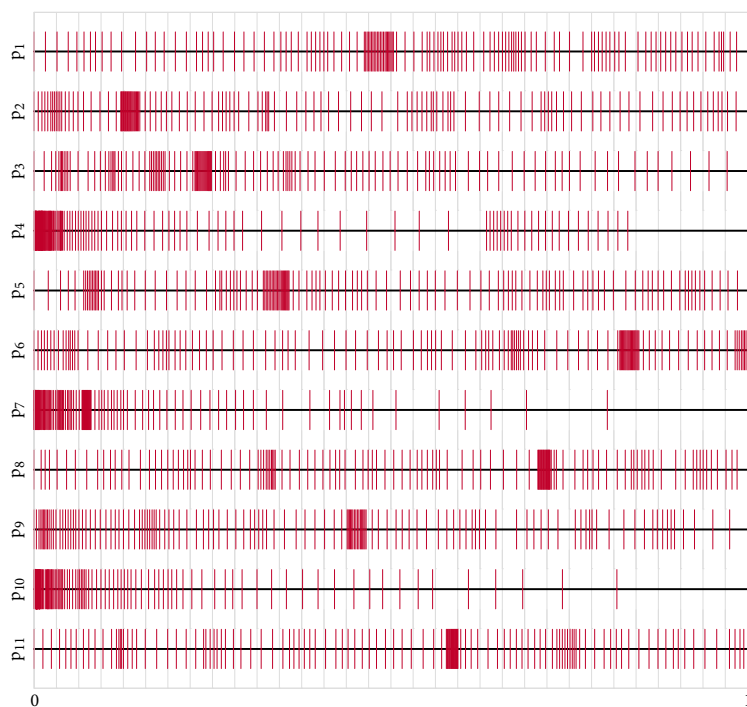
(b) Real emission with 4 Jets

Figure 4.8: Visualization of the *VEGAS* grid for 128 bins. Each row corresponds to one phase space dimension. The red bars mark the border between two adjacent bins. Both plots show the same basic structure where the grid adapts well to the invariants. The real emission grid shows some apparently randomly distributed peaks around which the grid is concentrated which explain the fluctuations observed in figure 4.7.

Helicity Sampling

5

In the previous chapter, we discussed the classical way of dealing with helicities in numerical programs. While conceptually simple to realize, the method of summing up helicity amplitudes comes with an inherent $\mathcal{O}\left(2^n\right)$ growth where n is the number of external particles. Especially for high particle multiplicities and in the evaluation of next–to–leading order observables, this can quickly become a roadblock: the subtraction method requires one to evaluate in general $\mathcal{O}\left(n^3\right)$ dipoles—meaning additional n–parton squared amplitudes—plus the $(n+1)$–parton real emission amplitude, all of which have to be summed over the helicities.

This is where this thesis steps in: we find and analyze methods that reduce the overhead created by the helicity summation. All methods that we present are governed by one central idea.

This idea is to turn the sum over all helicities into a Monte Carlo integral which can be combined with the existing phase space integration such that we obtain a single high dimensional integral. There are two ways to accomplish this. One is to re-interpret the sum as an expectation value which can be computed by a Monte Carlo integral. The second is to not use helicity eigenstates, but re-parameterizations that depend on continuous variables that have to be integrated over in order to obtain the helicity summed result. All methods effectively remove the helicity sum locally, leaving just one squared helicity amplitude to be evaluated per phase space point and thus reducing the $\mathcal{O}\left(2^n\right)$ growth to $\mathcal{O}\left(1\right)$. While this sounds like an enormous speed-up, we do not get anything for free. By re-writing the helicity sum into an integral, we add additional dimensions to the already high-dimensional Monte Carlo integration (how many dimensions depends on the realization of the method). This increases the volume of our integration space which means we need to throw in more points to cover it reasonably well. We will investigate the trade-off later on.

This chapter presents the simplest approach to getting rid of the helicity sum which we call *helicity sampling*. This approach has been used for a long time, although it has not been properly described in the literature, to the best of our knowledge. We first present the general idea and two different ways of implementing it in practice. Then we analyze

the compatibility with the dipole subtraction and present some necessary modifications that have already been published in [95]. Finally, we perform a similar analysis as in the previous chapter.

5.1 Gambling with Helicity Configurations

Helicity sampling is based on the first idea mentioned above, re-interpreting the helicity sum as an expectation value. Suppose we want to evaluate the sum of a function $f(x)$ over all elements x of a discrete set of values $\mathcal{X}$,

$$A = \sum_{x \in \mathcal{X}} f(x). \tag{5.1}$$

Now let X be a random variable such that each element in $\mathcal{X}$ occurs with equal probability $p(x \in \mathcal{X}) = p$. We choose $p(x)$ such that $\sum_{u \in X} p(u) = |\mathcal{X}| \, p = 1$, where $|\mathcal{X}|$ is the cardinality of the set $\mathcal{X}$. Then we can expand the original sum as follows [69]:

$$\sum_{x \in \mathcal{X}} f(x) = \frac{1}{p} \sum_{x \in \mathcal{X}} f(x) p = \frac{1}{p} E\big[f(X)\big] \tag{5.2}$$

Note that $p = p(x)$ acts as a probability function here, which enables us to write the sum as an expectation value. Also note that $1/p$ is simply the number of terms in the sum (see remark on cardinality above). The expectation value $E\big[f(X)\big]$ can then be performed in terms of a Monte Carlo integral.

The next step is to apply this to the sum over all helicities of the external particles. In the following we are going to present two ways of doing this.

5.1.1 n–Dimensional Sampling

The most direct and intuitive way to use equation (5.2) with the helicity sum is to turn each of the n sums in equation (4.1) into a separate Monte Carlo expectation value and hence perform it as a Monte Carlo integral. This amounts to a straight forward generalization of equation (5.2) from one to n dimensions. The probability function per dimension is $p = 1/2$ since each particle takes one of two discrete helicity eigenstates. For n dimensions we thus end up with $p_1 p_2 \cdots p_n = p^n = 1/2^n$.

The way we perform the summation can be written in integral form as follows:

$$\sum_{\lambda_1, \ldots, \lambda_n} |\mathcal{A}_{\lambda_1 \ldots \lambda_n}|^2 = 2^n \int_{[0,1)^n} \mathrm{d}^n u \, |\mathcal{A}_{\lambda_1(u_1) \ldots \lambda_n(u_n)}|^2. \tag{5.3}$$

When evaluating the amplitude, we use the following parameterization for polarizations:

$$\epsilon_\mu^{\lambda(u)}(p) = \begin{cases} \epsilon_\mu^-(p) & \text{for } u \in \big[0, 1/2\big) \\ \epsilon_\mu^+(p) & \text{for } u \in \big[1/2, 1\big). \end{cases} \tag{5.4}$$

In practice, we add n dimensions to the Monte Carlo integral, each of them resulting in an additional random number $u \in [0,1)$. We then map this random number to a discrete number and extract the corresponding helicity eigenstate by the prescription (5.4). Effectively, we sample one helicity amplitude with randomly chosen helicity eigenstates per phase space point, hence the name helicity sampling.

5.1.2   One–Dimensional Sampling

A second way to realize the helicity sum as a Monte Carlo integral is to re-interpret the helicity sum as follows:

$$\sum_{\lambda_1,\dots,\lambda_n} |\mathcal{A}_{\lambda_1\dots\lambda_n}|^2 = \sum_{i=0}^{2^n-1} |\mathcal{A}_{\Lambda(i)}|^2. \tag{5.5}$$

The above is a simple technical re-write which introduces the map

$$\Lambda : [0, 2^n) \to \mathfrak{H}_n. \tag{5.6}$$

Essentially, this means reinterpreting the sum over all helicities as one single sum over the 2^n different helicity configurations by assigning a unique (but arbitrary) number to each configuration. Note that the probability density is given by $p = {}^1\!/_{2^n}$ since the set $\mathfrak{H}_n$ has 2^n discrete elements. This is the same as the overall probability density of the n–dimensional variant.

In terms of a Monte Carlo integral, we find

$$\sum_{\lambda_1,\dots,\lambda_n} |\mathcal{A}_{\lambda_1\dots\lambda_n}|^2 = 2^n \int_0^1 \mathrm{d}u \, |\mathcal{A}_{\Lambda(u\cdot 2^n)}|^2, \tag{5.7}$$

which is merely a one-dimensional integral. To obtain the proper argument for Λ we multiply the random number by 2^n and truncate the non-integer part so that we end up with a value from zero to $2^n - 1$. How do we realize the map Λ? It turns out that this can be done in a simple and efficient way provided that all particles have only two helicity states. Let us denote the truncated integer value of $u \cdot 2^n$ by i. We now make use of the binary representation of i which is inherent to computers and therefore easily and cheaply accessible: each number $i \in [0, 2^n)$ has n binary digits at maximum (or less in which case we interpret it as an n-digit number with leading zeros) where each digit is either zero or one. If we now assign each digit to one particle, we can re-interpret the digit as negative (zero) or positive (one) helicity and thus choose the appropriate polarization vector for each particle. An example for four external particles is given in table 5.1.

Note that while the method of n–dimensional sampling has been mentioned in the literature and in personal discussions with other physicists, one–dimensional sampling represents a new development which has not been used or at least published before, to the best of our knowledge.

$i = 2^n \cdot u$ (truncated)		helicity	$i = 2^n \cdot u$ (truncated)		helicity
decimal	binary	configuration	decimal	binary	configuration
0	0000	$(-,-,-,-)$	8	1000	$(+,-,-,-)$
1	0001	$(-,-,-,+)$	9	1001	$(+,-,-,+)$
2	0010	$(-,-,+,-)$	10	1010	$(+,-,+,-)$
3	0011	$(-,-,+,+)$	11	1011	$(+,-,+,+)$
4	0100	$(-,+,-,-)$	12	1100	$(+,+,-,-)$
5	0101	$(-,+,-,+)$	13	1101	$(+,+,-,+)$
6	0110	$(-,+,+,-)$	14	1110	$(+,+,+,-)$
7	0111	$(-,+,+,+)$	15	1111	$(+,+,+,+)$

Table 5.1: Illustration of the assignment of helicity configurations based on integers using the binary representation. This method is fast and efficient and used for one–dimensional sampling.

5.2 Real Emission and Dipoles for Helicity Eigenstates

Having discussed the general method that can be applied to the Born contribution, let us now turn to next–to–leading order. The virtual contributions generally pose no problem since their structure with respect to the external particles is identical to the Born contribution. As we saw in the previous chapter, the real corrections and the subtraction terms cannot be dealt with as easily.

The classical dipole formalism as discussed in the last section was designed with helicity summation in mind. Figure 5.1 shows this based on the example of the dipoles for two jet real emission in electron–positron collisions. In our previous discussion, the dipoles $\mathcal{D}_{ij,k}$ were constructed such that they match the soft and collinear limits of the $(n+1)$–parton amplitude which were based on the helicity sum over partons i and j. With helicity sampling, our $(n+1)$–parton real emission amplitude is based on *helicity eigenstates* for all external particles. If we use the dipoles by Catani and Seymour, we will subtract poles for the *sum over all helicity configurations*. Doing so will result in double counting poles or even subtracting poles that are not present in the real emission amplitude.

The question that we will ask ourselves in this section is how can we use the method of *helicity sampling* together with subtraction. Obviously, we require expressions for the soft and collinear limits of $(n+1)$–parton amplitudes that depend on the helicity eigenstates of the partons and not their helicity sum. Fortunately, these terms have already been derived by Czakon, Papadopoulos and Worek in [95]. As it turns out they are not that different from what we presented in the previous section. The remainder of this section is devoted to presenting these results and their difference to the original Catani–Seymour formulation.

Note that we directly present the massive dipoles which approach the massless limit smoothly, in the same way as the classical dipole formalism. Also note that we do not distinguish here between n–dimensional and one–dimensional sampling since this affects only the realization of the sampling, not the formulation of the subtraction terms.
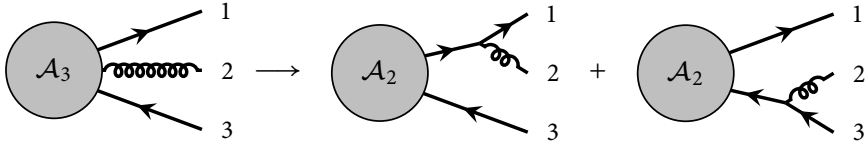
(a) $\quad\displaystyle\sum_{\{\lambda\}_3} |\mathcal{A}_3|^2 \qquad\qquad \sum_{\lambda_3} |\mathcal{A}_2|^2 \otimes V_{12,3} \qquad \sum_{\lambda_1} |\mathcal{A}_2|^2 \otimes V_{32,1}$

(b) $\quad |\mathcal{A}_3^{\{\lambda\}_3}|^2 \qquad\qquad |\mathcal{A}_2^{\lambda_3}|^2 \otimes V_{12,3}(\lambda_1, \lambda_2) \quad |\mathcal{A}_2^{\lambda_1}|^2 \otimes V_{32,1}(\lambda_2, \lambda_3)$

Figure 5.1: Example for the dipole contributions to the exclusive cross section $e^- e^+ \to 2$ jets. The left hand side is the real matrix element. The gluon (index 2) is the inserted parton (otherwise the corresponding dipole $\mathcal{D}_{13,2}$ would be made up of the amplitude for the process $e^- e^+ \to gg$ which is not physically possible at tree-level). Thus, we find two dipoles (right hand side). The equations in line (a) show the corresponding expressions for helicity summed amplitudes, as treated in section 4.2 while line (b) shows those for helicity eigenstates.

5.2.1 The Soft Limit for Helicity Eigenstates

In section 3.2.2, we derived the general singular behavior of an n–parton amplitude with one added soft gluon. By summing over all helicities, especially the helicity of the soft gluon, we showed in section 4.2.1 that the contraction of the soft gluon's polarization vectors $\epsilon_\mu(p_j)$ with the eikonal currents $J^\mu(p_j)$ resulted in the direct contraction of the eikonal currents,

$$J^{\mu\dagger}\left(\sum_{\lambda_j}\epsilon_\mu^*(p_j)\epsilon_\nu(p_j)\right)J^\nu = -J^{\mu\dagger}J_\mu, \qquad (5.8)$$

due to current conservation.

One can easily show that the use of helicity eigenstates yields the same result up to a factor [95]. In the case of definite helicity eigenstates, the above equation becomes

$$J^{\mu\dagger}\epsilon_\mu^{\pm*}\,\epsilon_\nu^\pm\,J^\nu = J^{\mu\dagger}\epsilon_\mu^\mp\,\epsilon_\nu^\pm\,J^\nu \qquad (5.9)$$

where we used the fact that the parameterization we use for helicity eigenstates, equation (3.8) on page 27, obeys $\epsilon^{\pm*} = \epsilon^\mp$. In the second line, the hermitian conjugate of the current merely has a symbolic meaning since the kinematic part is given by real-valued four-momenta and the color matrices are hermitian. Thus the whole second line is in fact hermitian and we can write

$$\begin{aligned}
J^{\mu\dagger}\left(\sum_\lambda\epsilon_\mu^{\lambda*}\,\epsilon_\nu^\lambda\right)J^\nu &= J^{\mu\dagger}\epsilon_\mu^{+*}\,\epsilon_\nu^+\,J^\nu + J^{\mu\dagger}\epsilon_\mu^{-*}\,\epsilon_\nu^-\,J^\nu \\
&= J^{\mu\dagger}\epsilon_\mu^-\,\epsilon_\nu^+\,J^\nu + J^{\mu\dagger}\epsilon_\mu^+\,\epsilon_\nu^-\,J^\nu \\
&= 2\,J^{\mu\dagger}\epsilon_\mu^{\pm*}\,\epsilon_\nu^\pm\,J^\nu.
\end{aligned} \qquad (5.10)$$

In conclusion, we find the identity

$$J^{\mu\dagger}\epsilon_\mu^{\pm*}\,\epsilon_\nu^{\pm}\,J^\nu = \frac{1}{2}J^{\mu\dagger}J_\mu. \tag{5.11}$$

Thus, the soft limit for helicity eigenstates is equal to the helicity summed limit, equation (4.59), up to a factor two and the sums over helicities:

$$\lim_{\lambda_{\text{soft}}\to0}\left|\mathcal{A}_{n+1}^{\{\lambda\}_{n+1}}\right|^2$$

$$= -4\pi\alpha_s\mu^{2\epsilon}\sum_{\substack{i=1\\i\neq j}}^{n+1}\frac{1}{p_ip_j}\sum_{\substack{k=1\\k\neq i\neq j}}^{n+1}\left(-\frac{m_i^2}{2p_ip_j}+\frac{p_ip_k}{p_ip_j+p_kp_j}\right)\mathcal{A}_n^{\{\lambda\}_n*}\,\mathbf{T}_i\mathbf{T}_k\,\mathcal{A}_n^{\{\lambda\}_n} \tag{5.12}$$

where we indicated the dependence on the helicity eigenstates by the superscripts $\{\lambda\}_{n+1/n}$.

5.2.2 The (Quasi-)Collinear Limit for Helicity Eigenstates

In the (quasi-)collinear limit for amplitudes with helicity eigenstates, we also proceed in the same fashion as we did before. To include masses from the beginning, we use the massive Sudakov parameterization from equation (4.61) and scale the masses together with λ_{coll}, as described in section 4.2.5.

The squared amplitude in the collinear limit then reads

$$\lim_{\lambda_{\text{coll}}\to0}\left|\mathcal{A}_{n+1}^{\{\lambda\}_{n+1}}\right|^2$$

$$= \frac{4\pi\alpha_s\mu^{2\epsilon}}{(p_i+p_j)^2-m_{ij}^2}\sum_{\eta,\eta'}\mathcal{A}_n^{*\widetilde{\{\lambda\}}_n}(\eta)\,\mathbf{P}_{(ij)\to i+j}^{\eta\eta'}(\lambda_i,\lambda_j)\,\mathcal{A}_n^{\widetilde{\{\lambda\}}_n}(\eta'). \tag{5.13}$$

Therein, $\mathbf{P}_{(ij)\to i+j}^{\eta\eta'}(\lambda_i,\lambda_j)$ are helicity-dependent Altarelli–Parisi splitting kernels which not only depend on the helicities of the splitting particle (ij), but also on the helicities of the splitting products i and j which we give below. First, let us focus on the helicities that appear in the above equation. Note that the $(n+1)$–parton amplitude on the left hand side depends on the helicities of all external particles which is indicated by the superscript $\{\lambda\}_{n+1}$; this can be any one of the 2^{n+1} helicity amplitudes obtained through the helicity sampling procedure. On the right hand side, we use an unusual notation for helicities whose purpose is to stress some details on the calculation. The amplitudes have a tilde superscript $\widetilde{\{\lambda\}}_n$ which indicates the set of all helicities of the external particles without those of partons i and j,

$$\widetilde{\{\lambda\}}_n = \{(\lambda_1,\lambda_2,\ldots,\lambda_{n+1})\setminus\lambda_i,\lambda_j\}, \tag{5.14}$$

since i and j are not part of the amplitude but are included in the splitting kernels as discussed above. Furthermore, the amplitudes have the helicities η and η' of the splitting particle as extra arguments. We also find that the sum over these helicities is still present. The reason for singling out the splitting particle in this way is to stress that it is only

reasonable to replace the helicity states of *external* particles. Since the splitting parton is an *internal* parton with respect to the $(n+1)$–parton amplitude and arises from its propagator (confer figure 3.6 on page 38 and the accompanying explanations) it is mandatory to compute the propagator in full (i.e. with the summation) in order to obtain a proper result for the amplitude. In that sense it is useful to regard η and η' as parameters rather than proper helicities.

In the following, we give the spin-dependent Altarelli–Parisi splitting kernels in four dimensions[1] (first given in [95] but slightly adapted to our conventions):

$$
\boldsymbol{P}^{\eta\eta'}_{g\to gg}(\lambda_i, \lambda_j) = 2C_{\mathrm{A}}\Bigg[-g_{\mu\nu}\delta_{\eta\eta'}\left(\frac{\delta_{\eta\lambda_i}}{\overline{x}} + \frac{\delta_{\eta\lambda_j}}{x} - 2\overline{\delta}_{\lambda_i\lambda_j} \right)
$$
$$
- 2\overline{\delta}_{\lambda_i\lambda_j}\, x\overline{x}\frac{(k_\perp)_\mu (k_\perp)_\nu}{k_\perp^2} \Bigg]\epsilon^\mu_\eta \epsilon^{*\nu}_{\eta'}, \tag{5.15a}
$$

$$
\boldsymbol{P}^{\eta\eta'}_{g\to q\overline{q}}(\lambda_i, \lambda_j) = T_{\mathrm{R}}\Bigg[-g^{\mu\nu}\delta_{\eta\eta'}\overline{\delta}_{\lambda_i\lambda_j} + 4\overline{\delta}_{\lambda_i\lambda_j}\frac{k_\perp^\mu k_\perp^\nu}{(p_i + p_j)^2}
$$
$$
\delta_{\eta\eta'}\Bigg\{ \overline{\delta}_{\lambda_i\lambda_j}\left(2x\delta_{\eta\lambda_i} + 2\overline{x}\delta_{\eta\lambda_j} - 1 \right) \tag{5.15b}
$$
$$
+ \left(\frac{\delta_{\eta\lambda_i} - \overline{\delta}_{\lambda_i\lambda_j}}{x} + \frac{\delta_{\eta\lambda_j} - \overline{\delta}_{\lambda_i\lambda_j}}{\overline{x}} \right)\frac{m_i^2}{(p_i + p_j)^2} \Bigg\} \Bigg]\epsilon^\mu_\eta \epsilon^{*\nu}_{\eta'},
$$

$$
\boldsymbol{P}^{\eta\eta'}_{q\to qg}(\lambda_i, \lambda_j) = 2C_{\mathrm{F}}\Bigg[\frac{\delta_{\eta\lambda_i}\left(x^2 + \delta_{\lambda_i\lambda_j}(1-x^2) \right)}{\overline{x}} - \delta_{\eta\lambda_j}\overline{\delta}_{\lambda_i\lambda_j}\frac{m_i^2}{p_i p_j} \tag{5.15c}
$$
$$
- \left\{ \frac{\delta_{\eta\lambda_i}\delta_{\lambda_i\lambda_j} - \overline{\delta}_{\eta\lambda_i}\overline{\delta}_{\lambda_i\lambda_j}}{x} + \overline{\delta}_{\lambda_i\lambda_j}\left(\delta_{\eta\lambda_i} - \delta_{\eta\lambda_j} \right)x\frac{m_i^2}{2p_i p_j} \right\} \Bigg]\delta_{\eta\eta'}.
$$

Therein, the we applied the "bar" notation also to Kronecker deltas for the helicities,

$$
\overline{\delta}_{ab} = 1 - \delta_{ab}. \tag{5.16}
$$

If one compares the above formulas, one notices many similarities to the helicity summed Altarelli–Parisi kernels in equation (4.16a) to (4.16c). However, the terms in curly brackets have no counterparts in the original kernels which is due to the fact that they are only necessary for helicity eigenstates and vanish upon summation over the helicities of partons i and j. In fact, one can easily verify that upon summation over these two helicities, the above kernels match those for the case of massive quarks, see page 74.

---

[1]Note that this is sufficient since we will require them in four dimensions only, as we will see. Helicity eigenstates always come with a chirality projector and thus with the Dirac matrix γ_5. This matrix is not easy to treat in dimensional regularization and thus it is convenient to resort to four dimensions whenever possible. Some insights on γ_5 in dimensional regularization can be found in [96, 97].

5.2.3   Dipoles for Helicity Eigenstates

Now that we analyzed the soft and collinear limits, let us take a look at the dipoles themselves. The subtraction is given by the same sum over dipoles we had before, compare equation (4.76). Due to the fact that we treat a specific helicity configuration here, the dipoles now depend on the helicity setting and lose the helicity sum:

$$
\mathcal{D}_{ij,k}^{\{\lambda\}_{n+1}} = -\frac{1}{2p_i p_j} \sum_{\eta,\eta'} \mathcal{A}_n^{*\widetilde{\{\lambda\}_n}}(\widetilde{ij},\widetilde{k}) \left(\frac{\mathbf{T}_k \cdot \mathbf{T}_{ij}}{\mathbf{T}_{ij}^2} V_{ij,k}^{\eta\eta'}(\lambda_i,\lambda_j) \right) \mathcal{A}_n^{\widetilde{\{\lambda\}_n}}(\widetilde{ij},\widetilde{k}). \tag{5.17}
$$

The above case is the final–final emission; we do not give the other cases explicitly since the modifications to them with respect to the Catani–Seymour terms are similar and only affect the helicities.

Turning the above soft and collinear limits into spin–correlation matrices is not very difficult since we already know the helicity summed terms. Basically, we have to add some Kronecker deltas to match the collinear limit and make use of table B.1 to find out how to promote the new terms in curly brackets to the dipole parameterization. We then arrive at the matrices given in [95], which we will not present here in their entirety—the interested reader can look them up. Our implementation will only deal with the final–final case, hence we will take a closer look at the corresponding spin–correlation matrices:

$$
V_{gg,k}^{\eta\eta'}(\lambda_i,\lambda_j) = 4\pi\alpha_{\mathrm{s}}(2C_{\mathrm{A}}) \Bigg[-g_{\mu\nu}\delta_{\eta\eta'} \left(\frac{\delta_{\eta\lambda_i}}{1-z\,\overline{y}} + \frac{\delta_{\eta\lambda_j}}{1-\overline{z}y} - \frac{4\overline{\delta}_{\lambda_i\lambda_j} - \kappa\,z_+z_-}{2v_{ij,k}} \right) \tag{5.18a}
$$

$$
+ \frac{\overline{\delta}_{\lambda_i\lambda_j}}{p_i p_j v_{ij,k}} K_\mu^{(m)} K_\nu^{(m)} + \frac{\delta_{\eta\eta'}}{v_{ij,k}} \left[\delta_{\eta\lambda_i}(1-2z) + \delta_{\eta\lambda_j}(1-2\overline{z}) \right] \Bigg] \epsilon_\eta^\mu \epsilon_{\eta'}^{*\nu},
$$

$$
V_{q\bar{q},k}^{\eta\eta'}(\lambda_i,\lambda_j) = 4\pi\alpha_{\mathrm{s}} \frac{2T_{\mathrm{R}}}{v_{ij,k}} \Bigg\{ -g_{\mu\nu}\delta_{\eta\eta'} \left[\frac{\overline{\delta}_{\lambda_i\lambda_j}}{2} - \frac{\kappa}{2}\left(z_+z_- - \frac{m_i^2}{(p_i+p_j)^2} \right) \right] \tag{5.18b}
$$

$$
- \frac{2\overline{\delta}_{\lambda_i\lambda_j}}{(p_i+p_j)^2} K_\mu^{(m)} K_\nu^{(m)} + \delta_{\eta\eta'} \left[\overline{\delta}_{\lambda_i\lambda_j} \left(\delta_{\eta\lambda_i}z + \delta_{\eta\lambda_j}\overline{z} - \frac{1}{2} \right) \right.
$$

$$
\left. + \left(\frac{\delta_{\eta\lambda_i} - \overline{\delta}_{\lambda_i\lambda_j}}{z} + \frac{\delta_{\eta\lambda_j} - \overline{\delta}_{\lambda_i\lambda_j}}{\overline{z}} \right) \frac{m_i^2}{(p_i+p_j)^2} \right] \Bigg\} \epsilon_\eta^\mu \epsilon_{\eta'}^{*\nu},
$$

$$
V_{qg,k}^{\eta\eta'}(\lambda_i,\lambda_j) = 4\pi\alpha_{\mathrm{s}}(2C_{\mathrm{F}}) \Bigg[\frac{\delta_{\eta\lambda_i}}{1-z\overline{y}} - \overline{\delta}_{\lambda_i\lambda_j}\frac{\tilde{v}_{ij,k}}{v_{ij,k}} \left(\delta_{\eta\lambda_i}(1+z) + \delta_{\eta\lambda_j}\frac{m_i^2}{p_i p_j} \right) \tag{5.18c}
$$

$$
- \frac{\tilde{v}_{ij,k}}{v_{ij,k}} \left(\frac{\delta_{\eta\lambda_i}\delta_{\lambda_i\lambda_j} - \overline{\delta}_{\eta\lambda_i}\overline{\delta}_{\lambda_i\lambda_j}}{z} + \overline{\delta}_{\lambda_i\lambda_j}\left(\delta_{\eta\lambda_i} - \delta_{\eta\lambda_j} \right)z \right) \frac{m_i^2}{2p_i p_j} \Bigg] \delta_{\eta\eta'}.
$$

Note that these dipoles use the same momentum parameterizations and symbols we used for the massive helicity summed dipoles, see table 4.1 and the surrounding discussion. The same also applies to the final–initial, initial–final, and initial–initial cases not presented here. Hence, transitioning from helicity summed dipoles to these helicity sampled terms

in a numerical program is a simple task.

5.2.4 Remark on the Integrated Subtraction Term

In the previous discussions of integrated subtraction terms, we claimed that they are not of great importance in the context of this work. Here, we can provide the justification for this statement which will also hold for all other helicity methods, as we will see.

Since all dipoles now depend on helicity eigenstates the total subtraction term for helicity eigenstates now depends on the helicities of all external particles:

$$\mathrm{d}\sigma_{\mathrm{CPW}}^{\mathrm{A}} = \mathrm{d}\sigma_{\mathrm{CPW}}^{\mathrm{A}}(\lambda_1, \ldots, \lambda_{n+1}; \lambda_a, \lambda_b). \tag{5.19}$$

In order to distinguish the subtraction terms from those by Catani and Seymour, we use the first letter of the names who first published these terms, Czakon, Papadopoulos, and Worek, as the subscript CPW.

To obtain the integrated term, we first perform the helicity summation which leads to the subtraction term of the original Catani–Seymour formulation (the massive version of [79] to be specific; see equation (4.76) on page 78):

$$\int_1 \sum_{\substack{\lambda_1, \ldots, \lambda_{n+1} \\ \lambda_a, \lambda_b}} \mathrm{d}\sigma_{\mathrm{CPW}}^{\mathrm{A}}(\lambda_1, \ldots, \lambda_{n+1}; \lambda_a, \lambda_b) = \int_1 \mathrm{d}\sigma_{\mathrm{CS}}^{\mathrm{A}}. \tag{5.20}$$

The result of the integration over the unresolved phase space obviously leads to the insertion operator we discussed previously, we denote it again with the index CS:

$$\int_1 \mathrm{d}\sigma_{\mathrm{CS}}^{\mathrm{A}} = \mathrm{d}\sigma^{\mathrm{B}} \otimes \boldsymbol{I}_{\mathrm{CS}}(\epsilon) \tag{5.21}$$

In this equation, $\mathrm{d}\sigma^{\mathrm{B}}$ contains a color-correlated squared leading–order amplitude which has to be *summed over all helicities* since it is derived on the basis of the helicity summed subtraction term. However, since the color correlations do not affect the kinematical parts of the amplitude (i.e. kinematically, it is a usual squared amplitude), we are free to calculate the amplitude with a helicity method of our choice.

To conclude, we can simply take the insertion operator $\boldsymbol{I}_{\mathrm{CS}}$ for the helicity summed subtraction term and calculate the full insertion term with helicity sampling:

$$\int_1 \mathrm{d}\sigma_{\mathrm{CPW}}^{\mathrm{A}} \propto \mathrm{d}\Phi_n \left(\mathcal{A}_n^{*\{\lambda\}_n} \boldsymbol{I}_{\mathrm{CS}}(\epsilon) \mathcal{A}_n^{\{\lambda\}_n} \right) J_n. \tag{5.22}$$

This and the fact that the subtraction term itself does not differ much from the original Catani–Seymour terms makes a modification from helicity summation to helicity sampling an easy endeavor.

5.3 Implementation for Leading Color $e^-e^+ \to n$ Jets

Again, we have implemented the integration over sampled helicities and the corresponding subtraction terms for leading color electron–positron annihilation. Most of what we detailed in section 4.3 is also valid here: the generation of all dipole indices, the color correlations and respective color factors, and the technical cut-off. Since there are no new helicity structures in the new spin–correlation matrices (i.e. only direct contraction and the same spin correlation), the implementation of these are also the same. However, we have to re-write them so that they are suitable for our color ordered amplitudes. Taking the massless limit with the help of table 4.1 and re-distributing the poles as we did in section 4.3, the spin–correlation matrices of equations (5.18) turn into:

$$
V_{gg,k}^{\eta\eta'}(\lambda_i, \lambda_j) = 2\pi\alpha_{\mathrm{s}}(2C_{\mathrm{A}})\Bigg[-g_{\mu\nu}\delta_{\eta\eta'}\left(\delta_{\eta\lambda_i}\left\{\frac{1}{1-z\,\overline{y}}+1-2z\right\} - \overline{\delta}_{\lambda_i\lambda_j}\right) \tag{5.23a}
$$

$$
+\frac{\overline{\delta}_{\lambda_i\lambda_j}}{2p_ip_j}K_{\mu}^{(m)}K_{\nu}^{(m)}\Bigg]\epsilon_{\eta}^{\mu}\epsilon_{\eta'}^{*\nu},
$$

$$
V_{qg,k}^{\eta\eta'}(\lambda_i, \lambda_j) = 2\pi\alpha_{\mathrm{s}}(2C_{\mathrm{F}})\delta_{\eta\eta'}\delta_{\eta\lambda_i}\left[\frac{1}{1-z\overline{y}}-\overline{\delta}_{\lambda_i\lambda_j}(1+z)\right]. \tag{5.23b}
$$

5.4 Checks and Analysis

We perform similar checks and analyses as for helicity summation. Let us start with the correctness of the subtraction procedure.

Checks of the Subtraction Terms

Figure 5.2 shows similar plots as the ones we analyzed in the helicity summation chapter, the given quantities and ratios are obtained in the same way as before. The only difference is that the underlying data were obtained for a fixed set of random numbers which this time also encompasses the helicity variables. Obviously, some choices of random numbers lead to helicity configurations for which the amplitudes vanish. In this case, all data points are zero. Hence, the plots show a set of random numbers whose matrix elements are non-zero. Both the soft and the collinear limits show the desired behavior and slopes; the ratios of the real matrix element and the subtraction terms are again close to one. Furthermore, the integrals also converge; we will see this partly in this chapter, but mainly in chapter 8. Thus, we can conclude that the subtraction terms work as expected.

Note that the difference between n–dimensional and one–dimensional sampling is of a technical nature only and does not affect the subtraction terms. Hence we did not differentiate between the two until now. In terms of the performance with respect to the *VEGAS* algorithm, however, the two are very different, thus requiring separate analyses.
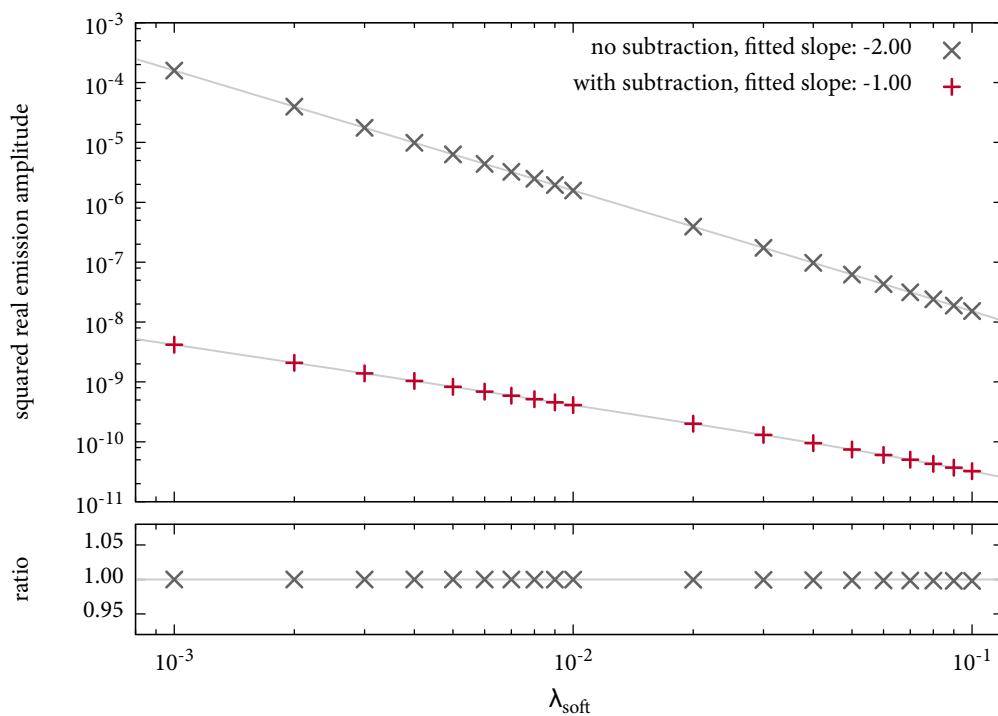
(a) Soft limit for $e^- e^+ \to q g_1 g_2 g_3 g_4 g_5 \boldsymbol{g_6} \overline{q}$; The unresolved soft gluon is g_6.
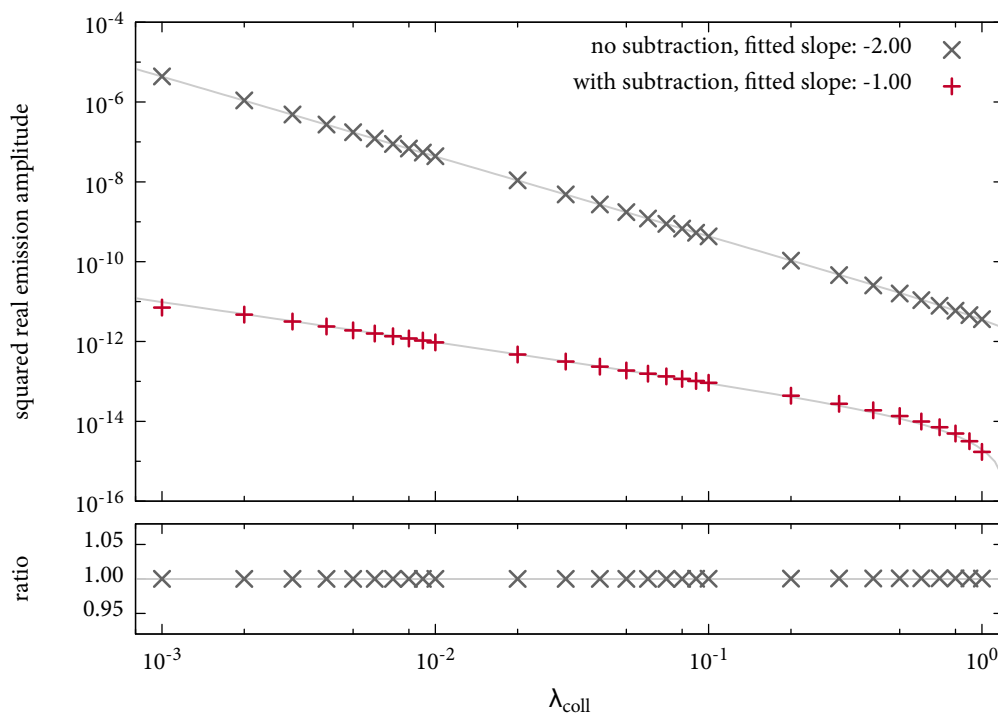
(b) Collinear limit for $e^- e^+ \to q g_1 g_2 g_3 g_4 g_5 \boldsymbol{g_6} \overline{\boldsymbol{q}}$; The collinear pair is $(g_6, \overline{q})$.

Figure 5.2: Soft (a) and collinear (b) behavior of the unsubtracted and subtracted real emission amplitudes for helicity sampling. The lower plots show the absolute ratio of the unsubtracted matrix element and the subtraction term; the expectation (gray line) is approximately 1.

(a) Born 5 Jets

(b) Real emission with 4 Jets
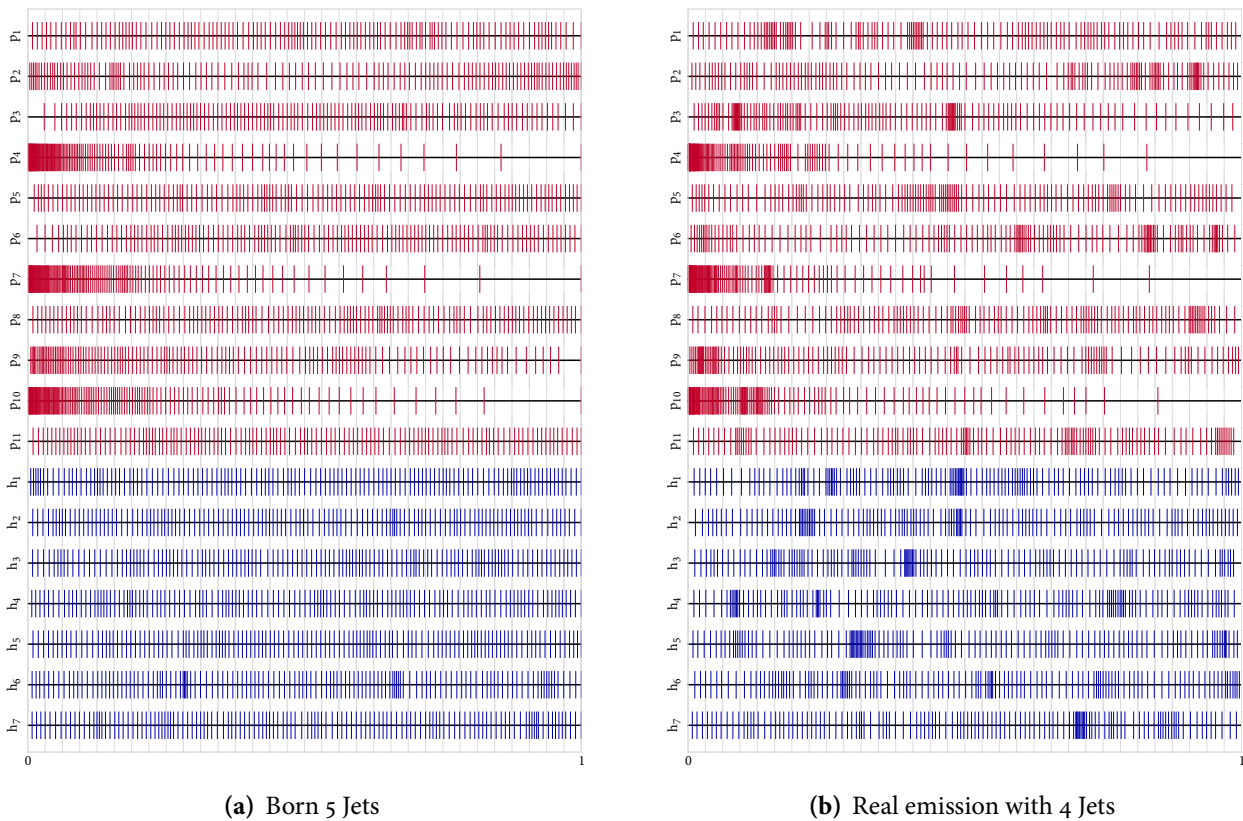
Figure 5.3: Visualization of the *VEGAS* grid. The red graphs show the borders between bins for the phase space dimensions. The blue graphs are the new helicity variables. The phase space grids look very similar to those for helicity sampling (figure 4.8). The helicity grid shows almost no adaptation for the Born contribution and randomly distributed points of dense bins for the real emission contribution.

5.4.1 n–Dimensional Sampling

We begin with n–dimensional sampling. Let us take a look at the grid first. Figure 5.3 shows similar plots for the *VEGAS* grid with 128 bins after six iterations as those we analyzed for helicity summation. The upper eleven (red) graphs show the grids for the random numbers that generate phase space. A direct comparison with the helicity summation results reveal that there is virtually no difference in grid adaptation. The big difference is obviously given by the blue colored additional random numbers that generate the helicities of all external particles. The grid is practically even with little adaptation, except for a few apparently random and not strongly pronounced peak structures. These points are more emphasized for the real emission contribution, figure 5.3(b), but the same fact holds for the phase space part of the grid (compare figure 4.8).

To see how this rather even behavior comes about, let us look at another set of plots. We again choose a fixed set of random numbers for both phase space and helicities. Then we select two particles for which we vary the corresponding helicity variables in the whole interval $[0, 1)$. The result is shown in figure 5.4 which depicts the Born contribution to
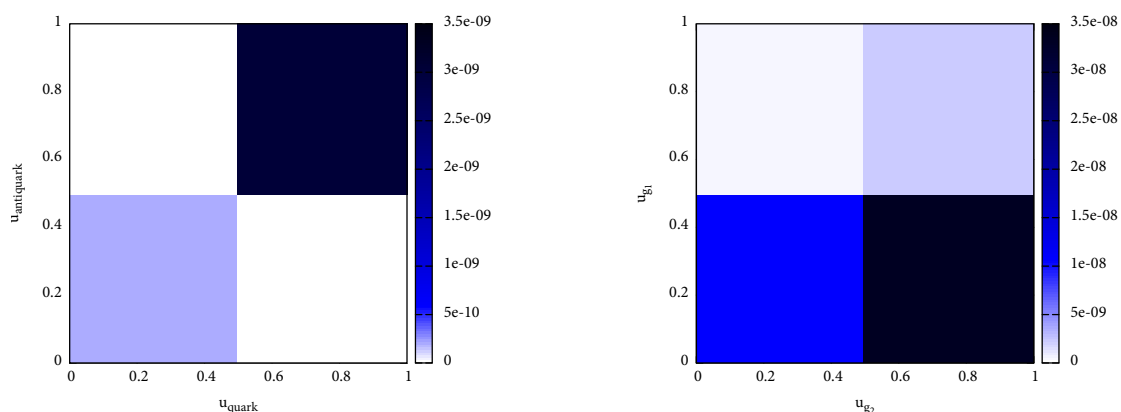
(a) Dependence on quark and antiquark helicity variables.

(b) Dependence on the helicity variables of the first two gluons.

Figure 5.4: Dependence of the squared amplitude on helicity variables u_i. The shown process is $e^+e^- \rightarrow \overline{q}qgggg$. The non-continuous mapping of the helicity variables to the polarization vectors is obvious. Graph (a) violates the factorization condition which is necessary for *VEGAS* to adapt.

$e^-e^+ \rightarrow \overline{q}qgggg$ (i.e. six jets). The left hand graph shows the case for varying quark and antiquark helicity variables, the right hand graph shows the variations of the first two gluon variables. While case (b) shows the desired factorization (confer figure 3.8 on page 49) and thus should work well with *VEGAS*, diagram (a) does not show a factorizable distribution. In fact, these two graphs are highly dependent on the helicity variables of the remaining particles in the process, i.e. the gluons and the electron–positron pair. Changing any of them results in a change of the two shown diagrams. In that sense, these graphs have to be regarded as snapshots for a specific random number configuration. The above, in combination with the fact that the mapping of random numbers to helicities is a function with a strong discontinuity at $u = 1/2$, obviously results in the fact that *VEGAS* cannot adapt to the helicity variables. The peak-like structures we observed before thus have to be regarded as "accidental".

We have also performed an analysis of the Monte Carlo estimate and its error with respect to the number of *VEGAS* bins. As can be expected from the previous discussion, we can find no obvious dependence on the grid other than what we already described in chapter 4, hence we do not display the graphs here. The quality of the integration depends more on the seed of the random number generator than on the number of bins.

5.4.2 One–Dimensional Sampling

We now turn to one–dimensional sampling which is characterized by adding only one helicity integral dimension that contains the full helicity information. Again, we analyze the grid first. Since our findings are similar for both the Born and the real emission contributions, we only show the Born grid, see figure 5.5. The grid for the 11 momentum
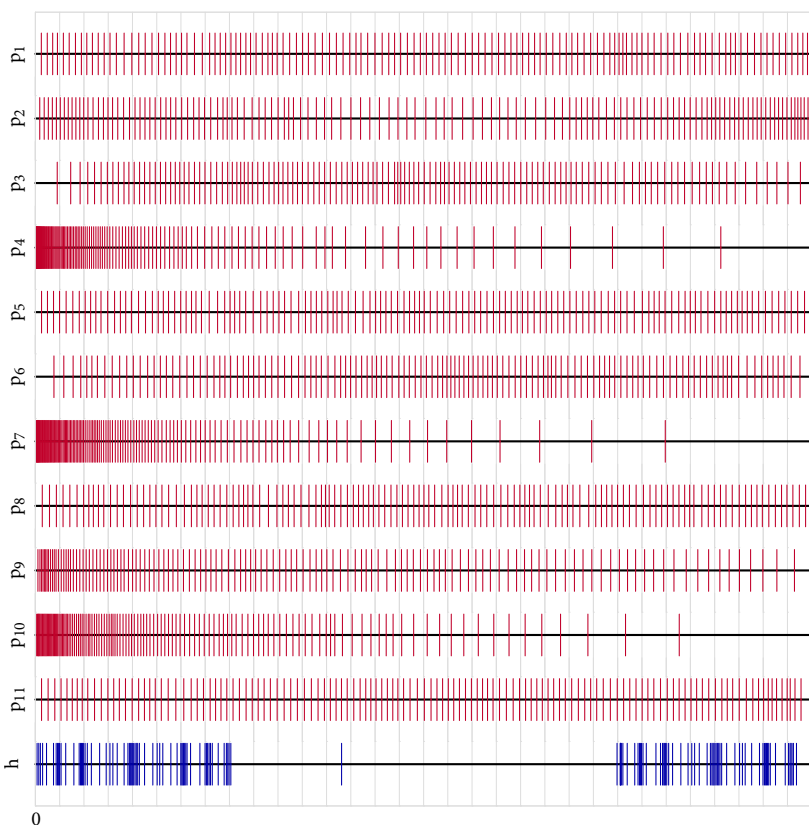
Figure 5.5: Visualization of the *VEGAS* grid for 128 bins and for five jet production at Born level. The red phase space variables agree well with the observation for helicity summation. The single helicity variable in blue shows significant adaptation.

variables looks very similar to the ones we analyzed for n–dimensional sampling and for helicity summation. The grid for the helicity variable, however, shows a very different behavior: it adapts strongly to several peaks that are located in the approximate intervals $[0, 0.25]$ and $[0.75, 1)$ while the range in between is empty. The reason for this can be seen in figure 5.6, where we show the value of the squared amplitude for a fixed phase space configuration while varying the value of the helicity variable; it is the equivalent to figure 5.4. The helicity variable axis is subdivided into $2^{(n+2)} = 2^8 = 256$ channels (we do not call them bins in order to avoid confusion with the *VEGAS* grid), each corresponding to one helicity configuration. This can be seen in the histogram-like structure of the plot. Among these channels are several sharp peaks, but many more configurations where the amplitude is zero or very small. The pattern matches the one we saw for the grid in figure 5.5; thus the *VEGAS* grid adjusts very well to the integrand behavior. In fact, we can even see the "zero valley" that we identified when discussing the grid. It has a simple explanation; the helicities are assigned to the following order of particles in our code: $(\overline{q}_0, q_1, g_2, g_3, \ldots, g_{n-1}, g_n, e^+_{n+1}, e^-_{n+2})$. With our pattern of assigning the helicities (i.e. extending table 5.1 to more particles, in the present case eight), the last two binary digits will be mapped to a fermion pair, in our case the electron–positron pair. Figure 5.4 reveals that neighboring fermion pairs only give a non-zero contribution for equal helicities,
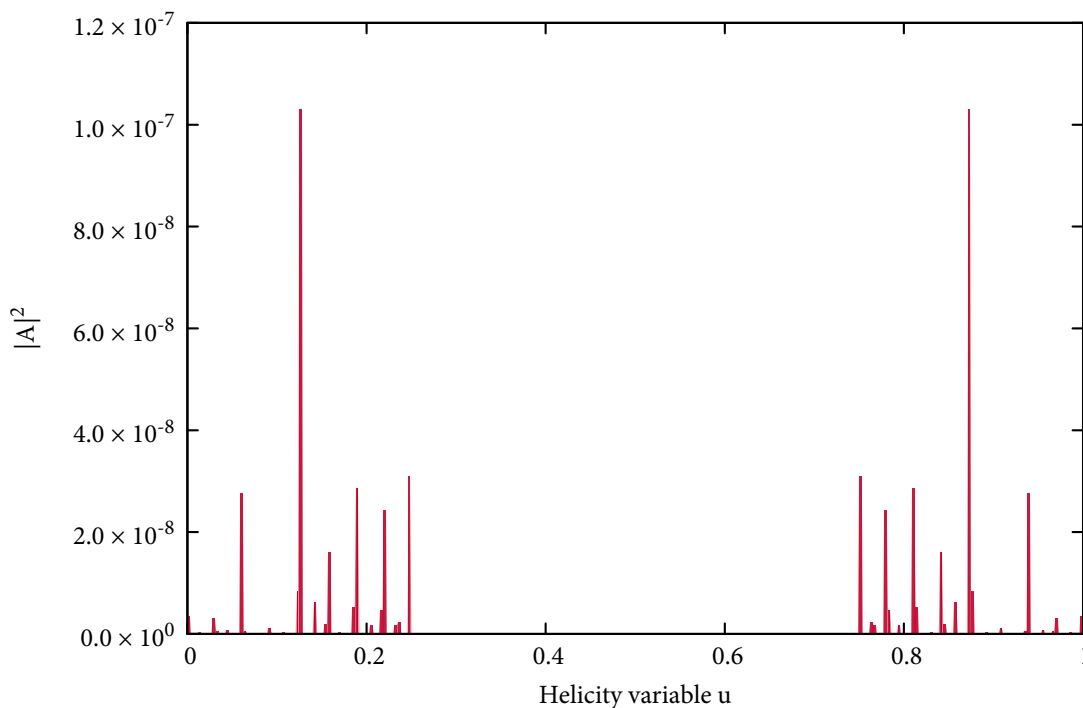
Figure 5.6: Dependence of the squared amplitude on the helicity variable for one–dimensional sampling. The shown process is $e^- e^+ \to \bar{q}qgggg$ where the horizontal axis shows different values for the overall helicity variable.

but not for opposite ones. The helicities for the electron–positron pair (e^-, e^+) have the following values in the given range of the helicity variable:

$$
\begin{aligned}
(-,-) &: [0, 0.25) \\
(+,-) &: [0.25, 0.5) \\
(-,+) &: [0.5, 0.75) \\
(+,+) &: [0.75, 1).
\end{aligned}
\tag{5.24}
$$

Since only the first and the last contributions give non-zero amplitudes, it is clear why we find the wide "zero valley" in between. The same argument also applies for the small gaps in between the peaks of figure 5.6, but with respect to the quark pair and also the gluons (Parke–Taylor formulas, etc.).

Let us now consider varying the number of *VEGAS* bins. Figure 5.7 shows the grid only for the helicity variable, but obtained for different numbers of bins while keeping all other settings identical (even the random number seed). While a number as low as eight bins already shows some reasonable adaptation, the grid adapts increasingly better the more bins one adds. This suggests that the Monte Carlo error should also become smaller with a higher number of bins. Figures 5.8 to 5.11 show the corresponding plots. In fact, we find a smaller Monte Carlo error for higher numbers of bins. All plots feature processes with eight particles and thus $2^8 = 256$ helicity configurations. Analyzing the Monte Carlo error
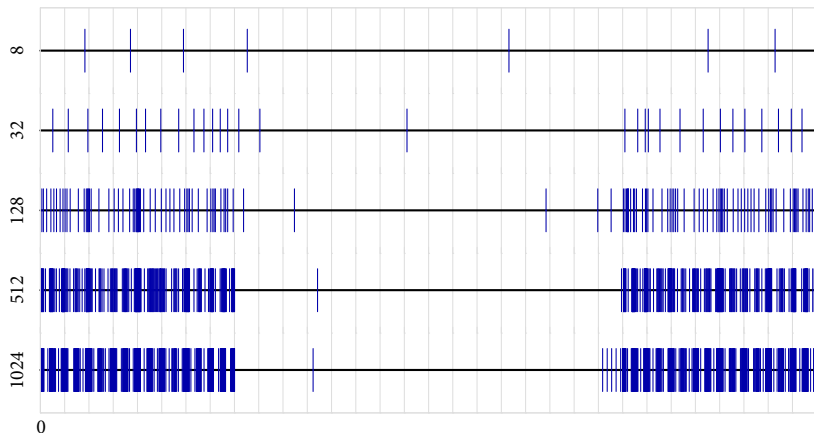
Figure 5.7: Visualization of the helicity variable *VEGAS* grid for different numbers of bins (indicated on the left) of the Born contribution to six jet production. While the 32 bin grid already shows very good adaptation, the pattern becomes increasingly better with growing bin numbers.

in detail, see the left hand sides of figures 5.9 and 5.11, we find a small gap in between the errors for bin numbers smaller than 256 and those larger than 256, which is the number of helicity configurations. Furthermore, the difference in bin numbers larger than the number of helicity configurations is small; in the case of the Born plot the errors for 512 and 1024 bins are even indistinguishable after a certain integration time.

For other jet numbers, we found a similar pattern that suggests the following conclusion. When using one–dimensional helicity sampling, one should choose the number of *VEGAS* bins such that it is twice as high as the number of corresponding helicity configuration provided one has control over the number of bins:

$$b = 2^{m+1} \qquad \text{where } m = \text{ number of external particles.} \qquad (5.25)$$
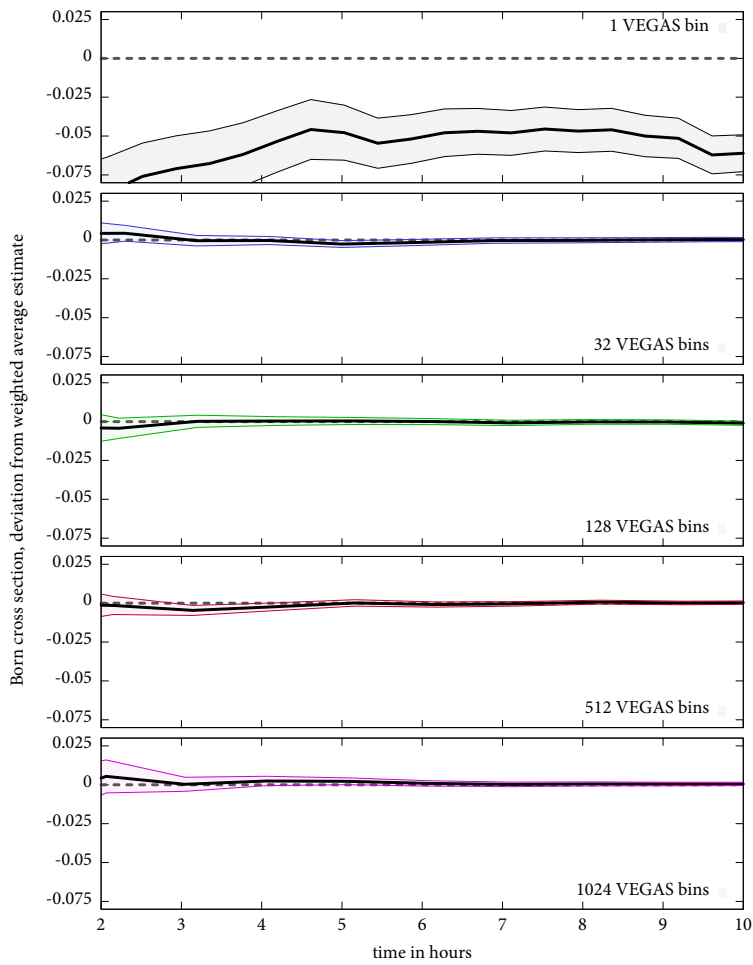
Figure 5.8: Integration behavior of the Born contribution to electron–positron annihilation to six jets for one–dimensional sampling, similar to figure 4.4. The vertical axis is normalized to the weighted average of all bin numbers after 10 hours integration time. The result with one *VEGAS* bin strongly underestimates all other integrations.
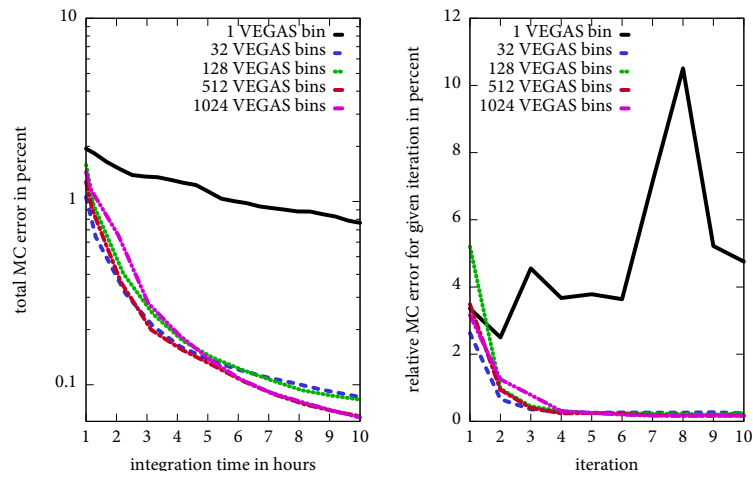
Figure 5.9: Detailed plots of errors for the data presented in figure 5.8. A small difference between bin numbers that are smaller and larger than 256 bins can be seen in the left hand plot.
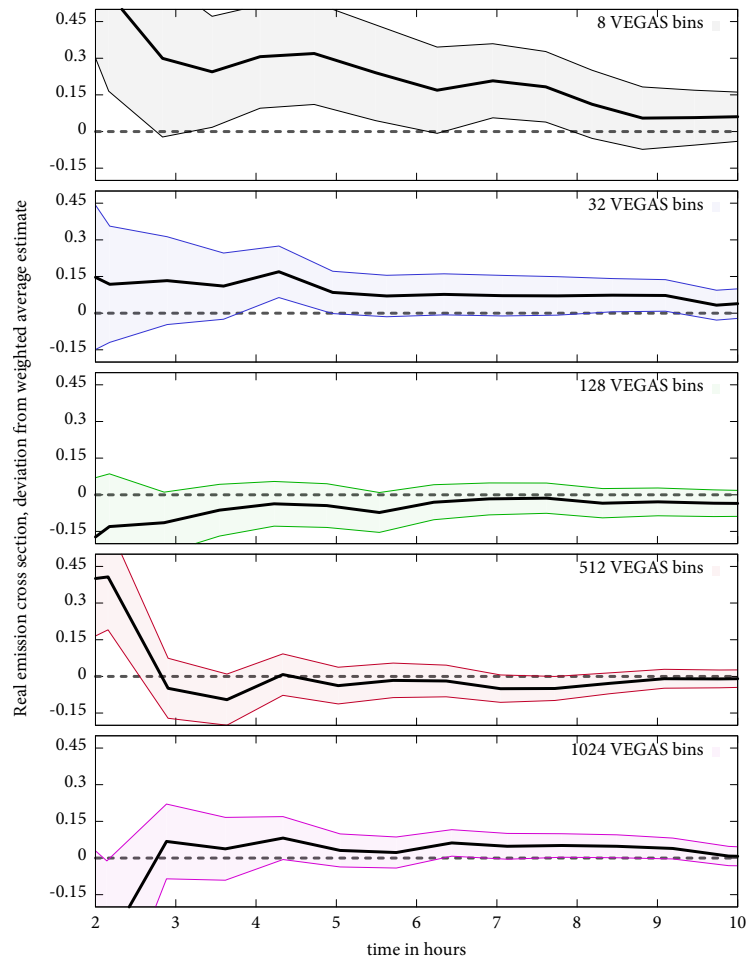
Figure 5.10: Similar plot as figure 5.8 but for the real emission contribution with four jets; also for one–dimensional sampling. All bin numbers agree well.
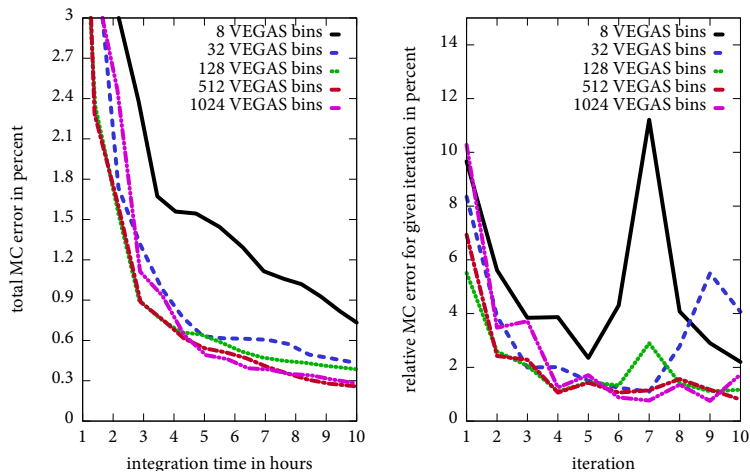
Figure 5.11: Detailed plots of errors for the data presented in figure 5.10. The right hand plot shows the adaptation of the grid with a few bumps due to the complicated phase space and integrand structure. On the left hand side, a separation between bin numbers smaller (and equal) 128 and larger can be seen. $2^{5+2} = 128$ is the number of helicity configurations.

Random Polarizations

In this chapter, we present a second method that avoids the computation of the helicity sum. Instead of re-interpreting the sum as a Monte Carlo expectation value, this method is based on a re-parameterization of the polarization vectors.

6.1   From Discrete Helicities to Continuous Angles

The basic idea is to parameterize the polarization vectors as a linear combination of the two helicity eigenstates weighted with a complex phase factor that depends on an angle ϕ which we will refer to as a *helicity angle*:

$$\epsilon(p, \phi) = e^{i\phi} \epsilon^+(p) + e^{-i\phi} \epsilon^-(p). \tag{6.1}$$

This parameterization has been mentioned in some publications so far[1], however without much analysis. It requires an integration over the helicity angle of each external particle which becomes obvious when looking at the structure of a squared amplitude, recall the example for gluon amplitudes from section 4.1:

$$\sum_{\lambda_1,\dots,\lambda_n} |\mathcal{A}_{\lambda_1\dots\lambda_n}|^2 = \prod_{m=1}^{n} \left[\sum_{\lambda_m} \epsilon_{\mu_m}^{\lambda_m} \epsilon_{\nu_m}^{\lambda_m}{}^* \right] \times \mathcal{M}^{\mu_1\dots\mu_n, \nu_1\dots\nu_n}. \tag{6.2}$$

The crucial quantity concerning external particles in the computation of amplitudes is the polarization sum. This means if equation (6.1) shall yield the correct helicity summed result, it must give rise to the polarization sum as contained in equation (6.2). If we start by replacing the helicity eigenstates with random polarizations in the computation of an amplitude and dropping the helicity sum accordingly, then the corresponding squared

---

[1] [95, 98, 99] and publications as part of this work: [47, 100]. In addition, the author of this work employed random polarizations previously in [36], but not for the computation of observables (i.e. only locally for a single phase space point).

amplitude will contain the product of two random polarizations:

$$
\begin{aligned}
\epsilon_\mu^{\lambda\,*} \epsilon_\nu^\lambda \longrightarrow \epsilon_\mu^*(\phi)\epsilon_\nu(\phi) &= \epsilon_\mu^{+\,*}\epsilon_\nu^+ + \epsilon_\mu^{-\,*}\epsilon_\nu^- + e^{-2i\phi}\epsilon_\mu^{+\,*}\epsilon_\nu^- + e^{+2i\phi}\epsilon_\mu^{-\,*}\epsilon_\nu^+ \\
&= \sum_{\lambda=\pm}\epsilon_\mu^{\lambda\,*}\epsilon_\nu^\lambda \quad + e^{-2i\phi}\epsilon_\mu^{+\,*}\epsilon_\nu^- + e^{+2i\phi}\epsilon_\mu^{-\,*}\epsilon_\nu^+
\end{aligned}
\tag{6.3}
$$

The product was calculated by inserting equation (6.1). It is clear that the first two terms make up the usual polarization sum, just as we need it. However, we also find two more terms with products of polarization vectors for unequal helicities. In contrast to the polarization sum term, both of these terms depend on the helicity angle. Since they are of vital importance for the subtraction term, we name them *helicity mixing terms*.

If we integrate over the helicity angle, the two superfluous terms vanish due to Cauchy's theorem:

$$
\frac{1}{2\pi}\int_0^{2\pi} d\phi \left(\epsilon_\mu(\phi)\right)^* \epsilon_\nu(\phi) = \sum_{\lambda=\pm}\left(\epsilon_\mu^\lambda\right)^* \epsilon_\nu^\lambda
\tag{6.4}
$$

The polarization sum term merely acquires a factor of 2π by the integration which we included in the integration as a normalization factor. Note that we will include this term in the integration measure $d\phi$ from now on.[2]

The above discussion was made on the basis of boson polarization vectors. Let us stress that random polarizations can analogously be defined for fermion spinors, even massive spinors, for example:

$$
u(p, \phi) = e^{i\phi}u^+(p) + e^{-i\phi}u^-(p).
\tag{6.5}
$$

In conclusion, we can use parameterization (6.1) instead of helicity eigenstates if we replace the helicity sum by an integration over the helicity angle.

What advantages does this method bring to the table? First of all, just like helicity sampling, we only have to evaluate one squared amplitude per phase space point. Instead of the helicity sum, we have n integrals over the helicity angle of each particle. These integrals can again be combined with the phase space integration to form one high-dimensional Monte Carlo integral, analogous to n–dimensional sampling. Helicity sampling has the property that unless *VEGAS* adapts really well (which is only possible for one–dimensional sampling, as we saw), some percentage of the calculation will be spent with computing zero in the form of vanishing helicity configurations. The method of random polarizations circumvents this problem entirely, since the phase factor in equation (6.1) never vanishes so that independent of the helicity angle, both helicity eigenstates contribute for each particle. As a direct consequence, the amplitude will never be zero due to the choice of helicity angles. Furthermore, random polarizations are continuous, smooth functions with respect to the angle, as opposed to the parameterization used for helicity sampling.

Before we do a practical analysis of random polarizations, let us first deal with the subtraction term for the next–to–leading order contribution.

---

[2]We do not only do this for a decluttered notation, but also because one can easily re-write the parameterization such that one integrates over the interval $[0, 1)$ where the factor 2π becomes equal to one. We discuss this in section 6.3. The current notation is used to stress the interpretation of ϕ as an angle.

6.2 Real Emission and Extension of the Catani–Seymour Method

Once more, it is straight forward to calculate the Born, real and virtual amplitudes with random polarizations due to the same arguments mentioned before. The part that requires a special treatment is again the subtraction term that we will denote by $d\sigma_{\mathrm{RP}}^{\mathrm{A}}$ for random polarizations.

When thinking about a subtraction term for random polarizations, a naive approach might be to try and construct it from the subtraction terms for helicity eigenstates that we discussed in the previous chapter—random polarizations are linear combinations of helicity eigenstates, after all. Unfortunately, it is not that simple. In fact, it is not sufficient to look at the parameterization (6.1) itself, but one must consider the product of random polarizations, equation (6.3).

To see why this is the case, let us look at the collinear limit of an amplitude as generally defined in equation (3.46). It depends on the squared splitting $\Upsilon_{(ij)\to i+j}^{*}\Upsilon_{(ij)\to i+j}$ wherein each splitting function contains the polarization vectors for partons i and j. A graphical representation of this situation is presented in figure 6.1 for helicity summation, sampling, and also in parts for random polarizations. As highlighted, the new helicity mixing terms that appear in products of random polarizations cannot be treated using the formulas for helicity eigenstates; the subtraction terms for helicity eigenstates are formulated for products of polarizations with equal helicities, but not for the mixing terms. Since these terms are implicitly included in the real emission matrix element, there will be additional soft and collinear poles that we have to subtract in order to render the integral finite.

Hence, it is clear that we need to derive new subtraction terms that match the corresponding poles. However, if we try to derive terms in analogy to the previous chapters, we soon encounter an obstacle: the soft limit does not exhibit the same structure as before.[3] When we discussed helicity summation and helicity eigenstates, we made use of gauge invariance to re-write the polarization sum of the soft gluon to $-g^{\mu\nu}$. This allowed us to contract the eikonal currents directly, see equations (4.8) for summation and (5.11) for eigenstates. Employing the product of random polarizations to the soft gluon, we obtain the following structure instead:

$$J^{\mu\dagger}\epsilon_{\mu}^{*}(\phi_j)\,\epsilon_{\nu}(\phi_j)\,J^{\nu} = -J^{\mu\dagger}J_{\mu} + \mathrm{e}^{-2\mathrm{i}\phi_j}\,J^{\mu\dagger}\epsilon_{\mu}^{+*}\,\epsilon_{\nu}^{-}\,J^{\nu} + \mathrm{e}^{+2\mathrm{i}\phi_j}\,J^{\mu\dagger}\epsilon_{\mu}^{-*}\,\epsilon_{\nu}^{+}\,J^{\nu} \qquad (6.6)$$

Obviously, the first term on the right hand side is the desired contraction that we already dealt with while the remaining helicity mixing terms are problematic: they cannot be re-written into a direct contraction of the currents. Even worse, the product of two polarization vectors with different helicities is difficult to treat analytically. In any case, the above formula exhibits a complicated structure that cannot be reduced to a simple kinematic factor times color correlations in the same style as we did before. In Catani and

---

[3]This has already been mentioned in [95]. In fact, the authors refrained from deriving new subtraction terms because of this.

Summation	$\displaystyle\sum_{\lambda_i,\lambda_j}\left(\widetilde{ij} \mathrel{\begin{smallmatrix}\epsilon^*_{\lambda_i} & \epsilon_{\lambda_i}\\ \epsilon^*_{\lambda_j} & \epsilon_{\lambda_j}\end{smallmatrix}} \widetilde{ij}\right)$	
Sampling	$\displaystyle\left(\widetilde{ij} \mathrel{\begin{smallmatrix}\epsilon^*_{\lambda_i} & \epsilon_{\lambda_i}\\ \epsilon^*_{\lambda_j} & \epsilon_{\lambda_j}\end{smallmatrix}} \widetilde{ij}\right)$	$\lambda_i \in \{+,-\}$ $\lambda_j \in \{+,-\}$
Example for random po- larizations	$\displaystyle\sum_{\lambda_i}\left(\widetilde{ij} \mathrel{\begin{smallmatrix}\epsilon^*_{\lambda_i} & \epsilon_{\lambda_i}\\ \epsilon^*_{j} & \epsilon_{j}\end{smallmatrix}} \widetilde{ij}\right)$ $+\mathrm{e}^{-2\mathrm{i}\phi_i}\left(\widetilde{ij} \mathrel{\begin{smallmatrix}\textcolor{red}{\epsilon^*_{+}} & \textcolor{red}{\epsilon_{-}}\\ \epsilon^*_{j} & \epsilon_{j}\end{smallmatrix}} \widetilde{ij}\right)$ $+\mathrm{e}^{+2\mathrm{i}\phi_i}\left(\widetilde{ij} \mathrel{\begin{smallmatrix}\textcolor{red}{\epsilon^*_{-}} & \textcolor{red}{\epsilon_{+}}\\ \epsilon^*_{j} & \epsilon_{j}\end{smallmatrix}} \widetilde{ij}\right)$	

Figure 6.1: Illustration of the squared splitting vertices $Y^*_{(ij)\to i+j}Y_{(ij)\to i+j}$ that make up the collinear limit and thus also the spin–correlation matrices $V_{ij,k}$. Both for helicity summation and for sampling the helicities in both the conjugated and the non-conjugated splittings are equal. For random polarizations, this is not the case; here, the illustration focuses on the upper parton i (ϵ_j is a dummy which itself is a random polarization) for which the product of the random polarization has been inserted yielding the three terms. The first is the same as the helicity summation result while the latter two contain the *helicity mixing terms*; these are not even part of the helicity eigenstate splittings.

Seymour's dipole formulation, the development of the unified spin–correlation matrices was possible because of the rather simple structure of the soft divergences. A structure such as we would obtain here would probably be difficult to combine with the collinear limit to form such a unified subtraction term. As the subjunctive formulation of the last few phrases suggests, we are going to choose a different approach.

6.2.1   The Basic Idea

The above discussion did not only expose problems but also allowed us some useful insights. Both equation (6.6) and figure 6.1 reveal that the soft and collinear limits of a randomly polarized amplitude are made up of the helicity summed terms plus extra helicity mixing terms. We will use this fact to our advantage.

The helicity summed contributions generate exactly those poles that the original

Catani–Seymour terms are meant to subtract. Hence, we can make use of the Catani–Seymour term $d\sigma_{CS}^A$ which we have to supplement with a new additional subtraction term $d\sigma^{\widetilde{A}}$ that subtracts all soft and collinear poles resulting from the helicity mixing terms. Thus the total subtraction term for random polarization reads

$$d\sigma_{RP}^A = d\sigma_{CS}^A + d\sigma^{\widetilde{A}}. \tag{6.7}$$

Note that by $d\sigma_{CS}^A$ we mean the Catani–Seymour subtraction term where the n–parton amplitude is evaluated using random polarizations; the important quantity is $\boldsymbol{V}_{ij,k}$ and all other spin–correlation matrices which contain the helicity summed parts for partons i and j.

So let us define more clearly what $d\sigma^{\widetilde{A}}$ has to describe. In the soft limit, this will be the two right terms of equation (6.6) that both come with a factor $e^{\pm 2i\phi_j}$. In the collinear limit, we gave an example for half the terms in figure 6.1. Therein, we have not yet inserted the random polarization for particle j which is missing to describe the full picture. The complete list of contributions is proportional to

$$
\begin{aligned}
&\epsilon_\mu^*(\phi_i)\,\epsilon_\nu(\phi_i)\,\epsilon_\rho^*(\phi_j)\,\epsilon_\sigma(\phi_j) \\[4pt]
&= \sum_{\lambda_i,\lambda_j=\pm} \epsilon_\mu^{\lambda_i\,*} \epsilon_\nu^{\lambda_i} \epsilon_\rho^{\lambda_j\,*} \epsilon_\sigma^{\lambda_j} \\
&\quad + \sum_{\lambda_i=\pm} \epsilon_\mu^{\lambda_i\,*} \epsilon_\nu^{\lambda_i} \left(e^{-2i\phi_j}\epsilon_{j\rho}^{+\,*}\epsilon_{j\sigma}^{-} + e^{+2i\phi_j}\epsilon_{j\rho}^{-\,*}\epsilon_{j\sigma}^{+} \right) \\
&\quad + \sum_{\lambda_j=\pm} \epsilon_\rho^{\lambda_j\,*} \epsilon_\sigma^{\lambda_j} \left(e^{-2i\phi_i}\epsilon_{i\mu}^{+\,*}\epsilon_{i\nu}^{-} + e^{+2i\phi_i}\epsilon_{i\mu}^{-\,*}\epsilon_{i\nu}^{+} \right) \\
&\quad + \left(e^{-2i\phi_i}\epsilon_{i\mu}^{+\,*}\epsilon_{i\nu}^{-} + e^{+2i\phi_i}\epsilon_{i\mu}^{-\,*}\epsilon_{i\nu}^{+} \right)\left(e^{-2i\phi_j}\epsilon_{j\rho}^{+\,*}\epsilon_{j\sigma}^{-} + e^{+2i\phi_j}\epsilon_{j\rho}^{-\,*}\epsilon_{j\sigma}^{+} \right).
\end{aligned}
\tag{6.8}
$$

Note that we omitted the momentum dependence which becomes clear from looking at the index of the helicity variables or the polarizations themselves. Only the first term on the right hand side is described by the collinear limit for helicity summed amplitudes. All other terms give rise to splittings that have to be described by $d\sigma^{\widetilde{A}}$. Each of these terms is proportional to $e^{\pm 2i\phi_i}$ and/or $e^{\pm 2i\phi_j}$. We know from section 6.1 that all these terms vanish upon integration over the corresponding helicity angle. As a consequence, the whole subtraction term $d\sigma^{\widetilde{A}}$ will vanish upon integration:

$$\int d\phi_i \int d\phi_j\, d\sigma^{\widetilde{A}} = 0. \tag{6.9}$$

Using this, we can argue in a similar way as in section 5.2.4 to see that the integrated term of the additional subtraction term vanishes: to determine the integrated subtraction term we first determine the helicity summed subtraction term by integrating over the helicity angles:

$$\int d^{n+1}\phi\, d\sigma_{RP}^A = \int d^{n+1}\phi\, d\sigma_{CS}^A + \int d^{n+1}\phi\, d\sigma^{\widetilde{A}} = d\sigma_{CS}^A \tag{6.10}$$

where the integration is over the helicity angles of *all* particles and leads to the fully helicity

summed subtraction term $\mathrm{d}\sigma^{\mathrm{A}}_{\mathrm{CS}}$. Thus, we immediately know the integrated subtraction term which is again given by

$$\int_1 \mathrm{d}\sigma^{\mathrm{A}}_{\mathrm{RP}} \propto \mathrm{d}\Phi_n \left(\mathcal{A}^{*\{\phi\}_n}_n \, \boldsymbol{I}_{\mathrm{CS}}(\epsilon) \mathcal{A}^{\{\phi\}_n}_n \right) J_n, \tag{6.11}$$

in analogy to equation (5.22).

Notice that this has major implications for $\mathrm{d}\sigma^{\widetilde{\mathrm{A}}}$ which we will exploit. Since it integrates to zero, we do not have to worry about the analytical integrability of the additional subtraction term when constructing it. More specifically, this means that we are free to include as many finite contributions as we want provided that it contains exactly those poles induced by the helicity mixing terms. We will use this fact to formulate both the soft and the collinear limit in a general way which requires no exact knowledge of the pole terms.

Before we do so, let us discuss the structure of the new subtraction term $\mathrm{d}\sigma^{\widetilde{\mathrm{A}}}$ in some more detail. As we will detail below, it consists of a sum over new dipoles $\widetilde{D}$ which are formulated in terms of new spin–correlation matrices $\widetilde{V}$; the whole mechanism is very similar to the Catani–Seymour structure. We will formulate the new spin–correlation matrices $\widetilde{V}$ in such a way that they can be used with arbitrary parameterizations for polarization vectors/spinors of the partons i and j. More specifically, they will be valid for random polarizations, for helicity eigenstates and consequently also for helicity summation. It is clear that we only need the helicity mixing terms since the helicity summed contributions are taken care of by $\mathrm{d}\sigma^{\mathrm{A}}_{\mathrm{CS}}$. In fact, it *cannot* contain poles for the helicity summed result, see the first term on the right hand of equation (6.8), because then these poles would be counted twice and subtraction would not work. The question arising from this argument is how do we extract the three latter terms in equation (6.8)?

One way of doing this is calculating $\widetilde{V}$ manually for each of the helicity mixing configurations in equation (6.8) by inserting the respective eigenstates for i and j together with the appropriate $\mathrm{e}^{\pm 2i\phi_{i/j}}$ factors. This is not efficient and requires some bookkeeping which we want to avoid as much as possible.

A simpler way is to to compute the full $\widetilde{V}$ with random polarizations. This avoids inserting eigenstates times the exponential factors and is thus easier to implement and more efficient. From this we subtract the helicity summed result for our terms, which is equivalent to computing just the first line in equation (6.8). To this end, we define an operator $\mathcal{R}$ that acts on the helicity parameterization of partons i and j as follows:

$$\mathcal{R}f(h_i, h_j) = f(\phi_i, \phi_j) - \sum_{\lambda_i, \lambda_j} f(\lambda_i, \lambda_j). \tag{6.12}$$

Here, we use a symbolic notation that should be understood as follows. f is an arbitrary function that depends on the polarization vectors/spinors of partons i and j (for example $\widetilde{V}$). With the arguments h_i and h_j, we indicate that the function is formulated for an arbitrary parameterization of polarizations/spinors. On the right hand side, we first

calculate the function using random polarizations—as indicated by the arguments ϕ_i and ϕ_j—and then subtract the helicity summed result as indicated by the sum over the helicity/spin settings. This guarantees that we are left with nothing but the helicity mixing terms.

As an example, one can apply the operator to equation (6.8) and see that only the last three lines one the right hand side survive.

Using this operator has another side effect: it provides a means to see if the $\widetilde{V}$ are formulated and implemented correctly. To see this, let us divide the subtraction term $d\sigma^{\widetilde{A}}$ into several terms as follows:

$$d\sigma^{\widetilde{A}} = d\sigma^{\phi} - d\sigma^{\lambda}. \tag{6.13}$$

The left hand term, $d\sigma^{\phi}$ contains all those terms that depend directly on random polarizations, i.e. the first term of the $\mathcal{R}$ operator. The second part, i.e. the subtracted helicity summed piece, makes up the other term $d\sigma^{\lambda}$. Using this notation, the full next–to–leading order cross section reads

$$
\begin{aligned}
\sigma^{\mathrm{NLO}} &= \int\limits_{n+1} \left(d\sigma^{\mathrm{R}} - d\sigma^{\mathrm{A}}_{\mathrm{CS}} - \left[d\sigma^{\phi} - d\sigma^{\lambda} \right] \right) + \int\limits_{n} \left(d\sigma^{\mathrm{V}} + \int\limits_{1} d\sigma^{\mathrm{A}}_{\mathrm{CS}} + d\sigma^{\mathrm{C}} \right) \\
&= \int\limits_{n+1} \left(d\sigma^{\mathrm{R}} - d\sigma^{\mathrm{A}}_{\mathrm{CS}} - d\sigma^{\phi} + d\sigma^{\lambda} \right) + \int\limits_{n} \left(d\sigma^{\mathrm{V}} + \int\limits_{1} d\sigma^{\mathrm{A}}_{\mathrm{CS}} + d\sigma^{\mathrm{C}} \right)
\end{aligned}
\tag{6.14}
$$

Let us focus on the real emission integral on the left. The following statements will be true and provide a good way of checking the correctness of the implementation and of the terms themselves:

- $d\sigma^{\mathrm{R}} - d\sigma^{\phi}$ performs a full subtraction for all poles of $d\sigma^{\mathrm{R}}$ and yields an integrable result of $\mathcal{O}\left(1/\lambda_{\mathrm{coll/soft}}\right)$ in the respective limit.

- $-d\sigma^{\mathrm{A}}_{\mathrm{CS}} + d\sigma^{\lambda}$ is also an integrable contribution of $\mathcal{O}\left(1/\lambda_{\mathrm{coll/soft}}\right)$. As we will see, the additional dipoles $\widetilde{\mathcal{D}}$ that we construct will match the poles of the Catani–Seymour term exactly—they have to, because otherwise our additional subtraction term would be wrong. However, they do not agree exactly because $d\sigma^{\lambda}$ will contain additional integrable contributions, as we stated before, i.e.

$$d\sigma^{\lambda} = d\sigma^{\mathrm{A}}_{\mathrm{CS}} + \mathcal{O}\left(\frac{1}{\lambda_{\mathrm{soft/coll}}} \right). \tag{6.15}$$

Later on, we will use the above two items to verify that our subtraction terms work as expected. However, we first need to derive the new spin–correlation matrices $\widetilde{V}$. To this end, we will again examine the soft and collinear limits and re-write the general expressions we obtained at the beginning of this chapter into a suitable form.

6.2.2 The Soft Limit for Random Polarizations

We begin with the soft limit, which we write down for *general* polarization vectors $\epsilon_j \equiv \epsilon(p_j)$. By general, we mean that this polarization vector can be parameterized in any convenient way as long as it is physically correct. We will use this formula with random polarizations and helicity eigenstates in this chapter, but it is also valid for "linear combination" polarizations that we will consider in the next chapter.

We start from the general soft limit we derived in equation (3.36) and use equation (3.37):

$$
\lim_{\lambda_{\text{soft}} \to 0} \left| \mathcal{A}_{n+1} \right|^2
$$

$$
= -4\pi\alpha_s \mu^{2\epsilon} \sum_{\substack{i,k=1 \\ i \neq k \neq j}}^{n+1} \mathcal{A}_n^* \, \mathbf{T}_i \mathbf{T}_k \left(\frac{(p_i \epsilon_j^*)(p_i \epsilon_j)}{(p_i p_j)^2} - \frac{(p_i \epsilon_j^*)(p_k \epsilon_j) + (p_k \epsilon_j^*)(p_i \epsilon_j)}{(p_k p_j)(p_i p_j + p_k p_j)} \right) \mathcal{A}_n
$$
(6.16)

$$
= -4\pi\alpha_s \mu^{2\epsilon} \sum_{\substack{i,k=1 \\ i \neq k \neq j}}^{n+1} \mathcal{A}_n^{*\,\xi} \, \mathbf{T}_i \mathbf{T}_k \big[S_{ij,k} \big]_{\xi\zeta} \, \mathcal{A}_n^{\zeta}
$$

The last line requires some explanation. In order to be able to treat the soft and the collinear limit on the same footing, we pulled the emitter parton's polarization vector/spinor out of the amplitude to create an open amplitude:

$$
\mathcal{A}_n = \begin{cases} \mathcal{A}_n^{\mu} \, \epsilon_{\mu}^{\lambda_i}{}^*(p_i) & \text{gluon emitter} \\ \mathcal{A}_n^{\alpha} \, \overline{u}_{\alpha}^{\lambda_i}(p_i) & \text{quark emitter} \\ \mathcal{A}_n^{\alpha} \, v_{\alpha}^{\lambda_i}(p_i) & \text{antiquark emitter.} \end{cases}
$$
(6.17)

Then, we defined a new tensor $S_{ij,k}$ that encompasses both these polarizations/spinors and the eikonal factors in between and reads

$$
\big[S_{ij,k} \big]_{\mu\nu} = \left(\frac{(p_i \epsilon_j^*)(p_i \epsilon_j)}{(p_i p_j)^2} - \frac{(p_i \epsilon_j^*)(p_k \epsilon_j) + (p_k \epsilon_j^*)(p_i \epsilon_j)}{(p_k p_j)(p_i p_j + p_k p_j)} \right) \epsilon_{\mu}(p_i) \, \epsilon_{\nu}^*(p_i),
$$
(6.18a)

$$
\big[S_{ij,k} \big]_{\alpha\beta} = \left(\frac{(p_i \epsilon_j^*)(p_i \epsilon_j)}{(p_i p_j)^2} - \frac{(p_i \epsilon_j^*)(p_k \epsilon_j) + (p_k \epsilon_j^*)(p_i \epsilon_j)}{(p_k p_j)(p_i p_j + p_k p_j)} \right) u_{\alpha}(p_i) \, \overline{u}_{\beta}(p_i),
$$
(6.18b)

and similarly for the antiquark splitting.

6.2.3 The Collinear Limit for Random Polarizations

In the collinear limit, we also start from the general formula we derived at the beginning of this chapter, equation (3.46), which we rewrite as follows:

$$
\lim_{\lambda_{\text{coll}} \to 0} |\mathcal{A}_{n+1}(p_1, \dots, p_{n+1})|^2 = 4\pi\alpha_s \mu^{2\epsilon} \, \mathbf{T}_{(ij) \to i+j}^2 \mathcal{A}_n^{*\,\xi} \big[\mathcal{P}_{(ij) \to i+j} \big]_{\xi\zeta} \, \mathcal{A}_n^{\zeta}.
$$
(6.19)

Therein, we defined new splitting kernels $\mathcal{P}_{(ij)\to i+j}$ which are given by the following expressions:

$$
[\mathcal{P}_{(ij)\to i+j}]_{\xi\zeta} = \frac{d_{\xi\xi'}}{2p_ip_j} \Upsilon^{*\,\xi'}_{(ij)\to i+j} \Upsilon^{\zeta'}_{(ij)\to i+j} \frac{d_{\zeta'\zeta}}{2p_ip_j}
$$

$$
= \begin{cases}
\displaystyle\sum_{\eta,\eta'} \epsilon^{\eta}_{\mu}(p_{ij}) \frac{\epsilon^{\eta\,*}_{\mu'}(p_{ij})\, \Upsilon^{*\mu'}_{(ij)\to i+j}}{2p_ip_j} \frac{\Upsilon^{\nu'}_{(ij)\to i+j}\, \epsilon^{\eta'}_{\nu'}(p_{ij})}{2p_ip_j} \epsilon^{\eta'\,*}_{\nu}(p_{ij}) & \text{(gluons)} \\[2em]
\displaystyle\sum_{\eta,\eta'} u^{\eta}_{\alpha}(p_{ij}) \frac{\overline{u}^{\eta}_{\alpha'}(p_{ij})\, \Upsilon^{*\alpha'}_{(ij)\to i+j}}{2p_ip_j} \frac{\Upsilon^{\beta'}_{(ij)\to i+j}\, u^{\eta'}_{\beta'}(p_{ij})}{2p_ip_j} \overline{u}^{\eta'}_{\beta}(p_{ij}) & \text{(quarks)} \\[2em]
\displaystyle\sum_{\eta,\eta'} v^{\eta}_{\alpha}(p_{ij}) \frac{\overline{v}^{\eta}_{\alpha'}(p_{ij})\, \Upsilon^{*\alpha'}_{(ij)\to i+j}}{2p_ip_j} \frac{\Upsilon^{\beta'}_{(ij)\to i+j}\, v^{\eta'}_{\beta'}(p_{ij})}{2p_ip_j} \overline{v}^{\eta'}_{\beta}(p_{ij}) & \text{(antiquarks)}
\end{cases}
\tag{6.20}
$$

$$
= \begin{cases}
\displaystyle\sum_{\eta,\eta'} \epsilon^{\eta}_{\mu}(p_{ij})\, \mathrm{Split}^{\eta\,*}_{(ij)\to i+j}\, \mathrm{Split}^{\eta'}_{(ij)\to i+j}\, \epsilon^{\eta'\,*}_{\nu}(p_{ij}) & \text{(gluons)} \\[1.5em]
\displaystyle\sum_{\eta,\eta'} u^{\eta}_{\alpha}(p_{ij})\, \mathrm{Split}^{\eta\,*}_{(ij)\to i+j}\, \mathrm{Split}^{\eta'}_{(ij)\to i+j}\, \overline{u}^{\eta'}_{\beta}(p_{ij}) & \text{(quarks)} \\[1.5em]
\displaystyle\sum_{\eta,\eta'} v^{\eta}_{\alpha}(p_{ij})\, \mathrm{Split}^{\eta\,*}_{(ij)\to i+j}\, \mathrm{Split}^{\eta'}_{(ij)\to i+j}\, \overline{v}^{\eta'}_{\beta}(p_{ij}) & \text{(antiquarks)}
\end{cases}
$$

Once again, it is obvious that the quark and antiquark emitter cases are related by replacing $u \leftrightarrow v$. Notice that we defined new scalar functions $\mathrm{Split}_{(ij)\to i+j}$ in there. Let us first give their full expressions:

$$
\mathrm{Split}^{\eta}_{g\to gg}(ij, i, j) = \frac{2}{2p_ip_j}\Big([\epsilon(p_i)\epsilon(p_j)][p_i\epsilon^{\eta\,*}(p_{ij})]
$$
$$
+ [\epsilon(p_j)\epsilon^{\eta\,*}(p_{ij})][p_j\epsilon(p_i)]
$$
$$
- [\epsilon(p_i)\epsilon^{\eta\,*}(p_{ij})][p_i\epsilon(p_j)]\Big)
\tag{6.21a}
$$

$$
\mathrm{Split}^{\eta}_{g\to q\overline{q}}(ij, i, j) = \frac{1}{2p_ip_j}\, \overline{u}(p_i)\,\gamma^{\mu}\, v(p_j)\, \epsilon^{\eta\,*}_{\mu}(p_{ij}),
\tag{6.21b}
$$

$$
\mathrm{Split}^{\eta}_{q\to qg}(ij, i, j) = \frac{1}{(p_i+p_j)^2 - m^2_{ij}}\, \overline{u}(p_i)\,\gamma^{\mu}\, u^{\eta}(p_{ij})\, \epsilon_{\mu}(p_j).
\tag{6.21c}
$$

$$
\mathrm{Split}^{\eta}_{\overline{q}\to g\overline{q}}(ij, i, j) = \frac{1}{(p_i+p_j)^2 - m^2_{ij}}\, \overline{v}^{\eta}(p_{ij})\,\gamma^{\mu}\, u(p_j)\, \epsilon_{\mu}(p_i).
\tag{6.21d}
$$

Essentially, these are the kinematical parts of the Feynman rules together with the polarizations/spinors of all particles, including the splitting parton (ij). The $g \to gg$ splitting is a re-written version of the original three gluon vertex (see equation (2.9)) where $p_{ij} \approx p_i + p_j$ (up to sub-leading terms) and gauge invariance were used. Note that we explicitly gave the $\overline{q} \to g\overline{q}$ splitting. Formally, it is identical with the $q \to qg$ splitting if one replaces $u \leftrightarrow \overline{v}$, $\overline{u} \leftrightarrow v$, and $i \leftrightarrow j$; we need it later on for initial state radiation. Unless we mention the splitting explicitly, the reader should assume that any statements concerning the

$q \to qg$ splitting that we make henceforth are also valid for $\overline{q} \to g\overline{q}$ with said replacements. Furthermore, note that each $\mathrm{Split}_{(ij)\to i+j}$ function contains the full denominator of the emitter propagator. Like in the soft limit, the above expressions are valid for all helicity parameterizations.

In the following, we will show that the product $\mathrm{Split}^{\eta^*}_{(ij)\to i+j}\mathrm{Split}^{\eta'}_{(ij)\to i+j}$ is actually a generalization of the Altarelli–Parisi splitting kernels as given in equation (4.13). To do so, we assume that we sum over the helicity eigenstates of particles i and j in the following. Aside from the fact that the Altarelli–Parisi kernels also contain the color factor which is not included in the $\mathrm{Split}_{(ij)\to i+j}$ function, the only other difference from a formal point of view is that $\mathcal{P}_{(ij)\to i+j}$ contains both propagator denominators as compared to only one for the Altarelli–Parisi kernels. When we defined the Altarelli–Parisi kernels earlier, we stressed that during their derivation, all integrable terms of $\mathcal{O}\left(k_\perp\right)$ are dropped. This is something that we do not do for the $\mathrm{Split}_{(ij)\to i+j}$ functions because to do so, we would have to insert specific parameterizations of polarization vectors and spinors instead of using general ones—which we do not do here on purpose. In conclusion, the helicity summed squared $\mathrm{Split}_{(ij)\to i+j}$ functions are related to the Altarelli–Parisi splitting kernels as follows:

$$\sum_{\lambda_i,\lambda_j} \mathrm{Split}^{\eta^*}_{(ij)\to i+j}\mathrm{Split}^{\eta'}_{(ij)\to i+j} = \frac{1}{\mathbf{T}^2_{(ij)\to i+j}} \frac{2}{(p_i+p_j)^2 - m^2_{ij}} \, \boldsymbol{P}^{\eta\eta'}_{(ij)\to i+j} + \cdots. \tag{6.22}$$

In turn, this means that the full limit in equation (6.19) is a generalization of the collinear limit for helicity summation. The fact that it contains additional integrable terms is of no concern, since we will use the above limit only for the helicity mixing terms that integrate to zero.

6.2.4 Construction of the Additional Dipoles

Let us think about the construction of the additional dipoles. We have to extend the existing dipoles so that they also subtract the poles due to the helicity mixing terms. Since this affects each dipole, our additional subtraction term has the same basic structure as $\mathrm{d}\sigma^{\mathrm{A}}_{\mathrm{CS}}$ (we also take initial state radiation into account from the beginning):

$$\mathrm{d}\sigma^{\widetilde{\mathrm{A}}} \propto \mathrm{d}\Phi_{n+1}\Bigg(\sum_{\substack{(i,j)\\k\neq i,j}} \widetilde{\mathcal{D}}_{ij,k}\, J_n(\tilde{p}_{ij},\tilde{p}_k) + \sum_{c\in\{a,b\}} \sum_{(i,j)} \widetilde{\mathcal{D}}^c_{ij}\, J_n(\tilde{p}_{ij};\tilde{p}_a)$$

$$+ \sum_{c\in\{a,b\}} \sum_{(j,k)} \widetilde{\mathcal{D}}^{cj}_k\, J_n(\tilde{p}_k;\tilde{p}_{cj}) + \sum_{\substack{c,d\in\{a,b\}\\c\neq d}} \sum_j \widetilde{\mathcal{D}}^{cj,d}\, J_n(\widetilde{\Phi}_n;\tilde{p}_{cj},p_d) \Bigg). \tag{6.23}$$

Therein, we defined new dipoles $\widetilde{\mathcal{D}}$ which in turn contain new spin–correlation matrices $\widetilde{V}$ times the same color correlations that we had before since there is no change in the color structure compared to the Catani–Seymour derivation.

Before we give the exact relation between the $\widetilde{D}$ and $\widetilde{V}$, we will first consider the

ingredients of the $\widetilde{V}$. To this end, let us restrict ourselves to the final–final case first. How do we turn the previously discussed expressions in the soft and collinear limits into a unified spin–correlation matrix? The answer is given by the following formula:

$$\widetilde{V}_{ij,k} = \mathbf{T}^2_{(ij)\to i+j} \, \mathcal{R} \left[\mathcal{P}_{(ij)\to i+j} + \mathcal{S}_{(ij)\to i+j} \right] \tag{6.24}$$

where $\mathcal{P}_{(ij)\to i+j}$ is the previously constructed collinear splitting kernel, see equation (6.20). $\mathcal{S}_{(ij)\to i+j}$ is a yet to be determined soft function. During our initial discussion of the dipole formalism, we discarded the possibility of simply adding the results of the two limits due to double counting of overlapping soft and (quasi-)collinear divergences. The way that we formulated the soft and (quasi-)collinear limits above, however, allows us to identify such doubly counted contributions and consequently drop them. In the following, we will construct $\mathcal{S}_{(ij)\to i+j}$ such that it contains all soft poles which are not already covered by $\mathcal{P}_{(ij)\to i+j}$.

We do this by analyzing the soft limit of the (quasi-)collinear function $\mathcal{P}_{(ij)\to i+j}$ and the (quasi-)collinear limit of the soft terms $S_{ij,k}$. A comparison of the two double limits reveals terms that are counted twice so that we can subsequently drop them.

Let us begin with the (quasi-)collinear limit of the soft term $S_{ij,k}$. The important terms to look at are the denominators in equations (6.18). Using Sudakov's parameterization for the momenta, we find that $(p_i p_j)^2 = \mathcal{O}\left(\lambda^2_{\mathrm{coll}}\right)$ and $(p_k p_j)(p_i p_j + p_k p_j) = \mathcal{O}\left(\lambda_{\mathrm{coll}}\right)$ and thus only the first term in parentheses yields a contribution to the overlapping divergence:

$$\lim_{p_i \| p_j} \left[S_{ij,k} \right]_{\mu\nu} = \frac{(p_i \epsilon_j^*)(p_i \epsilon_j)}{(p_i p_j)^2} \epsilon_\mu(p_i) \, \epsilon_\nu^*(p_i), \tag{6.25a}$$

$$\lim_{p_i \| p_j} \left[S_{ij,k} \right]_{\alpha\beta} = \frac{(p_i \epsilon_j^*)(p_i \epsilon_j)}{(p_i p_j)^2} u_\alpha(p_i) \, \overline{u}_\beta(p_i). \tag{6.25b}$$

As a second step, we analyze the soft limit of the (quasi-)collinear term $\mathcal{P}_{(ij)\to i+j}$. We do this separately for each splitting. For the $g \to gg$ splitting, we can use the fact that $p_j = \mathcal{O}\left(\lambda_{\mathrm{soft}}\right)$ as well as $p_{ij} = p_i + p_j \to p_i$ which cancels some terms due to gauge invariance so that we end up with

$$\lim_{p_j \to 0} \left[\mathcal{P}_{g \to gg} \right]_{\mu\nu} = \frac{(p_i \epsilon_j^*)(p_i \epsilon_j)}{(p_i p_j)^2} \epsilon_\mu(p_i) \, \epsilon_\nu^*(p_i). \tag{6.26}$$

Obviously, the $g \to q\overline{q}$ splitting has no soft limit since soft quarks do not yield a divergence, as we discussed before. In the case of the $q \to qg$ splitting, we can use $p_{ij} = p_i + p_j \to p_i$ together with the fact that the emitter mass is the same as the mass of quark i, $m_{ij} = m_i$. This enables us to use the Dirac equation in the form $(\not{p}_{ij} + m_{ij}) u(p_i) \to (\not{p}_i + m_i) u(p_i) = 0$. Other than that, some standard Dirac algebra suffices to obtain the result

$$\lim_{p_j \to 0} \left[\mathcal{P}_{q \to qg} \right]_{\alpha\beta} = \frac{(p_i \epsilon_j^*)(p_i \epsilon_j)}{(p_i p_j)^2} u_\alpha(p_i) \, \overline{u}_\beta(p_i). \tag{6.27}$$

Comparing these results[4], we find that the soft limit of the (quasi-)collinear expression agrees with the (quasi-)collinear limit of the soft expression, and that the resulting term is identical to the first term of the soft limit function $S_{ij,k}$. Thus, we can formulate a subtraction term by using the (quasi-)collinear operator $\mathcal{P}_{(ij)\to i+j}$ and supplementing it with an additional soft function that is composed of the second term of $S_{ij,k}$ and which reads:

$$[\widetilde{\mathcal{S}}_{g\to gg}]_{\mu\nu} = -\frac{(p_i\epsilon_j^*)(p_k\epsilon_j) + (p_k\epsilon_j^*)(p_i\epsilon_j)}{(p_kp_j)(p_ip_j + p_kp_j)}\epsilon_\mu(p_i)\,\epsilon_\nu^*(p_i)$$

$$-\frac{(p_j\epsilon_i^*)(p_k\epsilon_i) + (p_k\epsilon_i^*)(p_j\epsilon_i)}{(p_kp_i)(p_jp_i + p_kp_i)}\epsilon_\mu(p_j)\,\epsilon_\nu^*(p_j), \tag{6.28a}$$

$$[\widetilde{\mathcal{S}}_{g\to q\bar{q}}]_{\mu\nu} = 0 \tag{6.28b}$$

$$[\widetilde{\mathcal{S}}_{q\to qg}]_{\alpha\beta} = -\frac{(p_i\epsilon_j^*)(p_k\epsilon_j) + (p_k\epsilon_j^*)(p_i\epsilon_j)}{(p_kp_j)(p_ip_j + p_kp_j)}u_\alpha(p_i)\,\overline{u}_\beta(p_i). \tag{6.28c}$$

Notice that the term for the $g \to gg$ splitting contains the same expression twice, with exchanged indices $i \leftrightarrow j$. This is due to the fact that both gluons can become soft—obviously we have to subtract the poles for both cases. Also note that we made the fact that the $g \to q\bar{q}$ splitting has no soft poles explicit by setting the corresponding function to zero.

Unfortunately, the above formulation of the soft term is not yet correct; it contains a hidden trap which will lead to a malfunctioning subtraction. We will approach this problem by looking again at how we initially re-wrote the eikonal currents. We started from equation (3.36) where we we made the simplification

$$J^{\mu\dagger} d_{\mu\nu} J^\nu = \sum_\lambda J^{\mu\dagger}\left(-g_{\mu\nu} + \frac{p_{j_\mu}q_{j_\nu} + q_{j_\mu}p_{j_\nu}}{p_jq_j}\right)J^\nu = -J^{\mu\dagger}g_{\mu\nu}J^\nu \tag{6.29}$$

in equation (4.8). The gauge terms could be dropped due to current conservation. While this is a useful simplification, it does not have to be done. In fact, when we use the helicity eigenstates implemented in our code (see equation (3.8) on page 27) we automatically include the gauge terms. And since our $\widetilde{\mathcal{S}}_{(ij)\to i+j}$ contain the polarizations explicitly, there are additional contributions to $\widetilde{\mathcal{S}}_{(ij)\to i+j}$ due to the gauge terms. This is where our Catani–Seymour like subtraction term $d\sigma^\lambda$ differs from $d\sigma_{CS}^A$. If these terms were integrable contributions of order $\mathcal{O}\left(1/\lambda_{soft}\right)$, this would not be a problem. However, it turns out that some of these contributions are actually singular in the soft limit which is an artifact of our choice of reference momenta: the denominator of the gauge terms is p_jq_j which behaves like λ_{soft}^2 with the choice $q_j = (p_j^0, -\vec{p}_j)$. Due to cancellations, the numerator $p_{j_\mu}q_{j_\nu} \sim \lambda_{soft}^2 k_\mu k_\nu$ does not always compensate this behavior. This creates spurious *local* singularities per dipole that spoil the cancellation of $d\sigma_{CS}^A$ and $d\sigma^\lambda$; they have to be avoided.

The only way of getting rid of these divergences is to evaluate $d\sigma^\lambda$ analytically and

---

[4]Obviously this means comparing the total amplitudes and not just the limits of $S_{ij,k}$ and $\mathcal{P}_{(ij)\to i+j}$. However, using color algebra one can show that the amplitudes correspond up to these two functions.

comparing it to $d\sigma_{\text{CS}}^{\text{A}}$. We can do this by calculating our soft and collinear operators $\widetilde{\mathcal{S}}_{(ij)\to i+j}$ and $\mathcal{P}_{(ij)\to i+j}$ for helicity summation with respect to partons i and j and adding the negative Catani–Seymour term. There are two splittings with soft divergences, $q \to qg$ and $g \to gg$, which we need to analyze separately. Since these calculations contain some non-trivial aspects, the interested reader can find some details in appendix C. For clarity, we only present the final results in the following.

It turns out that there is one universal term that creates a spurious soft singularity due to the gauge terms. By universal, we mean that the term has the same structure for both splittings. As derived in the appendix, the proper soft terms read

$$
[\mathcal{S}_{g\to gg}]_{\mu\nu} = \left[-\frac{(p_i\epsilon_j^*)(p_k\epsilon_j) + (p_k\epsilon_j^*)(p_i\epsilon_j)}{(p_kp_j)(p_ip_j + p_kp_j)} + \frac{4(p_kq_j - p_iq_j)}{(p_jq_j)(p_ip_j + p_jp_k)} \right] \epsilon_\mu(p_i)\,\epsilon_\nu^*(p_i)
$$
$$
+ \left[-\frac{(p_j\epsilon_i^*)(p_k\epsilon_i) + (p_k\epsilon_i^*)(p_j\epsilon_i)}{(p_kp_i)(p_jp_i + p_jp_i)} + \frac{4(p_kq_i - p_jq_i)}{(p_iq_i)(p_jp_i + p_ip_k)} \right] \epsilon_\mu(p_j)\,\epsilon_\nu^*(p_j),
$$

$$\tag{6.30a}$$

$$
[\mathcal{S}_{g\to q\bar{q}}]_{\mu\nu} = 0 \tag{6.30b}
$$

$$
[\mathcal{S}_{q\to qg}]_{\alpha\beta} = \left[-\frac{(p_i\epsilon_j^*)(p_k\epsilon_j) + (p_k\epsilon_j^*)(p_i\epsilon_j)}{(p_kp_j)(p_ip_j + p_kp_j)} + \frac{4(p_kq_j - p_iq_j)}{(p_jq_j)(p_ip_j + p_jp_k)} \right] u_\alpha(p_i)\,\overline{u}_\beta(p_i),
$$

$$\tag{6.30c}$$

where the second term in each square bracket is new. Instead of the functions $\widetilde{\mathcal{S}}_{(ij)\to i+j}$, we will use these definitions. Notice that this will affect both $d\sigma^\phi$ and $d\sigma^\lambda$ and not only $d\sigma^\lambda$; if this were not the case, our additional subtraction term $d\sigma^{\widetilde{A}}$ would no longer integrate to zero which would spoil our method.

We are now ready to properly formulate the dipoles.

6.2.5 Subtraction for Helicity Mixing Terms

In the following, we will specify the dipoles four all four emitter–spectator cases. For each case, we will use exactly the same momentum parameterizations as presented earlier. As we will see, our general definitions of the soft and collinear functions make it easy to define proper spin–correlation matrices.

Final–Final Dipoles for Helicity Mixing Terms

In principle, the final–final case has already been discussed above. We use the exact same momentum parameterization that has been presented in equation (4.66) which equals the definition (4.18) in the massless case, as discussed before.

Concerning the dipoles themselves, there are only two minor differences to the original Catani–Seymour definitions which can be inferred from our earlier discussion. The dipoles

are defined by

$$\widetilde{\mathcal{D}}_{ij,k}(p_1,\ldots p_{n+1}) = -4\pi\alpha_s\mu^{2\epsilon}\mathcal{A}_n^{*\xi}(\widetilde{ij},\widetilde{k})\left(\frac{\mathbf{T}_k\cdot\mathbf{T}_{ij}}{\mathbf{T}_{ij}^2}[\widetilde{V}_{ij,k}]_{\xi\zeta}\right)\mathcal{A}_n^{\zeta}(\widetilde{ij},\widetilde{k}). \tag{6.31}$$

Compared to the original definition, equation (4.23) for the massless or equation (4.65) for the massive case, we have not included the coupling constant inside the spin–correlation matrices while our definition of $\widetilde{V}_{ij,k}$ contains the propagator instead. Thus, one could say that the differences reside only in the definition of the spin–correlation matrices, which in our case are given by the previously mentioned formula

$$\widetilde{V}_{ij,k} = \mathbf{T}_{(ij)\to i+j}^2\,\mathcal{R}\left[\mathcal{P}_{(ij)\to i+j} + \mathcal{S}_{(ij)\to i+j}\right]. \tag{6.32}$$

Final–Initial Dipoles for Helicity Mixing Terms

We use the same momentum parameterization as in equation (4.77) on page 79. The dipole is formally identical with the final–final case:

$$\widetilde{\mathcal{D}}_{ij}^a(p_1,\ldots p_{n+1}) = -4\pi\alpha_s\mu^{2\epsilon}\mathcal{A}_n^{*\xi}(\widetilde{ij};\widetilde{a})\left(\frac{\mathbf{T}_a\cdot\mathbf{T}_{ij}}{\mathbf{T}_{ij}^2}[\widetilde{V}_{ij}^a]_{\xi\zeta}\right)\mathcal{A}_n^{\zeta}(\widetilde{ij};\widetilde{a}). \tag{6.33}$$

However, the spin–correlation function is slightly different. Our general formulation of $\mathcal{P}_{(ij)\to i+j}$ and $\mathcal{S}_{(ij)\to i+j}$ allows us to relate this function to the final–final case by a simple manual momentum crossing:

$$\widetilde{V}_{ij}^a(\tilde{p}_{ij},p_i,p_j,p_a) = \widetilde{V}_{ij,a}(\tilde{p}_{ij},p_i,p_j,-p_a) \tag{6.34}$$

where we explicitly gave the momentum arguments for the spin–correlation functions.

Initial–Final Dipoles for Helicity Mixing Terms

The same applies to the initial–final case where we use the momentum parameterization from equation (4.82). The dipoles have the same form as before,

$$\widetilde{\mathcal{D}}_k^{aj}(p_1,\ldots p_{n+1}) = -4\pi\alpha_s\mu^{2\epsilon}\mathcal{A}_n^{*\xi}(\tilde{p}_k;\widetilde{aj})\left(\frac{\mathbf{T}_{aj}\cdot\mathbf{T}_k}{\mathbf{T}_{aj}^2}[\widetilde{V}_k^{aj}]_{\xi\zeta}\right)\mathcal{A}_n^{\zeta}(\tilde{p}_k;\widetilde{aj}), \tag{6.35}$$

while the spin–correlation matrices can again be related to the final–final case:

$$\widetilde{V}_k^{aj}(\tilde{p}_{aj},p_a,p_j,p_k) = \mathcal{C}_{a,(aj)}\,\widetilde{V}_{aj,k}(-\tilde{p}_{aj},-p_a,p_j,p_k). \tag{6.36}$$

Note, however, that we need to cross the emitter parton into the initial state. In the final–initial case, it was sufficient to cross the spectator momentum by negating it since the spectator does not appear in terms of a spinor or polarization. This is different here,

which is why we introduced the *crossing operator* $\mathcal{C}_i$ defined by

$$
\begin{aligned}
\mathcal{C}_i \, \epsilon(p_i) &= \epsilon^*(p_i) & \mathcal{C}_i \, \epsilon^*(p_i) &= \epsilon(p_i) \\
\mathcal{C}_i \, u(p_i) &= v(p_i) & \mathcal{C}_i \, v(p_i) &= u(p_i) \\
\mathcal{C}_i \, \overline{u}(p_i) &= \overline{v}(p_i) & \mathcal{C}_i \, \overline{v}(p_i) &= \overline{u}(p_i)
\end{aligned}
\tag{6.37}
$$

which applies to the parton i. Note that we use the operator with multiple parton indices which means that it acts on all indicated partons. Let us stress that it is important to consider all *four* splittings here including the $\overline{q} \rightarrow g\overline{q}$ splitting so that we obtain all four spin–correlation matrices $\widetilde{V}_k^{gg}$, $\widetilde{V}_k^{qq}$, $\widetilde{V}_k^{g\overline{q}}$, and $\widetilde{V}_k^{qg}$, in analogy to the discussion in section 4.2.6.

Initial–Initial Dipoles for Helicity Mixing Terms

In the double initial state case, we make use of the momentum re-parameterizations starting with equation (4.88) which includes the Lorentz transformation of all final state particles.

The dipoles read

$$
\begin{aligned}
\widetilde{\mathcal{D}}^{aj,b}&(p_1, \ldots p_{n+1}) \\
&= -4\pi\alpha_s\mu^{2\epsilon} \mathcal{A}_n^{*\,\xi}(\widetilde{\Phi}_n; \widetilde{aj}, p_b) \left(\frac{\mathbf{T}_{aj} \cdot \mathbf{T}_b}{\mathbf{T}_{aj}^2} [\widetilde{V}^{aj,b}]_{\xi\zeta} \right) \mathcal{A}_n^{\zeta}(\widetilde{\Phi}_n; \widetilde{aj}, p_b).
\end{aligned}
\tag{6.38}
$$

Again, the relevant information is contained in the spin–correlation matrices which are related to the final–final case by

$$
\widetilde{V}^{aj,b}(\tilde{p}_{aj}, p_a, p_j, p_b) = \mathcal{C}_{a,(aj)} \, \widetilde{V}_{aj,b}(-\tilde{p}_{aj}, -p_a, p_j, -p_b)
\tag{6.39}
$$

which again employs the crossing operator discussed before.

This concludes our discussion of dipole subtraction with random polarizations.

6.3 Implementation for Leading Color $e^- e^+ \rightarrow n$ Jets

The implementation of random polarizations in a numerical program is straight forward since they can be easily computed from helicity eigenstates. We mentioned earlier that we actually implement a slightly different version of the parameterization, which reads as follows:

$$
\epsilon(p, \phi) = e^{2\pi i\phi}\epsilon^+(p) + e^{-2\pi i\phi}\epsilon^-(p).
\tag{6.40}
$$

With this parameterization, ϕ takes values in the range $[0, 1)$ and thus it is perfectly suited for Monte Carlo integration. Furthermore, it avoids the normalization factor $1/2\pi$ that we had to multiply the integral over the angle with.

At next–to–leading order, it is also straight forward to use the existing terms with the
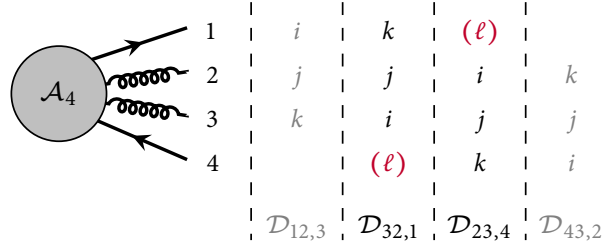
Figure 6.2: Real emission matrix element and leading color dipoles for $e^- e^+ \to 3\,jets$. The dipoles important for the discussion are $\mathcal{D}_{32,1}$ and $\mathcal{D}_{23,4}$. Note that k always indicates the spectator. The momentum of the parton (ℓ) is needed to implement the subtraction correctly for leading color amplitudes with color decomposition, see text.

new parameterization. The only entirely new aspect is the additional subtraction term $d\sigma^{\widetilde{A}}$. Since we constructed all terms in a very general way—meaning that they are based on Feynman rules and Lorentz products—they are easy to implement. However, we have to make some changes due to the fact that we use color decomposition and only make leading order computations.

$d\sigma^{\widetilde{A}}$ explicitly contains terms for the $g \to gg$ splitting that treat the case where gluon i becomes soft. Just like for helicity summation and sampling, these terms describe soft singularities that cannot appear in our computation (confer section 4.3). Let us consider the example of four jet production, see figure 6.2. The two $g \to gg$ dipoles are given in black. The only soft divergences our calculation should subtract are those where j becomes soft, i.e. where the invariant s_{ij} goes to zero. If parton i becomes soft, we also subtract terms where s_{ik} goes to zero; as explained in section 4.3, these are poles of non-neighboring partons and thus they cannot appear in our real emission matrix element. Again, we have to "shift" these terms among the dipoles, i.e. we have to subtract the associated pole, but not in the given kinematic configuration. We can achieve this by multiplying each gluonic dipole with the following factor:

$$\frac{2 s_{ik}}{s_{ik} + s_{j\ell}} \tag{6.41}$$

where i and k are the indices that appear in the dipole and ℓ is a parton that does not normally appear in the dipole: it is the spectator of the other dipole with the same emitter pair, hence it is the parton that is a direct neighbor to the emitter pair on the other side of the spectator. An illustration for the example of figure 6.2 can be found in the example box on the following page.

Note that with this modification, we can completely leave out the part of the soft function $\mathcal{S}_{g \to gg}$ that treats the soft parton i since it gives a finite contribution anyway. Doing so saves some unnecessary computations and thus make the algorithm more efficient.

In summary, we only have to change those dipoles that describe the splitting $g \to gg$. The modified spin–correlation matrix reads

$$\widetilde{V}_{gg,k} = \mathbf{T}^2_{g \to gg} \frac{2 s_{ik}}{s_{ik} + s_{j\ell}} \mathcal{R} \Big[\mathcal{P}_{g \to gg} + \mathcal{S}'_{g \to gg} \Big] \tag{6.42}$$

where the index ℓ is given by

$$\ell = \begin{cases} \max(i,j)+1 & \text{if } k < (i,j) \\ \min(i,j)-1 & \text{if } k > (i,j). \end{cases} \tag{6.43}$$

The modified soft function $\mathcal{S}'_{g\to gg}$ is given by the normal soft function, equation (6.30) without the terms for soft parton i:

$$[\mathcal{S}'_{g\to gg}]_{\mu\nu} = \left[-\frac{(p_i\epsilon_j^*)(p_k\epsilon_j)+(p_k\epsilon_j^*)(p_i\epsilon_j)}{(p_kp_j)(p_ip_j+p_kp_j)} + \frac{4(p_kq_j-p_iq_j)}{(p_jq_j)(p_ip_j+p_jp_k)} \right] \epsilon_\mu(p_i)\,\epsilon_\nu^*(p_i). \tag{6.44}$$

This finishes our discussion of the implementation of random polarization.

Example: Leading Color Dipoles for Random Polarizations, $e^-e^+ \to 3$ Jets

For $\mathcal{D}_{32,1}$ we have $\ell = 4$ and for $\mathcal{D}_{23,4}$ we have $\ell = 1$, they are also indicated in figure 6.2. We find the following table of variables:

	$\mathcal{D}_{32,1}$	$\mathcal{D}_{23,4}$
s_{ik}:	s_{13}	s_{24}
$s_{j\ell}$:	s_{24}	s_{13}

Note that the invariants that appear in equation (6.41) are the same for both dipoles, but interchanged: $s_{ik} \leftrightarrow s_{jk}$. Let us now consider what happens when p_3, and thus s_{13} tends to zero. In this case, we want the corresponding contribution to be subtracted by $\mathcal{D}_{23,4}$ which treats poles coming from parton 3 being soft. Indeed, we find the following for the factor:

$$\mathcal{D}_{32,1}: \qquad \frac{2s_{13}}{s_{13}+s_{24}} \xrightarrow{s_{13}\to 0} 0$$

$$\mathcal{D}_{23,4}: \qquad \frac{2s_{24}}{s_{24}+s_{13}} \xrightarrow{s_{13}\to 0} 2.$$

The case where gluon 3 becomes soft is now accounted for solely by dipole $\mathcal{D}_{23,4}$ which describes the soft limit correctly. We find a similar picture for the case where $s_{24} \to 0$ and parton 2 becomes soft; $\mathcal{D}_{32,1}$ subtracts this divergence in full.

6.4 Checks and Analysis

Random polarizations obviously also require one extra helicity variable per particle in the process. In that sense, the method is very similar to n–dimensional sampling and we can perform the same analyses. First, we verify that our subtraction terms work.

Checks of the Subtraction Terms

Once more, we can investigate the soft and collinear limits for an otherwise unaltered momentum configuration and for a fixed, randomly chosen set of helicity angles. The plots are shown in figure 6.3 for the soft limit, and in figure 6.4 for the collinear limit. The respective upper and lower graphs present the same information we also analyzed for helicity summation and sampling, i.e. the slopes for the unsubtracted and subtracted real emission matrix element (i.e. $d\sigma^R - d\sigma^A_{RP} = d\sigma^R - d\sigma^A_{CS} - d\sigma^{\widetilde{A}}$), as well as the ratio of the unsubtracted term and the subtraction term. All of them show the expected behavior. The ratios also distinctly reveal that the limits are approached smoothly: especially in the collinear case, the ratio of the subtraction term and the unsubtracted real matrix element approaches one more slowly than in the previous chapters.

The middle plots, however, are new. In section 6.2.1, we explained the separation of the total real emission integrand into the four components, recall equation (6.14):

$$\sigma^{NLO} = \int_{n+1} \left(d\sigma^R - d\sigma^A_{CS} - d\sigma^\phi + d\sigma^\lambda \right) + \int_n \left(d\sigma^V + \int_1 d\sigma^A_{CS} \right) \tag{6.45}$$

(we omit $d\sigma^C$ here because we do not consider hadronic initial states at present). As mentioned before, both the contributions $d\sigma^R - d\sigma^\phi$ and $-d\sigma^A_{CS} + d\sigma^\lambda$ should be separately integrable, i.e. of $\mathcal{O}\left(1/\lambda_{soft/coll} \right)$. We performed these two subtractions separately and plotted the resulting graphs in the two central plots of figures 6.3 and 6.4. The fits, which have been done using the same functions as the subtraction fits in the upper plots, reveal that the behavior of the contributions is in fact of $\mathcal{O}\left(1/\lambda_{soft/coll} \right)$.

In conclusion, we have three pieces of evidence that the subtraction terms work as they should. Again, we will see later on that the integration converges to a consistent value.

***VEGAS* Grid Adaptation and Performance**

To analyze the behavior of random polarizations with respect to *VEGAS*, let us first look at the adaptation of the grid. Figure 6.5 shows plots that have been performed under the same conditions as those shown for helicity summation and sampling, but this time with random polarizations. Both the Born and the real emission contribution plot are practically indistinguishable from the same plots for n–dimensional helicity sampling, see figure 5.3. Since this leads us to the same conclusions—that *VEGAS* cannot adapt to the helicity variables while the adaptation to the phase space grid is not negatively affected—let us directly move on and look at the value of the squared matrix element for a fixed momentum configuration and fixed helicity angles as we vary the value of two particle's helicity angles. The results are shown in figure 6.6 where the left hand plot shows a variation of the quark pairs helicity values while the right hand side displays the variation of the angles of two gluons. Note that the white spaces do not indicate zero as the plots suggest, but values around 10^{-12}, so neither of the plots is zero at any point. One can instantly recognize that we are dealing with a smooth distribution here. In fact, the
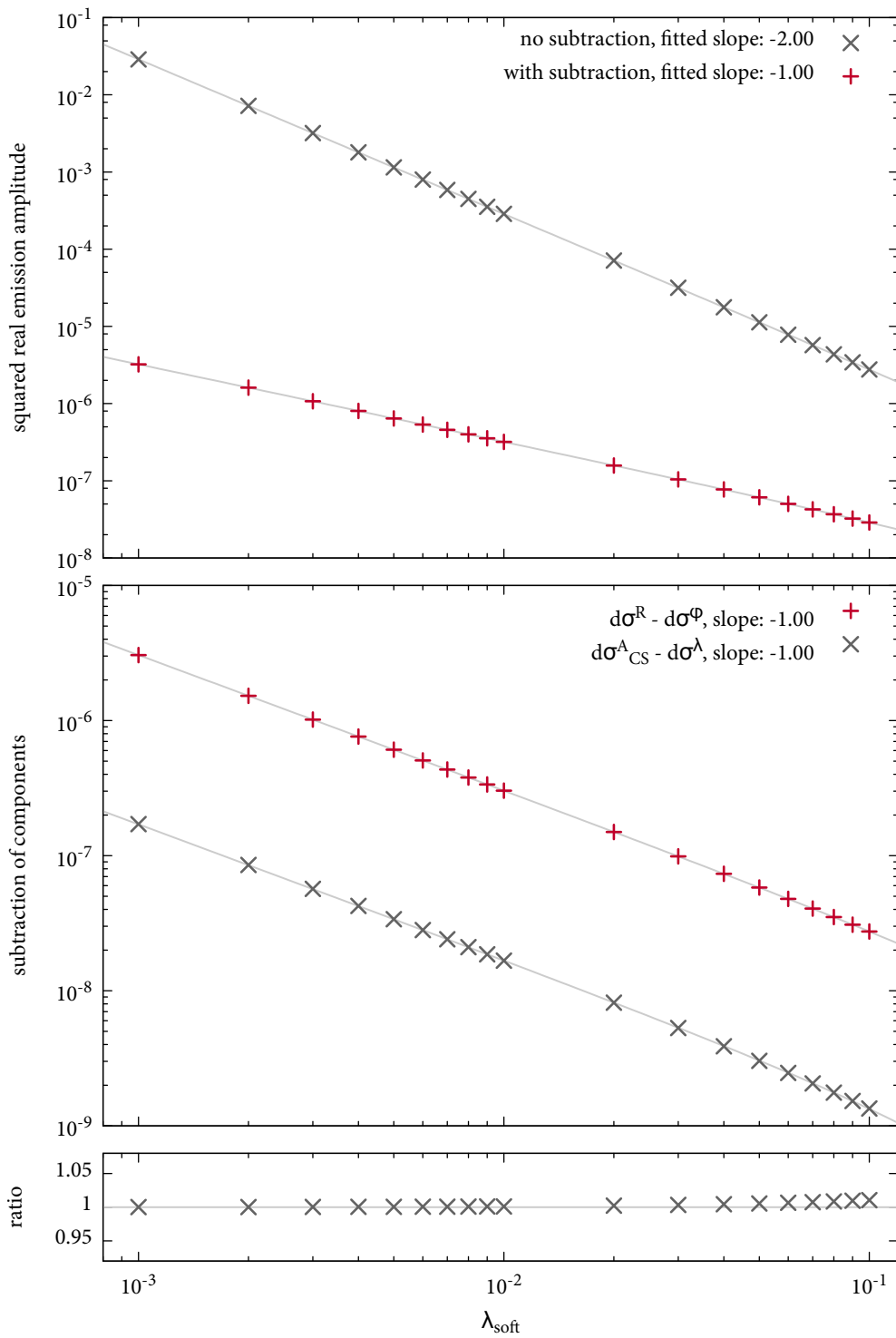
Figure 6.3: Soft behavior for $e^-e^+ \rightarrow q\boldsymbol{g}_1 g_2 g_3 g_4 g_5 g_6 \overline{q}$ with random polarizations; the unresolved soft gluon is g_1. The upper plot shows the unsubtracted and subtracted real emission amplitudes. In the middle the subtraction of the components is illustrated (see discussion in text). The lower plot show the absolute ratio of the unsubtracted matrix element and the total subtraction term; the expectation (gray line) is approximately one.
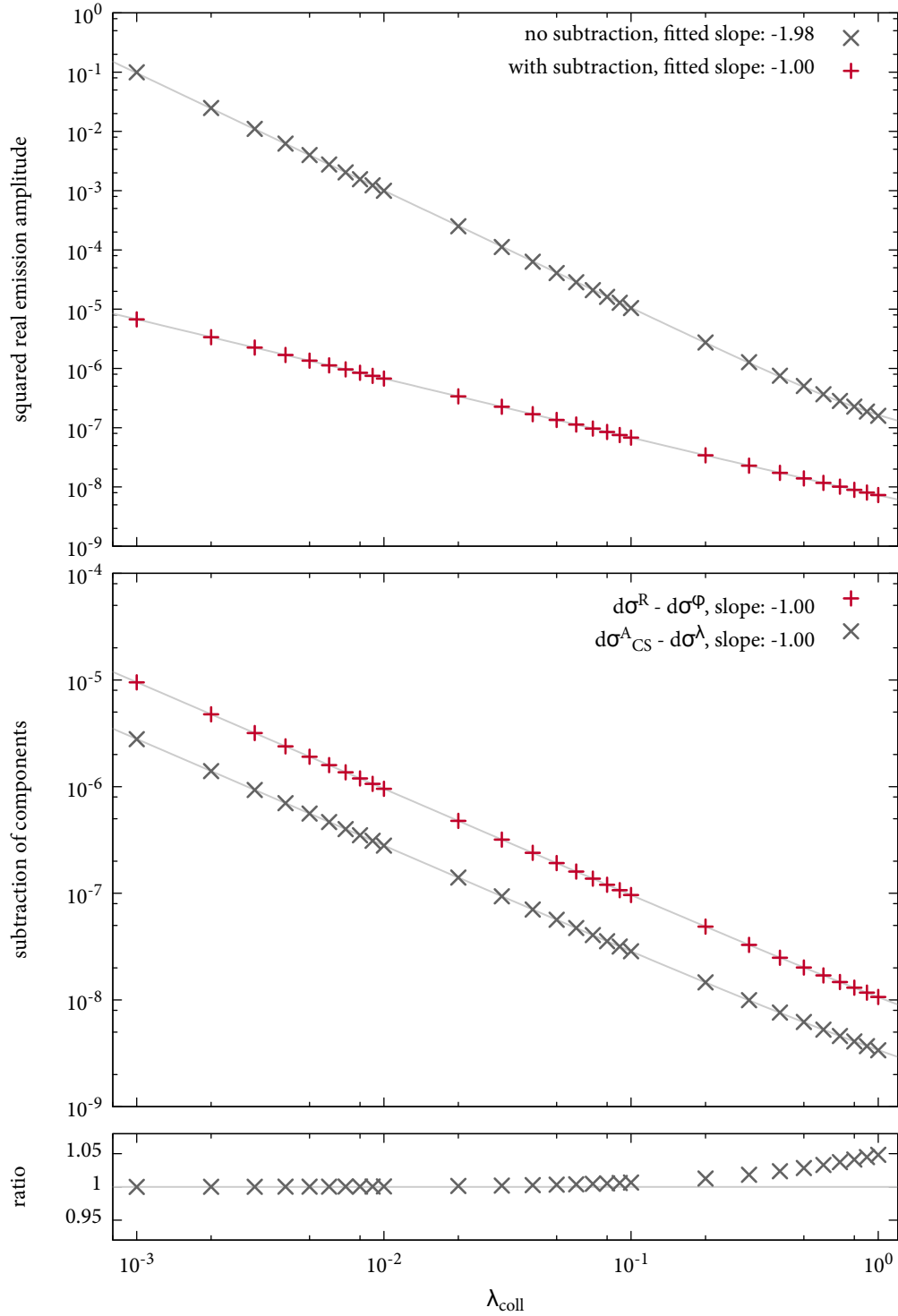
Figure 6.4: Collinear behavior for $e^-e^+ \rightarrow q g_1 g_2 g_3 g_4 g_5 \boldsymbol{g_6} \overline{q}$ with random polarizations; the collinear pair is $(g_6, \overline{q})$. The upper plot shows the unsubtracted and subtracted real emission amplitudes. In the middle the subtraction of the components is illustrated (see discussion in text). The lower plot show the absolute ratio of the unsubtracted matrix element and the total subtraction term; the expectation (gray line) is approximately one.

(a) Born 5 Jets

(b) Real emission with 4 Jets
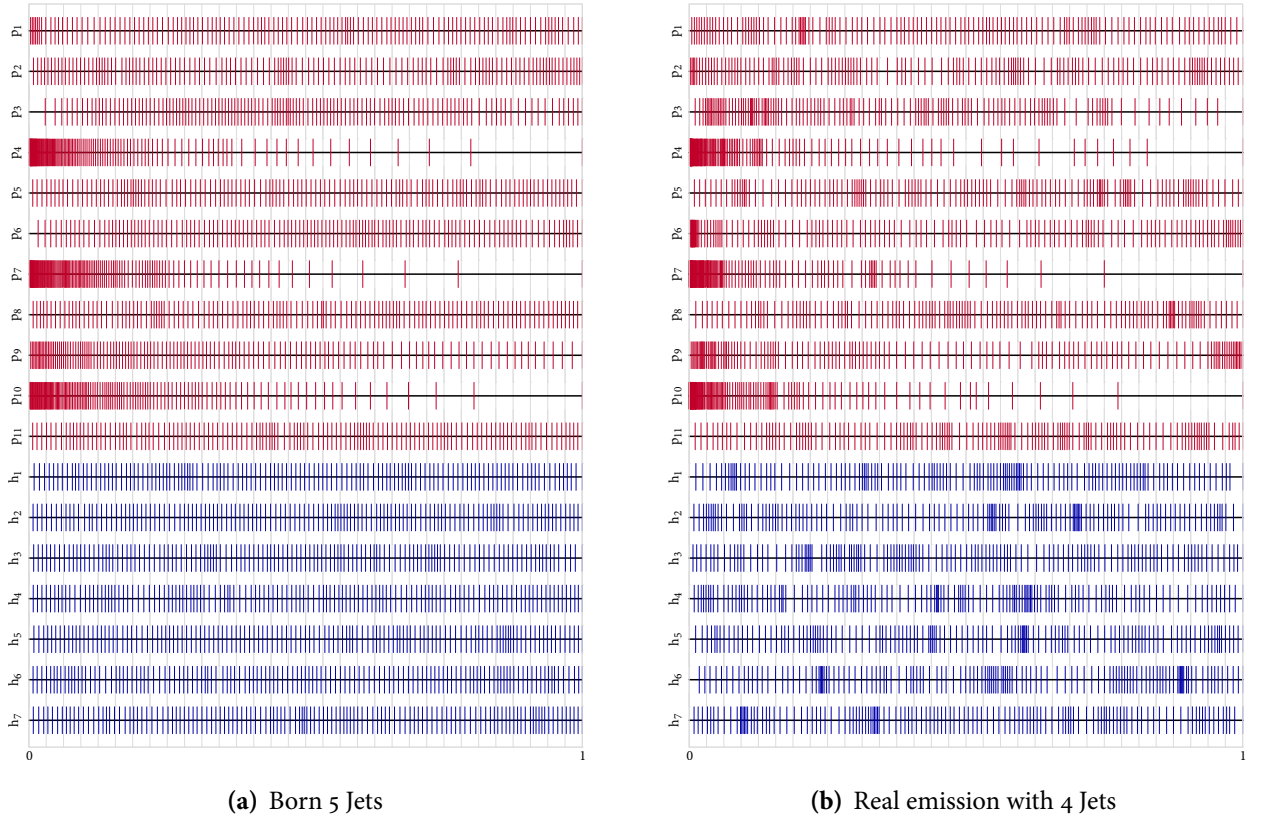
Figure 6.5: Visualization of the *VEGAS* grid for 128 bins. The red phase space variables are again very similar to those of the previous helicity methods. The blue helicity variables show almost no adaptation, similar to what we observed for n–dimensional helicity sampling.

plots show a sine or cosine-like superposition for the separate variables. This comes as no surprise since random polarizations are real-valued quantities due to $\epsilon^+ = \epsilon^{-*}$ and we can write the following:

$$\epsilon(\phi) = e^{i\phi}\epsilon^+ + e^{-i\phi}\epsilon^+ = e^{i\phi}\epsilon^+ + \text{cc.} = 2\Re\left\{e^{i\phi}\epsilon^+\right\} = 2\Re\left\{\left(\cos\phi + i\sin\phi\right)\epsilon^+\right\}. \qquad (6.46)$$

Based on these plots, it is clear that we have a similar situation as for n–dimensional sampling. While the variations of the squared amplitude are less extreme and the squared amplitude depends on the helicity angles like a smooth function, the n helicity angles are still interdependent and *VEGAS* cannot adapt to the function. However, one can also expect this to be less of a problem than for n–dimensional sampling since the matrix element never becomes zero and thus we do not "waste" a significant number of the *VEGAS* calls.

Based on this discussion, one can already guess that the number of *VEGAS* bins has no or almost no influence on the quality of the integration. Figures 6.7 and 6.8 show the corresponding plots for the Born contribution, figures 6.9 and 6.10 those for the real emission contribution. The Born contribution plot shows the typical underestimation of
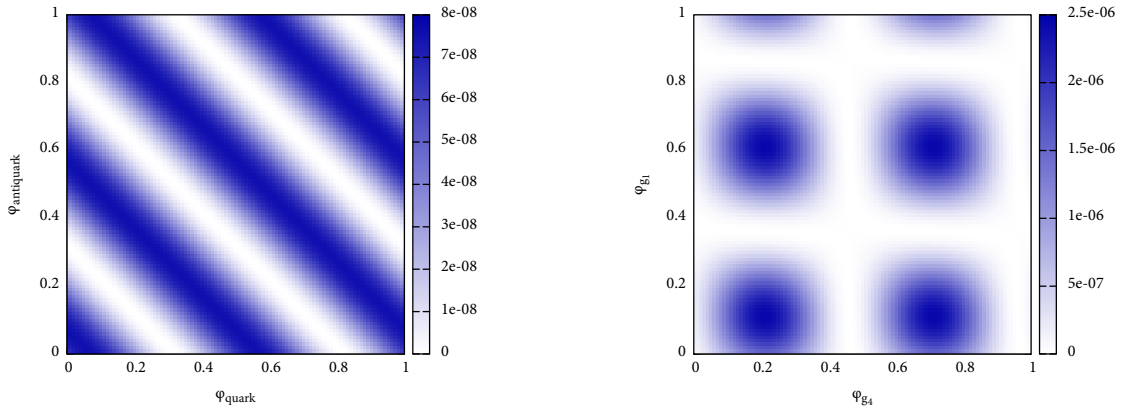
(a) Dependence on quark and antiquark helicity variables.

(b) Dependence on the helicity variables of the first and the last gluon.

Figure 6.6: Dependence of the squared amplitude on helicity variables ϕ_i. The shown process is $e^+e^- \rightarrow \bar{u}ugggg$. Both plots reveal continuous functions without factorization. However, the functions are never zero so one expects that this does not matter.

the one bin result while all other results agree well, with the 32 bin result standing out a bit. However, like before, this can be attested to the choice of the random numbers, this is no systematic behavior.

Thus, we can conclude that random polarizations do not harm the *VEGAS* grid, but they also do not make use of it. The only advantage to n–dimensional sampling is the fact that the evaluation of vanishing helicity configurations is not present—but whether this is really an advantage remains to be analyzed. We will do so in chapter 8.
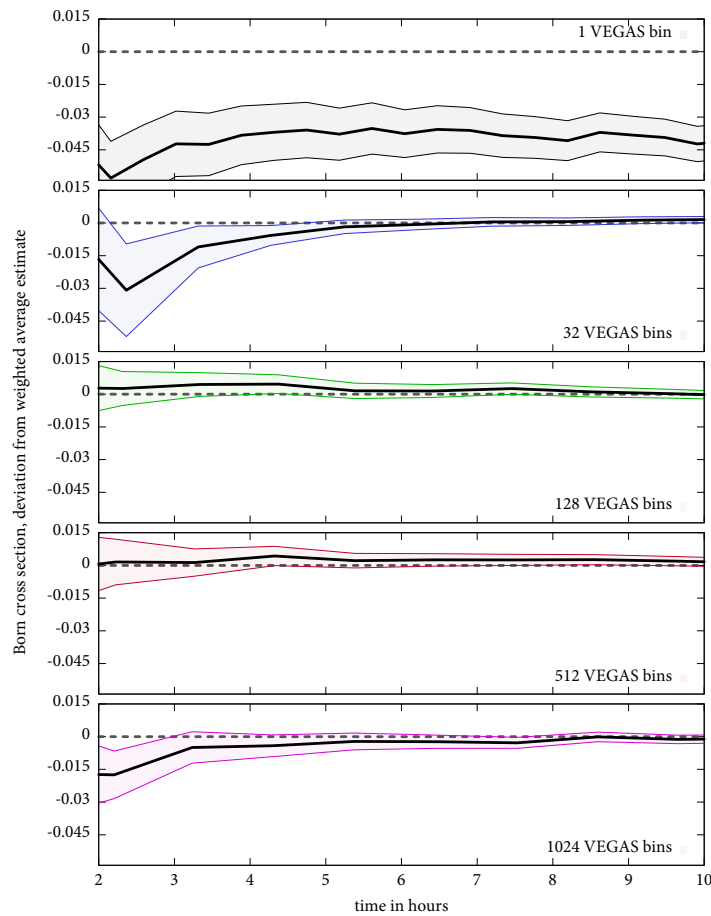
Figure 6.7: Dependence of the integration on the number of bins for the Born contribution to six jet production with random polarizations, similar to figure 4.4. Like for the other helicity methods, the one bin example underestimates the average result, while all other bin numbers agree with each other.
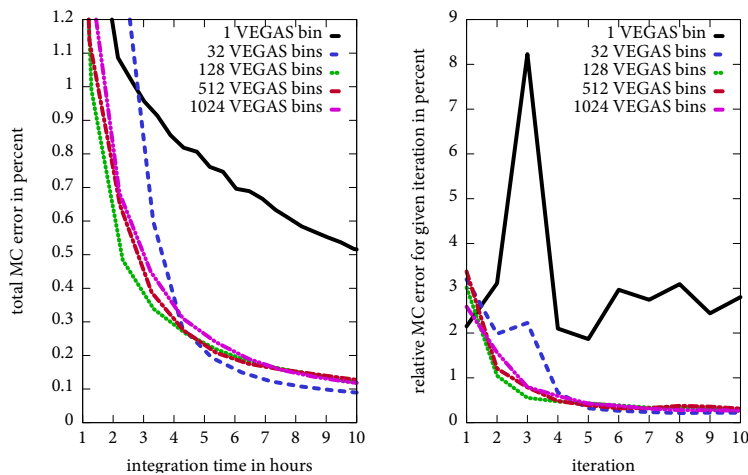
Figure 6.8: Error plots for the data in figure 6.7. All results but the one bin result are very similar and show the usual adaptation to the grid due to the phase space variables.
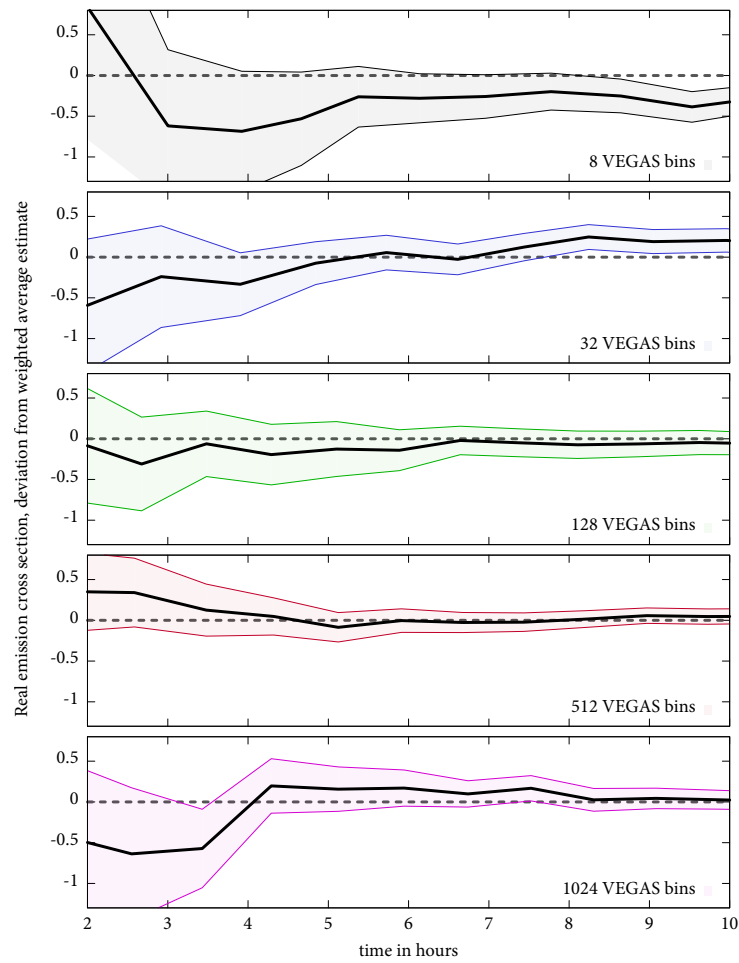
Figure 6.9: Similar figure as 6.7 but for the real emission contribution to five jet production.
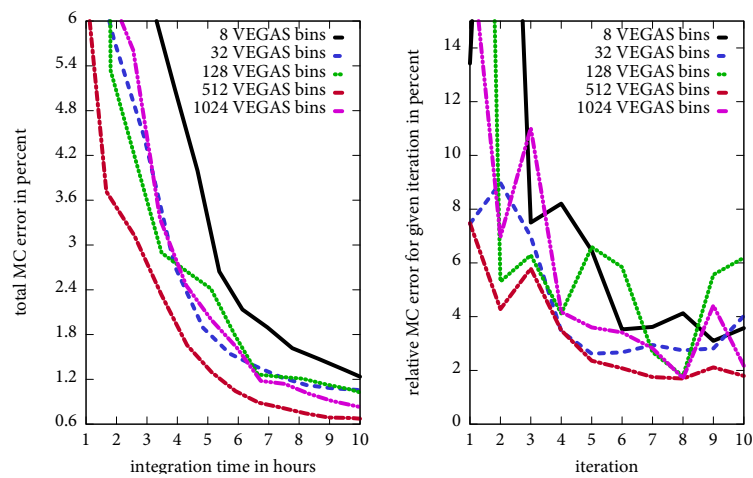
Figure 6.10: Error analysis of the data from figure 6.9. We see the usual behavior with the typical real emission fluctuations.

Linear Combination Sampling

The previous chapter introduced the concept of random polarizations which "cure" the problem of vanishing helicity amplitudes for helicity sampling. This is done by using a linear combination of the helicity eigenstates instead of one eigenstate only. It turns out that one can use a similar idea, which is essentially a change of basis in helicity space, to form two orthogonal helicity states that are rotated with respect to the eigenstates. These states can be used for helicity sampling as discussed in chapter 5. Essentially, the method presented here is not new; however, we test this method in the hope that the number of vanishing "helicity" configurations for the new states is smaller than for eigenstates and thus the integration might converge faster.

7.1   Helicity States in a Rotated Basis

For this parameterization, we introduce two new helicity states that are given by a rotation in helicity space:

$$\epsilon^{\oplus}(p) = \frac{1}{\sqrt{2}}\left(\epsilon^{+}(p) + \epsilon^{-}(p)\right), \qquad \epsilon^{\ominus}(p) = \frac{i}{\sqrt{2}}\left(\epsilon^{+}(p) - \epsilon^{-}(p)\right). \tag{7.1}$$

Instead of positive and negative helicities, we call them plus and minus helicities which we denote by the circled operators $\oplus$ and $\ominus$.

Let us stress again that this parameterization is strictly speaking not a new development, but merely a change of basis that is realized in terms of linear combinations of helicity eigenstates, hence the name *linear combination polarizations*. At the same time, it is also a special case of random polarizations with the choice $\phi = 0$ for $\epsilon^{\oplus}$ and $\phi = \pi/2$ for $\epsilon^{\ominus}$ (compare equation (6.1)), with an additional normalization factor $1/\sqrt{2}$.

We can form the products of these polarizations which read

$$
\begin{aligned}
\epsilon_\mu^{\oplus\,*}\epsilon_\nu^{\oplus} &= \frac{1}{2}\left(\epsilon_\mu^{+\,*}\epsilon_\nu^+ + \epsilon_\mu^{-\,*}\epsilon_\nu^- + \epsilon_\mu^{+\,*}\epsilon_\nu^- + \epsilon_\mu^{-\,*}\epsilon_\nu^+\right), \\
\epsilon_\mu^{\ominus\,*}\epsilon_\nu^{\ominus} &= \frac{1}{2}\left(\epsilon_\mu^{+\,*}\epsilon_\nu^+ + \epsilon_\mu^{-\,*}\epsilon_\nu^- - \epsilon_\mu^{+\,*}\epsilon_\nu^- - \epsilon_\mu^{-\,*}\epsilon_\nu^+\right).
\end{aligned}
\tag{7.2}
$$

Similar to random polarizations, we also find contributions with helicity mixing terms. Here, however, we do not integrate over an angle but we sum over the plus and minus helicities. Doing so, the helicity mixing terms cancel each other and the full polarization sum yields

$$
\sum_{\odot=\oplus,\ominus}\epsilon_\mu^{\odot\,*}\epsilon^{\odot\,\nu} = \epsilon_\mu^{\oplus\,*}\epsilon_\nu^{\oplus} + \epsilon_\mu^{\ominus\,*}\epsilon_\nu^{\ominus} = \epsilon_\mu^{+\,*}\epsilon_\nu^+ + \epsilon_\mu^{-\,*}\epsilon_\nu^- = \sum_{\lambda=\pm}\epsilon_\mu^{\lambda\,*}\epsilon_\nu^{\lambda}
\tag{7.3}
$$

which is the usual polarization sum.

Note that just like random polarizations, we can use similar parameterizations for (massive) fermion spinors.

Equation (7.3) allows us to use the above parameterization as a substitute for helicity eigenstates. As an example, we could calculate all "helicity" amplitudes for these new polarizations and sum them up, similar to section (4.1). Of course, this will not improve the calculation by any means since we still have to sum over two states per particle, equally resulting in 2^n terms. Instead, we will perform helicity sampling with this new parametrization. We can use the same two approaches as in chapter 5.

First, we can turn the sum over plus and minus helicities for each external particle into a Monte Carlo integral, giving us n additional integrals. In formulas, this is identical to n–dimensional sampling with the replacement $(+,-)\to(\oplus,\ominus)$: the integration reads

$$
\sum_{\odot_1,\ldots,\odot_n}|\mathcal{A}_{\odot_1\ldots\odot_n}|^2 = 2^n\int_{[0,1)^n}\mathrm{d}^n u\,|\mathcal{A}_{\odot_1(u_1)\ldots\odot_n(u_n)}|^2.
\tag{7.4}
$$

and uses the following parameterization for the helicity variables:

$$
\epsilon_\mu^{\odot(u)}(p) = \begin{cases}\epsilon_\mu^{\ominus}(p) & \text{for } u\in\left[0,\tfrac{1}{2}\right) \\ \epsilon_\mu^{\oplus}(p) & \text{for } u\in\left[\tfrac{1}{2},1\right).\end{cases}
\tag{7.5}
$$

The second realization is in terms of one–dimensional sampling where we again choose one random number which is then multiplied by 2^n and truncated so that we end up with an integer whose binary representation gives the assignment of plus and minus helicities. In the notation of section 5.1.2, this reads

$$
\sum_{\odot_1,\ldots,\odot_n}|\mathcal{A}_{\odot_1\ldots\odot_n}|^2 = 2^n\int_0^1\mathrm{d}u\,|\mathcal{A}_{\widetilde{\Lambda}(u\cdot 2^n)}|^2,
\tag{7.6}
$$

where $\widetilde{\Lambda}$ now maps to the space of all plus–minus helicity configurations:

$$\widetilde{\Lambda} : [0, 2^n) \to \{(\odot_1, \ldots, \odot_n) | \odot_i \in \oplus, \ominus \; \forall \; i\}. \tag{7.7}$$

What do we expect to gain from this? Essentially, we do not expect strong differences from helicity sampling with eigenstates. However, we found that many of the helicity configurations for eigenstates vanish (confer for example figure 5.6). In this rotated basis, we can hope that there are less vanishing configurations due to the fact that we always have a linear combination of eigenstates per particle. This would make the integrand flatter with respect to variations of the helicity configurations. If these assumptions hold, one can hope that there is less need for *VEGAS* to adapt while we also find less fluctuations in the numerical values of the integrand, thus leading to a better convergence.

Before we analyze the situation in section 7.3, let us discuss the subtraction terms.

7.2 Recycling Random Polarization Dipoles

If we perform sampling for the real emission contribution, then we have to subtract local poles that are due to fixed plus or minus helicities for the partons i and j. Thus, to determine the pole behavior, we have to look at the square of the polarizations which was given in equation (7.2):

$$\begin{aligned}
\epsilon_\mu^{\oplus\,*}\epsilon_\nu^\oplus &= \frac{1}{2}\left(\sum_\lambda \epsilon_\mu^{\lambda\,*}\epsilon_\nu^\lambda + \epsilon_\mu^{+\,*}\epsilon_\nu^- + \epsilon_\mu^{-\,*}\epsilon_\nu^+\right), \\
\epsilon_\mu^{\ominus\,*}\epsilon_\nu^\ominus &= \frac{1}{2}\left(\sum_\lambda \epsilon_\mu^{\lambda\,*}\epsilon_\nu^\lambda - \epsilon_\mu^{+\,*}\epsilon_\nu^- - \epsilon_\mu^{-\,*}\epsilon_\nu^+\right).
\end{aligned} \tag{7.8}$$

Like random polarizations, they contain both the usual polarization sum and also helicity mixing terms. Thus, we have already solved the principal problem in the previous chapter, meaning that we can use the same terms that $\mathrm{d}\sigma_{\mathrm{RP}}^{\mathrm{A}}$ is made up of to subtract the poles. Naively, it seems that using these terms with linear combination polarizations instead of random polarizations solves the problem. However, even though it seems to be an inconsequential constant factor, the normalization factor $1/\sqrt{2}$ requires some modifications that affect the different contributions within $\mathrm{d}\sigma_{\mathrm{RP}}^{\mathrm{A}}$ in different ways.

To see this, let us first go back and decompose $\mathrm{d}\sigma_{\mathrm{RP}}^{\mathrm{A}}$ into its components:

$$\mathrm{d}\sigma_{\mathrm{RP}}^{\mathrm{A}} = \mathrm{d}\sigma_{\mathrm{CS}}^{\mathrm{A}} + \mathrm{d}\sigma^{\widetilde{A}} = \mathrm{d}\sigma_{\mathrm{CS}}^{\mathrm{A}} + \mathrm{d}\sigma^\phi - \mathrm{d}\sigma^\lambda. \tag{7.9}$$

We will now discuss the application of each of the terms to linear combination sampling.

The Catani–Seymour Term $\mathrm{d}\sigma_{\mathrm{CS}}^{\mathrm{A}}$

$\mathrm{d}\sigma_{\mathrm{CS}}^{\mathrm{A}}$ is the original Catani–Seymour subtraction term where the n–parton amplitude is evaluated using the helicity method of choice which is linear combination sampling in

the present case. This subtracts the helicity summed parts for both partons i and j. As equation (7.8) reveals, each of the partons polarization product contains the helicity sum with an additional factor of $1/2$. Since the Catani–Seymour term was derived without this normalization factor, we have to account for it here. Both partons i and j contribute a factor $1/2$ to the splitting, thus we have to multiply the subtraction term with a factor $1/4$ in order to get the normalization right:

$$\mathrm{d}\sigma_{\mathrm{CS}}^{\mathrm{A}} \to \frac{1}{4}\mathrm{d}\sigma_{\mathrm{CS}}^{\mathrm{A}}. \tag{7.10}$$

The Fully Randomly Polarized Term $\mathrm{d}\sigma^\phi$

$\mathrm{d}\sigma^\phi$ is the contribution given by the $\widetilde{V}$ evaluated using full random polarizations for partons i and j. Obviously, we have to evaluate this using linear combination polarizations here. Still, there is a small problem lurking inside the soft correction term. Let us recall the structure of the terms briefly and analyze what has to be changed. The collinear function $\mathcal{P}_{(ij)\to i+j}$ poses no problem; partons i and j are evaluated using linear combination polarizations which already include the normalization factor. The soft function, once again, contains a hidden trap. Let us look at the example of the $q \to qg$ splitting, equation (6.30):

$$[\mathcal{S}_{q\to qg}]_{\alpha\beta} = \left[-\frac{(p_i\epsilon_j^*)(p_k\epsilon_j) + (p_k\epsilon_j^*)(p_i\epsilon_j)}{(p_kp_j)(p_ip_j + p_kp_j)} + \frac{4(p_kq_j - p_iq_j)}{(p_jq_j)(p_ip_j + p_jp_k)} \right] \times \\ \times\, u_\alpha(p_i)\,\overline{u}_\beta(p_i). \tag{7.11}$$

The first term in brackets poses no problems; we simply insert linear combination polarizations for $\epsilon(p_j)$ and for $u(p_i)$ and the normalization factor is automatically taken care of. However, the second term—the correction factor that we derived in appendix C—only depends on $u(p_i)$ but no longer on the polarization of parton i. This is due to the fact that this term was constructed such that the helicity summed version of the term matches the Catani–Seymour term. Hence, the formula contains an implicit helicity summation over parton j. With linear combination polarizations, this will only match the corresponding Catani–Seymour term discussed above when we take the normalization of linear combination polarizations into account. Since the helicity summation therein is only over the parton j, the additional factor we have to apply is $1/2$. Note that the same argument also applies to the other splittings, namely $g \to gg$ and $\overline{q} \to g\overline{q}$.

Before we re-define the soft term, let us discuss the helicity summed contribution.

The Helicity Summed Contribution $\mathrm{d}\sigma^\lambda$

For random polarizations, $\mathrm{d}\sigma^\lambda$ is composed by the same terms as $\mathrm{d}\sigma^\phi$ with the difference that partons i and j are evaluated with helicity summation instead of random polarizations or linear combination polarizations. Just like for Catani–Seymour term $\mathrm{d}\sigma_{\mathrm{CS}}^{\mathrm{A}}$, this affects the whole contribution which we have to multiply again with a factor $1/4$. Note that we do *not* have to treat the soft correction term specially here, because all terms treat parton

j with helicity summation; the factor $1/2$ we have to add for $d\sigma^\phi$ is thus included in the overall normalization for $d\sigma^\lambda$.

Summary of Modified Terms

Let us summarize our findings on additional factors with respect to the random polarization subtraction terms:

- $d\sigma_{CS}^A$ acquires a factor $1/4$.

- The soft correction term in $d\sigma^\phi$ (i.e. the left hand side of the $\mathcal{R}$ operator, equation (6.12)) acquires a factor $1/2$. All other terms in $d\sigma^\phi$ are unchanged.

- The helicity summed term $d\sigma^\lambda$ also acquires a factor $1/4$; the soft correction term does *not* require an additional factor.

Let us wrap this into formulas. The total subtraction term reads as follows:

$$d\sigma_{LCS}^A = \frac{1}{4}d\sigma_{CS}^A + d\sigma^{\widehat{A}}. \tag{7.12}$$

This contains the normalization factor for the Catani–Seymour term. The additional subtraction term is defined by

$$d\sigma^{\widehat{A}} \propto d\Phi_{n+1}\Bigg(\sum_{\substack{(i,j) \\ k \neq i,j}} \widehat{\mathcal{D}}_{ij,k} J_n(\tilde{p}_{ij}, \tilde{p}_k) + \sum_{c\in\{a,b\}} \sum_{(i,j)} \widehat{\mathcal{D}}_{ij}^c J_n(\tilde{p}_{ij}; \tilde{p}_a)$$
$$+ \sum_{c\in\{a,b\}} \sum_{(j,k)} \widehat{\mathcal{D}}_k^{cj} J_n(\tilde{p}_k; \tilde{p}_{cj}) + \sum_{\substack{c,d\in\{a,b\} \\ c \neq d}} \sum_j \widehat{\mathcal{D}}^{cj,d} J_n(\widetilde{\Phi}_n; \tilde{p}_{cj}, p_d) \Bigg). \tag{7.13}$$

We will deal with the final–final case only since the others follow directly by comparison to the random polarization dipoles. The dipole is defined by

$$\widehat{\mathcal{D}}_{ij,k}(p_1, \ldots p_{n+1}) = -4\pi\alpha_s\mu^{2\epsilon} \mathcal{A}_n^{*\,\xi}(\widetilde{ij}, \widetilde{k}) \left(\frac{\mathbf{T}_k \cdot \mathbf{T}_{ij}}{\mathbf{T}_{ij}^2} [\widehat{V}_{ij,k}]_{\xi\zeta} \right) \mathcal{A}_n^\zeta(\widetilde{ij}, \widetilde{k}). \tag{7.14}$$

which is identical to the random polarization dipole (6.31) with the exception of the spin–correlation matrices. These are now defined by

$$\widehat{V}_{ij,k} = \mathbf{T}_{(ij)\to i+j}^2 \, \widehat{\mathcal{R}} \left[\mathcal{P}_{(ij)\to i+j}^{LCS} + \mathcal{S}_{(ij)\to i+j}^{LCS} \right]. \tag{7.15}$$

This definition contains a modified version of the $\mathcal{R}$ operator:

$$\widehat{\mathcal{R}} f(h_i, h_j, N_h) = f(\odot_i, \odot_j, 1/2) - \frac{1}{4} \sum_{\lambda_i, \lambda_j} f(\lambda_i, \lambda_j, 1), \tag{7.16}$$

This contains the normalization factor for the helicity summed part on the right. The left hand side is now evaluated using linear combination polarizations which we denote by $\odot$. In addition, the operator acts on a new variable N_h, the *helicity normalization*. The collinear function $\mathcal{P}^{\text{LCS}}_{(ij)\to i+j}$ is unaffected with respect to the earlier definition in equation (6.20):

$$\mathcal{P}^{\text{LCS}}_{(ij)\to i+j}(h_i, h_j, N_h) = \mathcal{P}_{(ij)\to i+j}(h_i, h_j). \tag{7.17}$$

Note that we explicitly gave the helicity arguments and the normalization variable that the $\widehat{\mathcal{R}}$ operator acts on. Obviously, N_h is ignored for the evaluation of the collinear function. The soft function, on the other hand, experiences a modification:

$$[\mathcal{S}^{\text{LCS}}_{g\to gg}]_{\mu\nu}(N_h) \tag{7.18a}$$
$$= \left[-\frac{(p_i \epsilon_j^*)(p_k \epsilon_j) + (p_k \epsilon_j^*)(p_i \epsilon_j)}{(p_k p_j)(p_i p_j + p_k p_j)} + N_h \frac{4(p_k q_j - p_i q_j)}{(p_j q_j)(p_i p_j + p_j p_k)} \right] \epsilon_\mu(p_i)\, \epsilon_\nu^*(p_i)$$
$$+ \left[-\frac{(p_j \epsilon_i^*)(p_k \epsilon_i) + (p_k \epsilon_i^*)(p_j \epsilon_i)}{(p_k p_i)(p_j p_i + p_j p_i)} + N_h \frac{4(p_k q_i - p_j q_i)}{(p_i q_i)(p_j p_i + p_i p_k)} \right] \epsilon_\mu(p_j)\, \epsilon_\nu^*(p_j),$$

$$[\mathcal{S}^{\text{LCS}}_{g\to q\bar{q}}]_{\mu\nu}(N_h) = 0 \tag{7.18b}$$

$$[\mathcal{S}^{\text{LCS}}_{q\to qg}]_{\alpha\beta}(N_h) \tag{7.18c}$$
$$= \left[-\frac{(p_i \epsilon_j^*)(p_k \epsilon_j) + (p_k \epsilon_j^*)(p_i \epsilon_j)}{(p_k p_j)(p_i p_j + p_k p_j)} + N_h \frac{4(p_k q_j - p_i q_j)}{(p_j q_j)(p_i p_j + p_j p_k)} \right] u_\alpha(p_i)\, \overline{u}_\beta(p_i)$$

(As usual, the $\bar{q} \to g\bar{q}$ splitting follows from $q \to qg$). What is new with respect to definition (6.30) is the normalization factor N_h. Together with the $\widehat{\mathcal{R}}$ operator, this creates the correct normalization for the soft correction term.

Since the dipoles for initial state radiation only differ by their momentum parameterizations and the way that particle content of $\widetilde{V}$ is crossed into the initial state, but not by the definitions of $\widetilde{V}$ themselves, it is straight forward to construct all other dipoles from the random polarization dipoles by replacing $\widetilde{V}$ with $\widehat{V}$.

The Integrated Subtraction Term

Just like for random polarizations and for helicity sampling, the integrated subtraction term is identical to the integrated Catani–Seymour term. Our total subtraction term $d\sigma^{\text{A}}_{\text{LCS}} = {}^1\!/\!4\, d\sigma^{\text{A}}_{\text{CS}} + d\sigma^{\widehat{\text{A}}}$ is again made up of the Catani–Seymour contribution and an additional term that contains helicity mixing terms. Performing a Monte Carlo integration over the plus–minus helicities yields the usual helicity summed result while the helicity

mixing terms cancel in the sum/integration, see equation (7.3):

$$\sum_{\odot = \oplus, \ominus} d\sigma^{\widehat{A}} = 0 \quad \Rightarrow \quad \int_0^1 du_i \int_0^1 du_j \, d\sigma^{\widehat{A}} = 0$$

$$\Rightarrow \quad \int d^{n+1}u \, d\sigma^A_{LCS} = \int d^{n+1}u \, \frac{1}{4} d\sigma^A_{CS} + \int d^{n+1}u \, d\sigma^{\widehat{A}} = d\sigma^A_{CS}. \tag{7.19}$$

The integrated subtraction term can thus be computed by using the Catani–Seymour insertion operator while using linear combination sampling for the computation of the amplitudes:

$$\int_1 d\sigma^A_{LCS} \propto d\Phi_n \left(\mathcal{A}_n^{*\{\odot\}_n} \boldsymbol{I}_{CS}(\epsilon) \mathcal{A}_n^{\{\odot\}_n} \right) J_n, \tag{7.20}$$

where the index $\{\odot\}_n$ denotes an evaluation using linear combination polarizations.

7.3 Checks and Analysis

Since the implementation of linear combination sampling is straight forward after having detailed the implementation of helicity sampling and random polarizations[1], we can go right into the analysis.

Checks of the Subtraction Terms

As usual, we begin our analysis by verifying that the subtraction terms remove the non-integrable $1/\lambda^2_{\text{soft/coll}}$ terms. Since the basic structure of the subtraction terms is the same as for random polarizations, we present similar plots, see figures 7.1 and 7.2. The middle plots again show the subtraction of the components; just like for random polarizations, we can decompose $d\sigma^{\widehat{A}}$ into two pieces that contain the left and right hand part of the $\widehat{R}$ operator:

$$d\sigma^{\widehat{A}} = d\sigma^{\odot} - \frac{1}{4} d\sigma^{\lambda} \quad \Rightarrow \quad d\sigma^A_{LCS} = \frac{1}{4} d\sigma^A_{CS} + d\sigma^{\odot} - \frac{1}{4} d\sigma^{\lambda}. \tag{7.21}$$

Due to the same arguments as for random polarizations, we expect integrable behavior of the components:

$$\frac{1}{4} \left(d\sigma^A_{CS} - d\sigma^{\lambda} \right) = \mathcal{O}\left(\frac{1}{\lambda_{\text{soft/coll}}} \right) \quad \text{and} \quad d\sigma^R - d\sigma^{\odot} = \mathcal{O}\left(\frac{1}{\lambda_{\text{soft/coll}}} \right). \tag{7.22}$$

Looking at the figures, we find that all slopes are as expected and the plots show the desired behavior. We thus conclude that the subtraction terms work and are implemented

---

[1]Note that for the implementation of the $g \to gg$ terms in $d\sigma^{\widehat{A}}$, we require the same multiplicative factor

$$\frac{2s_{ik}}{s_{ik} + s_{j\ell}}$$

that we used for random polarizations.
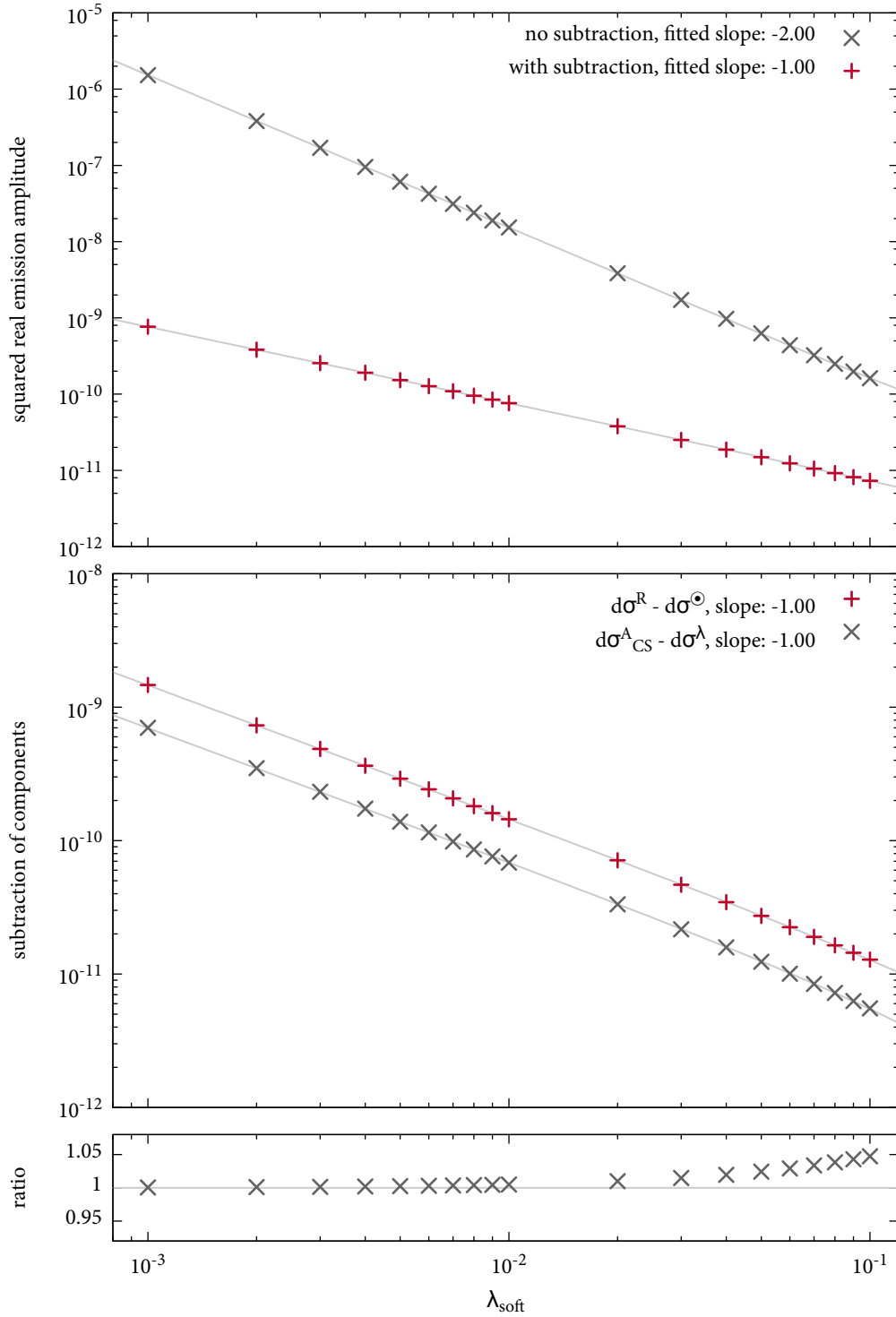
Figure 7.1: Soft behavior for $e^- e^+ \to q g_1 g_2 g_3 g_4 g_5 \mathbf{g_6} \bar{q}$ with linear combination sampling; the unresolved soft gluon is g_6. The upper plot shows the unsubtracted and subtracted real emission amplitudes. In the middle the subtraction of the components is illustrated (see discussion in text). The lower plot show the absolute ratio of the unsubtracted matrix element and the total subtraction term; the expectation (gray line) is approximately 1.
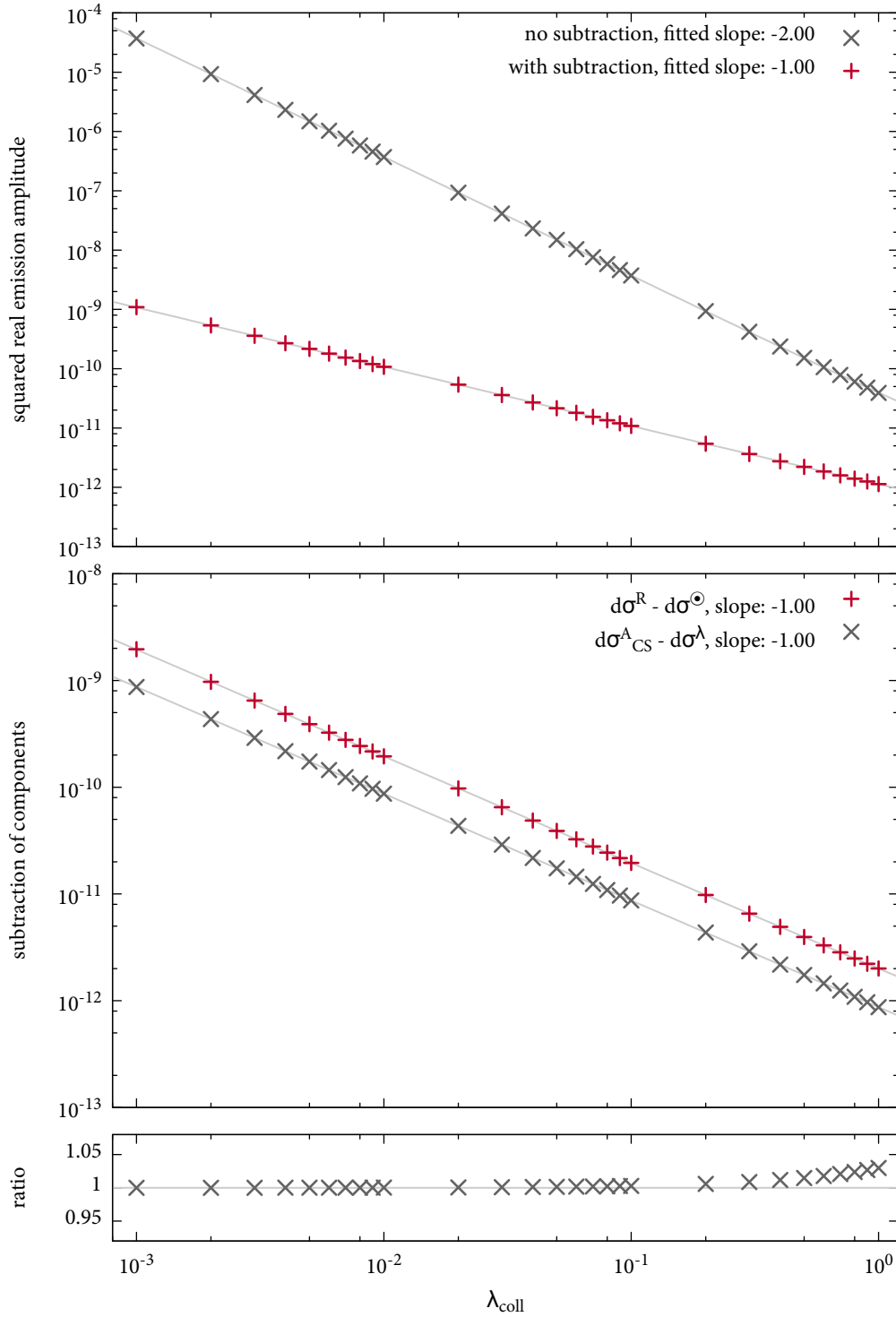
Figure 7.2: Collinear behavior for $e^-e^+ \to q\boldsymbol{g_1}g_2g_3g_4g_5g_6\overline{q}$ with linear combination sampling; the collinear pair is (q, g_1). The upper plot shows the unsubtracted and subtracted real emission amplitudes. In the middle the subtraction of the components is illustrated (see discussion in text). The lower plot show the absolute ratio of the unsubtracted matrix element and the total subtraction term; the expectation (gray line) is approximately 1.

(a) Born 5 Jets

(b) Real emission with 4 Jets
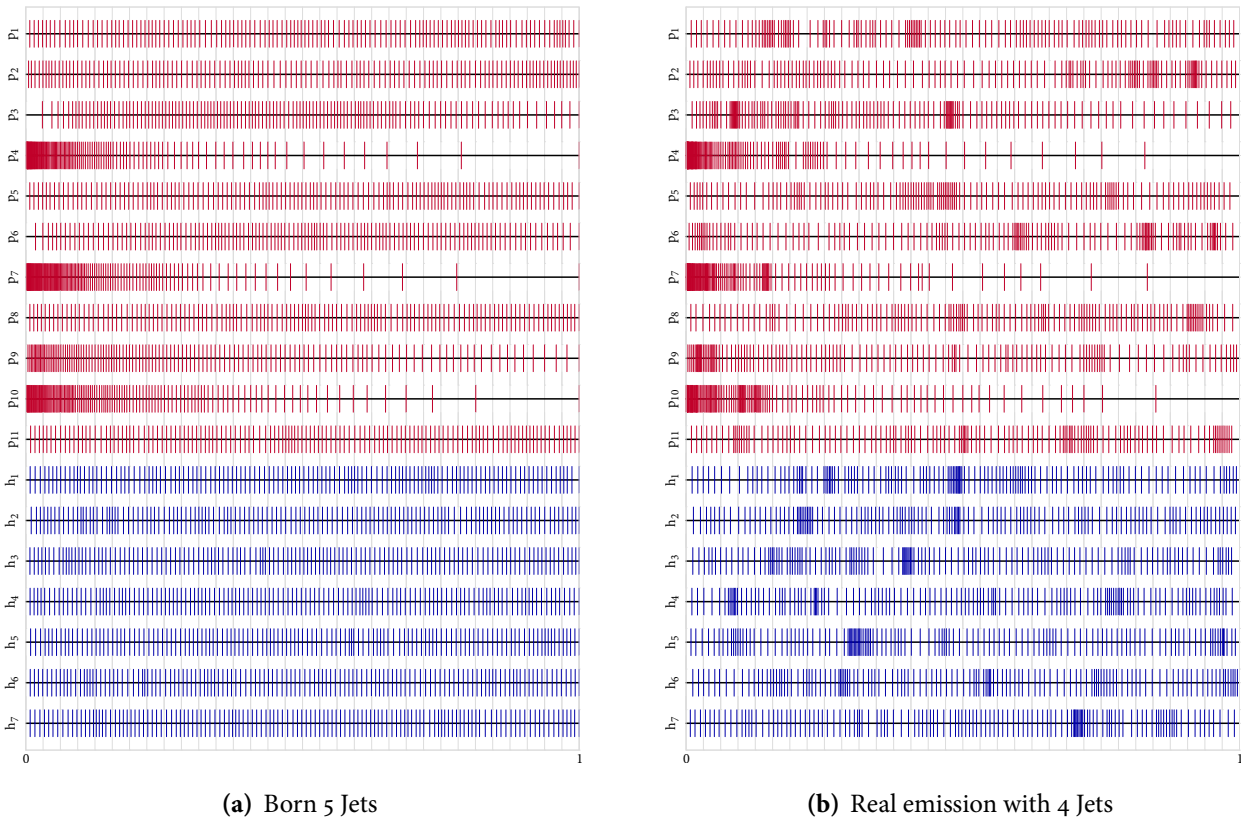
Figure 7.3: Visualization of the *VEGAS* grid with 128 bins or n–dimensional linear combination sampling. The result is very similar to the other methods with n helicity variables: We find hardly any grid adaptation for the helicity variables apart from the apparently randomly occurring dense spots for the real emission contribution.

correctly.

7.3.1 n–Dimensional Linear Combination Sampling

Since we have again the two different ways of realizing the sampling, we perform two different analyses. We begin with n–dimensional sampling, where we can once again look at the adaptation of the *VEGAS* grid. It is no surprise to see that figure 7.3 shows no great difference to the grids that we analyzed for random polarizations and for n–dimensional helicity sampling. Figure 7.4 is more interesting: it shows the dependence of the squared amplitude on the helicity variable of the quark pair (plot (a)) and on two gluons (plot (b)). The structure is similar to helicity sampling, however, the shown plots do not reveal any helicity configurations that vanish. This supports our expectation that the integrand is distributed more evenly. Still, the general picture is similar to sampling.

Based on this and on our analyses in the previous chapters, we would expect to find that the number of *VEGAS* bins does not have a strong impact on the quality of the integration. Indeed, our integrations for different jet and bin numbers show exactly said behavior, figure 7.5 shows one example of the errors for a 5 jet Born integration.
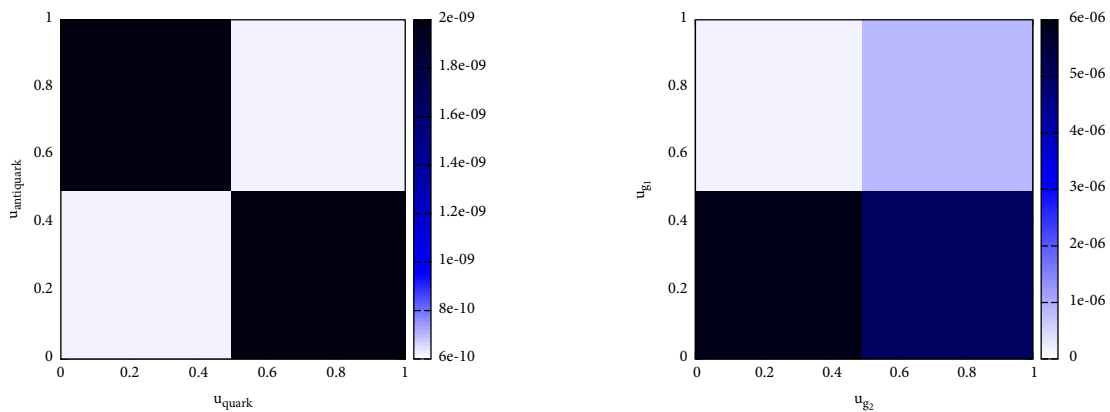
(a) Dependence on quark and antiquark helic-
ity variables.

(b) Dependence on the helicity variables of the
first two gluons.

Figure 7.4: Dependence of the squared amplitude on helicity variables u_i. The shown
process is $e^+e^- \to \bar{u}ugggg$. While the basic structure is similar to n–dimensional
sampling, the integrand never becomes zero.

7.3.2 One–Dimensional Linear Combination Sampling

For one-dimensional sampling, the situation is quite different. If we analyze the grid, we
find a distribution as in figure 7.6. Again, the momentum variables show no difference
from any other helicity method we have seen so far. The helicity variable appears to not
have adapted at all, which verifies the expectation that the squared amplitude is more even
with respect to the helicity variable as compared to one-dimensional helicity sampling
with its strong peaks.

Figure 7.7 shows the dependence of the squared amplitude on the helicity variable u. The
distribution is in fact much more even. When trying different momentum configurations
for the creation of these plots, one finds that the structure is entirely unstable in the sense
that what one would identify as "peaks" in figure 7.7 is not a peak any more for a different
configuration—the peaks move with the random numbers. Note that while something
similar happens for one-dimensional helicity sampling, the fact that many of the helicity
channels always vanish largely reduces the locations where peaks can appear, thus enabling
the algorithm to adapt much better.

Looking at the influence of the number of bins to the adaptation, we find virtually no
difference in adaptation, see figure 7.8. Thus, one would expect no difference in the quality
of the integration with respect to different bin numbers. Figure 7.9 shows an example for a
six jet Born integration which confirms this.

It will be especially interesting to compare the integration of one-dimensional helicity
sampling to one-dimensional linear combination sampling: the former variant has sharp
peaks to which *VEGAS* adapts very well, as we saw, while the latter creates a much more
even distribution to which we find no adaptation. After having presented six different
techniques for implementing helicities in numerical algorithms, we finally turn to a direct
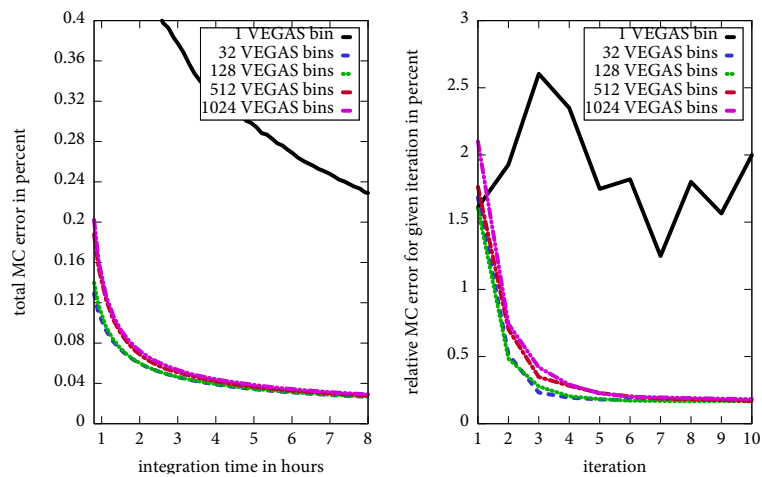
Figure 7.5: Dependence of the integration error of a five jet Born contribution on the number of *VEGAS* bins for n–dimensional linear combination sampling, similar to the analyses in the last chapters, e.g. figure 6.8. The one bin result shows the slowest convergence while all other bin numbers are almost indistinguishable.

comparison of the methods in the following chapter.
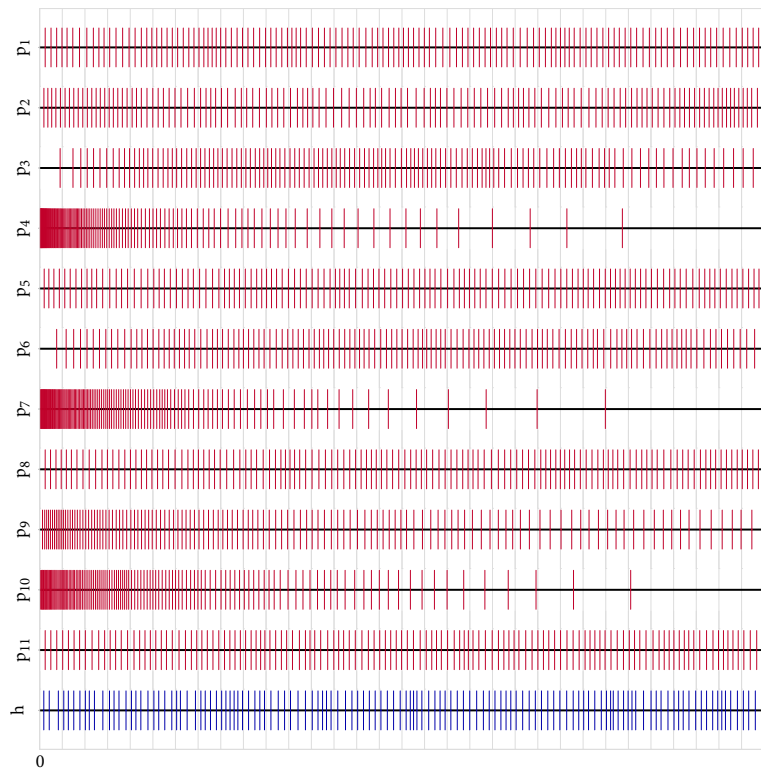
Figure 7.6: Visualization of the *VEGAS* grid for the Born contribution to five jet production. The phase space grid is unchanged from all other helicity methods. The helicity variable shows almost no adaptation.
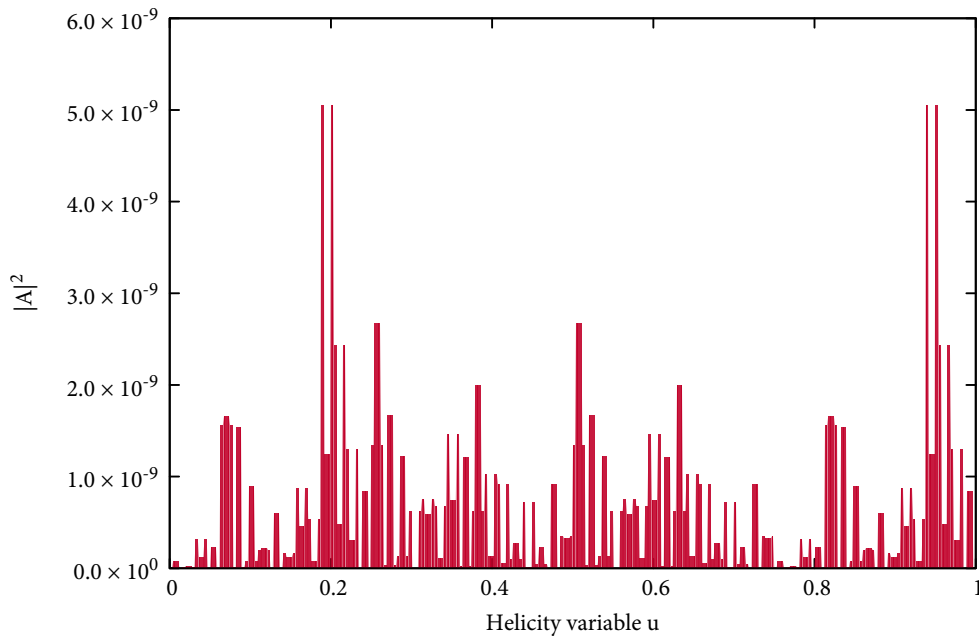
Figure 7.7: Dependence of the squared amplitude on the helicity variable for one-dimensional linear combination sampling. The shown process is $e^-e^+ \rightarrow \bar{q}qgggg$ where the horizontal axis shows different values for the overall helicity variable.
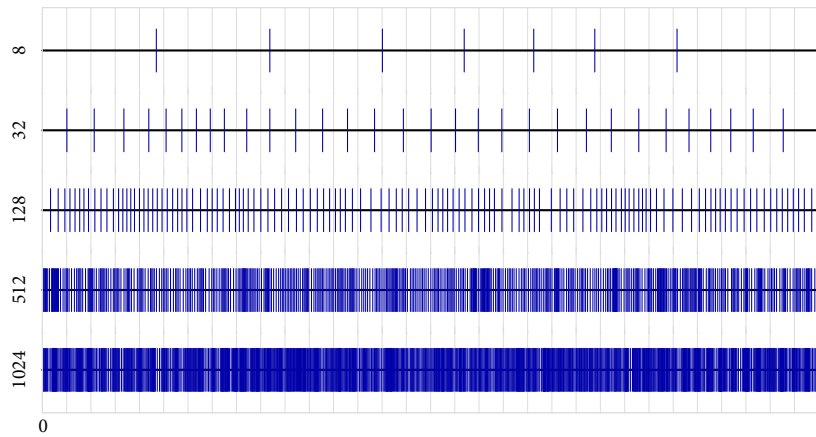
Figure 7.8: Visualization of the helicity variable *VEGAS* grid for different numbers of bins (indicated on the left) of the Born contribution to six jet production. Neither of the bin numbers shows any particular adaptation.
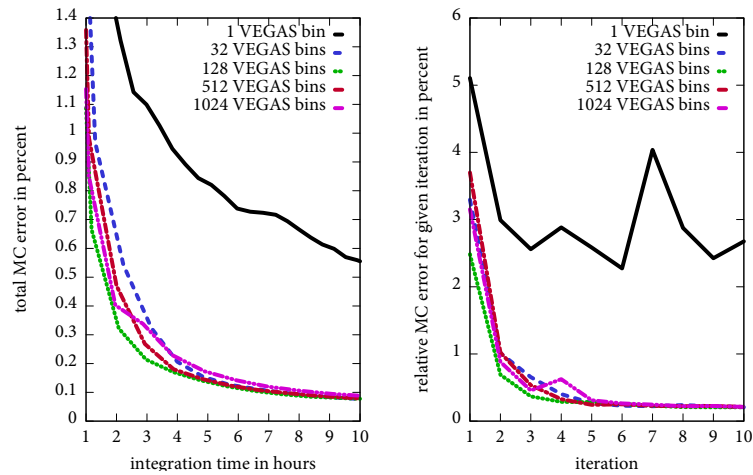
Figure 7.9: Dependence of the integration error of a six jet Born contribution on the number of *VEGAS* bins for one–dimensional linear combination sampling. The one bin result shows the slowest convergence while all other bin numbers are almost indistinguishable.

Checks, Comparisons and Results

<div style="text-align: right">8</div>

In the previous four chapters, we presented a total of six different methods for implementing the summation over helicities in numerical programs. While we analyzed the behavior with respect to the *VEGAS* grid, we have not yet performed a direct comparison of the methods. This chapter will take care of this.

First, we present some results for the Born contribution that we compare to literature values, thereby establishing that our integration yields correct results. Then, we recapitulate the results of our analysis from the previous four chapters before we investigate differences between the different helicity methods. We give results both for the Born and the real emission contribution and show that the results for different helicity methods agree. Afterwards, we compare the efficiency of the methods and analyze their numerical precision. Finally, we give a recommendation as to which method is most useful in terms of efficiency and ease of both implementation and use.

8.1 Results for Exclusive $e^+e^- \to n$ Jet Production

Near the beginning of the work for this thesis, a paper [24] was published by the Weinzierl group that presented the world's first computation of a one loop eight-point function as part of the computation of jet rates in electron–positron annihilation. It served as a proof-of-concept for the method of virtual subtraction which we introduced in section 3.2.4. At the time of publishing, the idea of using random polarizations for all contributions was well established, but the corresponding subtraction term from chapter 6 had not yet been developed. Hence, the real emission contribution was evaluated with helicity summation. However, all other contributions[1] have been evaluated using random polarizations.

The publication presents jet rates from $n = 3$ up to 7. While the results for $n = 6, 7$ were new, the lower jet rates were compared to existing results in order to verify the correctness of the method. Since the results in [24] were generated using the same basic framework of

---

[1]Note that this includes the integrated subtraction term and thus the full virtual contribution and the insertion term.

color-flow decomposition, recursion relations, etc. it is very easy to compare the results of our implementation with the one used for the publication; note that the two are *separate* programs. We use this to verify that our integration routines work as expected.

Before we do so, let us take a closer look at how these jet rates have been calculated. An exclusive jet rate is defined as the ratio of the exclusive cross section σ_n^{excl} for n jet production and the total hadronic cross section σ_{tot}:

$$R_n(\mu) = \frac{\sigma_n^{\text{excl}}(\mu)}{\sigma_{\text{tot}}(\mu)}. \tag{8.1}$$

Note that the jet rate depends on the renormalization scale μ which obeys the renormalization equation (2.12). Hence, it is sufficient to compute the jet rate at a freely chosen scale which in our case is the center-of-mass energy which was chosen to be equal to the mass of the Z boson, $\mu_0 = Q = m_Z \approx 91.2\,\text{GeV}$ [14]. In practice, this amounts to using the value

$$\alpha_{\text{s}} = 0.118 \tag{8.2}$$

for the strong coupling constant. Notice that the total hadronic cross section involves all possible hadronic final states and thus cannot be computed in practice. But since it serves the purpose of a normalization factor, we approximate it by the leading order contribution to the total hadronic cross section which is equal to the exclusive two jet cross section at Born level, i.e. the cross section for the process $e^- e^+ \to \bar{q}q$:

$$\sigma_{\text{tot}} = \sigma_2^{\text{B,excl}} + \mathcal{O}(\alpha_{\text{s}}). \tag{8.3}$$

This can be computed very precisely by our numerical code and we use the following value:

$$\sigma_2^{\text{B,excl}} = (45.13433 \pm 0.00003)\,\text{pb}. \tag{8.4}$$

Let us turn to the numerator of the jet rate, i.e. the exclusive cross section. Since we only compare the Born contributions of cross sections, we write

$$\sigma_n^{\text{excl}} = \sigma_n^{\text{B,excl}} + \mathcal{O}(\alpha_{\text{s}}^{n-2}). \tag{8.5}$$

Note that both the results presented in [24] and the results from our work are obtained using five massless quark flavors, $N_f = 5$. Naively, this would mean computing the cross sections for all five processes $e^- e^+ \to \bar{q}_f q_f g \cdots g$ where $f = u, d, c, s, b$. However, since all quarks are treated as massless, they only differ by their electromagnetic charges given by

$$Q_f = \begin{cases} +\frac{2}{3} & f = u, c \\ -\frac{1}{3} & f = d, s, b \end{cases} \tag{8.6}$$

with respect to the elementary charge e. Since this charge enters the calculation only at one point, namely the quark–photon vertex which is proportional to the charge, we can

write

$$|\mathcal{A}(e^-e^+ \rightarrow \overline{q}_f q_f g \cdots g)|^2 = Q_f^2 |\mathcal{M}|^2 \tag{8.7}$$

where $\mathcal{M}$ is the amplitude without the charge factor (or, equivalently, with charge $Q = 1$). We can then write

$$\sum_{\substack{f=u,d, \\ c,s,b}} |\mathcal{A}(e^-e^+ \rightarrow \overline{q}_f q_f g \cdots g)|^2 = \left[2 \cdot \left(\frac{2}{3} \right)^2 + 3 \cdot \left(-\frac{1}{3} \right)^2 \right] |\mathcal{M}|^2 = \frac{11}{9} |\mathcal{M}|^2. \tag{8.8}$$

Thus, we only need to calculate one process and the quark charges act as a multiplicative factor.

With this knowledge, we can now turn to the full jet rate which we re-write as follows

$$R_n(\mu) = \left(\frac{\alpha_s}{2\pi} \right)^{n-2} A_n, \tag{8.9}$$

i.e. we write it as a coefficient times the coupling constants. The results we are going to present below are just the coefficients A_n. Since we perform only leading color computations, we have to expand these coefficients in terms of the color factor N_c:

$$A_n = N_c \left(\frac{N_c}{2} \right)^{n-2} \left[A_n^{\mathrm{lc}} + \mathcal{O}\left(\frac{1}{N_c} \right) \right]. \tag{8.10}$$

We neglect all sub-leading contributions, as has been done in [24]. The coefficient A_n^{lc} together with the color factors in front is exactly the contribution we obtain by applying the leading color approximation according to section 3.1.4.

Let us make another remark concerning a difference in implementation of our code with respect to [24]. In this thesis, we do not discuss electroweak bosons and thus, we only treat the process $e^-e^+ \rightarrow \gamma^* \rightarrow n$ jets, whereas [24] also takes an intermediate Z boson into account: $e^-e^+ \rightarrow \gamma^*/Z \rightarrow n$. While this changes the value of the individual cross sections, the jet rates are not affected. The reason for this is that the basic process $e^-e^+ \rightarrow q\overline{q}$ which we use for the total hadronic cross section forms the "skeleton" for all higher jet multiplicities, meaning that additional jets (which are described by gluons) are given as radiations off the quark legs. One can show that this leads to a factorization with respect to the "skeleton" process. The conclusion of this is that this skeleton part always cancels between the numerator and the denominator in the jet rate, thus the jet rates we investigate are invariant under the addition of a virtual Z boson.

Now we are ready to compare results. Note that for the Born contribution only the results for five, six, and seven jet coefficients A_n are given in [24]. These results, along with the ones that were obtained with our code, are presented in table 8.1. The error ΔR_n of our jet rate is determined by

$$\Delta R_n = R_n \sqrt{ \left(\frac{\Delta\sigma_n^{\mathrm{B,\,excl}}}{\sigma_n^{\mathrm{B,\,excl}}} \right)^2 + \left(\frac{\Delta\sigma_2^{\mathrm{B,\,excl}}}{\sigma_2^{\mathrm{B,\,excl}}} \right)^2 } \tag{8.11}$$

Jets	y_{cut}	LO jet rate from [24]	LO jet rate this work	unit
5	0.002	5.0529 ± 0.0004	5.056 ± 0.009	10^3
	0.001	1.3291 ± 0.0001	1.319 ± 0.005	10^4
	0.0006	2.4764 ± 0.0002	2.471 ± 0.007	10^4
6	0.001	1.1470 ± 0.0002	1.142 ± 0.003	10^5
	0.0006	2.874 ± 0.002	2.88 ± 0.01	10^5
7	0.0006	2.49 ± 0.08	2.42 ± 0.01	10^6

Table 8.1: Jet rates in electron–positron annihilation. The results from this work agree reasonably well with those from [24]. Note that the given values are actually only the coefficients A_n as given in equations (8.9) and (8.10). The cut parameters apply to the Durham jet algorithm.

where the cross section errors are pure Monte Carlo errors. The values for our exclusive n jet cross sections were calculated using one dimensional helicity sampling, but we will verify in the following section that all helicity methods yield the same results. As one can see, the jet rates agree reasonably well.

From this, we conclude that our code yields correct jet rates and we can move on to compare the different helicity methods.

8.2 Summary of the Analyses from the Previous Chapters

To this end, let us first summarize what we found out in the analyses of the different helicity methods, chapters 4 to 7. First of all, we analyzed classical helicity summation where we showed that the phase space is very well suited for the *VEGAS* algorithm. All following chapters revealed that there is no recognizable change in the way the phase space part of the *VEGAS* grid adapts if we use different helicity methods. We thus conclude that there is no correlation with respect to the performance of *VEGAS*/ the phase space generator and our tested helicity methods.

If we look at the adaptation of the *VEGAS* grid with respect to the helicity variables, we found that only one of the tested helicity methods provides *VEGAS* with a possibility to adapt its grid. All methods with n helicity integral dimensions have correlations between the different helicity variables; random polarizations and linear combination sampling try to reduce this effect by reducing the fluctuations of the amplitude with respect to different helicity variables. The two methods that require only one integral dimension for the helicity only differ by the fact that one–dimensional helicity sampling uses helicity eigenstates, while linear combination sampling uses rotated helicity states. We found that the difference in terms of *VEGAS* adaptation is enormous: the eigenstate method is zero for a large range of values of the helicity variable. This enables *VEGAS* to adapt very well. The linear combination method, on the other hand, makes the integrand more even (in

particular, it never vanishes) such that *VEGAS* cannot adapt.

Finally, we also investigated the effect of the number of *VEGAS* bins on the performance of the integration. We found that the grid number only matters for one–dimensional helicity sampling where a good choice is to have more bins (e.g. twice as much) than there are helicity configurations for the desired observable. All other methods do not show any dependence on the bin number. The reason is clear considering the result from the last paragraph.

Our next goal is to compare some results of integrations with different helicity methods in order to determine how our previous findings affect the performance of the Monte Carlo integration.

8.3 Checks and Comparison of Helicity Methods

As all of our previous discussion clearly shows, calculating observables such as cross sections is a very complex operation requiring up to many billions of evaluations of squared matrix elements, which in itself are complicated objects. This raises the question of how to compare different helicity methods properly.

Obviously, amplitudes depend on physical parameters such as scales (coupling constants, center-of-mass energy), jet algorithm and jet definition parameter. In order to be able to compare the different helicity methods, those variables should be identical for all methods. In the analyses presented in this section, we make the following choice:

$$Q = 90\,\text{GeV}, \qquad y_{\text{cut}} = 0.0006, \qquad \alpha_s = 0.118, \qquad \alpha = \frac{1}{127.9}, \tag{8.12}$$

where the jet cut is used with the Durham jet algorithm.

In the context of Monte Carlo integration, the end result depends on many more technical parameters: the random number generator, its seed value, the number of integrand evaluations (calls) per Monte Carlo iteration, to name a few. Unlike the physical parameters, it is neither possible nor desirable to keep all of these variables constant for all helicity methods; this is rooted in the fact that the six helicity methods we want to compare have different numbers of integral dimensions. What we do is keep the random number generator constant—we use the *Mersenne–Twister MT 19937* [101] with both the Cuba and the hep-mc libraries. Keeping the seed value constant is only reasonable when comparing methods with the same number of integrand dimensions. In this case, we can investigate the impact of the helicity variable(s) on the integration while keeping phase space exactly identical. As for the number of calls per Monte Carlo iteration, those methods with more integral dimensions obviously require more calls to cover the integration space reasonably well. Thus, the number of calls *has to be* separately tuned for each helicity method.

As a consequence of this discussion, one might say that there is no proper way of directly comparing different helicity methods that gives a quantifiable result as to which method is better and by which degree. In light of this, we chose to take the approach of the end user of an event generator. An end user does not want to concern himself with

choosing the right set of technical parameters; we will assume that he wants to describe the observable together with all relevant physical parameters while using the default technical parameters. In particular, we assume that the seed value of the random number generator will be a random number in the sense we cannot predict it.[2] Two typical use cases would be then be the following:

1. The user wants to compute an observable to a given precision, for example up to a relative error of 0.1 %. Obviously, it is desirable to use the helicity method which reaches this goal in the shortest time. This motivates the following test: set a goal for the minimum precision of the integral result and have the Monte Carlo integration stop upon reaching that precision. We can measure the time it takes to reach this goal and compare it for the different helicity methods.

2. The user has a certain time frame for running the Monte Carlo simulation. Clearly, one wants to use the helicity method that reaches the most accurate result in the given time. A corresponding test would be to perform a Monte Carlo integration for a given time and measuring the reached accuracy. By comparing the errors of the different helicity methods afterwards one can determine the most suitable method.

In this section, we will display results obtained for both use cases.

Note that we still have to determine the number of calls per Monte Carlo iteration that should be used. If this number is too small, the *VEGAS* grid cannot adapt properly; it only does so when the integration space (i.e. phase space plus helicity space) have been sufficiently covered. Evaluating each iteration with "too many" integrand evaluations, on the other hand, does not have any bad consequences other than "wasting" integration time with a non-adapted grid. For a Born level integration with helicity summation, we found it sufficient to use 10^5 calls for the two jet result while seven jets require 5×10^7 calls. For the real emission contribution, we analogously found 10^5 calls to be sufficient for the two jet cross section with helicity summation, while we need comparatively more points for the higher jet multiplicities: cross sections with more than four jets require at least ten times as many calls as the corresponding Born cross section. This is partly due to the fact that the real emission integration space includes one more particle than the corresponding Born value, but also because of the more complicated phase space structure. All other helicity methods obviously require more calls; we found that multiplying the helicity summation calls by a factor of 50 or 100 (for jet numbers greater than four and for both Born and real emission contribution) yields good results.

Let us now take a look at some results we obtained. Table 8.2 shows some results we obtained for both Born and real emission contribution. Those tests were run according to what we described as "use case 2" above, i.e. we specified a fixed time frame after which the

---

[2]A typical seed for random number generators is the current date and time given in terms of an integer value.

| Jets | Time | Summation | Sampling | | Random Polarizations | L.C. Sampling | |
			n	1		n	1
2	2 h	45.134 32 ±0.000 03	45.137 ±0.003	45.133 ±0.001	45.134 ±0.001	45.135 ±0.001	45.1331 ±0.0009
3	2 h	47.825 ±0.003	47.825 ±0.006	47.827 ±0.003	47.828 ±0.003	47.824 ±0.003	47.825 ±0.003
4	3 h	23.752 ±0.005	23.751 ±0.006	23.745 ±0.004	23.752 ±0.004	23.751 ±0.004	23.749 ±0.004
5	5 h	7.400 ±0.004	7.401 ±0.004	7.408 ±0.003	7.405 ±0.003	7.400 ±0.003	7.405 ±0.002
6	8 h	1.605 ±0.003	1.610 ±0.003	1.612 ±0.002	1.613 ±0.002	1.613 ±0.002	1.617 ±0.002
7	~ 40 h	0.255 ±0.002	0.2557 ±0.0008	0.2562 ±0.0005	0.257 ±0.002	0.252 ±0.001	0.2560 ±0.0004

(a) Born contribution

| Jets | Time | Summation | Sampling | | Random Polarizations | L.C. Sampling | |
			n	1		n	1
2	2 h	−48.466 ±0.003	−48.465 ±0.007	−48.469 ±0.004	−48.459 ±0.005	−48.456 ±0.006	−48.459 ±0.005
3	4 h	−34.21 ±0.02	−34.22 ±0.03	−34.27 ±0.02	−34.25 ±0.04	−34.32 ±0.04	−34.32 ±0.03
4	16 h	−13.91 ±0.07	−13.78 ±0.08	−13.80 ±0.05	−13.8 ±0.1	−13.7 ±0.1	−13.80 ±0.06
5	~ 45 h	−3.5 ±0.1	−3.6 ±0.1	−3.61 ±0.01	−3.2 ±0.1	−3.5 ±0.2	−3.74 ±0.09

(b) Real emission contribution

Table 8.2: Results for cross sections for $e^-e^+ \to n$ jets obtained with all six helicity method implementations. All results are given in picobarn (pb) and were obtained for $Q =$ 90 GeV and $y_{\text{cut}} = 0.0006$. *VEGAS* was set such that it stops as soon as the first iteration finishes after the given time. In those examples where the time has a "~" sign, the results have to be treated carefully: due to the long durations per iteration, the actual integration times differ by several hours for the different methods.

integration should stop and give a result.[3] All results are given in picobarn together with the Monte Carlo error in the second line of each table row. We marked the most precise results in red. Let us add a remark on the real emission results: the given results are those of the fully subtracted real emission contributions. These are no physical results and taken on their own, they have no meaning. They only become meaningful when one adds the virtual contribution and the insertion term. However, we can use these unphysical values to check consistency between the helicity methods and to measure their precision.

Let us first consider the Born contribution in table 8.2(a). All values show a good agreement between the different methods from which we can conclude that each of the methods produces valid results. Together with the comparison to literature values in the previous section, this serves as a verification that our code yields proper integration results. Note that the exact values and errors should not be treated too literally, they merely reflect the general trend that we observed.[4] This trend clearly shows that helicity summation is best suited for small numbers of jets. For two and three jets, we have $2^4 = 16$ and $2^5 = 32$ helicity configurations, respectively. These numbers are apparently too small to be replaced by any of the advanced helicity methods. Starting with four or more jets, it is clear that the amount of helicity configurations that one has to sum over grows so large that the advanced helicity methods overcome the penalty of having additional integral dimensions. In other words, the speed up of having only one squared amplitude per phase space point is greater than the penalty obtained from having a larger integration space. We see that the n–dimensional version of helicity sampling is always the slowest of all methods. On the other hand, both one-dimensional sampling methods are (among) the fastest with linear combination sampling being apparently slightly better. As one would expect, we can conclude that the one–dimensional methods where there are no correlations between the helicity variables (since there is only one) create less overhead that the *VEGAS* algorithm has to deal with and are thus faster.

Let us now turn to the real emission contribution. With the additional burden of having one more external parton with respect to the corresponding Born jet cross section plus having to compute all $(2n - 2)$ dipoles, the integration becomes increasingly difficult for higher jet numbers. Furthermore, technical values such as random number seeds have a larger impact which is also due to the more complicated structure of the real emission phase space. Still, the results presented in table 8.2(b) exhibit an even clearer pattern than the Born results. Again, for small jet numbers helicity summation is at least as good as

---

[3]In detail, this works as follows: after every Monte Carlo iteration, a user-defined so-called *callback* function is called in `hep-mc`. Within this function, we measured the elapsed time since the start of the integration. Once this time is larger than the set time frame, the integration stops. Note that for small jet numbers the given time is accurate while for larger jet numbers, especially those indicated with a "~" sign, the times are rather rough estimates. The reason is that for higher jet numbers, the matrix elements take longer to compute, and we also need more calls per iteration, making each iteration several hours long. Thus, some of the actual integration times exceed the indicated times by up to a few hours.

[4]By this, we mean that different seeds will produce different integration results and also slightly fluctuating errors. Thus, one should not conclude that method A will always produce a result twice as accurate as that of method B when B's error is twice as large as that for method A given in the table. However, one can conclude that in general, method *A* yields a smaller error than *B*.

Method	Result	Rel. Error [%]	Time Ratio
helicity summation	-3.49 ± 0.09	2.5	4.19
n–dim. sampling	-3.53 ± 0.08	2.3	5.18
1–dim. sampling	-3.66 ± 0.07	1.9	1.00
random polarizations	-3.52 ± 0.09	2.5	9.19
n–dim. l.c. sampling	-3.48 ± 0.08	2.3	8.63
1–dim. l.c. sampling	-3.75 ± 0.09	2.5	2.11

Table 8.3: Results for real emission contribution to process $e^- e^+ \to 5$ jets. The integration was set to stop as soon as an accuracy of at least 2.5 % is reached. All values are rounded; note that the given relative error is the one used by the integrator which is determined by *not* using the rounded results. Thus, the given relative error does not always correspond to the result obtained from the "Result" column. Instead of absolute times, we give the ratio to the fastest method, which is one–dimensional helicity sampling.

any advanced method. For higher jet numbers, however, *VEGAS* seems to clearly prefer the method of one–dimensional sampling over all other methods, also one–dimensional linear combination sampling. Surprisingly, all three n–dimensional helicity methods (i.e. both n–dimensional sampling methods and random polarizations) are less accurate than helicity summation in our tests.

Finally, let us take a look at a result for the first use case from above, where a certain precision of the cross section should be reached, no matter how long it takes to integrate. The example we show in table 8.3 is the five jet cross section for the real emission contribution which we integrated with every one of the six helicity methods. The goal for the precision was set to a relative error of 2.5 %. Again, the shown results are unphysical, but they allow us to compare the values. We see that the values agree within three standard deviations, but one notices that the one–dimensional sampling methods—especially linear combination sampling—stand out as relatively high compared to the rest. The relative error we give in the third column is the final error determined by the Monte Carlo integration; note that it is calculated using the original un-rounded double–precision values of the result and thus differ from the relative error one obtains from column two. The last column shows the total integration time divided by the time of the fastest method, which is one–dimensional helicity sampling. We can see that the desired precision in this case was reached more than two times faster than the second fastest method, one–dimensional linear combination sampling, and more than nine times faster than the slowest method, random polarizations. Note that if this computation is performed on a single core of a modern desktop PC[5] the difference between fastest and slowest method is more than five days of computation time.

Again, we find a surprisingly good result for helicity summation compared to all other variants but the one–dimensional sampling methods, which produce by far the fastest results.

---

[5]The PC used for the generation of all values and plots is a quad–core `Intel® Core™ i5 CPU 750` with 2.67 GHz.

8.4 Numerical Precision of Different Helicity Methods

One more aspect that we can analyze is the numerical precision of the various helicity methods; since all are based on helicity eigenstates in the end, one does not expect any differences. However, one might expect some differences due to the different subtraction terms that we use: the extra terms $d\sigma^{\widetilde{A}}$ and $d\sigma^{\widehat{A}}$ which are based on random polarizations and linear combination polarizations, respectively, lead to a double subtraction of large numbers, as discussed in the corresponding chapters.

How do we go about measuring the numerical precision of the algorithm? The basic idea[6] is to compute the squared amplitude for two sets of momenta that are related by the following re-scaling:

$$p_i' = \xi p_i \quad \forall\, i,$$ (8.13)

i.e. we re-scale all quantities with a non-zero mass dimension by the same scale parameter ξ (which in principle also includes masses; in our case they are zero, however). The squared amplitudes of these two sets of momenta, we denote them by $|\mathcal{A}|^2$ and $|\mathcal{A}'|^2$, are then related by

$$|\mathcal{A}'|^2 = \xi^{-2(n-4)}|\mathcal{A}|^2.$$ (8.14)

One can see this by starting from the simple process of a fermion pair to fermion pair scattering where all possible diagrams yield a factor of ξ^0. Adding an external fermion pair or gluon/photon then yields an additional factor ξ^{-2}, which leads to the generalized formula above. We can then define the precision Δ by

$$\Delta = \left| \frac{|\mathcal{A}'|^2 \, \xi^{2(n-4)}}{|\mathcal{A}|^2} - 1 \right|.$$ (8.15)

Analytically, the fraction is identical to one and thus $\Delta = 0$. In a numerical program however, this ratio is never equal to one but only up to a certain amount of digits. Since the calculation uses numerically different momenta for the calculation, the deviation of the ratio from one tells us how precise the calculation is. Note that we can also extract the number of digits d up to which a numerical value can be trusted:

$$d = \lfloor -\log_{10} \Delta \rfloor.$$ (8.16)

Note that to obtain the correct integer value, we have to truncate the result of the logarithm which we achieved here with the floor operation, $\lfloor x \rfloor = \max\{y \in \mathbb{Z} \mid y \le x\}$.

Figure 8.1 shows plots for $e^-e^+ \to 6$ jets. We chose[7] $\xi = 10000$ and computed both the normal and the re-scaled squared amplitudes for 10^5 phase space and helicity points with the same parameters $Q = 90\,\text{GeV}$ and $y_{\text{cut}} = 0.0006$. For each point we determined the

---

[6] See for example [7].

[7] Note that the exact value is not important (we verified this) since the precision does not depend on ξ but it relies solely on the fact that the numerical values of the dimensionful quantities (i.e. momenta) vary sufficiently enough when comparing the re-scaled polarizations, spinors, etc. to those that are not re-scaled.

(truncated) precision Δ. Figure 8.1 shows the number of events per truncated precision; note that we chose to display them as lines instead of a proper histogram so that the diagram is still readable and the different helicity methods can be compared. Note that since the maximum number of valid digits for double precision is around 16, we only show the precision down to 10^{-16} (equaling 16 valid digits). Furthermore, note that for the two helicity sampling methods, we discarded all events where the helicity configuration led to vanishing helicity amplitudes since this only contributes to maximum precision and thus distorts the performance with respect to the other methods.

In figure 8.1(a), we see events for the Born contribution. Unlike our expectation that all methods should perform equally, there is a clear difference between helicity summation and sampling as opposed to those methods that are based on linear combinations, i.e. random polarizations and linear combination sampling. While the eigenstate methods all show a precision better than 10^{-10}, the linear combination methods are slightly worse with a precision better than 10^{-7}. We verified that this behavior is reproducible and not just an artifact of the chosen random number seed or anything similar.

The lower plot, figure 8.1(b) shows the real emission contribution. Here, the distinction between the eigenstate and the linear combination methods is no longer visible. Comparing the two plots, we note that the real emission is less precise on the whole, as expected. Due to the subtraction of large numbers that are almost equal in the context of the subtraction method, we find a few events that expose a precision of only two or three digits. Since the plot is doubly logarithmic, however, one has to stress that the percentage of very imprecise events is below 1 % so there is no need for concern.

8.5 Conclusion: Which Helicity Method Should Be Used?

By taking all information we gathered in this chapter as well as in the previous chapters, we now attempt to form a conclusion as to which helicity method is best suited for Monte Carlo integration with *VEGAS*.

The most important aspects of this consideration are

- speed and accuracy,

- numerical precision, and

- ease of implementation.

In terms of speed and accuracy, we found that both one–dimensional sampling methods are superior to any other method, with linear combination sampling being slightly better at Born level while helicity sampling proved to be the best method for the real emission contribution.

Regarding numerical precision, we found a small difference between the linear combination methods and the eigenstate methods for the Born contribution. However, the worst case precision of eight valid digits is still better than the precision one usually requires of
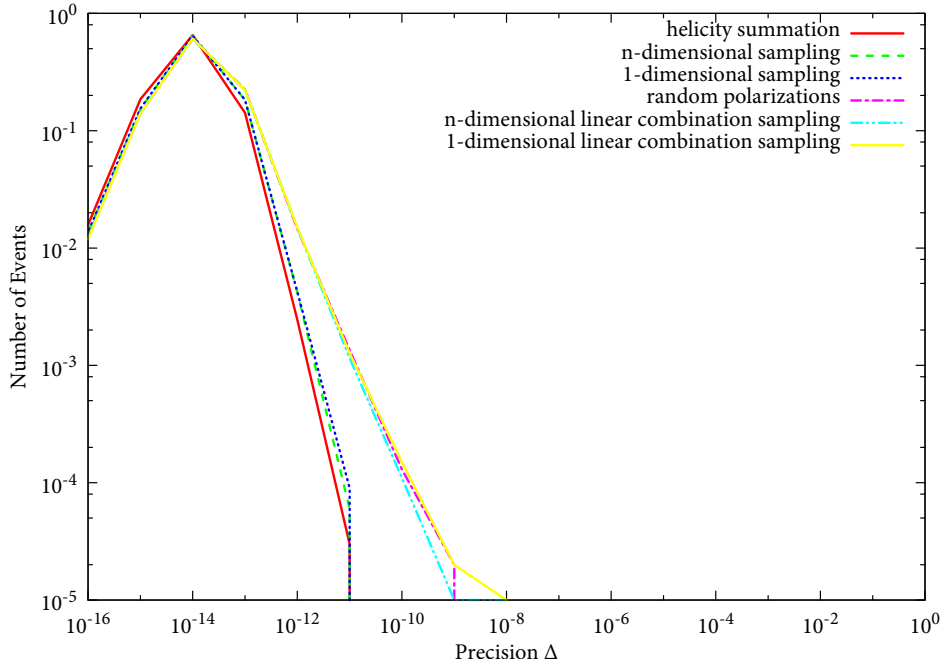
(a) Born contribution
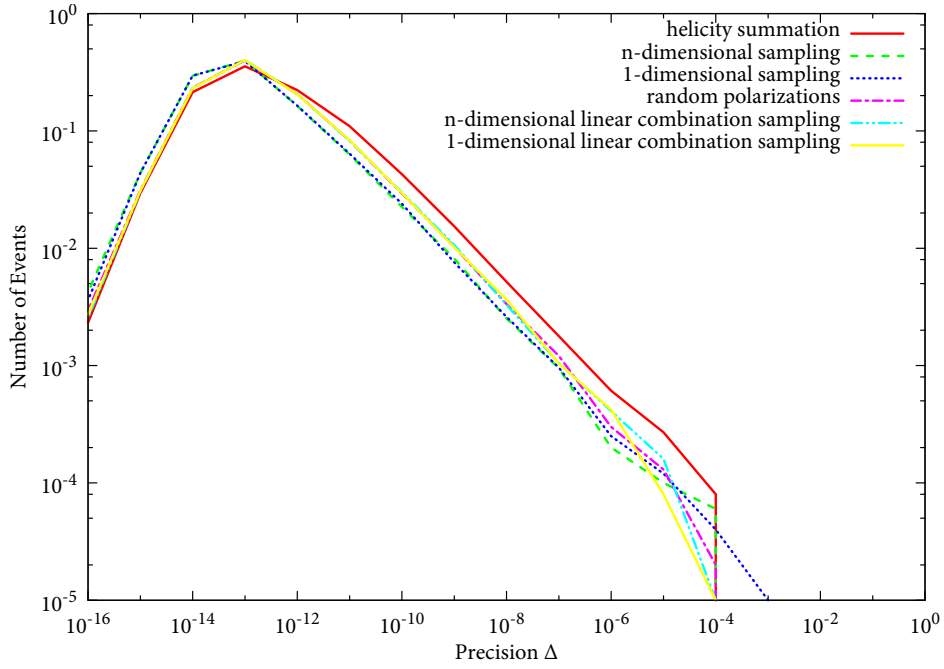
(b) Real emission contribution

Figure 8.1: Precision for 10^5 randomly chosen phase space and helicity variables for $e^- e^+ \to$ 6 jets. Since helicity configurations for which the amplitude vanishes always produce maximum precision (i.e. 10^{-16}), we did not count those contributions (only affects helicity sampling).

observables. For the real emission contribution, we found no visible difference between the methods.

With respect to the ease of implementation, the helicity sampling methods have a clear advantage over the linear combination methods for the real emission part since the linear combination methods require both the Catani–Seymour terms and additional helicity mixing dipoles, whereas the helicity sampling method is only a modification of the Catani–Seymour terms. At Born level, there is much less of a distinction since all methods rely on helicity eigenstates which makes all methods equally simple to implement.

In order to draw a completely proper conclusion, one would have to perform similar tests with the virtual contribution, which is however beyond the scope of this thesis. As we argued before, the virtual contribution should essentially behave like the Born contribution. We will assume this for the final decision.

Culminating all information we have gathered into one recommendation, we arrive at the conclusion that

<div align="center">**one–dimensional helicity sampling**</div>

is the method that any developer of an event generator should put to use. For the Born contribution alone, it is also reasonable to implement one–dimensional linear combination sampling since it requires no more effort to implement but yields slightly better results.

Summary and Outlook 9

9.1 Summary

In this work, we presented several methods to optimize the calculation of helicity and spin sums in numerical leading and next–to–leading order calculations. All methods require the use of Monte Carlo integration for the phase space integration in order to be efficient; we specifically analyzed all methods with respect to the adaptive *VEGAS* integration algorithm. We tested all methods separately and compared their efficiency by calculating cross sections for electron–positron annihilation into n QCD jets.

The basic idea of all methods is to replace the helicity sum by an integral. We investigated three basic ways of realizing this:

1. The summation over helicities can be re-interpreted as an expectation value which in turn can be evaluated by Monte Carlo methods such that the continuous integration variables are mapped to discrete values for the helicities; this is called *helicity sampling*. This method is known but apart from being mentioned in an abstract way in a few publications, there is not much known with respect to its implementation or performance. Contrary to the above, subtraction terms for infrared singularities at next–to–leading order have been developed which can be used with the method.

2. By a re-parameterization of the polarization states in terms of a linear combination of helicity eigenstates, each weighted by a continuous parameter (*helicity angle*), one replaces the helicity sum by an integral over the continuous parameter. We call this method *random polarizations*. It is mentioned in a few publications, however, there have not been any known subtraction terms that enable next–to–leading order calculations.[1] We provided a new extension of the dipole formalism that allows for random polarizations at next–to–leading order.

---

[1] The subtraction method used in this thesis is the common *dipole formalism* [26, 79]. Since work has begun for this thesis, a different subtraction method was published which can treat random polarizations without modifications [59]. A comparison of the methods proves an interesting avenue for future research.

3. The last method is a combination of the two methods above: by fixing two helicity angles for random polarizations, e.g. $\phi_1 = 0, \phi_2 = \pi/2$, we obtain two polarization states that are rotated with respect to helicity eigenstates. Summing over these states yields the usual polarization sum. Thus, these states can be used to implement the sampling procedure from item 1. The corresponding subtraction terms can be constructed from those for random polarizations. We refer to this method as *linear combination sampling*.

The most intuitive way of implementing all methods is to add an integration over a new helicity variable for each particle in the desired process; i.e. the integration dimension increases by n with respect to the phase space integration, where n is the number of external particles in the process. Since these additional integrations are not specifically suited for *VEGAS*, we found that they provide some speed up for more than two jets at leading order (with methods 2 and 3 being better than method 1), but none for next–to–leading order (in fact, they proved to be worse than helicity summation in most cases).

However, methods 1 and 3 can be implemented in a different which has a huge effect on the performance. The helicity information for all particles can be encoded in a single integer number which in turn can be rescaled to a decimal value between zero and one. Thus, it is sufficient to use one additional integral for all helicities. In this context, method 1 is very well suited for *VEGAS* since it can adapt very well to the helicity variable, while method 3 is not suited in the sense that there is no adaptation necessary. It turns out that both methods perform almost equally well at leading order, with method 3 yielding slightly better results. At next–to–leading order, however, method 1 shows a better convergence, especially for higher jet rates (we specifically investigated five jets).

In total, we found that the one–dimensional implementation of methods 1 and 3 shows better convergence than any of the n–dimensional methods. Especially at next–to–leading order they proved to be superior.

In addition to the performance of the methods, we also investigated the numerical precision of the methods. At leading order, methods 2 and 3 show slightly worse precision while still being accurate to at least seven digits which is better than the error one normally expects from any Monte Carlo integration. Next–to–leading order shows some less precise events which is expected due to the subtraction of large numbers . Still, the fraction of events with small precision is low so that there is no reason for concern.

Since the implementation at next–to–leading order only requires small modifications to the Catani–Seymour dipole terms, thus proving advantageous with respect to method 3 which requires more work, we concluded that one–dimensional helicity sampling is the method that should be recommended in general.

9.2   Outlook

Speeding up numerical calculations will always be of vital importance. The increasing complexity of calculations for observables with higher numbers of jets/particles and higher

order in the coupling constant makes efficient (automated) numerical algorithms even more important as these calculations become necessary. With next–to–leading order calculations being on the verge of automation, the focus is shifting towards next–to–next–to–leading order which is even more complex and requires more elaborate subtraction terms. Obviously, it is desirable to apply those methods that emerged as most efficient in this thesis to this order, too.

In addition, there is much left that one can examine in the closer vicinity of this work:

- We have only studied the effects for electron–positron annihilation in the leading color approximation. Although one would not expect significant deviations from our results naively, it would still be desirable to verify our results both for initial state hadrons and for full color calculations.

- The work presented in this thesis is restricted to QED and QCD processes. Obviously, processes including electroweak interactions and particles are also of vital importance for the LHC. Thus, it would be desirable to extend the whole automated algorithm including the helicity methods to the full Standard Model.

- This work was done with dipole subtraction in mind. We already mentioned that there is one other subtraction scheme that allows for random polarizations (Nagy–Soper subtraction [59]). One interesting avenue would be to compare the performance of the two. Thinking further, one could perform a comparison of several different subtraction schemes and analyze their behavior with respect to the different helicity methods (which would involve modifying the subtraction terms to make them suitable, if this has not been done yet).

- In a soon-to-be published thesis by C. Schwan [93], random polarizations are examined further: since they are purely real-valued objects, they enable one to perform the computation of massless observables using only real numbers instead of complex numbers, thus providing a speed up for the computation. Even though we found that one–dimensional helicity sampling yields better results compared to random polarizations, this speed up might make random polarizations even more feasible than the sampling procedure.

These are just a few possibilities for future research, which goes to show that the field of numerical calculations in high energy physics is very active and still provides lots of room for improvement.

Lorentz Transformation for the Phase Space Generator

A

This appendix shows the explicit expressions for the Lorentz transformations that are used in the phase space generator described in section 3.4. Note that the formulas here are directly taken from [18, 75, 76] with slightly changed naming conventions.

In order to be easily able to parameterize the newly inserted momentum p_s and its two slightly shifted "parent" momenta p'_a and p'_b, we transform from the existing reference frame to the center-of-mass frame of $p_a + p_b$ (which are the unshifted momenta before the insertion of p_s) such that p'_b is oriented along the $+z$-axis. Quantities in this new frame are denoted with a tilde. The transformation is given by equation (3.95) which we repeat here for convenience:

$$p = \Lambda_{\text{boost}} \Lambda_{xy}(\phi) \Lambda_{xz}(\theta) \, \widetilde{p} \tag{A.1}$$

The formula applies to all three momenta p'_a, p'_b and p_s.

First, let us define $P = \sqrt{s_{ab}}$ and $Q = p_a + p_b$ (note that this is the center-of-mass momentum in our new frame and has nothing to do with the center-of-mass energy in the collision). In the new reference frame, $\widetilde{p}_b$ is given by

$$\widetilde{p}_b = \left(\frac{Q^0}{P} p_b^0 - \frac{\vec{p}_b \cdot \vec{Q}}{P}, \; \vec{p}_b + \left[\frac{\vec{p}_b \cdot \vec{Q}}{P(Q^0 + P)} - \frac{p_b^0}{P} \right] \vec{Q} \right) \tag{A.2}$$

We find the transformed angles

$$\theta = \arccos\left(1 - \frac{\widetilde{p}_b \cdot \widetilde{p}'_b}{2\widetilde{p}_b^0 \widetilde{p}_b'^0} \right), \quad \phi = \arctan\left(\frac{\widetilde{p}_b^2}{\widetilde{p}_b^1} \right). \tag{A.3}$$

The Lorentz transformations $\Lambda_{xz}(\theta)$ and $\Lambda_{xy}(\phi)$ are then simple rotations around these

angles:

$$
\Lambda_{xz}(\theta) = \begin{pmatrix} 1 & 0 & 0 & 0 \\ 0 & \cos\theta & 0 & \sin\theta \\ 0 & 0 & 1 & 0 \\ 0 & -\sin\theta & 0 & \cos\theta \end{pmatrix}, \quad \Lambda_{xy}(\phi) = \begin{pmatrix} 1 & 0 & 0 & 0 \\ 0 & \cos\phi & -\sin\phi & 0 \\ 0 & \sin\phi & \cos\phi & 0 \\ 0 & 0 & 0 & 1 \end{pmatrix}. \tag{A.4}
$$

Finally, we need to know the boost matrix Λ_{boost} which takes the form

$$
\Lambda_{\text{boost}} = \begin{pmatrix} \dfrac{Q^0}{P} & \dfrac{\vec{Q}}{P} \\ \dfrac{\vec{Q}}{P} & \mathbb{1} + \dfrac{\vec{Q}\vec{Q}^T}{P(Q^0 + P)} \end{pmatrix}, \tag{A.5}
$$

where $\vec{Q}\vec{Q}^T$ indicates an outer product resulting in a matrix. Another way to write this matrix is in terms of its action on a vector q, such that $q' = \Lambda_{\text{boost}}\, q$:

$$
q' = \left(\frac{Q^0}{P} q^0 + \frac{\vec{q}\cdot\vec{Q}}{P}, \ \vec{q} + \left[\frac{\vec{q}\cdot\vec{Q}}{P(Q^0 + P)} + \frac{q^0}{P} \right] \vec{Q} \right). \tag{A.6}
$$

Catani-Seymour Variables in the Soft and Collinear Limit

B

In this appendix, we gather all variables (and frequently occurring combinations thereof) that are used in the Catani-Seymour dipole subtraction framework (final–final case) and, consequently, also in our extension to random polarizations. We analyze each of them both in the collinear and in the soft limit so that the resulting formulas can be used to easily determine the behavior of any subtraction term in the respective limits.

All expressions are gathered in table B.1. The first column shows the variables themselves and their definitions, if applicable. The two remaining columns show the terms re-written into the collinear and soft limit. Note that we rarely give the full term, but only up to some order in λ_{coll} or λ_{soft}, respectively. The given precision is always sufficient to do a proper analysis of the terms occurring in this thesis.

Variable	Collinear limit	Soft limit
p_i^μ	$x p_{\text{coll}}^\mu + \lambda_{\text{coll}} k^\mu + \mathcal{O}\left(\lambda_{\text{coll}}^2\right)$	p_i^μ
p_j^μ	$\overline{x} p_{\text{coll}}^\mu - \lambda_{\text{coll}} k^\mu + \mathcal{O}\left(\lambda_{\text{coll}}^2\right)$	$\lambda_{\text{soft}} k^\mu$
$s_{ij} = 2p_i p_j$	$-\lambda_{\text{coll}}^2 \dfrac{k^2}{x\overline{x}}$	$\lambda_{\text{soft}}(2p_i k)$
$s_{ik} = 2p_i p_k$	$2x p_{\text{coll}} p_k + \mathcal{O}\left(\lambda_{\text{coll}}\right)$	s_{ik}
$s_{jk} = 2p_j p_k$	$2\overline{x} p_{\text{coll}} p_k + \mathcal{O}\left(\lambda_{\text{coll}}\right)$	$\lambda_{\text{soft}}(2k p_k)$
$P^2 = s_{ij} + s_{ik} + s_{jk}$	$2p_{\text{coll}} p_k + \mathcal{O}\left(\lambda_{\text{coll}}^2\right)$	$s_{ik} + \mathcal{O}\left(\lambda_{\text{soft}}\right)$
$y = \dfrac{s_{ij}}{P^2}$	$-\lambda_{\text{coll}}^2 \dfrac{k^2}{(2p_{\text{coll}} p_k)x\overline{x}} + \mathcal{O}\left(\lambda_{\text{coll}}^4\right)$	$\lambda_{\text{soft}} \dfrac{2p_i k}{s_{ik}}$
$\overline{y} = 1 - y$	$1 + \mathcal{O}\left(\lambda_{\text{coll}}^2\right)$	$1 + \mathcal{O}\left(\lambda_{\text{soft}}\right)$
$z = \dfrac{s_{ik}}{s_{ik} + s_{jk}}$	$x + \mathcal{O}\left(\lambda_{\text{coll}}^2\right)$	$1 + \mathcal{O}\left(\lambda_{\text{soft}}\right)$
$\overline{z} = 1 - z$	$\overline{x} + \mathcal{O}\left(\lambda_{\text{coll}}^2\right)$	$0 + \mathcal{O}\left(\lambda_{\text{soft}}\right)$
$(z p_i^\mu - \overline{z} p_j^\mu)$	$(zx - \overline{z}\overline{x}) p_{\text{coll}}^\mu + \lambda_{\text{coll}} k^\mu + \mathcal{O}\left(\lambda_{\text{coll}}^2\right)$	p_i^μ
$\dfrac{y}{\overline{y}}$	$-\lambda_{\text{coll}}^2 \dfrac{k^2}{(2p_{\text{coll}} p_k)x\overline{x}} + \mathcal{O}\left(\lambda_{\text{coll}}^4\right)$	$\lambda_{\text{soft}} \dfrac{2p_i k}{s_{ik}}$
$\dfrac{1}{1 - z\overline{y}}$	$\dfrac{P^2}{s_{ij} + s_{jk}}$	$\dfrac{1}{\lambda_{\text{soft}}} \dfrac{p_i p_k}{(p_i + p_k)k}$
$\dfrac{1}{1 - \overline{z}\overline{y}}$	$\dfrac{P^2}{s_{ij} + s_{ik}}$	$1 + \mathcal{O}\left(\lambda_{\text{soft}}\right)$
$\tilde{p}_k^\mu = \dfrac{1}{\overline{y}} p_k^\mu$	$p_k^\mu + \mathcal{O}\left(\lambda_{\text{coll}}^2\right)$	$p_k^\mu + \mathcal{O}\left(\lambda_{\text{soft}}\right)$
$\tilde{p}_{ij}^\mu = p_i^\mu + p_j^\mu - y\tilde{p}_k$	$p_{\text{coll}}^\mu + \mathcal{O}\left(\lambda_{\text{coll}}^2\right)$	$p_i^\mu + \mathcal{O}\left(\lambda_{\text{soft}}\right)$

Table B.1: Reference table for all dipole variables in the collinear and soft limits.

Details on the Soft and Collinear Limits for Random Polarization Functions

<div style="text-align: right;">**C**</div>

This chapter details the calculations of the functions $\mathcal{P}_{(ij)\to i+j}$ and $\widetilde{\mathcal{S}}_{(ij)\to i+j}$ for helicity summed partons i and j which exhibit spurious poles due to our choice of reference momenta. In section 6.2.4 we only showed the results. The calculations themselves, however, contain some non-trivial steps which we want to highlight in this chapter.

C.1   The Splitting $q \to qg$

In the following, we treat the three relevant contributions separately. Note that to keep them all on the same footing, we leave out all spinors of the emitter quarks that are directly contracted with the n–parton amplitude.

The Collinear Function

In terms of the collinear function, this means that instead of the full $\left[\mathcal{P}_{q\to qg}\right]_{\alpha\beta}$ definition, it is sufficient to look at

$$
\begin{aligned}
\mathcal{P}'_{\text{RP}} &\equiv \sum_{\lambda_i,\lambda_j,\eta} \text{Split}^{\eta*}_{q\to qg} \text{Split}^{\eta}_{q\to qg} \\
&= \frac{1}{(2p_ip_j)^2} \sum_{\lambda_i,\lambda_j,\eta} \epsilon_\mu^{\lambda_j*}(p_j)\epsilon_\nu^{\lambda_j}(p_j) \left[\overline{u}^{\eta}(\tilde{p}_{ij})\,\gamma^\mu\,u^{\lambda_i}(p_i)\right]\left[\overline{u}^{\lambda_i}(p_i)\,\gamma^\nu\,u^{\eta'}(\tilde{p}_{ij})\right]
\end{aligned}
\tag{C.1}
$$

Notice that this equation differs from $\mathcal{P}_{q\to qg}$ not only by the missing emitter spinors, but also by the helicity assignment. Writing the above is possible since there are no spin correlations for quark emitters (see for example the spin delta in the original Catani–Seymour definition (4.25c) on page 66), so the end result is the same as performing the full sums in $\mathcal{P}_{q\to qg}$.

    The second line in the above computation can be re-expressed using Dirac algebra, the full polarizations and spin sums and by inserting the dipole momentum parameterization.

The final result which is not difficult to obtain, reads

$$\mathcal{P}'_{\text{RP}} = \frac{1}{P^2}\left[\frac{2}{y} + 2\frac{1+z}{y}\frac{p_i q_j}{p_j q_j} - \frac{2}{\overline{y}}\frac{p_k q_j}{p_j q_j}\right] + \mathcal{O}\left(\epsilon\right) \tag{C.2}$$

where $P^2 = 2(p_i p_j + p_i p_k + p_k p_j)$ as defined in appendix B. Note that this is the full result without any approximation. Since we evaluate these functions in $d = 4$ anyway, we do not explicitly give terms that do not vanish if $d \neq 4$.

The Soft Function

We treat the soft term $\widetilde{\mathcal{S}}_{q \to qg}$ in the same vein as the collinear function by defining

$$\mathcal{S}'_{\text{RP}} \equiv -\sum_{\lambda_j} \frac{\left(p_i \epsilon^{\lambda_j *}(p_j)\right)\left(p_k \epsilon^{\lambda_j}(p_j)\right) + \left(p_k \epsilon^{\lambda_j *}(p_j)\right)\left(p_i \epsilon^{\lambda_j}(p_j)\right)}{(p_k p_j)(p_i p_j + p_k p_j)} \tag{C.3}$$

without the spinors for the emitter parton. Inserting the full polarization sum for parton j leaves one with the result

$$\mathcal{S}'_{\text{RP}} = \frac{1}{P^2}\left[\frac{4z\overline{y}}{y(1-z\overline{y})} - \frac{4}{y}\frac{p_i q_j}{p_j q_j} - \frac{4}{1-z\overline{y}}\frac{p_k q_j - p_i q_j}{p_j q_j}\right]. \tag{C.4}$$

The Catani–Seymour Term

Finally, we have to re-write the Catani–Seymour dipole term that we use for comparison is defined such that it matches the above definitions. The relevant part is the spin–correlation matrix $V_{q \to qg}$ *without* the color factor and the coupling constant. However, note that the Catani–Seymour term lacks a factor $1/2p_i p_j$ with respect to our definitions which is due to a different definition of the dipoles themselves. After matching all the relevant terms, we end up with

$$V'_{\text{CS}} \equiv \frac{1}{p_i p_j}\left[\frac{2}{1-z\overline{y}} - (1+z) - \epsilon\overline{z}\right] \tag{C.5}$$

which can easily be re-written to read

$$V'_{\text{CS}} = \frac{1}{P^2}\left[\frac{4}{y(1-z\overline{y})} - 2\frac{1+z}{y}\right] + \mathcal{O}\left(\epsilon\right). \tag{C.6}$$

Analysis of the Sum

The next step is to compute the sum of the soft and collinear functions and subtracting the Catani–Seymour dipole result. A quick calculation reveals

$$\mathcal{P}'_{\text{RP}} + \mathcal{S}'_{\text{RP}} - V'_{\text{CS}} = \frac{1}{P^2}\left[\frac{1}{y}\left(2z - 2\overline{z}\frac{p_i q_j}{p_j q_j}\right) - \frac{2}{\overline{y}}\frac{p_k q_j}{p_j q_j} - \frac{4}{1-z\overline{y}}\frac{p_k q_j - p_i q_j}{p_j q_j}\right] + \mathcal{O}\left(\epsilon\right). \tag{C.7}$$

We now have to analyze these terms in the soft and collinear limits to find out if they are singular in any of the limits. If our terms properly matched the Catani–Seymour terms, they would all be finite.

First, let us verify that there are no further collinear singularities by making use of table B.1 from appendix B. We analyze the terms separately:

$$\frac{1}{y}\left(2z - 2\bar{z}\frac{p_i q_j}{p_j q_j}\right) \xrightarrow{\lambda_{\text{coll}} \to 0} \frac{1}{y}\left(2x - 2\bar{x}\frac{x\, p_{\text{coll}} q_j}{\bar{x}\, p_{\text{coll}} q_j}\right) = 0 \tag{C.8a}$$

$$\frac{2}{\bar{y}}\frac{p_k q_j}{p_j q_j} \xrightarrow{\lambda_{\text{coll}} \to 0} 2\frac{p_k q_j}{\bar{z}\, p_{\text{coll}} q_j} \tag{C.8b}$$

$$\frac{4}{1 - z\bar{y}}\frac{p_k q_j - p_i q_j}{p_j q_j} \xrightarrow{\lambda_{\text{coll}} \to 0} \frac{1}{x}\frac{p_k q_j - p_i q_j}{p_{\text{coll}} q_j}. \tag{C.8c}$$

It turns out that all terms are integrable.

Let us do the same for the soft limit. We find

$$\frac{1}{y}\left(2z - 2\bar{z}\frac{p_i q_j}{p_j q_j}\right) \xrightarrow{\lambda_{\text{soft}} \to 0} \frac{1}{\lambda_{\text{soft}}}\frac{p_i p_k}{p_i k}, \tag{C.9a}$$

$$\frac{2}{\bar{y}}\frac{p_k q_j}{p_j q_j} \xrightarrow{\lambda_{\text{soft}} \to 0} \frac{2}{\lambda_{\text{soft}}}\frac{p_k q_j}{k q_j} \tag{C.9b}$$

$$\frac{4}{1 - z\bar{y}}\frac{p_k q_j - p_i q_j}{p_j q_j} \xrightarrow{\lambda_{\text{soft}} \to 0} \frac{1}{\lambda_{\text{soft}}^2}\frac{(p_i p_k)(p_k q_j - p_i q_j)}{(p_i k + p_k k)(k q_j)}. \tag{C.9c}$$

The first two terms are integrable while the last term is clearly divergent in the soft limit. This is the term that causes the spurious pole because of which our subtraction terms as defined above do not work properly.

In order to get rid of the spurious singularity, we can correct our soft term $\widetilde{\mathcal{S}}_{q \to qg}$ with a new term

$$\begin{aligned}[\mathcal{S}_{q\to qg}^{\text{corr}}]_{\alpha\beta} &= \left[\frac{1}{P^2}\frac{4}{1-z\bar{y}}\frac{p_k q_j - p_i q_j}{p_j q_j}\right]u_\alpha(p_i)\bar{u}_\beta(p_i) \\ &= 4\left[\frac{p_k q_j - p_i q_j}{(p_j q_j)(p_i p_j + p_j p_k)}\right]u_\alpha(p_i)\bar{u}_\beta(p_i).\end{aligned} \tag{C.10}$$

There, we re-attached the spinors to make the term match the original soft term $\widetilde{\mathcal{S}}_{q \to qg}$. We can now define the proper soft term $\mathcal{S}_{q \to qg}$ by

$$\mathcal{S}_{q \to qg} = \widetilde{\mathcal{S}}_{q \to qg} + \mathcal{S}_{q \to qg}^{\text{corr}}. \tag{C.11}$$

C.2 The Splitting $g \to gg$

In the case of the gluonic splitting, we have to take a slightly different avenue. If we again leave out the emitter polarizations that are directly contracted with the amplitude, we face the difficult task of dealing with helicity mixing polarization products of the type

$$\epsilon_\mu^+(\tilde{p}_{ij}) \, \epsilon_\nu^-(\tilde{p}_{ij}) \tag{C.12}$$

in the collinear function $\mathcal{P}_{g \to gg}$ which is due to the non-vanishing spin correlations. Fortunately, this can be easily avoided by including *all* emitter polarizations in our calculations. Doing so allows us to avoid the above combinations by contracting full polarization sums instead.

Because of this, the terms that we analyze in the following will all have two open Lorentz indices which we will denote by ρ and σ. These indices then contract directly into the open n–parton amplitudes $\mathcal{A}_n^{*\rho}$ and $\mathcal{A}_n^\sigma$. Since the resulting quantities are symmetric in the indices, we write

$$\begin{pmatrix} [\widetilde{\mathcal{P}}_{\mathrm{RP}}'']_{\rho\sigma} \\ [\widetilde{\mathcal{S}}_{\mathrm{RP}}'']_{\rho\sigma} \\ [\widetilde{V}_{\mathrm{CS}}'']_{\rho\sigma} \end{pmatrix} = \left(g_{\alpha\mu} g_{\beta\nu} + g_{\alpha\nu} g_{\beta\mu} \right) \begin{pmatrix} [\mathcal{P}_{\mathrm{RP}}'']^{\mu\nu} \\ [\mathcal{S}_{\mathrm{RP}}'']^{\mu\nu} \\ [V_{\mathrm{CS}}'']^{\mu\nu} \end{pmatrix} \tag{C.13}$$

and we only give results for the right hand quantities with indices μ and ν.

Furthermore, we define the quantity

$$Q_x^\mu \equiv \frac{q_x^\mu}{p_x q_x} \tag{C.14}$$

which will shorten many expressions.

The Collinear Function

Before giving any results, let us define the basis for our calculation very clearly. We do this for the *unsymmetrized* version. Using the above argument, we rewrite the collinear function as follows:

$$[\widetilde{\mathcal{P}}_{\mathrm{RP}}'']_{\rho\sigma} = \sum_{\lambda_i, \lambda_j} [\mathcal{P}_{g \to gg}]_{\rho\sigma}$$

$$= \sum_{\substack{\lambda_i, \lambda_j, \\ \eta, \eta'}} \epsilon_\rho^\eta(\tilde{p}_{ij}) \, \mathrm{Split}_{g \to gg}^{\eta^*} \mathrm{Split}_{g \to gg}^\eta \, \epsilon_\sigma^{\eta'\,*}(\tilde{p}_{ij})$$

$$= \frac{1}{(p_i p_j)^2} d^{\gamma\delta}(p_i) \, d^{\kappa\tau}(p_j) \, d_\rho^{\ \chi}(\tilde{p}_{ij}) \, d_\sigma^{\ \omega}(\tilde{p}_{ij}) \Big($$

$$g_{\gamma\kappa} g_{\delta\tau} p_{i_\chi} p_{i_\omega} + g_{\gamma\kappa} g_{\tau\omega} p_{i_\chi} p_{j_\delta} - g_{\gamma\kappa} g_{\delta\omega} p_{i_\chi} p_{i_\tau}$$

$$+ g_{\kappa\chi} g_{\delta\tau} p_{j_\gamma} p_{i_\omega} + g_{\kappa\chi} g_{\tau\omega} p_{j_\gamma} p_{j_\delta} - g_{\kappa\chi} g_{\delta\omega} p_{j_\gamma} p_{i_\tau}$$

$$- g_{\gamma\chi} g_{\delta\tau} p_{i_\kappa} p_{i_\omega} - g_{\gamma\chi} g_{\tau\omega} p_{i_\kappa} p_{j_\delta} + g_{\gamma\chi} g_{\delta\omega} p_{i_\kappa} p_{i_\tau} \Big) \tag{C.15}$$

The last line was obtained by inserting $\mathrm{Split}_{g \to gg}$ and re-writing the Minkowski products into contractions using the Minkowski metric. Also note that we re-wrote all sums and their corresponding polarization vectors into polarization sums. This form of the splitting can be fed into FORM [102, 103] along with several conditions that simplify the expression, such as gauge invariance with respect to the emitter momentum $\tilde{p}_{ij}$, etc. After some more manual work, one ends up with the still long (symmetrized) result

$$
\begin{aligned}
&[\mathcal{P}''_{\mathrm{RP}}]^{\mu\nu} \\
&= \frac{4}{s_{ij}^2} \Big(p_i^\mu p_j^\nu \big[-1 + (p_i Q_j) \big] + p_j^\mu p_j^\nu (p_i Q_j) \Big) \\
&\quad + \frac{2}{s_{ij}} \Big(p_i^\mu p_j^\nu (Q_i Q_j) \\
&\qquad + p_i^\mu Q^\nu \Big((p_i Q_j)(-(p_j Q_i) - 2) - (p_j Q_i) + (p_i Q_j)\bar{z} - \bar{z} + \frac{y}{\bar{y}}(p_k Q_j)\big[(p_j Q_i) + 1 \big] \Big) \\
&\qquad + p_i^\mu Q_j^\nu ((p_j Q_i) + 1) \\
&\qquad + p_j^\mu Q^\nu \Big(-z + (p_i Q_j) \big[-\bar{z} - (p_j Q_i) - \frac{y}{\bar{y}}(p_k Q_i) \big] \\
&\qquad\qquad\qquad + 2(p_j Q_i) \big[-1 + (p_k Q_j)y \big] + (p_k Q_j)y \Big) \\
&\qquad + p_j^\mu Q_j^\nu (2(p_j Q_i) + 1) \\
&\qquad - p_j^\mu Q_i^\nu (p_i Q_j) \\
&\qquad - g^{\mu\nu} \big((p_i Q_j) + (p_j Q_i) \big) \Big) \\
&\quad + \frac{P^2}{2} \Big(Q^\mu Q^\nu (Q_i Q_j) z \bar{z} y \Big) \\
&\quad - p_i^\mu Q^\nu (Q_i Q_j) z \\
&\quad - p_j^\mu Q^\nu (Q_i Q_j) \bar{z} \\
&\quad - Q_i^\mu Q_j^\nu \\
&\quad + Q^\mu Q^\nu \Big(-z\bar{z} + (p_i Q_j)(p_k Q_i) \frac{y(1+z)}{\bar{y}} \\
&\qquad\qquad\qquad + (p_j Q_i) \big[z + (p_k Q_j) \frac{zy}{\bar{y}} \big] + (p_k Q_i) \big[\frac{y}{\bar{y}} - (p_k Q_j) \frac{y^2}{\bar{y}^2} \big] \Big) \\
&\quad + Q^\mu Q_j^\nu \big[-(p_j Q_i)z - \frac{y}{\bar{y}}(p_k Q_i) \big] \\
&\quad + Q^\mu Q_i^\nu \big[1 + (p_i Q_j)(1+z) + (p_k Q_j) \frac{y}{\bar{y}} \big].
\end{aligned}
$$

The Soft Function

Again, we treat the soft term $\widetilde{\mathcal{S}}''_{g \to gg}$ in the same vein as the collinear function by defining

$$
\begin{aligned}
[\widetilde{\mathcal{S}}''_{\text{RP}}]_{\rho\sigma} &\equiv \sum_{\lambda_i, \lambda_j} [\widetilde{\mathcal{S}}_{g\to gg}]_{\rho\sigma} \\
&= -\sum_{\lambda_i, \lambda_j} \Bigg(\frac{\big(p_i \epsilon^{\lambda_j*}(p_j)\big)\big(p_k \epsilon^{\lambda_j}(p_j)\big) + \big(p_k \epsilon^{\lambda_j*}(p_j)\big)\big(p_i \epsilon^{\lambda_j}(p_j)\big)}{(p_k p_j)(p_i p_j + p_k p_j)} \\
&\qquad + \frac{\big(p_j \epsilon^{\lambda_i*}(p_i)\big)\big(p_k \epsilon^{\lambda_i}(p_i)\big) + \big(p_k \epsilon^{\lambda_i*}(p_i)\big)\big(p_j \epsilon^{\lambda_i}(p_i)\big)}{(p_k p_i)(p_j p_i + p_k p_i)} \Bigg)
\end{aligned}
\tag{C.16}
$$

We can feed this into FORM once again by re-writing the term in a similar way as the collinear function. We end up with the unsymmetrized result

$$
\begin{aligned}
[\mathcal{S}''_{\text{RP}}]^{\mu\nu} = \frac{2}{s_{ij}} \Bigg(& (2 p_j^\mu Q_j^\nu - g^{\mu\nu}) \left[\frac{\overline{z}y}{1 - \overline{z}y} - (p_j Q_i) + \frac{y}{1 - z\overline{y}}\big((p_j Q_i) - (p_k Q_i)\big) \right] \\
&+ (2 p_i^\mu Q_i^\nu - g^{\mu\nu}) \left[\frac{z\overline{y}}{1 - z\overline{y}} - (p_i Q_j) + \frac{y}{1 - z\overline{y}}\big((p_i Q_j) - (p_k Q_j)\big) \right] \Bigg).
\end{aligned}
$$

The Catani–Seymour Term

Lastly, we deal with the Catani–Seymour term which contains the same spin correlations as the collinear function above. We have to add the same factors as for the $q \to qg$ splitting, and we also have to add another set of polarization vectors from the amplitudes. The Catani–Seymour spin correlation term then reads

$$
\begin{aligned}
[\widetilde{V}''_{\text{CS}}]_{\rho\sigma} &\equiv \frac{1}{p_i p_j} \left[-g^{\mu\nu} \left(\frac{1}{1 - z\overline{y}} + \frac{1}{1 - \overline{z}y} - 2 \right) + \frac{1-\epsilon}{p_i p_j} K^\mu K^\nu \right] \times \\
&\qquad \times \sum_{\eta, \eta'} \epsilon_\mu^{\eta*}(\tilde{p}_{ij}) \, \epsilon_{\eta'}^\nu(\tilde{p}_{ij}) \, \epsilon_\rho^\eta(\tilde{p}_{ij}) \, \epsilon_\sigma^{\eta'*}(\tilde{p}_{ij})
\end{aligned}
\tag{C.17}
$$

where we again find two polarization sums for the emitter gluon. Using FORM once more, we get

$$
\begin{aligned}
[V''_{\text{CS}}]^{\mu\nu} = \frac{4}{s_{ij}^2} & \left(-p_i^\mu p_i^\nu z^2 + 2 p_i^\mu p_j^\nu z\overline{z} - p_j^\mu p_j^\nu \overline{z}^2 \right) \\
&+ \frac{2}{s_{ij}} \left(-2 p_i^\mu Q^\nu z(1 - 2z)y + p_j^\mu Q^\nu \left[-(1+2z)^2 + 2z \right] + g^{\mu\nu} \left(-2 + \frac{1}{1 - \overline{z}y} + \frac{1}{1 - z\overline{y}} \right) \right) \\
&- 8 Q^\mu Q^\nu z\overline{z}.
\end{aligned}
$$

Analysis of the Sum

Just looking at the above results reveals that there is hardly any cancellation when summing the three terms. This does not mean that the terms do not match; instead, the cancellations are not as obvious as before. Furthermore, the above expressions still contain many finite terms that are not divergent in either of the limits.

Hence, we take a different route in the $g \to gg$ case: this time, we evaluate each of the three terms separately in the collinear and soft limits, drop all non-singular terms and look at the sum of the three terms afterwards.

Let us begin by analyzing the collinear limit. Again, we can make use of table B.1 from appendix B. However, we also need to be able to treat products of reference momenta. Note that with our choice of reference momenta, we find $q_i q_j = p_i p_j$. This gives us the relation

$$(Q_i Q_j) = \frac{(q_i q_j)}{(p_i q_i)(p_j q_j)} = \frac{(p_i p_j)}{(p_i q_i)(p_j q_j)} = -\frac{k_\perp^2}{2x\overline{x}} \frac{1}{(p_i q_i)(p_j q_j)} \tag{C.18}$$

which is clearly not singular. Additionally, we use Sudakov's parameterization for the momenta p_i and p_j. After a simple but lengthy computation we can drop all non-singular terms so that we end up with

$$[\mathcal{P}''_{\mathrm{RP}}]^{\mu\nu} \xrightarrow{\lambda_{\mathrm{coll}} \to 0} k_\perp^\mu k_\perp^\nu \frac{4x^2\overline{x}^2}{(k_\perp^2)^2} + \frac{2x\overline{x}}{k_\perp^2} g^{\mu\nu} \left((p_i Q_j) + (p_j Q_i) \right) + \mathcal{O}\left(\frac{1}{k_\perp}\right)$$

$$[\mathcal{S}''_{\mathrm{RP}}]^{\mu\nu} \xrightarrow{\lambda_{\mathrm{coll}} \to 0} \frac{2x\overline{x}}{k_\perp^2} g^{\mu\nu} \left(\left[\frac{s_{jk}}{s_{ik}} + \frac{s_{ik}}{s_{jk}} \right] - \left[(p_j Q_i) + (p_i Q_j) \right] \right) + \mathcal{O}\left(\frac{1}{k_\perp}\right)$$

$$[V''_{\mathrm{CS}}]^{\mu\nu} \xrightarrow{\lambda_{\mathrm{coll}} \to 0} 4x^2\overline{x}^2 \frac{k_\perp^\mu k_\perp^\nu}{(k_\perp^2)^2} + 2g^{\mu\nu} x\overline{x} \left[\frac{s_{jk}}{s_{ik}} + \frac{s_{ik}}{s_{jk}} \right] \frac{1}{k_\perp^2} + \mathcal{O}\left(\frac{1}{k_\perp}\right).$$

The total sum of these terms is of $\mathcal{O}\left(\frac{1}{k_\perp}\right) = \mathcal{O}\left(\frac{1}{\lambda_{\mathrm{coll}}}\right)$ and thus integrable:

$$[\mathcal{P}''_{\mathrm{RP}}]^{\mu\nu} + [\mathcal{S}''_{\mathrm{RP}}]^{\mu\nu} - [V''_{\mathrm{CS}}]^{\mu\nu} \xrightarrow{\lambda_{\mathrm{coll}} \to 0} \mathcal{O}\left(\frac{1}{\lambda_{\mathrm{coll}}}\right). \tag{C.19}$$

Hence, there are no spurious collinear poles due to gauge terms.

Let us now do the same for the soft limit. Again, we can use table B.1, gauge invariance with respect to the n–parton amplitude, plus the fact that the momentum Q_j scales like $\frac{1}{\lambda_{\mathrm{soft}}}$:

$$Q_j = \frac{q_j}{(p_j q_j)} \xrightarrow{\lambda_{\mathrm{soft}} \to 0} \frac{1}{\lambda_{\mathrm{soft}}} \frac{q_j}{(kq_j)}. \tag{C.20}$$

We then obtain as a final result:

$$[\mathcal{P}''_{\mathrm{RP}}]^{\mu\nu} \xrightarrow{\lambda_{\mathrm{soft}} \to 0} -\frac{1}{\lambda_{\mathrm{soft}}^2} \frac{1}{(p_i k)} g^{\mu\nu} \frac{(p_i q_j)}{(kq_j)} + \mathcal{O}\left(\frac{1}{\lambda_{\mathrm{soft}}}\right)$$

$$[\mathcal{S}''_{\mathrm{RP}}]^{\mu\nu} \xrightarrow{\lambda_{\mathrm{soft}} \to 0} -g^{\mu\nu} \frac{1}{\lambda_{\mathrm{soft}}^2} \left[\frac{s_{ik}}{(p_i + p_k)k} \frac{1}{2(p_i k)} - \frac{(p_i q_j)}{(p_i k)(kq_j)} - \frac{1}{P^2} \frac{s_{ik}}{(p_i + p_k)k} \frac{(p_k q_j) - (p_i q_j)}{(kq_j)} \right]$$

$$+ \mathcal{O}\left(\frac{1}{\lambda_{\text{soft}}}\right)$$

$$[\boldsymbol{V}_{\text{CS}}'']^{\mu\nu} \xrightarrow{\lambda_{\text{soft}} \to 0} \frac{1}{2\lambda_{\text{soft}}^2} g^{\mu\nu} \frac{1}{(p_i k)} \frac{s_{ik}}{(p_i + p_k)k} + \mathcal{O}\left(\frac{1}{\lambda_{\text{soft}}}\right)$$

If we perform the sum here, we find that only the last term in the bracket of the soft function survives:

$$[\mathcal{P}_{\text{RP}}'']^{\mu\nu} + [\mathcal{S}_{\text{RP}}'']^{\mu\nu} - [\boldsymbol{V}_{\text{CS}}'']^{\mu\nu} \xrightarrow{p_j \to 0} \frac{g^{\mu\nu}}{\lambda_{\text{soft}}^2} \frac{1}{P^2} \frac{s_{ik}}{(p_i + p_k)k} \frac{(p_k q_j) - (p_i q_j)}{(k q_j)} + \mathcal{O}\left(\frac{1}{\lambda_{\text{soft}}}\right). \quad \text{(C.21)}$$

If we trace this term back to its origin *before* taking the limit, we find almost the same term as for the $q \to qg$ splitting:

$$[\mathcal{P}_{\text{RP}}'']^{\mu\nu} + [\mathcal{S}_{\text{RP}}'']^{\mu\nu} - [\boldsymbol{V}_{\text{CS}}'']^{\mu\nu} = -\frac{2}{s_{ij}} g^{\mu\nu} \frac{y}{1 - z\overline{y}} \frac{(p_k q_j) - (p_i q_j)}{(p_j q_j)} + \text{ non-singular terms.}$$

$$\text{(C.22)}$$

The only difference is due to the additional polarization vectors which give us a $g^{\mu\nu}$ in the formula above, and the fact that this term actually appears symmetrized, which gives us an additional factor two after applying equation (C.13).

Hence, we proceed analogously as for the splitting $q \to qg$. In order to get rid of the spurious singularity, we have to correct our soft term $\widetilde{\mathcal{S}}_{g \to gg}$ with a new term

$$[\mathcal{S}_{g \to gg}^{\text{corr}}]_{\rho\sigma} = 4 \frac{p_k q_j - p_i q_j}{(p_j q_j)(p_i p_j + p_j p_k)} \epsilon_\mu(p_i) \epsilon_\mu^*(p_i)$$

$$+ 4 \frac{p_k q_i - p_j q_i}{(p_i q_i)(p_j p_i + p_i p_k)} \epsilon_\mu(p_j) \epsilon_\mu^*(p_j). \quad \text{(C.23)}$$

There are two things to note about this term. First, the metric tensor is now encoded inside the polarization vectors. In our calculation above, we implicitly showed that these polarizations result in the metric plus gauge terms, which are not singular.[1] Second, the above equation consists of two terms; we derived only the first. Since for the gluon splitting, both gluons can become soft, the original $\widetilde{\mathcal{S}}_{g \to gg}$ consists of two terms: one if particle i becomes soft, one for particle j. In principle, we have to repeat the above steps for the case where gluon i becomes soft. This yields the same result only with i and j reversed.

Finally, we can define the proper soft term $\mathcal{S}_{g \to gg}$ by

$$\mathcal{S}_{g \to gg} = \widetilde{\mathcal{S}}_{g \to gg} + \mathcal{S}_{g \to gg}^{\text{corr}}. \quad \text{(C.24)}$$

---

[1] Admittedly, this is not easy to read off of the above calculation. However, when performing the calculation in detail, this becomes obvious immediately.

Bibliography

[1] G. P. Salam, "Elements of QCD for hadron colliders,"
    arXiv:1011.5131 [hep-ph].

[2] C. Berger, Z. Bern, L. J. Dixon, F. Febres Cordero, D. Forde, *et al.*, "An Automated
    Implementation of On-Shell Methods for One-Loop Amplitudes,"
    Phys.Rev. **D78** (2008) 036003, arXiv:0803.4180 [hep-ph].

[3] C. Berger, Z. Bern, L. J. Dixon, F. Febres Cordero, D. Forde, *et al.*, "Precise
    Predictions for $W + 3$ Jet Production at Hadron Colliders,"
    Phys.Rev.Lett. **102** (2009) 222001, arXiv:0902.2760 [hep-ph].

[4] C. Berger, Z. Bern, L. J. Dixon, F. Febres Cordero, D. Forde, *et al.*, "Next-to-Leading
    Order QCD Predictions for $W + 3$-Jet Distributions at Hadron Colliders,"
    Phys.Rev. **D80** (2009) 074036, arXiv:0907.1984 [hep-ph].

[5] C. Berger, Z. Bern, L. J. Dixon, F. Febres Cordero, D. Forde, *et al.*, "Precise
    Predictions for $W + 4$ Jet Production at the Large Hadron Collider,"
    Phys.Rev.Lett. **106** (2011) 092001, arXiv:1009.2338 [hep-ph].

[6] Z. Bern, L. Dixon, F. Febres Cordero, S. Höche, H. Ita, *et al.*, "Next-to-Leading
    Order $W + 5$-Jet Production at the LHC," *Phys.Rev.* **D88** no. 1, (2013) 014025,
    arXiv:1304.1253 [hep-ph].

[7] F. Cascioli, P. Maierhofer, and S. Pozzorini, "Scattering Amplitudes with Open
    Loops," *Phys.Rev.Lett.* **108** (2012) 111601, arXiv:1111.5206 [hep-ph].

[8] G. Cullen, N. Greiner, G. Heinrich, G. Luisoni, P. Mastrolia, *et al.*, "Automated
    One-Loop Calculations with GoSam," *Eur.Phys.J.* **C72** (2012) 1889,
    arXiv:1111.2034 [hep-ph].

[9] G. Cullen, H. van Deurzen, N. Greiner, G. Heinrich, G. Luisoni, *et al.*, "GoSam-2.0:
    a tool for automated one-loop calculations within the Standard Model and beyond,"
    arXiv:1404.7096 [hep-ph].

[10] S. Badger, B. Biedermann, P. Uwer, and V. Yundin, "NLO QCD corrections to multi-jet production at the LHC with a centre-of-mass energy of $\sqrt{s}$ = 8 TeV," *Phys.Lett.* **B718** (2013) 965–978, arXiv:1209.0098 [hep-ph].

[11] S. Badger, B. Biedermann, P. Uwer, and V. Yundin, "Next-to-leading order QCD corrections to five jet production at the LHC," *Phys.Rev.* **D89** (2014) 034019, arXiv:1309.6585 [hep-ph].

[12] P. Z. Skands, "QCD for Collider Physics," arXiv:1104.2863 [hep-ph].

[13] M. E. Peskin and D. V. Schroeder, *An Introduction to quantum field theory.* Westview Press, 1995.

[14] **Particle Data Group** Collaboration, J. Beringer *et al.*, "Review of Particle Physics (RPP)," *Phys.Rev.* **D86** (2012) 010001.

[15] **CTEQ** Collaboration, R. Brock *et al.*, "Handbook of perturbative QCD: Version 1.0," *Rev.Mod.Phys.* **67** (1995) 157–248.

[16] A. Martin, W. Stirling, R. Thorne, and G. Watt, "Parton distributions for the LHC," *Eur.Phys.J.* **C63** (2009) 189–285, arXiv:0901.0002 [hep-ph].

[17] F. Maltoni, T. McElmurry, R. Putman, and S. Willenbrock, "Choosing the Factorization Scale in Perturbative QCD," arXiv:hep-ph/0703156 [HEP-PH].

[18] S. Weinzierl, "Introduction to Monte Carlo methods," arXiv:hep-ph/0006269 [hep-ph].

[19] C. Bollini and J. Giambiagi, "Dimensional Renormalization: The Number of Dimensions as a Regularizing Parameter," *Nuovo Cim.* **B12** (1972) 20–25.

[20] G. 't Hooft and M. Veltman, "Regularization and Renormalization of Gauge Fields," *Nucl.Phys.* **B44** (1972) 189–213.

[21] T. Kinoshita, "Mass singularities of Feynman amplitudes," *J.Math.Phys.* **3** (1962) 650–677.

[22] T. Lee and M. Nauenberg, "Degenerate Systems and Mass Singularities," *Phys.Rev.* **133** (1964) B1549–B1562.

[23] R. Kleiss and H. Kuijf, "Multi–Gluon Cross-sections and Five Jet Production at Hadron Colliders," *Nucl.Phys.* **B312** (1989) 616.

[24] S. Becker, D. Goetz, C. Reuschle, C. Schwan, and S. Weinzierl, "NLO results for five, six and seven jets in electron-positron annihilation," *Phys.Rev.Lett.* **108** (2012) 032005, arXiv:1111.1733 [hep-ph].

[25] R. K. Ellis, W. J. Stirling, and B. Webber, *QCD and collider physics.* Cambridge University Press, 1996.

[26] S. Catani and M. Seymour, "A General algorithm for calculating jet cross-sections in NLO QCD," *Nucl.Phys.* **B485** (1997) 291–419, arXiv:hep-ph/9605323 [hep-ph].

[27] S. Weinzierl, "Jet algorithms in electron-positron annihilation: Perturbative higher order predictions," *Eur.Phys.J.* **C71** (2011) 1565, arXiv:1011.6247 [hep-ph].

[28] S. Catani, Y. L. Dokshitzer, M. Olsson, G. Turnock, and B. Webber, "New clustering algorithm for multi–jet cross-sections in e+ e- annihilation," *Phys.Lett.* **B269** (1991) 432–438.

[29] W. J. Stirling, "Hard QCD working group: Theory summary," *J.Phys.* **G17** (1991) 1567–1574.

[30] P. Nason and B. Webber, "Next-to-Leading-Order Event Generators," *Ann.Rev.Nucl.Part.Sci.* **62** (2012) 187–213, arXiv:1202.1251 [hep-ph].

[31] T. Gleisberg, S. Hoeche, F. Krauss, M. Schonherr, S. Schumann, *et al.*, "Event generation with SHERPA 1.1," *JHEP* **0902** (2009) 007, arXiv:0811.4622 [hep-ph].

[32] T. Sjostrand, S. Mrenna, and P. Z. Skands, "PYTHIA 6.4 Physics and Manual," *JHEP* **0605** (2006) 026, arXiv:hep-ph/0603175 [hep-ph].

[33] T. Sjostrand, S. Mrenna, and P. Z. Skands, "A Brief Introduction to PYTHIA 8.1," *Comput.Phys.Commun.* **178** (2008) 852–867, arXiv:0710.3820 [hep-ph].

[34] M. Bahr, S. Gieseke, M. Gigg, D. Grellscheid, K. Hamilton, *et al.*, "Herwig++ Physics and Manual," *Eur.Phys.J.* **C58** (2008) 639–707, arXiv:0803.0883 [hep-ph].

[35] S. Dittmaier, P. Uwer, and S. Weinzierl, "NLO QCD corrections to t anti-t + jet production at hadron colliders," *Phys.Rev.Lett.* **98** (2007) 262002, arXiv:hep-ph/0703120 [HEP-PH].

[36] D. Goetz, "Efficient Automated Computation of Tree-Level Amplitudes in QCD and QED," Master's thesis, Johannes Gutenberg-Universität, Mainz, 2011.

[37] M. L. Mangano and S. J. Parke, "Multiparton amplitudes in gauge theories," *Phys.Rept.* **200** (1991) 301–367, arXiv:hep-th/0509223 [hep-th].

[38] F. A. Berends and W. Giele, "The Six Gluon Process as an Example of Weyl-Van Der Waerden Spinor Calculus," *Nucl.Phys.* **B294** (1987) 700.

[39] M. L. Mangano, S. J. Parke, and Z. Xu, "Duality and Multi–Gluon Scattering," *Nucl.Phys.* **B298** (1988) 653.

[40] F. Maltoni, K. Paul, T. Stelzer, and S. Willenbrock, "Color flow decomposition of QCD amplitudes," *Phys.Rev.* **D67** (2003) 014026, `arXiv:hep-ph/0209271 [hep-ph]`.

[41] S. Weinzierl, "Automated computation of spin- and colour-correlated Born matrix elements," *Eur.Phys.J.* **C45** (2006) 745–757, `arXiv:hep-ph/0510157 [hep-ph]`.

[42] F. A. Berends and W. Giele, "Recursive Calculations for Processes with n Gluons," *Nucl.Phys.* **B306** (1988) 759.

[43] L. J. Dixon, "Calculating scattering amplitudes efficiently," `arXiv:hep-ph/9601359 [hep-ph]`.

[44] P. De Causmaecker, R. Gastmans, W. Troost, and T. T. Wu, "Multiple Bremsstrahlung in Gauge Theories at High-Energies. 1. General Formalism for Quantum Electrodynamics," *Nucl.Phys.* **B206** (1982) 53.

[45] J. Gunion and Z. Kunszt, "Improved Analytic Techniques for Tree Graph Calculations and the $ggq\bar{q}\ell\bar{\ell}$ Subprocess," *Phys.Lett.* **B161** (1985) 333.

[46] R. Kleiss and W. J. Stirling, "Spinor Techniques for Calculating $p\bar{p} \to W^{\pm}/Z^0 +$ Jets," *Nucl.Phys.* **B262** (1985) 235–262.

[47] D. Goetz, C. Schwan, and S. Weinzierl, "Random Polarisations of the Dipoles," *Phys.Rev.* **D85** (2012) 116011, `arXiv:1205.4109 [hep-ph]`.

[48] B. L. van der Waerden, "Spinoranalyse," *Göttinger Nachrichten* (1929) 100–109.

[49] O. Laporte and G. E. Uhlenbeck, "Application of Spinor Analysis to the Maxwell and Dirac Equations," *Phys. Rev.* **37** no. 11, (June, 1931) 1380–1397.

[50] S. Dittmaier, "Weyl-van der Waerden formalism for helicity amplitudes of massive particles," *Phys.Rev.* **D59** (1998) 016007, `arXiv:hep-ph/9805445 [hep-ph]`.

[51] Z. Kunszt and D. E. Soper, "Calculation of jet cross-sections in hadron collisions at order α_s^3," *Phys.Rev.* **D46** (1992) 192–221.

[52] A. Bassetto, M. Ciafaloni, and G. Marchesini, "Jet Structure and Infrared Sensitive Quantities in Perturbative QCD," *Phys.Rept.* **100** (1983) 201–272.

[53] V. Sudakov, "Vertex parts at very high-energies in quantum electrodynamics," *Sov.Phys.JETP* **3** (1956) 65–71.

[54] V. Gribov, "A Reggeon Diagram Technique," *Sov.Phys.JETP* **26** (1968) 414–422.

[55] H. Caprasse, "Parton Model With Transverse Momentum,"
Phys.Rev. **D24** (1981) 185–196.

[56] S. Catani and M. Seymour, "The Dipole formalism for the calculation of QCD jet
cross-sections at next–to–leading order," *Phys.Lett.* **B378** (1996) 287–301,
`arXiv:hep-ph/9602277 [hep-ph]`.

[57] S. Frixione, Z. Kunszt, and A. Signer, "Three jet cross-sections to next–to–leading
order," *Nucl.Phys.* **B467** (1996) 399–442, `arXiv:hep-ph/9512328 [hep-ph]`.

[58] S. Frixione, "A General approach to jet cross-sections in QCD,"
Nucl.Phys. **B507** (1997) 295–314, `arXiv:hep-ph/9706545 [hep-ph]`.

[59] G. Bevilacqua, M. Czakon, M. Kubocz, and M. Worek, "Complete Nagy-Soper
subtraction for next–to–leading order calculations in QCD," *JHEP* **1310** (2013) 204,
`arXiv:1308.5605 [hep-ph]`.

[60] T. Robens, "Nagy-Soper Subtraction: A Review,"
Mod.Phys.Lett. **A28** (2013) 1330020, `arXiv:1306.1946 [hep-ph]`.

[61] S. Becker, C. Reuschle, and S. Weinzierl, "Numerical NLO QCD calculations,"
JHEP **1012** (2010) 013, `arXiv:1010.4187 [hep-ph]`.

[62] S. Becker, C. Reuschle, and S. Weinzierl, "Efficiency Improvements for the
Numerical Computation of NLO Corrections," *JHEP* **1207** (2012) 090,
`arXiv:1205.2096 [hep-ph]`.

[63] M. Assadsolimani, S. Becker, and S. Weinzierl, "A Simple formula for the infrared
singular part of the integrand of one-loop QCD amplitudes,"
Phys.Rev. **D81** (2010) 094002, `arXiv:0912.1680 [hep-ph]`.

[64] S. Becker and S. Weinzierl, "Direct numerical integration for multi-loop integrals,"
Eur.Phys.J. **C73** (2013) 2321, `arXiv:1211.0509 [hep-ph]`.

[65] S. Becker and S. Weinzierl, "Direct contour deformation with arbitrary masses in
the loop," *Phys.Rev.* **D86** (2012) 074009, `arXiv:1208.4088 [hep-ph]`.

[66] C. Reuschle and S. Weinzierl, "Decomposition of one-loop QCD amplitudes into
primitive amplitudes based on shuffle relations," *Phys.Rev.* **D88** (2013) 105020,
`arXiv:1310.0413 [hep-ph]`.

[67] W. Gong, Z. Nagy, and D. E. Soper, "Direct numerical integration of one-loop
Feynman diagrams for N-photon amplitudes," *Phys.Rev.* **D79** (2009) 033005,
`arXiv:0812.3686 [hep-ph]`.

[68] F. James, "Monte Carlo Theory and Practice," *Rept.Prog.Phys.* **43** (1980) 1145.

[69] E. C. Anderson, "Monte Carlo Methods and Importance Sampling." Lecture Notes, Berkeley, 1999.

[70] G. P. Lepage, "A New Algorithm for Adaptive Multidimensional Integration," *J.Comput.Phys.* **27** (1978) 192.

[71] G. P. Lepage, "VEGAS: An Adaptive Multidimensional Integration Program," 1980.

[72] T. Hahn, "CUBA: A Library for multidimensional numerical integration," *Comput.Phys.Commun.* **168** (2005) 78–95, arXiv:hep-ph/0404043 [hep-ph].

[73] T. Hahn, "The CUBA library," *Nucl.Instrum.Meth.* **A559** (2006) 273–277, arXiv:hep-ph/0509016 [hep-ph].

[74] "hep-mc — A C++11 Template Library for Monte Carlo Integration." https://github.com/cschwan/hep-mc.

[75] S. Weinzierl, *QCD corrections to $e^+e^- \to 4$ jets.* PhD thesis, Université de Paris-Sud, Orsay, 1998.

[76] S. Weinzierl and D. A. Kosower, "QCD corrections to four jet production and three jet structure in e+ e- annihilation," *Phys.Rev.* **D60** (1999) 054028, arXiv:hep-ph/9901277 [hep-ph].

[77] S. J. Parke and T. Taylor, "An Amplitude for *n* Gluon Scattering," *Phys.Rev.Lett.* **56** (1986) 2459.

[78] R. Kleiss, W. J. Stirling, and S. Ellis, "A New Monte Carlo Treatment of Multiparticle Phase Space at High-energies," *Comput.Phys.Commun.* **40** (1986) 359.

[79] S. Catani, S. Dittmaier, M. H. Seymour, and Z. Trocsanyi, "The Dipole formalism for next–to–leading order QCD calculations with massive partons," *Nucl.Phys.* **B627** (2002) 189–265, arXiv:hep-ph/0201036 [hep-ph].

[80] L. Phaf and S. Weinzierl, "Dipole formalism with heavy fermions," *JHEP* **0104** (2001) 006, arXiv:hep-ph/0102207 [hep-ph].

[81] G. Altarelli and G. Parisi, "Asymptotic Freedom in Parton Language," *Nucl.Phys.* **B126** (1977) 298.

[82] Institute of Electrical Electronics Engineers, "IEEE Standard for Floating-Point Arithmetic," *IEEE Std 754-2008* (Aug, 2008) 1–70.

[83] S. Catani, S. Dittmaier, and Z. Trocsanyi, "One loop singular behavior of QCD and SUSY QCD amplitudes with massive partons," *Phys.Lett.* **B500** (2001) 149–160, arXiv:hep-ph/0011222 [hep-ph].

[84] F. Bloch and A. Nordsieck, "Note on the Radiation Field of the Electron,"
Phys.Rev. **52** (1937) 54–59.

[85] R. Doria, J. Frenkel, and J. Taylor, "Counter Example to Nonabelian
Bloch-Nordsieck Theorem," *Nucl.Phys.* **B168** (1980) 93.

[86] C. Di'Lieto, S. Gendron, I. Halliday, and C. T. Sachrajda, "A Counter Example to
the Bloch-Nordsieck Theorem in Nonabelian Gauge Theories,"
Nucl.Phys. **B183** (1981) 223.

[87] S. Catani, M. Ciafaloni, and G. Marchesini, "Noncancelling Infrared Divergences in
QCD Coherent State," *Nucl.Phys.* **B264** (1986) 588–620.

[88] S. Catani, "Violation of the Bloch-Nordsieck Mechanism in General Nonabelian
Theories and SUSY QCD," *Z.Phys.* **C37** (1988) 357.

[89] S. Dittmaier, "A General approach to photon radiation off fermions,"
Nucl.Phys. **B565** (2000) 69–122, arXiv:hep-ph/9904440 [hep-ph].

[90] S. Dittmaier, A. Kabelschacht, and T. Kasprzik, "Polarized QED splittings of
massive fermions and dipole subtraction for non-collinear-safe observables,"
Nucl.Phys. **B800** (2008) 146–189, arXiv:0802.1405 [hep-ph].

[91] J. Alwall, R. Frederix, S. Frixione, V. Hirschi, F. Maltoni, *et al.*, "The automated
computation of tree-level and next–to–leading order differential cross sections, and
their matching to parton shower simulations," arXiv:1405.0301 [hep-ph].

[92] M. Dinsdale, M. Ternick, and S. Weinzierl, "Parton showers from the dipole
formalism," *Phys.Rev.* **D76** (2007) 094003, arXiv:0709.1026 [hep-ph].

[93] Schwan, Christopher, *Efficient Algorithms for NLO QCD Event Generators.* PhD
thesis, Johannes Gutenberg-Universität Mainz, 2014.

[94] "GSL — GNU Scientific Library." http://www.gnu.org/software/gsl. Version
considered: GSL-1.15.

[95] M. Czakon, C. Papadopoulos, and M. Worek, "Polarizing the Dipoles,"
JHEP **0908** (2009) 085, arXiv:0905.0883 [hep-ph].

[96] F. Jegerlehner, "Facts of life with γ_5," *Eur.Phys.J.* **C18** (2001) 673–679,
arXiv:hep-th/0005255 [hep-th].

[97] S. Weinzierl, "Equivariant dimensional regularization,"
arXiv:hep-ph/9903380 [hep-ph].

[98] P. Draggiotis, R. H. Kleiss, and C. G. Papadopoulos, "On the computation of
multigluon amplitudes," *Phys.Lett.* **B439** (1998) 157–164,
arXiv:hep-ph/9807207 [hep-ph].

[99] P. D. Draggiotis, R. H. Kleiss, and C. G. Papadopoulos, "Multijet production in hadron collisions," *Eur.Phys.J.* **C24** (2002) 447–458, `arXiv:hep-ph/0202201 [hep-ph]`.

[100] D. Goetz, C. Schwan, and S. Weinzierl, "Dipole subtraction with random polarisations," *PoS* **RADCOR2013** (2014) 021, `arXiv:1311.5746 [hep-ph]`.

[101] M. Matsumoto and T. Nishimura, "Mersenne twister: A 623-dimensionally equidistributed uniform pseudo-random number generator," *ACM Trans. Model. Comput. Simul.* **8** no. 1, (Jan., 1998) 3–30. `http://doi.acm.org/10.1145/272991.272995`.

[102] J. Kuipers, T. Ueda, J. Vermaseren, and J. Vollinga, "FORM version 4.0," *Comput.Phys.Commun.* **184** (2013) 1453–1467, `arXiv:1203.6543 [cs.SC]`.

[103] J. Vermaseren, "New features of FORM," `arXiv:math-ph/0010025 [math-ph]`.